Tracing the radiative cooling from supernova shocks in the interstellar medium

INAUGURAL-DISSERTATION

zur
Erlangung des Doktorgrades
der Mathematisch-Naturwissenschaftlichen Fakultät
der Universität zu Köln

vorgelegt von

Ekaterina Makarenko
aus Taganrog, Russland

Accepted in 2025

Главное — делайте всё с увлечением: это страшно украшает жизнь[1].
Лев Ландау

[1]The main thing is to do everything with passion, it embellishes life enormously. (c) Lev Landau

ABSTRACT

Supernovae are the main drivers of a galaxy's chemical, thermal, and dynamic evolution. They also play a central role in regulating star formation by limiting the gas supply in star-forming disk galaxies. Each supernova deposits $\sim 10^{51}$ erg into the interstellar medium, and about 70% of it is lost by radiative cooling. While numerical simulations often include shock heating, the fate of cooling radiation is generally neglected, assuming the surrounding medium is optically thin to such radiation. This simplification underestimates the interaction between cooling photons and the environment, leaving the interaction between supernova remnants and the turbulent interstellar medium inadequately modelled. Analytical (adiabatic expansion) and semi-analytical models, which have traditionally excluded the reabsorption of cooling radiation, are overestimating the momentum and energy injection from supernovae into their surroundings.

To address this issue, we first estimate what energy bands are the most important for radiative cooling. We have developed a post-processing module based on MAPPINGS V, which computes cooling radiation from shock-heated gas (from 10^4 K to 10^8 K). This module can also calculate line emissions under conditions of collisional ionisation equilibrium in hot plasma, such as those found in supernova remnants. Using this approach, we generate realistic emission maps from 3D simulations of supernovae remnant interacting with molecular cloud. This allows direct comparisons with observational data and provides a critical test of observational diagnostics. Additionally, we investigate the application of unsupervised machine learning methods to analyse large datasets of synthetic supernova remnants observations. These allow us to explore the influence of different parameters, such as magnetic field strength and density distribution, in a statistically significant manner. Furthermore, we added new X-ray source terms (energies more than 100 eV) to the on-the-fly radiative transfer module TreeRay/XrayTheSpot to follow the cooling energy of the supernova remnants, improving the dynamical modelling of the radiative cooling in hydrodynamical simulation. We developed a method for on-the-fly radiative transfer of cooling radiation into the FLASH adaptive mesh refinement code, improving the dynamical modelling of radiative cooling in hydrodynamic simulations in the X-ray energy band (energies more than 100 eV). Simulations of the supernova remnant evolution with processed radiative cooling in the X-ray energy band are crucial for calculating X-ray luminosity, often the primary energy band for supernova remnant observations. These are the first simulations to incorporate on-the-fly radiative transfer physics of radiative cooling at this level of detail, offering new insights into the role of supernovae within the interstellar medium.

CONTENTS

List of Figures

1

INTRODUCTION

In our universe, there exists a phenomenon both beautiful and catastrophic: supernova explosion. It is reliably known that already in 1006 AD, astronomers all around the world observed a "guest star", or SN 1006 (see Fig. 1), in the constellation of Lupus which was visible even during the day. However, at that time it was not known yet what a supernova is. So, how does a supernova event occur? Imagine a star one hundred times more massive than our own Sun ($M > 8\ M_{\odot}$), approaching the end of its life. When the core of a massive star exhausts its nuclear fuel, it can no longer generate enough outward pressure from nuclear fusion to counteract the inward pull of gravity. The core collapses under its own weight, sometimes forming a dense neutron star. The collapse triggers a rebound, which, combined with the shock wave generated during the collapse, ejects the outer layers of the star in a powerful supernova explosion. In a moment, a massive star becomes a supernova, releasing a giant amount of energy (around 10^{51} erg) and matter into the surrounding interstellar medium (ISM).

What remains after this event is a supernova remnant (SNR). SNR is a memory of the life cycle of the matter in space: due to the chain of nuclear reactions in the interior of a massive star, metals are released into the ISM during the supernova (SN) explosion. While not every element originates in a SN (some, like s-process elements such as barium and strontium, are formed in asymptotic giant branch stars and other low-mass stars), the most crucial ones, particularly the alpha elements like oxygen, silicon, and magnesium, are primarily generated in SN explosions. These alpha elements are vital in supporting life as we know it. In astrophysics, SNRs are essential because, in addition to enriching the ISM with heavy elements, they also drive turbulence, influence star formation, and provide insights into stellar evolution and cosmic ray acceleration. SNRs are "cosmic laboratories", where some of the most complex and extreme processes in the universe take place.

Nowadays, multi-wavelength observations and simulations of SNRs play a vital role in our understanding of these astrophysical objects. Observations involve studying SNRs across a range of electromagnetic wavelengths, including radio, infrared, optical, X-ray, and gamma-ray. Different wavelengths reveal different aspects of the SNR's structure, composition, and physical processes (for example: magnetic field strength and the distribution of relativistic electrons, identification of shocked regions, determination of chemical composition of ejected material, obtaining the temperature and density of plasma, etc.). On the other hand, numerical simulations are a means for understanding the complex physical processes occurring within SNRs. These simulations involve solving the equations of fluid dynamics, magnetohydrodynamics (MHD), and radiative transfer. MHD simulations are particularly useful for studying the interplay between the SNR's expanding shell and the surrounding interstellar medium (ISM). However, one of the primary challenges in simulations is accurately accounting for the cooling radiation of SNR shocks. Since these are expensive calculations for a wide range of physical parameters (even for a

single SN simulation), the cooling radiation is usually assumed to be optically thin[1] and escaping the simulation box without interaction with the surrounding ISM. In addition to altering the state of the plasma (primarily its temperature), this cooling radiation is the key physical mechanism responsible for the observation of SNRs across infrared, optical, ultraviolet, and soft X-ray wavelengths.

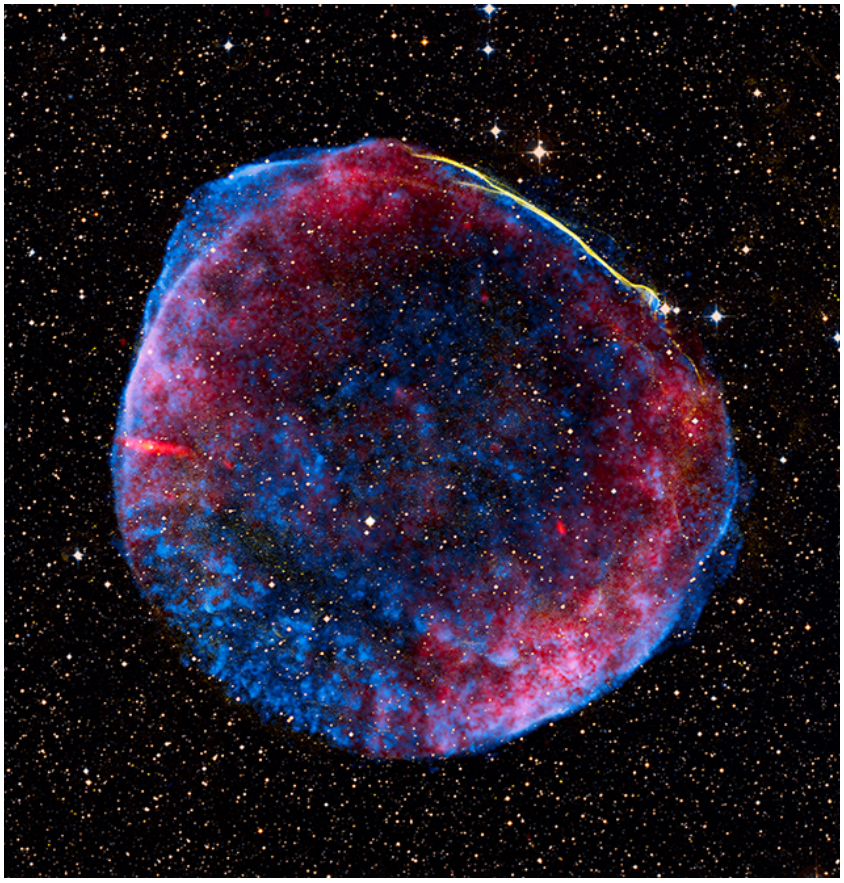

Figure 1: Composite image of the SN 1006 SNR[1], based on data from Chandra (blue), CTIO (yellow), and VLA/GBT (red). In the upper right region of the remnant, a twisting ribbon of light reveals the expanding blast wave interacting with the diffuse surrounding gas.

In this thesis, we aim to explore the significance of radiative cooling in SNRs and how it can be effectively modelled using 3D (magneto-)hydrodynamic simulations. The primary questions we seek to address are as follows:

- How can the radiative cooling from supernova shock waves be calculated during the post-processing step? In which energy band does radiative cooling play the most significant role?
- In what ways can machine learning algorithms be employed to analyse large dataset of synthetic supernova remnants observations?

[1]Optically thin radiation refers to radiation from a source that travels through the ISM with minimal interaction (no absorption or scattering occurs). In reality, the ISM has a complex density structure, such that radiation should interact with the medium, changing the physical parameters of the gas. Accurately capturing this requires a radiative transfer scheme capable of tracking these interactions without being too computationally expensive.

[2]https://sky.esa.int

- What is the most realistic approach for dynamical modelling radiative cooling in 3D hydrodynamic simulations of supernova remnants?

This dissertation is structured in the following way: I first first introduce a theoretical background for the research questions. In **Chapter 1**, I introduce SNRs and their classification as well as the necessary physics describing SNRs. Then I describe the main radiation processes (especially radiative cooling), and the basics of the ISM, including molecular clouds and stellar feedback mechanisms. After discussing the theoretical background that plays an important role for SNRs and the surrounding ISM, I describe SN observations in different wavelengths. I introduce the methods used to model and analyse the physics of the simulations in **Chapter 3**. Here I present the equations of ideal (magneto-)hydrodynamics along with the underlying assumptions and limitations. I give details of the code FLASH used for simulations, tests, and the specific setups. Next, the thesis addresses these questions in detail through scientific papers. The rationale for the main scientific chapters is given in **Chapter 4**. Following this, three papers are included in **Chapter 5, 6 and 7**, respectively, and relate to the three questions highlighted above correspondingly. Finally, I summarise the findings in **Chapter 8**, discuss the conclusions, and outline future research directions.

2

THEORETICAL BACKGROUND

This chapter establishes the theoretical foundation for the thesis, focusing on the key concepts of SNe and SNRs. It provides a detailed explanation of the radiative processes occurring within the plasma, which are critical for a physical understanding of these phenomena. Lastly, the chapter addresses the fundamental properties of the interstellar medium and its significant role in the evolution and dynamics of SNRs.

2.1 Key figures: supernova remnants

2.1.1 Back to the origin: supernova

To define a supernova remnant (SNR), it is essential to first address its origin: a supernova event. Although the term "supernova" (first introduced by Walter Baade and Fritz Zwicky, Baade & Zwicky 1934) nowadays suggests a distinct and well-defined phenomenon, supernovae (SNe) are typically categorised into two main classes (Hoyle & Fowler, 1960). These classes represent two distinct scenarios: different progenitors and completely unrelated physical mechanisms of explosion:

1. **core-collapse SN** (including all **Type II**) is the explosion of a massive star ($M > 8\ M_{\odot}$) which undergoes a gravitational collapse of the stellar core,
2. **thermonuclear explosion (Type Ia)** is the explosion of a carbon-oxygen white dwarf, powered by nuclear fusion of carbon and oxygen to heavier elements.

In the first scenario, a massive star begins hydrogen fusion in its core via the CNO (Carbon-Nitrogen-Oxygen cycle) cycle (Bethe, 1939; Bahcall, 1989), maintaining hydrostatic equilibrium between the gravity (inwards to the star core) and pressure (outwards from the core). The CNO cycle is a few nuclear fusion reactions in which hydrogen is converted into helium in the cores of massive stars, using carbon, nitrogen, and oxygen as catalysts. As the hydrogen is exhausted, the core contracts and heats up, igniting successive fusion stages, including helium, carbon, neon, oxygen, and silicon burning, occurring over progressively shorter timescales. These nuclear reactions produce heavier elements, forming an iron core, which cannot undergo fusion to release energy. As the core mass approaches the Chandrasekhar limit (a maximum mass that a stellar core made primarily of electron-degenerate matter can support), it becomes unstable, collapsing under gravity and leading to a rebound that ejects the star's outer layers and produces a SN Type II explosion.

The evolution of a star that will result in a Type Ia SN typically involves a binary system where a white dwarf accretes material from a companion star. The progenitor star evolves through the main sequence, expelling its outer layers and forming a planetary nebula, leaving behind a carbon-oxygen white dwarf. In a

close binary configuration, the white dwarf can accumulate hydrogen or helium-rich material from its companion via the Roche lobe overflow (the teardrop-shaped region around a star in a binary system where the material is gravitationally bound to that star) or stellar winds. As the white dwarf approaches the Chandrasekhar limit (approximately 1.4 $M_\odot$, Nomoto et al. 1984), the increasing temperature and pressure ignite runaway carbon fusion in its core. The lack of a stabilising core-collapse mechanism results in a thermonuclear explosion that completely disrupts the white dwarf, producing a Type Ia SN.

It is worth noting that some theoretical calculations suggest an upper mass limit for core-collapse SNe. It is generally assumed that stars more massive than 20–25 $M_\odot$ can produce black holes, which may form directly through a "direct collapse" (where all the stellar mass ends up in the black hole without resulting in a SN explosion), referred to as a "failed SN" (Heger et al., 2003; Nomoto et al., 2011). In this thesis, since black hole formation is not included in the simulation, we assume that stars with masses ranging from 8 to 120 $M_\odot$ will produce a SN.

Another commonly used classification for SNe is based on the observed elements in optical spectra and the early phase of the light curve appearance. Furthermore, the classification of SNe is not strictly limited to Types Ia and II. Over years of observation, additional sub-classes (Type Ib, Type IIb, etc.) have been identified through the analysis of SN light curves. However, since our focus does not include simulating these details, in this thesis we will limit ourselves to only mentioning the variety in SNe classification. For those interested in a more comprehensive overview, Branch & Wheeler (2017) or Alsabti & Murdin (2017a) provide an extensive and up-to-date classification of SNRs.

Overall, SNe Type Ia tend to be more luminous so they can be observed at larger distances in the Universe. Type Ia SNe are usually brighter than Type II, as a larger fraction of their energy is converted to light due to less hydrogen in their outer layers, which allows for less energy absorption. This often makes Type Ia appear more "powerful" observationally, though their total energy is comparable to that of Type II SNe. But intrinsically (for spiral galaxies where star formation is ongoing), Type II SNe are more common and located within the galactic disk or near it (Li et al., 2011). For this reason, we use the term SN to refer to SN Type II. In terms of total explosion energy, Type Ia and Type II SNe are generally similar, both releasing on the order of 10^{51} erg into the ISM (Woosley & Weaver, 1986) and this is the most crucial parameter for ISM simulations.

A small remark should be made about the total energy of SN explosions. In core-collapse SNe (type II), the total energy released is approximately 10^{53} erg, but the majority of this energy (about 99%) is carried away by neutrinos. Only about 1% of the energy (about 10^{51} erg), is transferred into the kinetic energy of the ejected material and the shock wave that propagates into the ISM (Bethe, 1990; Burrows et al., 1995). For Type Ia SNe (thermonuclear explosions of white dwarfs), neutrino emission is much less significant, and nearly all of the explosion energy (around 10^{51} erg) is in the ejected material and shock wave, directly impacting the ISM (Hillebrandt & Niemeyer, 2000). Although neutrinos are not included in our simulations, it is important to note the distinction between the two types of SNe regarding their energy distribution (particularly relevant for multimessenger observations, as neutrino detectors, such as Super-Kamiokande or IceCube, are sensitive to the intense neutrino burst from core-collapse SNe).

2.1.2 Supernova rate

Over the years, observational data on SNRs has been collected to study their population. But how rare is a SN event in the local Universe ($z < 1$)? This question is difficult to answer, as all available observational data is influenced by various biases, like interstellar extinction, the galaxy's position, etc. However, we have a more or less clear understanding of the SN rate within our own Galaxy. The estimated core-collapse SN rate according to Rozwadowska et al. (2021) is around 1–2 SN per 100 years. If we assume that a typical SNR stays visible for around 10^5 yr, we should expect to detect around 3000 SNRs in the Milky Way. Although, we know only about 310 SNRs, for example, from the Green catalogue (Green, 2019, 2024). Despite the uncertainty in the visibility time (it can vary a lot, especially due to the local density), we have a lot of factors that bring even more errors: for example, we do not know for sure sources nearby are contaminating the field of view. That would mean that we cannot detect extended (or old) SNRs that evolve in low density regions or those not bright enough compared to the background sky. Hence, we cannot be sure how many SNRs are in the Milky Way, but the known number of 300 is definitely underestimating the complete population of SNRs.

Recent advancements using telescopes like MeerKAT[3] have started to close this gap by identifying new SNRs at lower flux thresholds, enabling to detect remnants with previously too weak signals (Anderson et al., 2024). In its survey, MeerKAT made significant progress by revealing previously undetected SNRs in dense regions of the Galactic plane, although the survey still falls short of the theoretical number, highlighting the continued observational challenges. Expanding the reach and sensitivity of surveys with next-generation telescopes, including those in the upcoming Square Kilometre Array (SKA) project[4], is expected to further narrow this gap by unveiling even more faint and distant remnants. However, to fully match the number of SNRs from theory with observations will likely require a combination of enhanced observational coverage, improved detection algorithms, and refined theoretical models.

2.1.3 The ISM: Birthplace of SNRs

Massive stars are not born in empty space. They are born and live their lives in the surrounding medium — the interstellar medium. The ISM is all the matter and fields that fill interstellar space inside galaxies. The ISM consists of gas, dust (around 1% of the gas mass), interstellar electromagnetic fields, cosmic rays, and dark matter (Draine, 2011). The overview of physical parameters of the components of the ISM can be found in Table 2.1. The chemical composition of the ISM is a product of primary nucleosynthesis and nuclear fusion in stars. Throughout their lives, stars emit stellar winds, which return elements from the star's atmosphere into the environment. SNe enrich the ISM with chemical elements, cosmic rays, energy, and form new morphological structures in their surroundings. Thus, there is a continuous exchange of matter and energy. In addition, all the states of ISM are not uniformly distributed; they typically exhibit a hierarchical structure, consisting of molecular clouds, filaments, and cores. We will discuss molecular clouds in

[3] https://www.sarao.ac.za
[4] https://www.skao.int/en

greater detail later in this thesis, as they serve as nurseries of massive stars, which eventually explode as SNe.

Phase	Temperature (K)	Density (cm^{-3})	Volume fraction
Molecular cloud	10-20	$>10^2$	< 1%
Cold neutral medium (CNM)	50-100	20-50	1-5%
Warm neutral medium (WNM)	6000-10000	0.2-0.5	10-20%
Warm ionised medium (WIM)	$\sim$ 8000	0.2-0.5	$\sim$40%
Hot ionised medium (HIM)	10^6-10^7	$\sim 10^{-2}$	$\sim$50%

Table 2.1: Different phases of the ISM. The table presents the name of the ISM phase, temperature, density, and volume fraction. Each phase has the typical physical conditions, with molecular clouds being the densest and coldest, while the hot ionised medium is the most diffuse and hottest, occupying the largest volume fraction in the ISM. Adapted from Klessen & Glover (2016) and de Avillez & Breitschwerdt (2004).

2.1.4 "Young" and "old" supernova remnants

After reading many observational and theoretical studies about SNRs, it becomes evident that the terminology for referring to a SNR as "young" or "old" is not standardised as different authors apply these terms to varying age ranges of SNRs. For clarity, we will adopt the following definitions in this dissertation:

- A "young" SNR refers to one in the earliest stages of SNR development, when the emission is primarily in X-rays (as at this stage a significant part of the SN explosion is lost via the X-ray energy band). It also has high shock wave velocities (more than 1000 km/s).

- An "old" SNR predominantly emits in ultraviolet or optical light and is characterised by lower shock wave velocities. At this stage, radiative cooling plays a significant role, although the remnant has not yet mixed with the ISM, so still can be detected.

2.1.5 Classification of supernova remnants

It would be logical to assume that the classification of SNRs corresponds to the two types of SN explosions. However, we do not know for sure the explosion mechanism or precursor object for the majority of observed SNRs. Instead, for most of the observed SNRs, the explosion mechanism and progenitor object are still uncertain. Consequently, SNRs are classified according to their morphology into the following types (see Figure 2 for an example of each type):

a) **shell-type**: the most common category, characterised by a clearly distinguishable shell. A "shell" is the outward-moving, shock-heated layer of ejected stellar material and ISM compressed by the SN explosion, which radiates across multiple wavelengths (as it expands and interacts with its surroundings, like in Cas A, Reed et al. 1995),

b) **filled centre**: in these SNRs, the shell is less distinct, and the morphology is dominated by the pulsar wind nebulae in radio and X-ray observations (like for the Crab nebula, Weisskopf et al. 2000; Bietenholz et al. 2004). This is a rare type, comprising only about 6% of all SNRs in Green's catalogue,

c) **composite**: the second most common type, representing a combination of shell-type and filled-centre characteristics (like Vela SNR, Helfand et al. 2001),

d) **mixed-morphology**: typically older SNRs that exhibit shell-type morphology in radio, but a filled-centre morphology in X-rays (Rho & Petre, 1998). In these remnants, the X-ray emission is thermal, rather than generated by a pulsar wind nebula. Currently, around 25 SNRs have been classified as mixed-morphology.

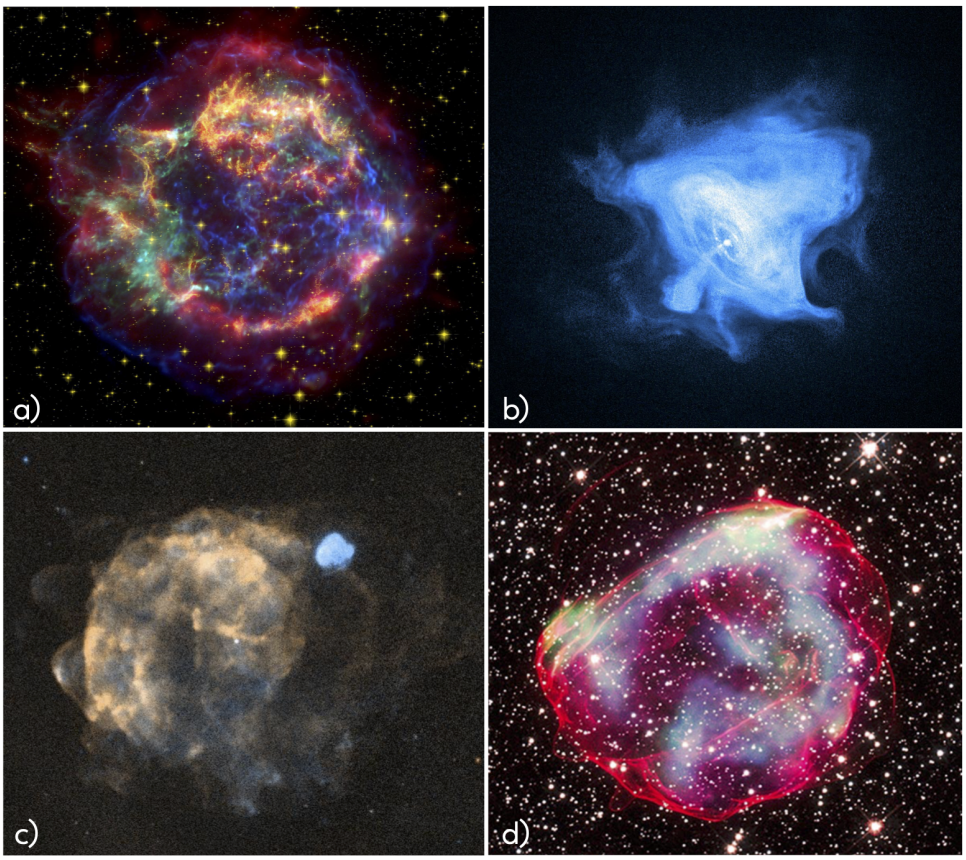

Figure 2: Different types of SNR morphologies. **a)** A false colour image of Cassiopeia A, shell-type morphology SNR[5]; **b)** Crab Nebula pulsar, filled centre type[6]; **c)** Vela Supernova Remnant, composite type[7]; **d)** SNR 0519-69.0, mixed-morphology type[8].

[5]Credit: Chandra/Spitzer/Hubble, NASA/JPL-Caltech.
[6]Credit: Chandra,NASA/CXC/SAO/F.Seward et al..
[7]Credit: ROSAT.
[8]Credit: X-ray: NASA/CXC/GSFC/B. J. Williams et al.; Optical: NASA/ESA/STScI.

2.1.6

Evolution of the supernova remnant

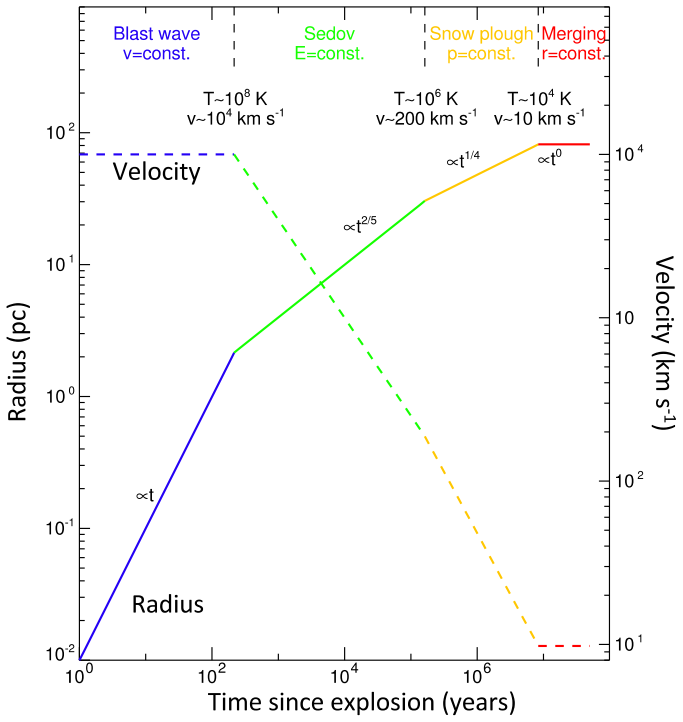

Figure 3: Characteristic phases of a SNR evolution (top part of the figure). The radius of the SNR (left y-axis) grows with time, the blast-wave (forward shock) velocity (right axis) decreases. The Figure is taken from Micelotta et al. (2018).

The evolution of the SNR can be divided into four stages (Woltjer, 1972), see Figure 3 (where r is a radius of SNR and t is the evolution time after the explosion):

1. **Ejecta-dominated phase ($r \propto t$):** sometimes called a free expansion phase, when most of the explosion energy is in the expanding ejecta. The ejecta mass is still more than the swept up mass, and shock velocities are approximately 5000 to 10000 km s^{-1} (Chevalier, 1977).

2. **Sedov-Taylor phase (ST, $r \propto t^{2/5}$):** starts when the swept up mass is higher than the ejected mass. The radius of the SNR follows the self-similar Sedov solution (Taylor, 1950; Sedov, 1959). The explosion energy is transformed into the internal energy and kinetic energy of the hot, expanding shell. Radiative losses are negligible at the ST stage.

3. **Pressure driven snow-plough phase (PDS, $r \propto t^{2/7}$)**: starts when the radiative losses become significant (the radiative losses timescale is around the same order as the SNR age (Ostriker & McKee, 1988; Cioffi et al., 1988).

4. **The merging phase:** when the blast wave velocity approaches the sound speed or Alfvén velocity[9], the shock wave begins to dissipate, and the shell

[9]The Alfvén velocity (v_A) is the speed at which waves propagate along magnetic field lines in a magnetised plasma, given by $v_A = B/\sqrt{4\pi\rho}$, where B is the magnetic field strength and ρ is the mass density of the plasma.

expands subsonically. This phase marks the end of the SNR's active life, though some residual characteristics remain as the remnant leaves behind a hot plasma bubble.

After these stages are completed, the distinct boundary between the SNR and the ISM blurs, as the remnant's expanding shell and the surrounding ISM blend together. This process marks the end of the SNR's life as it becomes part of the broader ISM environment.

Sometimes, the "**transition phase (TR)**" (Haid et al., 2016) of SNR evolution is also described between the ST phase and the PDS phase. During this phase, the SNR undergoes significant changes as it evolves from an era where energy loss is negligible to a stage where radiative losses become significant. In this phase, the SNR's expansion rate slows, and the dynamics of the remnant start to be influenced more by the energy radiated away and less by the initial explosion energy. This transition marks the shift from an energy-conserving phase to a phase where momentum conservation becomes more dominant.

2.1.7 Observational signatures

SNRs at different stages of evolution can be observed in almost the entire frequency range, each providing different insights into their properties and evolution. The main energy bands where SNRs are observed are:

- **Radio ($\sim$ 1 GHz to 100 GHz)**: observations in the radio band reveal the synchrotron radiation from high-energy electrons accelerated by the shock waves in the SNR. This emission is often associated with the remnant's shell structure and can provide information about the magnetic fields and particle acceleration processes (Dubner & Giacani, 2015). Most of the SNRs in our Galaxy are detected in the radio band.

- **Optical (roughly 400 nm to 700 nm)**: highlights the emission from ionised gas and emission lines from elements such as hydrogen (Hα 6563 Å), oxygen ([O III] 5007 Å), nitrogen ([N II] 6583 Å)and sulphur ([S II] 6517, 6731 Å). This band provides detailed information about SNR's age (typically, old SNRs are observed in the optical), and diagnostics to study the shocked gas and interactions with the surrounding ISM (Fesen et al., 1985; Blair & Kirshner, 1985).

- **Infrared (IR) (around 1 to 100 μm)**: valuable for probing the cooler, dust-rich regions of SNRs. These wavelengths are well-suited for detecting thermal emission from dust and molecules within the SNR, providing insights into regions obscured by optical and ultraviolet light, offering a more complete picture of the SNR (see for a detailed review a chapter "Infrared Emission from Supernova Remnants: Formation and Destruction of Dust", from Alsabti & Murdin 2017b).

- **Ultraviolet (UV) (about 10 nm to 400 nm)**: can reveal the emission from hotter, ionised gas and the details about the remnant's interaction with the interstellar medium. UV light can also provide information about the thermal emission from shocked gas and the presence of different ions (Dopita et al., 1984).

- **X-ray (approximately 0.1 keV to 12 keV)**: crucial for studying the high-energy processes in SNRs. They reveal thermal emission from hot plasma (shock-heated gas) and non-thermal emission from accelerated electrons. X-rays provide insights into the remnant's thermal structure, shock velocities, and energy distribution (see for a detailed review a chapter "X-Ray Emission Properties of Supernova Remnants", from Alsabti & Murdin 2017b).

- **Gamma-ray (above 511 keV)**: used to study the highest-energy processes in SNRs. They can reveal information about cosmic ray acceleration and interactions with the surrounding medium (Slane et al., 2015). Gamma-rays are often associated with the decay of neutral pions or interactions of high-energy particles with ambient matter (see for a detailed review a chapter "High-Energy Gamma Rays from Supernova Remnants", from Alsabti & Murdin 2017b).

Each of these energy bands contributes unique information, helping to understand the different phases and processes occurring within and around a SNR. That is why multi-wavelength observations of SNRs (and synthetic observations from simulations) are crucial nowadays as they provide a comprehensive view of the complex physical processes involved, that cannot be obtained from a single wavelength alone.

2.1.8 What is left after all?

After a SNR has evolved and merged with the ISM, several key components may remain. These include a neutron star (Landau, 1932) or black hole (if the core of the exploded star is sufficiently massive), and possibly a pulsar wind nebula (if a neutron star is present). Additionally, the remnant may leave behind a hot plasma bubble that cools and mixes with the interstellar medium, along with dispersed heavy elements and dust that contribute to the enrichment of the surrounding ISM. High-energy cosmic rays from the explosion can also persist and diffuse through the ISM.

2.2 Radiation processes

There are various radiation processes that can occur in a SNR or next to it. We will describe only the most relevant ones for this thesis.

2.2.1 Thomson scattering

We begin with the simplest radiation mechanism from moving charged particles: Thomson scattering. Thomson scattering is a scattering of electromagnetic radiation by a free charged particle, typically an electron. While this effect is not directly relevant to this work, it is important as it serves as the classical limit (i.e. low energy) of the Compton effect (Compton, 1923), so we will briefly outline its concept.

Thomson scattering is named after the English physicist J.J. Thomson, who studied the behaviour of charged particles interacting with electromagnetic waves.

When exposed to the alternating electric field of the wave, the charged particle oscillates at the wave's frequency, experiencing varying acceleration. A charged particle undergoing acceleration emits radiation, with the emitted energy drawn from the primary wave and re-radiated in all directions at the same frequency. The Thomson cross section can be expressed as:

$$\sigma_T = \frac{8\pi}{3} r_e^2 \simeq 6.65 \times 10^{-25}\ [cm^2], \tag{2.1}$$

where r_e is a radius of electron and $r_e = e^2/(m_e c^2)$ in a non-relativistic case. A similar type of scattering occurs with atomic nuclei. But because the scattering cross-section is inversely proportional to the square of the particle's mass, for a proton, the cross-section is almost 4 million times smaller than that of Thomson scattering on a free electron (Rybicki & Lightman, 1979). Thomson scattering plays a significant role in the opacity of stellar interiors. It affects the radiation spectrum of hot stars and influences the profile of spectral lines in the atmospheres of hot stars (Mihalas, 1978). Additionally, it also contributes to the formation of X-ray spectra in accretion disks, white dwarfs, and other high-energy astrophysical environments (Frank et al., 2014).

2.2.2 Compton scattering

Compton scattering (also known as the Compton effect) is the elastic scattering of a photon by a charged particle, typically an electron (see Figure 4). The Compton effect was discovered by Arthur Compton in 1923 during experiments with X-ray radiation, a discovery for which he received the Nobel Prize in Physics in 1927 (Compton, 1923).

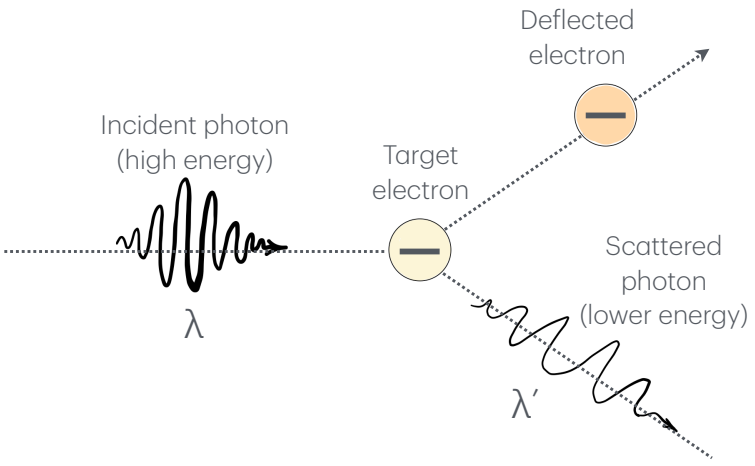

Figure 4: Sketch of a Compton scattering.

The full cross section can be calculated as:

$$\sigma_c = 2\pi r_e^2 \left[\frac{1+\epsilon}{\epsilon^3} \left(\frac{2\epsilon(1+\epsilon)}{1+2\epsilon} - \ln(1+2\epsilon) \right) + \frac{\ln(1+2\epsilon)}{2\epsilon} - \frac{1+3\epsilon}{(1+2\epsilon)^2} \right], \tag{2.2}$$

where $\epsilon = E_\gamma / m_e c^2$ is the energy of the photon in terms of the electron rest energy and r_e is the electron radius. When $E_\gamma \ll m_e c^2$ (the low-energy limit), we can get the Thompson scattering cross section. Compton scattering can occur with any charged particle (not only on electrons), such as protons, but because the scattering cross-section is inversely proportional to the square of the particle's mass, it is far less effective for heavy particles.

In astrophysics, there is the inverse Compton effect and the Compton effect. Here is the distinction:

- If scattering leads to a decrease in photon energy, then this process is called the Compton effect (since part of the photon's energy is transferred to the deflected electron, which corresponds to an increase in the wavelength of the photon. It can be an X-ray or gamma photon). For example, in young SNRs, high-energy X-ray and gamma-ray photons can scatter off electrons, e.g. Compton scattering.
- If scattering occurs when a charged particle transfers part of its energy to the photon, then this is inverse Compton (also resulting in a decrease in the photon's wavelength). Inverse Compton scattering, for example, happens in the nebulae surrounding pulsars, where energetic electrons from the pulsar wind scatter off lower-energy photons, boosting them to X-ray or gamma-ray energies. Inverse Compton effect also occurs when low-energy photons (such as those from the cosmic microwave background or synchrotron radiation) are boosted to higher energies (typically X-ray or gamma-ray) by interacting with highly relativistic electrons in jets from Active Galactic Nuclei.

Both effects are crucial in understanding high-energy astrophysical environments.

2.2.3 Synchrotron radiation

Synchrotron radiation is the electromagnetic radiation emitted by relativistic charged particles as they gyrate around magnetic field lines. Because the power radiated by a charged particle is proportional to the square of its acceleration, the lightest charged particles (electrons and positrons) emit synchrotron radiation most efficiently (Jackson, 1998). Therefore, in nearly all cases, when we refer to synchrotron radiation, we are specifically discussing radiation from electrons or positrons.

In SNRs, electrons accelerated to relativistic speeds by shock waves emitting synchrotron radiation, especially in the radio and X-ray because the thermal emission is not too bright in these bands. This synchrotron radiation helps map magnetic fields and particle acceleration in the SNR (Reynolds, 2008).

2.2.4 Bremsstrahlung or Free-Free Emission

The radiation processes discussed so far involve constant or oscillating accelerations of charged particles. However, one of the most important continuum radiation processes arises from the interactions between charged particles, leading to impulsive accelerations and subsequent radiation. As with previous processes, the emission is primarily dominated by the lightest charged particles, such as electrons and positrons, because they accelerate most efficiently under an electric field (e.g.

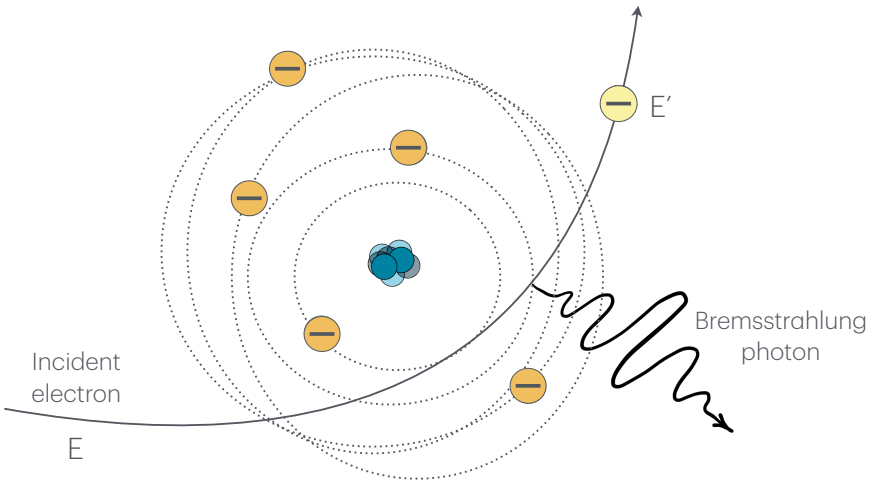

Figure 5: Sketch of a Bremsstrahlung emission.

the deflection of a charged particle happens in the electric field of another charged particle, Jackson 1998). This radiation process is known as bremsstrahlung (German for "braking radiation") in high-energy astrophysics, while in radio and infrared astronomy, it is commonly referred to as free-free emission, see Figure 5.

Bremsstrahlung is especially important in ionised gas (plasma) and becomes prominent at temperatures above 5000 K. For example, in H II regions, which typically have temperatures around T $\sim$ 10 000 K, bremsstrahlung dominates the continuum radiation from the radio to infrared bands (Osterbrock & Ferland, 2006). One might expect that radio bremsstrahlung also plays a significant role in mature SNRs, where the shock becomes radiative, and the plasma behind it cools to temperatures of T $\sim$ 5 000 – 20 000 K. However, even in old remnants, radio synchrotron emission usually dominates over bremsstrahlung (Condon & Ransom, 2016). The identification of free-free emission is often used to distinguish H II regions, dominated by bremsstrahlung, from SNRs, where synchrotron emission prevails. In contrast, bremsstrahlung is much more significant in the X-ray regime for SNRs. For X-ray-emitting plasmas with temperatures exceeding 10^6 K, bremsstrahlung is often the dominant source of continuum radiation. In these cases, the electrons responsible for the emission follow a Maxwellian velocity distribution, and the process is typically referred to as thermal bremsstrahlung.

2.2.5 Radiative cooling

Typically, hot gas is ionised by collisions with electrons (due to a nearby SN event, stellar winds, etc). When the gas gains the energy, it can loose it through multiple collisions, e.g. via radiative cooling. We say that plasma is in collisional ionisation equilibrium (CIE) when the plasma is optically thin to its own radiation and when there is no external radiation field or sources that affect the ionisation balance, but also that the plasma has had enough time to relax to an equilibrium state. Photoionisation and Compton ionisation therefore can be neglected in the case of CIE.

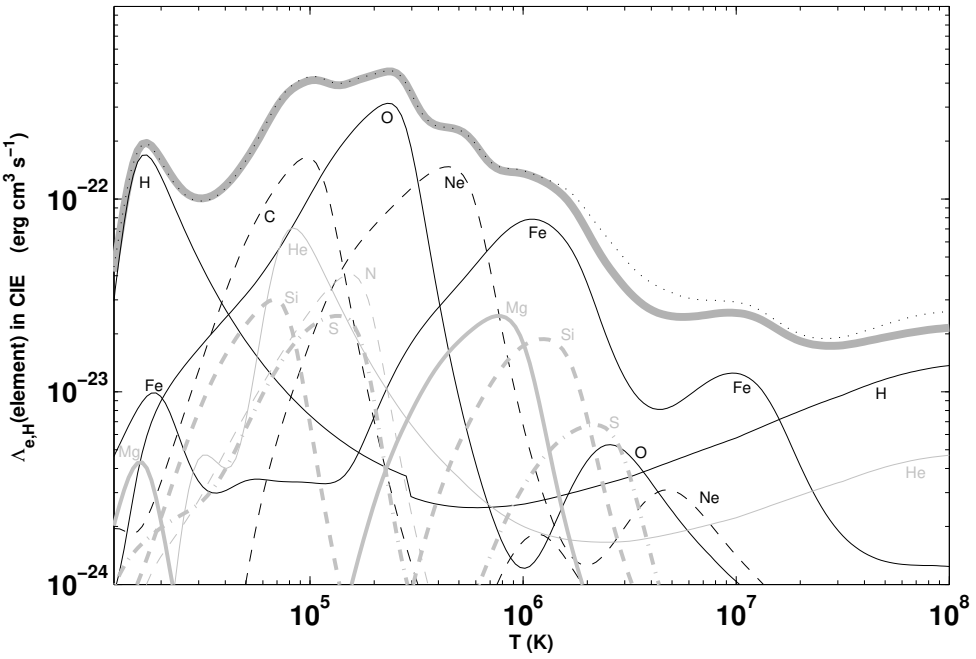

Figure 6: Element-by-element cooling efficiencies versus temperature (solar metallicity). The total CIE cooling efficiency due to all elements is shown by the upper thick grey curve. Here $\Lambda_{e,H}$ means $\Lambda/n_e/n_H$. The figure is taken from Gnat & Ferland (2012).

CIE is an ideal state of the plasma in the sense that it is rarely achieved in detail in astrophysical plasmas. Despite this, it is the basic starting point of most models of hot astrophysical plasmas and it can give us useful insights into the physics of such plasmas even if CIE is not strictly achieved in reality.

For the temperatures T > 10^4 K, we can write the rate loss of thermal energy from the gas per unit volume:

$$\Lambda = n_e n_H \cdot f_{\rm cool}(T), \tag{2.3}$$

where $f_{\rm cool}(T)$ is a radiative cooling function, n_e is the electron density, n_H is the hydrogen density.

To calculate a CIE cooling curve, first determine the ionisation fractions for each element by balancing ionisation and recombination rates at each temperature. Next, compute the population of energy levels for each ion by solving the statistical equilibrium equations, which account for collisional and radiative processes. Then, calculate the cooling rate for each transition by summing the energy emitted via radiative decays. Combine the contributions from all ions and elements to determine the total radiative cooling rate as a function of temperature, normalising by the square of the gas density. We would look next at the example of the CIE curve calculated with CLOUDY code. In a hot ionised plasma, cooling occurs both from the ionisation process itself and through various line and continuum emission processes (see Figure 6 showing the cooling function for lines (solid) and continuum (dashed)):

- **Hydrogen & Helium.** Cooling is primarily driven by the collisional excitation of neutral hydrogen and neutral helium at temperatures between 2×10^4 K and 4×10^4 K, followed by line emission. As temperatures rise above $\sim 4 \times 10^5$ K, the collisional excitation of singly ionised helium (He^+) also becomes significant. However, at even higher temperatures, the efficiency of emission-line cooling from hydrogen and helium decreases. Once hydrogen and helium atoms are almost fully ionised, they lose the ability to contribute significantly to cooling via line emission because there are no bound electrons to transition between energy levels and emit photons. Line cooling also relies on bound-bound transitions of electrons within atoms or ions. Higher-energy collisions strip electrons from the atoms and ions as temperatures increase, leaving fewer bound electrons to participate in such transitions. This effect is particularly important for hydrogen and helium, which have simple atomic structures. At higher temperatures, cooling becomes dominated by heavier elements (metals) and bremsstrahlung.

- **Line emission (from Metal Ions).**

  At temperatures $T \sim 1.5 \times 10^4$ K forbidden lines from collisionally excited metal ions (e.g. [O II] and [N II]) are the primary emission-line coolants. At higher temperatures, cooling is increasingly driven by collisionally excited resonant permitted lines (e.g. C IV, N V, and O VI), which reach peak cooling efficiency at $\sim 2.5 \times 10^5$ K, depending on the gas's metallicity. Around 10^5 K, collisional excitation of "inter-system" [10] (e.g. [O III], [Si III], [Fe III]) and fine-structure lines[11] (e.g, [C II]) also contributes significantly. In the low-density ISM, these lines contribute significantly to cooling, as the low collision rates allow these "forbidden" transitions to emit radiation rather than being collisionally de-excited. Other important low-density cooling ions above 10^5 K include [O VI], [S IV], [C IV] and [N V], each producing strong emission lines in the far-ultraviolet range. At higher densities, optical lines of Fe X and Fe XIV can be observed. Generally, metal-line cooling dominates in the temperature range of approximately 4×10^4 to 10^7 K, depending on the gas metallicity.

- **Free-Free emission (continuum).** At temperatures above 10^6 – 10^7 K, free-free cooling becomes the primary cooling mechanism and remains dominant as temperatures increase. The free-free cooling rate scales with $T^{1/2}$, with contributions from hydrogen, helium, and metal ions. For metals, the cooling rate depends on both their relative abundances and their atomic number squared. This cooling produces a thermal bremsstrahlung continuum that appears in the extreme ultraviolet (EUV) and soft X-ray regions of the spectrum, shaping the overall spectrum of hot ionised plasma.

[10] These are transitions between energy levels of different spin states within an ion, such as singlet-triplet transitions. Because these transitions are "forbidden" under normal conditions (due to quantum mechanical spin selection rules), they occur with low probability.

[11] These transitions arise from small energy differences between closely spaced electronic states due to spin-orbit coupling within ions.

2.3 Environment: basics of the interstellar medium

2.3.1 Composition of the ISM

Massive stars are formed within the dense regions of the ISM. The environment of the ISM, particularly within molecular clouds (MCs), supports the complex processes of star formation, allowing massive stars to form from the matter around them. The ISM consists of gas, dust, radiation field, magnetic field and cosmic rays that fill all the space between stars. In our Galaxy, the gas, primarily hydrogen (mass weighted in total around 70%: in the form of H^+ with the volume filling factor 0.64, H with 0.31 and H_2 with 0.05 respectively) and helium (around 28%), makes up about 98% of the ISM (Tielens, 2005). All the other elements or "metals" contribute around 2% and are produced in stars and are ejected into the ISM through stellar winds, as well as during SNe events. The dust, which accounts for about 1% of the ISM's mass, consists of small solid particles made of elements like carbon, silicon, and oxygen. As we described in Sec. 2.1.3, gas in the ISM exists in various phases: cold molecular clouds, warm and cool atomic regions, and hot ionised gas. Gas can also be in transitional states between these phases due to ongoing physical processes such as heating, cooling, and ionisation. The next component, the interstellar radiation field (ISRF) (Mathis et al., 1983), consists of: starlight from stars across various ages and temperatures, thermal infrared emission from interstellar dust heated by starlight, the cosmic microwave background (corresponds to a blackbody temperature of 2.725 K), which represents the relic radiation from the Big Bang, Galactic synchrotron emission and X-ray emission from the hot plasma (Doroshkevich & Novikov, 1964). The ISRF is particularly important in the ultraviolet regime (4–13.6 eV) and is noted as G_0. G_0 = 1.7 in the solar neighbourhood in Habing units (where 1 Habing unit = 1.2×10^{-4} erg cm^{-2} s^{-1} sr^{-1}, Habing 1968), but it can vary depending on the proximity of the sources of ISRF mentioned above. Cosmic rays are high-energy particles (primarily protons and atomic nuclei, with energies from 100 MeV to more than 1 TeV) that move through space at nearly the speed of light. Cosmic rays originate from SNe, Active Galactic Nuclei, and other high-energy environments. These particles interact with the ISM, contributing to ionisation, heating, and chemical processes (Grenier et al., 2015). Together, these components play a crucial role in the lifecycle of stars and galaxies, facilitating processes such as star formation.

2.3.2 Heating and cooling processes

To accurately model the various phases of the ISM across its full range of temperatures and densities, it is essential to define the primary heating and cooling processes that dominate in each regime.

Heating

H_2 formation When molecular hydrogen (H_2) forms on dust grains in the ISM, $\sim$ 4.48 eV of energy is released per molecule. This energy is initially stored as rotational or vibrational excitation in the newly formed H_2 molecule and is subsequently transferred to the surrounding gas through collisions. This mechanism is

particularly significant in molecular clouds where H_2 formation is rapid and drives local heating in dense star-forming regions (Goldsmith & Langer, 1978).

Photoelectric heating When UV photons hit dust grains in the ISM, they can eject electrons. The ejected electron's energy equals the difference between the photon energy and the dust grain's binding energy and ionising potential. This excess energy is transferred as heat to nearby gas particles. This process is a key heating source in the diffuse ISM and contributes significantly to the thermal balance in photodissociation regions (PDRs) near young, massive stars (Bakes & Tielens, 1994).

Photodissociation of H_2 UV photons can dissociate molecular hydrogen (H_2), creating atoms with higher-than-average kinetic energy. This process releases approximately 0.4 eV per dissociation, which contributes to the heating of gas near young, massive stars in H II regions. Photodissociation thus serves as a primary heat source in the outer layers of molecular clouds, where UV photons permeate and actively shape the ISM's temperature structure (van Dishoeck & Black, 1986).

UV pumping UV pumping occurs when an H_2 molecule absorbs a UV photon and then releases this energy via collisions before radiatively decaying to the ground state. This collisional de-excitation heats the gas effectively in denser regions, as seen in the cores of molecular clouds and star-forming regions where radiative decay rates are slow. UV pumping thereby contributes to the energy balance in high-density gas exposed to UV fields (Hollenbach & Tielens, 1999; Burton et al., 1990).

Cosmic rays Cosmic rays can penetrate deep into dense molecular clouds, ionising atoms and molecules via collision. The energy transferred per collision is often greater than the ionisation energy, imparting substantial kinetic energy to dissociation products, which can lead to further secondary ionisations and subsequent heating. This process is particularly important in shielded regions far from stellar sources, such as the interiors of molecular clouds where cosmic rays are the primary heat source (Goldsmith & Langer, 1978).

X-rays X-ray photons also contribute to ISM heating, particularly in regions surrounding X-ray binaries or Active Galactic Nuclei, where high-energy radiation ionises and heats the surrounding gas. X-rays drive heating in the hot ISM and X-ray-dominated regions near black holes or SNRs, impacting both the thermal and ionisation states of the surrounding medium (Maloney et al., 1996).

Adiabatic compression Adiabatic compression is often driven by gravitational collapse or large-scale compression. As the gas is compressed, its volume decreases, and the kinetic energy of its particles is converted into thermal motion, leading to an increase in temperature. This type of dynamical heating is generally observed in star-forming regions, where gravitational contraction heats the gas without significantly changing its entropy.

Shock heating Shock heating is an irreversible process when a shock wave compresses the gas. Unlike adiabatic compression, shocks dramatically increase the

entropy of the gas, converting bulk kinetic energy into heat. This mechanism is prevalent around SNRs, where shock waves heat the surrounding gas to 10^7 K. Shock heating also plays a critical role in galaxy cluster mergers, where large-scale shocks driven by colliding clusters elevate the gas temperature significantly.

Cooling

Molecular H_2 Cooling Molecular hydrogen (H_2) cooling becomes relevant for gas temperatures above approximately 100 K, for the first permitted rotational transition. In star-forming regions and shock-heated gas, H_2 can act as an effective coolant due to the high energy spacing of its rotational levels, despite its restricted transition rules (Hollenbach & McKee, 1979). This cooling is essential in dense molecular clouds and post-shock regions, where temperatures can reach these thresholds.

HD Cooling Although hydrogen deuteride (HD) is much less abundant than H_2, it can be a crucial coolant at low temperatures (below 50 K), particularly in early-universe conditions and cold molecular clouds. HD's lower rotational energy spacing enables it to cool efficiently at low temperatures, where H_2 cooling would be ineffective (Klessen & Glover, 2016).

Dust Cooling Dust grains, particularly in dense molecular clouds, play a role in cooling by radiating energy in the infrared continuum. The dust temperature is regulated by a balance between infrared emission and heating from the ISRF. When dust and gas temperatures differ, collisions can transfer heat from gas to dust, causing cooling (Goldsmith, 2001).

CO Cooling Carbon monoxide (CO) is an efficient coolant in molecular clouds, as it provides low-energy transitions between rotational states. CO cooling is critical in dense molecular regions, where neutral and ionised carbon has combined with oxygen to form CO. However, CO cooling may become inefficient in high-density cores of molecular clouds where it becomes optically thick or "frozen out" onto dust grains, reducing its cooling efficiency (Goldsmith, 2001). This process is key in the colder regions of star-forming clouds and regions where CO remains in the gas phase.

Dipole Transitions At higher temperatures, particularly in ionised or atomic gas, dipole-allowed electronic transitions are a primary cooling process. These quantum-mechanically permitted transitions occur when an electron spontaneously jumps from a higher energy state to a lower one, emitting a photon. Around 10^4 K, the Lyman-α transition is dominant, where electrons in hydrogen atoms transition back to the ground state, releasing a UV photon. At higher temperatures, metals such as C, O, Ne, and Fe contribute more significantly to cooling through line emissions. These emissions are significant in hot gas environments, such as the warm ionised medium and the intracluster medium (Allen et al., 2008; Gnat & Ferland, 2012).

Fine Structure Transitions Due to spin-orbit coupling, atoms and ions may exhibit small energy differences within otherwise degenerate levels, leading to a fine structure cooling. These quantum-mechanically permitted but "forbidden" transitions

occur at lower temperatures, typically below 10^4 K, when electronic transitions become less probable. Fine-structure cooling is significant in the warm neutral medium and photodissociation regions near star-forming regions, where lines such as carbon ([C II]) and oxygen ([O I]) dominate the cooling process (Wolfire et al., 1995).

Forbidden Lines Beyond Fine Structure Forbidden transitions are not limited to fine-structure lines but also include emissions from metastable states in atoms and ions. For example, optical lines like [O III] 5007 Å originate from energy levels with lifetimes long enough to be considered metastable. These lines, with energies of a few eV, play a key role in cooling ionised gas in regions such as H II regions and planetary nebulae (Tielens, 2005). Forbidden transitions are important across a wide range of environments, complementing fine-structure transitions as a cooling mechanism.

Ionisation Ionisation (bound-free emission) occurs when an electron is ejected from an atom or ion due to the absorption of a high-energy photon. This process is critical in cooling photoionised gas, such as H II regions around young massive stars. The cooling efficiency depends on the abundance and ionisation state of elements like hydrogen and helium, which are the most abundant contributors. Bound-free transitions often dominate cooling in temperatures ranging from 10^3 to 10^4 K (Osterbrock & Ferland, 2006).

Recombination Recombination (free-bound radiation) occurs when a free electron is captured by an ion, transitioning to a bound state and emitting a photon. This process typically produces continuum radiation, particularly at low energies, and is most significant in partially ionised gas. Recombination cooling is essential in regions such as the warm ionised medium and planetary nebulae, where temperatures range from 10^3 to 10^4 K. Hydrogen and helium are the primary contributors to recombination cooling (Draine, 2011).

Free-Free (Bremsstrahlung) Radiation Free-free radiation occurs when free electrons are deflected by the electric fields of ions, causing the emission of photons. This process becomes significant in fully ionised gas at high temperatures ($T > 10^6$ K), such as in the intracluster medium of galaxy clusters or SNRs. The emitted radiation is primarily bright in the X-ray. It is proportional to the square of the electron density and the square root of the temperature. Bremsstrahlung is a dominant cooling mechanism in hot astrophysical plasmas (Rybicki & Lightman, 1979).

2.3.3 Turbulence

Turbulence in the ISM is a chaotic motion of gas and dust within at different scales. Despite the chaotic nature, it is indeed possible to describe the velocities and energies of a turbulent medium in terms of spatial correlation in velocity and energy. In classical turbulence theory, introduced by Andrey Nikolaevich Kolmogorov (Kolmogorov, 1941), kinetic energy cascades from large to small scales in incompressible, isotropic fluids. This energy transfer follows a power law of $k^{-5/3}$ within the inertial range. Here, k is the wavenumber, defined as $k = \frac{2\pi}{\ell}$, where ℓ represents the length scale of the turbulent eddies. However, in the ISM flow velocities often

exceed the speed of sound and turbulence becomes shock-dominated ("Burgers turbulence") with a steeper energy spectrum, k^{-2}, due to continuous dissipation across scales.

The energy sources maintaining ISM turbulence vary across spatial scales. In the absence of driving forces, turbulence dissipates. Consequently, continuous energy injection from processes such as large-scale gas accretion, galactic disk rotation, magnetorotational instabilities, and stellar feedback mechanisms – particularly SN explosions, stellar winds, and protostellar outflows – are essential. SNe, especially, are energy sources in the ISM, where they inject kinetic energy that cascades into smaller vortices, significantly shaping the dynamics and thermodynamics of the ISM turbulence (Klessen & Glover, 2016)

2.3.4 Molecular clouds

The ISM is highly structured and hierarchical, consisting of various phases with distinct densities, temperatures, and ionisation states. These phases range from the hot, diffuse ionised medium to the cooler atomic and molecular regions, where the density of gas and dust increases substantially. Within this hierarchy, molecular clouds (MCs) represent the densest and coldest phase, forming within regions where gas density is high enough to protect against dissociating ultraviolet radiation. MCs, are primarily composed of hydrogen molecules (H_2) and have masses ranging from 10^2–10^4 $M_\odot$ and sizes of several parsecs, densities often exceeding 10^2 – 10^4 cm^{-3} and temperatures around 10 – 30 K, forming a crucial component of the galactic ecosystem (Draine, 2011). Empirical relationships that describe the properties of MCs are Larson-like scaling relations, which R. B. Larson initially identified in 1981 (Larson, 1981). These relationships include correlations between cloud size, velocity dispersion, and density, and they are often used to characterise the structure and dynamics of MCs in both observational (Solomon et al., 1987; Roman-Duval et al., 2011) and simulated data (Federrath et al., 2010; Kritsuk et al., 2013; Padoan et al., 2016). R. B. Larson interpreted this hierarchical behaviour as a result of energy transfer across successive spatial scales (noting its similarity to the A. N. Kolmogorov's law).

The formation of MCs is a complex and extended process influenced by various astrophysical factors. In galaxies like the Milky Way, MCs are believed to arise from the accumulation and compression of atomic gas in the ISM, facilitated by processes like gravitational instabilities, turbulence, and galactic spiral arm dynamics. Large-scale turbulence within the ISM, combined with gravitational instabilities, helps create high-density regions where molecular gas can accumulate. As these clouds grow in density, gas phase reactions and surface chemistry on dust grains enable the formation of H_2, converting atomic hydrogen into molecular form.

Typical timescales for molecular cloud formation are estimated to be on the order of several million years. Recent overviews, such as Chevance et al. (2023) (or older papers such as Clark et al. (2012); Dobbs et al. (2014)), suggest that clouds may form relatively quickly on a timescale of 10^{6-7} years, depending on factors such as initial gas density, the strength of the magnetic field, and external perturbations. For example, in spiral galaxies, cloud formation is accelerated as gas is compressed within spiral arms, creating dense regions where molecular hydrogen formation can proceed more efficiently Dobbs et al. (2006); Roman-Duval et al. (2010); Dobbs et al. (2014). Once formed, these clouds remain in a turbulent state, with kinetic en-

ergy injection from various sources such as galactic rotation, SN shocks, and stellar feedback helping sustain turbulence and potentially prolonging the MC lifetime.

In addition to these large-scale formation mechanisms, magnetic fields and cosmic rays also play a critical role in MC evolution. Magnetic fields can provide additional support against gravitational collapse, altering the timescale over which clouds evolve and influencing the overall structure of these clouds (Hennebelle & Inutsuka, 2019; Ganguly et al., 2023; Pattle et al., 2023). Cosmic rays, on the other hand, contribute to ionising the gas, which can affect the chemistry and cooling rates within the cloud (Padovani et al., 2009; Gaches et al., 2022).

MCs are embedded within larger atomic clouds and are interconnected through filaments and diffuse gas, which create a network of structures across various spatial scales (Hacar et al., 2023). The hierarchical nature of the ISM means that MCs are influenced by processes occurring on both smaller and larger scales, such as turbulence, magnetic fields, and feedback from SNe. This hierarchical structure of the ISM, combined with the complex interactions between its phases, makes MCs dynamic environments, where stars form, evolve, and, ultimately, influence the surrounding medium through stellar feedback.

2.3.5 Stellar feedback

Molecular clouds serve as the birthplaces of stars. Massive stars (typically exceeding 8 $M_\odot$) inject significant energy and momentum back into their surroundings MC through mechanisms like stellar winds, ionising radiation, radiation pressure, and SN explosions (Dale, 2015; Walch & Naab, 2015). These feedback processes have the following impacts: they heat, ionise, and in some cases, entirely disrupt their parent MC, changing its density and stability. Such stellar feedback is essential, as it can either trigger further star formation in dense areas within the cloud or inhibit it by dispersing the gas, shaping both the lifecycle of the MC and the structure of the ISM as a whole (Spitzer, 1978; Hopkins, 2015). For example, SN feedback alone can create cavities or "superbubbles" in the ISM, which influence large-scale ISM dynamics and star formation across galaxies (Mac Low & McCray, 1988; Kim et al., 2017). The main feedback mechanisms are the following:

Supernovae: MCs are often found near SNRs (Hewitt et al., 2009; Zhou et al., 2023), where they can be strongly influenced by the energy and shock waves generated by SN explosions. When a SN occurs near a MC, the resulting shock waves compress and heat the surrounding gas, creating pressure waves that propagate through the cloud (Klein et al., 1994). These shocks can initiate the gravitational collapse of regions within the cloud, triggering new star formation. This connection between SNRs and MCs is a key aspect of the feedback cycle in galaxies, where massive stars end their lives in SN explosions and, in doing so, influence the next generation of star formation within MCs (Iffrig & Hennebelle, 2015; Rathjen et al., 2021).

The interaction between SNRs and MCs also has important implications for cloud chemistry and structure. Shock waves from SNRs can drive high-velocity turbulence within clouds, affecting cloud morphology and mixing different gas phases. As the shock fronts penetrate MCs, they can enhance molecular dissociation and ionisation rates, significantly altering the chemical composition within affected regions. This high-energy environment can lead to the production of unique mo-

lecules and increase the abundance of ions, such as HCO^+ and CH_3OH, which can be traced through millimetre-wave observations to study SNR-cloud interactions (e.g., observations of W44 and IC 443, Pihlström et al. 2014).

Timescales associated with SNR influence on MCs vary depending on the remnant's age and the cloud's initial density. For example, young SNRs, which are still expanding at high velocities, can rapidly compress nearby gas within hundreds of thousands of years, potentially accelerating the formation of dense cores within MCs. However, as the remnant expands and slows, the interactions become more diffuse and less impactful over a longer timescale, often up to a few million years. In the work of Padoan & Nordlund (2011); Padoan et al. (2016), they proposed that the structure and dynamics of molecular clouds naturally arise from a SN-driven scenario, where SN energy injection is essential for establishing and sustaining the observed turbulent cascade. However, this work does not account for large-scale gravitational potential or differential rotation.

According to another study, nearby SNe (nearby, in this case, is within distances of less than 50 pc) drive turbulence only for a short time (Seifried et al., 2018). So, the exact impact of SNe on MCs and their dynamics remains a topic of debate.

Stellar winds: All stars eject material continuously through stellar winds during their life, though the strength and impact of these winds vary with the stellar type and stellar evolution stage. In massive O- and B-type stars, radiation-driven winds become particularly significant for the surrounding ISM, as these stars expel mass at rates often on the order of $\sim 1\ M_\odot\ \mathrm{Myr}^{-1}$ and at velocities reaching 1000 – 3000 km/s (Puls et al., 2008). This ejected material carves out cavities, or "bubbles," within the surrounding medium, reducing the density, increasing the temperature, and forming low-density regions in the ISM (Naab & Ostriker, 2017).

Over the lifetime of a massive star, the cumulative energy and momentum transferred by stellar winds to the ISM can be similar, and in some cases exceed, that injected by SN (Haid et al., 2018). However, the impact of stellar winds differs from that of the SNe, as stellar winds continuously influence the ISM over the star's lifetime (3–100 Myr depending on the initial mass of the star) rather than delivering a sudden energy release. This extended injection of energy promotes the formation of shock fronts and turbulent flows within the ISM, disrupting molecular clouds and influencing the local star formation rate. As a result, stellar winds play a significant role in self-regulation within star-forming regions by limiting the collapse of gas that would otherwise form stars.

Ionising radiation and radiation pressure: In terms of energy input, ionising radiation is the most powerful stellar feedback mechanism. A massive star typically emits around $\sim 10^{53}$ erg of energy in Lyman continuum photons over its lifetime. These photons ionise a region of the parent MC, extending to the so-called Strömgren radius (R_S, Strömgren 1939), where the recombination rate of ionised hydrogen equals the ionisation rate due to the stellar photon field. This radius can be calculated via the following formula:

$$R_S = \left(\frac{3 Q_{\mathrm{ion}}}{4\pi \alpha_B n_H^2} \right)^{1/3}, \tag{2.4}$$

where Q_{ion} is the ionising photon rate, α_B is the recombination coefficient, and n_H is the hydrogen number density. Beyond this radius, residual energy from ion-

ising photons heats the ISM, increasing both temperature and pressure within the H II region and driving a shock wave that can expand up to approximately 10 – 100 pc into the ISM.

While the degree to which photon momentum is transferred to the bulk gas is still unclear, it could also play a role in driving and maintaining turbulence within MCs (Gritschneder et al., 2009; Agertz & Kravtsov, 2015). Ionising radiation often lowers the density in the MC regions associated with massive star formation, amplifying the impact of subsequent SNe explosions (Fichtner et al., 2024).

Photon pressure, whether from ionising or non-ionising radiation, also exerts a force on gas and dust. Despite that it is negligible at typical ISM densities, this radiation pressure becomes significant in dense molecular clouds, where it can drive turbulence and influence gas dynamics (Gritschneder et al., 2009).

3

METHODOLOGY

In the methodology section, we introduce the critical aspects and parameters of the simulations. First, we define the ideal magnetohydrodynamics (MHD) equations with all assumptions and imitations and introduce how the numerical calculations deal with shocks. We then describe the FLASH code for solving the MHD equations and necessary physical modules. At the end of this section, we explain the initial setups, code changes to better deal with radiative cooling and test setups with these changes.

3.1 Magneto-Hydrodynamics

We start this chapter with the most essential concept: the ideal magnetohydrodynamics (MHD) equations. MHD equations are the foundation for understanding the behaviour of electrically conducting fluids under the influence of magnetic fields. The ISM is a highly dynamic and magnetised plasma composed of different parts as described in Section 2.3.1. Treating the ISM with MHD is important as magnetic fields significantly influence the dynamics of gas flows and the overall structure of the ISM. Ideal MHD is used to model the ISM because it assumes that the plasma is perfectly conductive, allowing the magnetic field to be "frozen" into the fluid and follow the motion of the gas. This approximation simplifies the complex interactions between the gas and magnetic fields, enabling us to study large-scale phenomena like shock waves and stellar winds while focusing on the large-scale dynamics and structure of the ISM without the added complexity of resistive or turbulent dissipation that would arise in non-ideal MHD.

3.1.1 Assumptions of ideal MHD

We use the same core assumptions as in "Electrodynamics of Continuous Media" by Landau and Lifshitz (Landau & Lifshitz, 1960) for ideal MHD:

1. **Non-relativistic velocities.** The fluid velocity is assumed to be much lower than the speed of light, allowing relativistic effects to be ignored.
2. **Single-fluid approximation.** We assume the plasma is a single, conducting fluid rather than a mix of ions and electrons. We also assume collisions between particles are frequent enough to ensure a general collective behaviour.
3. **Perfect conductivity.** The plasma is assumed to have infinite electrical conductivity, leading to zero resistivity. This results in the magnetic field lines being "frozen" into the plasma, meaning they move with the fluid (mathematically, this implies the absence of an electric field in the plasma's rest frame).

4. **No charge separation.** The plasma is considered quasineutral, meaning any small electric charges are averaged over the volume, resulting in a net zero charge density.

5. **Negligible viscosity.** In ideal MHD, viscosity and heat conduction effects are neglected. It simplifies the fluid equations but simultaneously limits the model's applicability where these processes play significant roles (for example, it is important for solar flares simulations, as shown in González-Servín & González-Avilés 2024).

6. **Negligible displacement current.** The displacement current in Maxwell's equations is assumed to be negligible, which is reasonable for non-relativistic speeds and low-frequency.

These assumptions make ideal MHD suitable for describing large-scale, low-resistance plasma dynamics where magnetic fields dominate over particle collisions and resistive effects.

3.1.2 MHD EQUATIONS

The MHD equations describe the behaviour of a conducting fluid (such as a plasma) in the presence of a magnetic field (field strength $\mathbf{B}$). The main equations for ideal MHD include the following:

$$\frac{\partial \rho}{\partial t} + \nabla \cdot (\rho \mathbf{v}) = 0, \tag{3.1}$$

$$\frac{\partial \rho \mathbf{v}}{\partial t} + \nabla \cdot \left[\rho \mathbf{v} \otimes \mathbf{v} + \left(P + \frac{||\mathbf{B}||^2}{8\pi} \right) \mathbf{I} - \frac{\mathbf{B} \otimes \mathbf{B}}{4\pi} \right] = \rho \mathbf{g}, \tag{3.2}$$

$$\frac{\partial E}{\partial t} + \nabla \cdot \left[\left(E + \frac{||\mathbf{B}||^2}{8\pi} + P \right) \mathbf{v} - \frac{(\mathbf{B} \cdot \mathbf{v})\mathbf{B}}{8\pi} \right] = \rho \mathbf{v} \mathbf{g} + \dot{u}_{\text{heat}}, \tag{3.3}$$

$$\frac{\partial \mathbf{B}}{\partial t} - \nabla \times (\mathbf{v} \times \mathbf{B}) = 0, \tag{3.4}$$

where ρ is density of the fluid, $\mathbf{v}$ is velocity of the fluid, P is the thermal pressure, $\mathbf{g}$ is the local gravitational acceleration, E is the total energy, u is the internal energy, and $\dot{u}_{\text{heat}}$ is the internal energy input rate (due to heating and cooling processes as discussed in Section 2.3.2). The $\otimes$ symbol presents the outer product[12]. The equations represent mass, momentum, energy conservations and induction equations.

The total energy density (in erg per unit volume) and the thermal pressure are computed as follows:

$$E = u + \frac{\rho \mathbf{v}^2}{2} + \frac{||\mathbf{B}||^2}{8\pi}, \tag{3.5}$$

$$P = (\gamma - 1)u, \tag{3.6}$$

where γ is the adiabatic index and u is the internal energy per unit volume. For magnetic fields, the divergence-free constraint on the magnetic field is applied by

$$\nabla \cdot \mathbf{B} = 0. \tag{3.7}$$

[12] $(\mathbf{a} \otimes \mathbf{b})_{ij} = a_i b_j$

3.1.3 Challenges of ideal MHD in astrophysical modeling

In astrophysics, the limitations of ideal MHD become especially significant due to the extreme and diverse conditions found in astrophysical environments, especially for SNRs:

- **Magnetic reconnection**. Where magnetic field lines break and reconnect, large amounts of energy are released. It can happen during events like solar flares, SNe explosions, and the formation of jets around black holes. Ideal MHD lacks the resistivity needed to capture this process accurately, leading to inaccuracies in simulating these energetic events (Lazarian et al., 2020).

- **Ambipolar diffusion**. In the ideal MHD approximation, ambipolar diffusion is not included, as it assumes perfect coupling between magnetic fields and the conducting fluid. Ambipolar diffusion is the process in partially ionised plasmas where neutral particles drift relative to ions and electrons. This relative motion allows magnetic fields to decouple from the bulk motion of the neutral gas, causing magnetic flux to dissipate over time. While ideal MHD does not consider this effect, ambipolar diffusion can be crucial in star formation processes (Masson et al., 2016). It can help magnetic fields to dissipate, enabling the gravitational collapse of molecular clouds (Hennebelle & Inutsuka, 2019).

- **Cosmic Ray Acceleration**. Shock waves, such as those produced by SNRs, are important sites for cosmic ray acceleration. The ideal MHD framework can capture the shock but lacks the kinetic and small-scale physics necessary to model particle acceleration accurately. This is especially problematic when studying SNRs and their impact on the ISM, as ideal MHD cannot fully simulate how these particles gain energy (Snodin et al., 2006; Ferrand et al., 2010; Hanasz et al., 2021).

- **Single fluid assumption.** Ideal MHD treats the plasma as a single, homogeneous fluid, ignoring the presence of distinct populations like electrons, ions, and neutrals. This approximation fails when different particle species have different dynamics or temperatures (e.g., partially ionised regions, as often found in SNR shocks), where ions and neutrals can have different velocities and reactions to magnetic fields.

- **Infinite conductivity.** Ideal MHD assumes infinite conductivity, suppressing the Hall effect (an effect where different forces on electrons and ions cause a drift perpendicular to the magnetic field and current). The Hall effect is essential for accurately simulating magnetic reconnection and wave dispersion in certain contexts. For example, the Hall effect seems to play a significant role in regulating the angular momentum of the disc during the core formation (Wurster et al., 2016).

To address these limitations, extended MHD models (e.g., resistive MHD, Hall MHD), particle-in-cell (PIC) simulations for kinetic effects, or hybrid models that combine MHD with other physical approximations to capture small-scale processes can be employed. These modifications make simulations more complex and computationally intensive.

We acknowledge all the limitations mentioned above, but these limitations are not that relevant as a first attempt at our study's physical and temporal scales (Kowal et al., 2009). An ideal MHD still provides a solid foundation for effectively describing SNRs in the ISM simulations, particularly in shock treatment and cooling. After the simplest solution to describe physical processes is achieved, we can move to a more comprehensive description of the fluid and plasma behaviour.

3.2 Shock physics

3.2.1 The Rankine-Hugoniot jump conditions

One of the main components of SNRs is shock waves. Changes in the state of the plasma in the shock-transition layer must, as a rule, obey the laws of conservation of mass, momentum, and energy. The Rankine-Hugoniot jump conditions represent the physical points of possible final states of material behind the front of a shock wave under given initial conditions (Landau & Lifshitz, 1959).

Because transition layers are typically much thinner than the radius of curvature of shock waves, and because evolutionary changes occur on time scales larger than the time scale of shock heating, we can approximate shock waves as plane-parallel structures[13] fixed in time when viewed in the shock reference frame (the frame that accompanies the shock itself). Let us consider in this moving reference frame the conservation laws as:

$$\rho_1 v_1 = \rho_2 v_2, \tag{3.8}$$

$$P_1 + \rho_1 v_1^2 = P_2 + \rho_2 v_2^2, \tag{3.9}$$

$$\left(P_1 + U_1 + \frac{1}{2}\rho_1 v_1^2\right) v_1 = \left(P_2 + U_2 + \frac{1}{2}\rho_2 v_2^2\right) v_2, \tag{3.10}$$

where ρ is density, v is velocity, P is pressure and U is internal energy of the gas. All quantities in the pre-shock region (often called the upstream region) are labelled with an index of 1, and all quantities in the post-shock region (the downstream region) are labelled with an index of 2. Thus, the gas enters the shock with a velocity v_1, and after passes through the shock wave, the gas moves away from the shock wave at speed v_2. The three relations represent mass, momentum, and energy conservation.

For convenience, we can rewrite these equations in terms of the Mach number of the flow ($\mathcal{M} = v_1/c_1$, where c_1 is the sound speed):

[13] Whether the shock thickness in SNRs is better characterised by the gyroradius or the ion inertial length, it is clear that this scale is far smaller than what current or near-future telescopes can resolve. However, confirming that this length scale is smaller than other relevant physical scales remains vital.

$$\frac{\rho_2}{\rho_1} = \frac{v_1}{v_2} = \frac{(\gamma+1)\mathcal{M}_1^2}{2+(\gamma-1)\mathcal{M}_1^2} \tag{3.11}$$

$$\frac{P_2}{P_1} = \frac{2\gamma\mathcal{M}_1^2-(\gamma-1)}{\gamma+1} \tag{3.12}$$

$$\frac{T_2}{T_1} = \frac{\left(2\gamma\mathcal{M}_1^2-(\gamma-1)\right)\left(2+(\gamma-1)\mathcal{M}_1^2\right)}{(\gamma+1)^2\mathcal{M}_1^2} \tag{3.13}$$

These relations are helpful to treat shocks numerically: we would approximate the discontinuity in the solution to the Euler equations. In SNRs shocks are typically supersonic ($\mathcal{M} \gg 1$) and if we treat the gas as monatomic ($\gamma = 5/3$), then the maximum density contrast would be $\frac{\gamma+1}{\gamma-1} = 4$.

If $\mathcal{M}_1 = 1$, then $\rho_2 = \rho_1$, $P_2 = P_1$ and $T_2 = T_1$, i.e. there is no shock. Therefore, we can conclude that shocks only occur when the pre-shock gas is supersonic. If the pre-shock gas is subsonic, then the solution generated by the jump conditions suggests that the temperature, and therefore the entropy, of the post-shock gas are lower than those of the pre-shock gas, i.e., that the second law of thermodynamics is violated. Therefore, shocks are associated with supersonic flows.

3.2.2 Radiative shocks

In the subsection above, we assumed that the energy of the shocks is conserved. However, this is not true for some types of shocks, particularly for radiative shocks. This means that energy can be lost due to radiative cooling. To estimate for which shock velocities radiative cooling is crucial, let us introduce the cooling timescale:

$$\tau_{\text{cool}} = \frac{\frac{\gamma}{\gamma-1}\cdot\frac{n}{n_p}\cdot n_p k_{\text{B}} T}{n_e n_p \Lambda(t)}, \tag{3.14}$$

where n is the number density of ions and electrons, n_e is the electron number density, n_p is the proton number density, k_{B} is a Boltzmann constant, T is the gas temperature and $\Lambda(t)$ is the volumetric cooling rate (as discussed in Section 2.2.5). If we assume $\gamma = \frac{5}{3}$ and $n/n_p \approx 2.3$ then the cooling timescale is:

$$\tau_{\text{cool}} \approx \frac{5}{7}\cdot\frac{k_B T}{n_e \Lambda(T)}. \tag{3.15}$$

Knowing the characteristic time scale we can define the characteristic length scale. This length is a distance downstream of the shock where the plasma will become substantially cooler than the immediate post-shock temperature:

$$l_{\text{cool}} = v_2 \tau_{\text{cool}} \approx \frac{1}{4} v_s \tau_{\text{cool}}, \tag{3.16}$$

where $v_s = v_1$ is the speed with which plasma enters the shock, and v_2 is the speed with which the downstream plasma moves away from the shock (note: the relation $v_2 = \frac{1}{4}v_1$ can be obtained from the jump conditions above). The cooling timescale is shown in Figure 7. For velocities $v_s < 200$ km s^{-1} cooling becomes increasingly important, as the cooling time scale falls below the age of the SNR. For $v_s < 200$ km

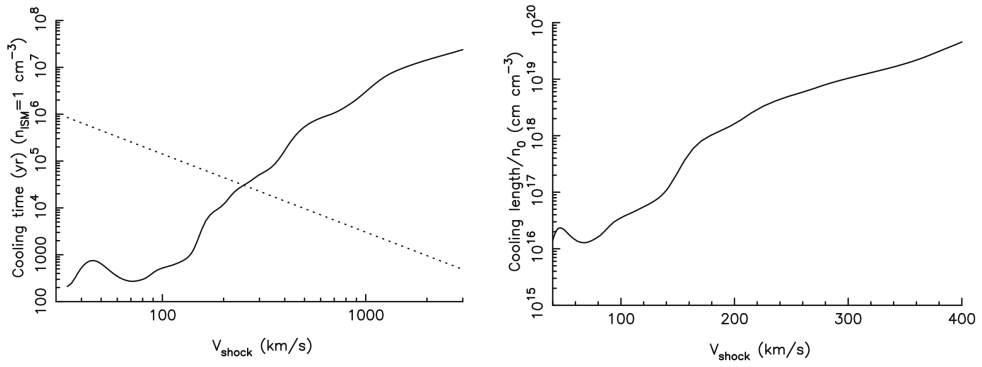

Figure 7: Left panel: This plot shows the characteristic cooling time (in years) as a function of shock velocity for a pre-shock density of n_H = 1 cm $^{-3}$. The solid line represents the cooling time of shocked plasma across different shock velocities, while the dotted line illustrates the relationship between shock velocity and the age of a SNR, following the Sedov-Taylor solution. When the cooling timescale drops below a certain fraction of the SNR's age, shock waves enter the radiative regime, meaning that energy losses due to radiation become significant in shaping the shock dynamics. Right panel: This plot displays the cooling length, normalised by the initial density, as a function of shock velocity. The cooling length is the distance over which the plasma cools down significantly after being shocked. At higher shock velocities, the cooling length increases, indicating that shocks with higher velocities dissipate energy over larger distances compared to slower shocks. The figure is taken from Vink (2020) using the model from Raymond (1979).

s^{-1} the cooling length is less than a parsec, and for even lower velocities the length scales will be of the order of $10^{16}/n_e$ cm (Vink, 2020).

When radiative cooling becomes significant, it initiates a runaway process: pressure balance ($P = nkT$) causes the plasma to compress, but the higher density increases the emissivity. This process slows once the plasma cools below 10^4 K, with a longer cooling time. However, the magnetic field pressure more likely stops further compression, which becomes dominant at high compression ratios. The cooling process is shown in Figure 8, based on the Raymond shock models (Raymond, 1979). We start from the shock, and as the temperature decreases due to radiative cooling, the near-constant pressure behind the shock requires a steady increase in density. Below 10^4 K, ion recombination further reduces thermal pressure by lowering the number of free electrons.

Rapid cooling and increasing density give rise to narrow, optically and UV-bright filaments on cooling length scales. Prominent Lyα and Hα line emissions characterise the spectra of these filaments, as well as forbidden lines from ionised N, O, and S. Shocks with rapid post-shock cooling are known as **radiative shocks**. These optical filaments are visible in various SNRs, e.g., the Cygnus Loop (Bedogni & Woodward, 1990; Hester et al., 1994; Blair et al., 2005), IC 443 (Fesen & Kirshner, 1980; Chevalier, 1999) and many more.

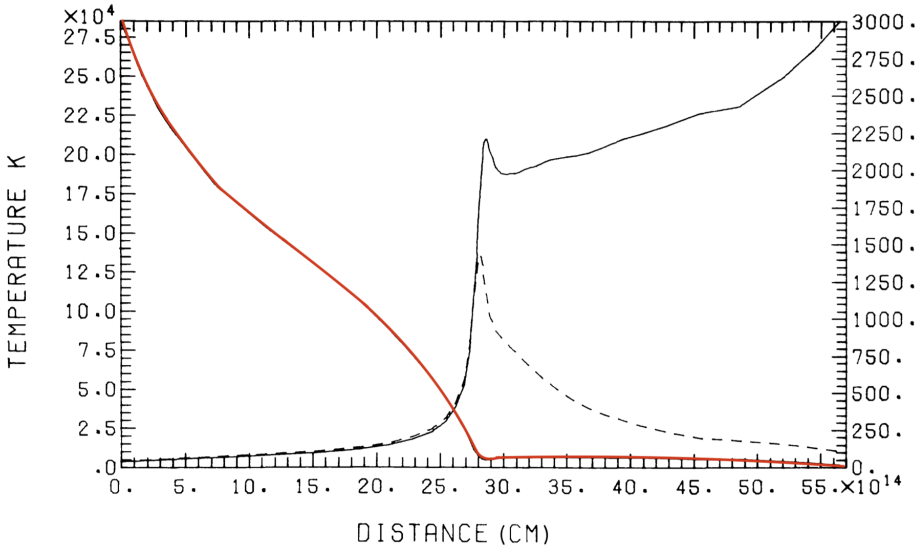

Figure 8: Temperature (red solid line), density (black solid line), and electron density (dashed line) for the shock model G from Raymond (1979) (shock velocity: v_s = 141 km s^{-1}, pre-shock ambient density: n_H = 10 cm $^{-3}$, pre-shock magnetic field: B = 1 μG). The figure is taken from Raymond (1979).

3.3 FLASH 4

In this section, we present a short overview of the FLASH code (Fryxell et al., 2000) and its modules, which are used to perform the simulations presented in this thesis. FLASH is a highly parallelised, three-dimensional (magneto-)hydrodynamic grid code that employs adaptive mesh refinement (AMR) to solve the MHD equations. It was developed by the FLASH Center for Computational Science at the University of Chicago. In the following, I describe key modules which are important in the context of this work. For a more comprehensive discussion of the basics and architecture of FLASH, see Fryxell et al. (2000); Dubey et al. (2009); Dubey et al. (2012).

3.3.1 Grid structure

FLASH is a grid-based code which uses AMR to follow regions of interest. The grid uses blocks as its base unit, which consist of cells. In the simplest case, the simulation domain consists of a single root block, but multiple root blocks can be used to cover non-cubic domains (e.g. SILCC). Starting from a root block, the simulation code uses an AMR technique to refine and derefine the simulation domain. Hereby, refining means to split a block into 2^d smaller blocks, where d gives the dimension. To determine if a block needs to be refined, a normalised second-order derivative of a user-defined quantity (e.g. density, pressure) is used in combination with threshold values for refinement and derefinement (FLASH manual Section 8.6.3; Lohner 1987). Additionally, a minimum and maximum refinement level can be set to achieve the required resolution range. The implementation of the AMR technique is handled by the PARAMESH library (MacNeice et al., 2000). An ex-

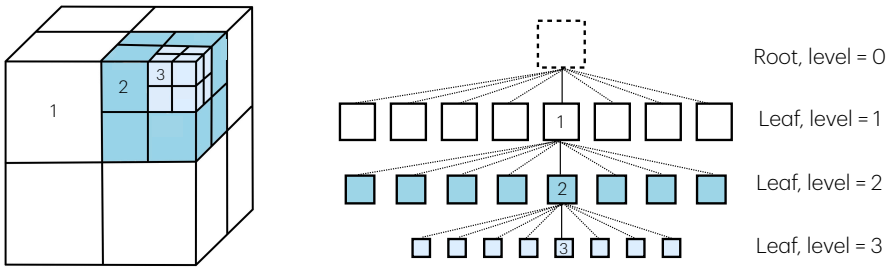

Figure 9: Example of the AMR grid structure and the corresponding tree structure in 3-D. We start from the root block and step-by-step follow the refinement rule to increase the refinement level (from white to light blue).

ample of the AMR grid is shown in Figure 9. One of the main benefits of this approach is that one can achieve a high dynamical spatial range without having to perform simulations with uniform high resolution, reducing computational cost and required storage space (Berger & Oliger, 1984; Berger & Colella, 1989).

3.3.2 Solver for MHD equations

To perform our simulations, we need to solve the MHD equations (Eq.3.1–3.4). to calculate the resulting values at the interfaces of our grid cells. We use a Riemann solver to calculate the mass flux, momentum, energy, and magnetic field between neighbouring cells. By resolving these fluxes accurately, we can model the motion of a fluid and follow other physical key properties of our astrophysical models.

The Piecewise Parabolic Method (PPM) solver in FLASH (Godunov, 1959; Colella & Woodward, 1984) is a high-order, accurate solver designed explicitly for capturing shocks and complex flow structures in hydrodynamical simulations. Developed to solve the Euler equations of gas dynamics, the PPM solver uses a parabolic interpolation scheme to achieve high resolution within each computational cell. It is particularly effective at preserving sharp discontinuities and capturing shock fronts without excessive numerical diffusion. Therefore, the PPM solver is well suited for astrophysical applications involving supersonic flows, such as SNe explosions and stellar wind interactions. The PPM solver in FLASH also includes features like contact steepening and entropy conservation, enhancing its accuracy and stability across different simulation scales.

The hydrodynamic simulations analysed in this thesis employ the directionally split Bouchut 5-wave HLL5R (5-wave Harten-Lax-van Leer) MHD solver, with the magnetic field set to zero (Bouchut et al., 2007, 2010). The Bouchut 5 solver is a stable, approximate Riemann solver known for preserving positive density and entropy, even in highly supersonic flows. This solver is particularly suitable for scenarios where maintaining stable, non-negative states of density and entropy is essential, making it effective for simulations with significant shock fronts and rapid fluid motion.

I mainly used the PPM solver for simulations in this thesis (in Paper III), but for simulations (the SILCC-Zoom, which will be discussed later), which I analysed

with my post-processing routine (in Paper I and Paper II), the Bouchut 5 solver was used.

3.3.3 Radiative transfer

In our simulations, we account for radiative transfer. This is necessary to account for the absorption, emission, and scattering processes caused by radiation's propagation through the medium. This process is governed by the radiative transfer equation, which describes the radiation intensity change as it travels through a medium with varying properties. The equation accounts for sources and sinks of radiation within the medium and is typically expressed in terms of the specific intensity I as a function of position, direction, and wavelength (Zeldovich & Raizer, 1966):

$$\frac{dI_\nu}{ds} = -\alpha_\nu I_\nu + j_\nu, \tag{3.17}$$

where I_ν is the specific intensity of the radiation at frequency ν along a path s, α_ν is the wavelength-dependent absorption coefficient (or opacity) of the medium, which determines how much radiation is absorbed per unit length, j_ν is the emission coefficient of the medium, describing how much radiation is emitted per unit volume and per unit frequency.

Solving the radiative transfer equation accurately can be challenging, particularly in complex, inhomogeneous environments. Overall, there are different schemes to perform radiative transfer, which can be categorised into forward and backward schemes, see the overview by Wünsch (2024) for a detailed description. Forward radiative transfer schemes solve the radiative transfer equation starting from the source of the radiation and calculating the intensity as it propagates through the medium. In this thesis, we use a backward radiative scheme called TreeRay (Wünsch et al., 2018). Here, the radiative transfer is performed backwards from the target (e.g., an observer's location) to the source. This improves computational efficiency as the scheme does not depend on the number of sources and stability in optical depth calculations. A detailed description of the radiative transfer scheme can be found in Wünsch et al. (2018, 2021).

Following radiation propagation solely along the initial hydrocode grid axes is typically restrictive. For this reason, radiative transfer codes use alternative schemes to create and trace rays. One approach, also used in our TreeRay implementation, involves casting rays from the source in spherical coordinates, with each ray corresponding to an equally sized spherical segment. Hereby, using a HEALPix sphere (see Figure 10, Górski et al. 2005) is common to represent the angular distribution of radiation effectively, particularly in simulations requiring precise directional resolution. HEALPix (Hierarchical Equal Area isoLatitude Pixelisation) divides a sphere into equal-area segments, enabling efficient and accurate sampling of directions in 3D space. It is essential to capture the anisotropic nature of radiation sources and calculate the effects of radiation on various points within the simulated medium (Baczynski et al., 2015).

The TreeRay/Optical Depth module is an advanced radiative transfer tool in FLASH (Wünsch et al., 2018). It enables the calculation of optical depth and radiation shielding, which is crucial for accurately representing interactions between radiation and interstellar material, specifically for heating and cooling processes and chemical (photo-dissociation) reactions (Kim & Ostriker, 2017; Peters et al.,

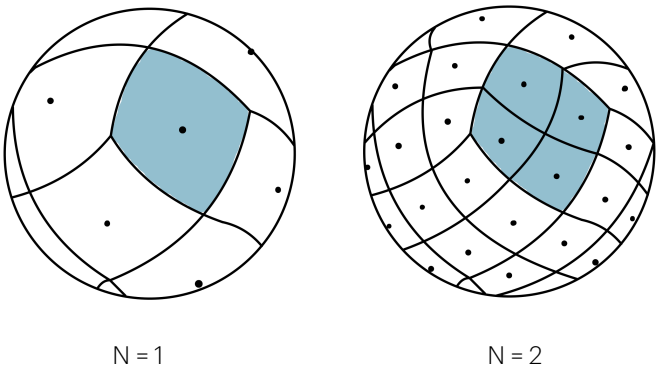

Figure 10: Sketch of a HEALPix grid resolution for different NSIDE values. NSIDE = 1 shows a low resolution of the sphere, and NSIDE = 2 is increased resolution dividing each segment into smaller, equal-area sections, resulting in 48 points. The shaded blue region demonstrates a specific segment at different levels of resolution (e.g. "a single pixel").

2017). Its tree-based algorithm, adapted for grid-based FLASH simulations, offers a computationally efficient way to calculate optical depths across complex structures. The module performs cumulative radiation calculations by hierarchically grouping cells, significantly lowering computational costs compared to direct integration along all sightlines. Adding to FLASH's radiative capabilities, the XRayTheSpot module introduced by Gaches et al. (2023) further enhances radiation modelling, specifically targeting X-ray radiation and adding frequency-dependent X-ray radiation. XRayTheSpot considers the high-energy photons that can penetrate deeper into dense clouds than ultraviolet or optical radiation. This module is particularly valuable for simulating environments near high-energy sources, such as young stellar clusters or active galactic nuclei. X-rays play a critical role in ionisation and heating (Lepp & Shull, 1983; Maloney et al., 1996; Dalgarno et al., 1999; Mackey et al., 2019). Using XRayTheSpot with OnTheSpot provides a comprehensive radiative transfer toolkit within FLASH, covering both the lower-energy radiative processes and the high-energy interactions critical for realistic astrophysical simulations. Together, these modules allow for detailed modelling of both UV and X-ray shielding effects, enabling simulations to more accurately capture feedback from massive stars or black holes on their surrounding ISM.

3.3.4 Chemistry network

Some simulations, which we use in this work, use a simplified non-equilibrium chemical network. We call it in the following NL97 network based on Nelson & Langer (1997) and Glover & Mac Low (2007a,b); Micic et al. (2012). The chemical network traces the evolution of H_2, H, H^+, CO, C^+, e^- and O.

Another set of the simulations used here employs an extended chemical network that consists of 17 species, of which 9 are solved numerically, the so-called the NL99 network (Glover & Clark, 2012). The rest of the species are calculated through conservation equations. It consists of a model for hydrogen chemistry (Glover & Mac Low, 2007a,b) and a model for CO chemistry (Nelson & Langer, 1999) with

updated reaction rates from Gong et al. (2017). For more details about the network or how the X-ray radiation is coupled to the chemistry, see Mackey et al. (2019).

A given chemical species i is evolved according to the equation:

$$\frac{\partial \rho_i}{\partial t} + \nabla \cdot (\rho_i \mathbf{v}) = C_i(\rho, T, \ldots) - D_i(\rho, T, \ldots), \tag{3.18}$$

where ρ_i is the density of the ith species, and C_i and D_i are the creation and destruction rates of the given species. C_i and D_i depend on the temperature, and density of the i-th species, as well as densities of other species, the cosmic ray ionisation rate and the strength of the ISRF. To solve the equations, the advection and the source terms are treated separately. The first part of the operator splitting fashion contains the advection of the chemical species:

$$\frac{\partial \rho_i}{\partial t} + \nabla \cdot (\rho_i \mathbf{v}) = 0. \tag{3.19}$$

The right hand side of this equation can then be treated as a set of coupled ordinary differential equations:

$$\frac{\partial \rho_i}{\partial t} = C_i(\rho, T, \ldots) - D_i(\rho, T, \ldots). \tag{3.20}$$

These equations are solved using the implicit solver Dvode (Brown et al., 1989). The net heat (positive or negative) generated in the chemical reactions contributes to the $\dot{u}_{\text{heat}}$ term in the equation of energy 3.3.

The gas in simulations is typically set to solar metallicity (Sembach et al., 2000), with fixed elemental abundances with respect to hydrogen.

We need the column density of dust, H_2 and CO for some of the chemical reactions. These are calculated with TreeRay/OpticalDepth, then providing the dust extinction, as well as the self-shielding factors for H_2 and CO. OpticalDepth stores the average visual extinction A_V, as well as shielding coefficients. The three-dimensional visual extinction is calculated as (Bohlin et al., 1978):

$$\mathrm{A_V} = \frac{\mathrm{N_{H,tot}}}{1.87 \times 10^{21}\ \mathrm{cm^{-2}}}, \tag{3.21}$$

where the hydrogen column density $\mathrm{N_{H,tot}} = \mathrm{N_{H^+}} + \mathrm{N_H} + 2\mathrm{N_{H_2}}$ is calculated for/along each Healpix pixel (see Clark et al. (2012) for more details).

3.3.5 Heating and cooling processes in chemistry

We account for the radiative heating of the gas from cosmic rays, soft X-rays, and photoelectric emission by small grains and polycyclic aromatic hydrocarbons. We adopt a cosmic ray ionisation rate for neutral atomic hydrogen (typically 3×10^{-17} $\mathrm{s^{-1}}$) and a rate twice this size for the cosmic ray ionisation of H_2. The effects of photoelectric heating are modelled using a heating rate derived from the work of Bakes & Tielens (1994) and Bergin et al. (2004). The ISRF is typically set to $G_0 = 1.7$ in Habing units (Habing, 1968) in the Solar neighbourhood, but it can be changed depending on the environment in simulations as well as due to the intrinsic shielding by dust (see Section 3.3.4). The changes in thermal energy account for the heating from H2 formation, H2 photodissociation, and UV pumping of vibrationally excited states of H2 by the ISRF.

We self-consistently calculate the dust temperature in every grid cell, assuming that the dust is in thermal equilibrium. Heating of the dust grains by the ISRF and by collisions with the gas is balanced by their thermal emission. To treat the attenuation of the ISRF by dust absorption, lowering the heating rate of the dust in denser parts of the ISM, we use the column density dependent attenuation by Glover & Clark (2012) and we use the attenuation of dust described in Section 3.3.4. We assume that the dust-to-gas ratio is 0.01 and the dust has a size distribution typical for the Milky Way.

For radiative cooling, we employ a detailed atomic and molecular cooling function as described in Glover et al. (2010); Glover & Clark (2012) (and in Section 2.2.5). This incorporates contributions from fine-structure lines (e.g., C^+ and O), the rotational and vibrational transitions of H_2 and CO, and electronic transitions in atomic hydrogen, such as Lyman-α cooling. For gas above 10^4 K, cooling is primarily due to line emission from metal ions (such as C, O, Si, and Fe). Here, we use cooling rates incorporating these contributions, based on calculations from studies by Gnat & Ferland (2012). It provides a table with metal cooling rates for specific temperatures, considering different ionisation states of the elements. For each simulation cell, knowing the temperature, it is possible to calculate the specific cooling rate using precalculated tables for a given metallicity. We will discuss the changes to this chemistry part in Section 3.4.2. In addition, we account for changes in the thermal energy of the gas due to cooling from H^+ recombination, the collisional ionisation of H and the collisional dissociation of H_2

3.3.6 Stellar feedback: winds from massive stars and supernovae

We use the implementation of stellar winds and SNe in FLASH described by Gatto et al. 2015. The stellar wind is incorporated by modelling the mass loss from stars through a continuous, steady outflow. The feedback is centred on the position of the sink, representing a massive star. This wind is characterised by a mass-loss rate ($\dot{M}_{\rm wind}$) and a wind velocity ($v_{\rm wind}$), which are linked to the properties of the central star. In the FLASH framework, the stellar wind is treated as a source term in the hydrodynamic equations, modifying the local gas density and energy as the wind material interacts with the surrounding ISM. With the information from the tabulated stellar tracks (Ekström et al., 2012) of a mass loss rate and calculated the approximate terminal wind velocity, we can obtain the total mass injected by the wind to the ISM and the luminosity (depending on the metallicity and age of the star). The stellar wind is injected into the simulation as a momentum and energy source, contributing to the evolution of the ISM around the star. The wind's interaction with the ISM is modelled by adjusting the energy deposition and the velocity of the surrounding gas, leading to the formation of bubble-like structures.

Once a star has reached the end of its lifetime, according to the stellar tracks, it explodes as a SN. SNe are implemented in FLASH as an injection of energy within a spherical region with radius $R_{\rm inj}$. The minimum of $R_{\rm inj}$ is at least four computational cells, and it is chosen to ensure the proper resolution of the expanding shock front. The injection energy is typically 10^{51} erg. This energy is injected as thermal energy if the adiabatic phase of the SNR is resolved. Typically the gas in the injection region is then heated up to temperatures around 10^7 K. The corresponding pressure increase causes a Sedov-Taylor blast wave to expand into the ambient ISM. If the

adiabatic phase cannot be resolved, the momentum injection is used. More details about the SN injection schemes can be found in Gatto et al. (2015).

3.4 Simulations

In (magneto-)hydrodynamical simulations, we first need to define the initial setup. It refers to defining the parameters, physical processes included, and computational domain required to model a specific system. Initial conditions specify this system's starting state, including properties like density, temperature, chemical composition, and velocity, which subsequently evolve according to the governing MHD equations over time.

First, we briefly describe the simulation setup used in this thesis for the post-processing work in Chapter 5 and Chapter 6. Next, we describe different tests and changes in the FLASH code, which serves as a foundation to perform state-of-the-art simulations in Chapter 7.

3.4.1 The SILCC and SILCC-Zoom simulations

The SILCC simulations[14] (Simulating the Life-Cycle of Molecular Clouds) (Walch et al., 2015; Girichidis et al., 2016) model the multi-phase ISM within a stratified computational domain of 500 pc $\times$ 500 pc $\times$ $\pm$ 4 kpc, representing a localised region of a galactic disc. The setup is designed to investigate ISM dynamics in environments similar to the solar neighbourhood in the present-day Universe (redshift z = 0). The multi-phase ISM is formed through turbulence driven by SN explosions, with the SN rate determined by the gas surface density following the Kennicutt–Schmidt relation (Kennicutt, 1998). The initial gas surface density is typically set to $\Sigma_{\rm gas} = 10\ {\rm M}_\odot\ {\rm pc}^{-2}$, although subsequent studies have examined cases with different surface densities (Rathjen et al., 2023). The initial conditions include an exponential gas density profile, magnetic fields, and a gravitational potential due to stars. Gas temperatures represent colder conditions near the galactic midplane and hotter halo gas, with initial compositions of ionised carbon and atomic hydrogen. As a result, the multi-phase ISM is modelled and dense molecular clouds form, merge, and evolve. The base resolution for the SILCC simulations is 3.9 pc near the midplane and 7.8 pc outside of it. See more about these simulations in the following papers: Walch et al. (2015); Girichidis et al. (2016); Gatto et al. (2017); Peters et al. (2017); Girichidis et al. (2018); Rathjen et al. (2021, 2023, 2024)

To focus more on the molecular clouds with better resolution, SILCC-Zoom simulations (Seifried et al., 2017) refine specific regions of molecular cloud formation, enabling detailed studies of their early evolution. A careful refinement strategy mitigates numerical artefacts, allowing the resolution to reach 0.122 pc while preserving the clouds' physical characteristics. The comparison of scales is shown in Figure 11. This approach provides insights into the dynamics of molecular cloud formation and feedback processes within the ISM. You can find more details about SILCC-Zoom simulations in Seifried et al. (2017, 2020); Ganguly et al. (2024).

[14] https://hera.ph1.uni-koeln.de/~silcc/

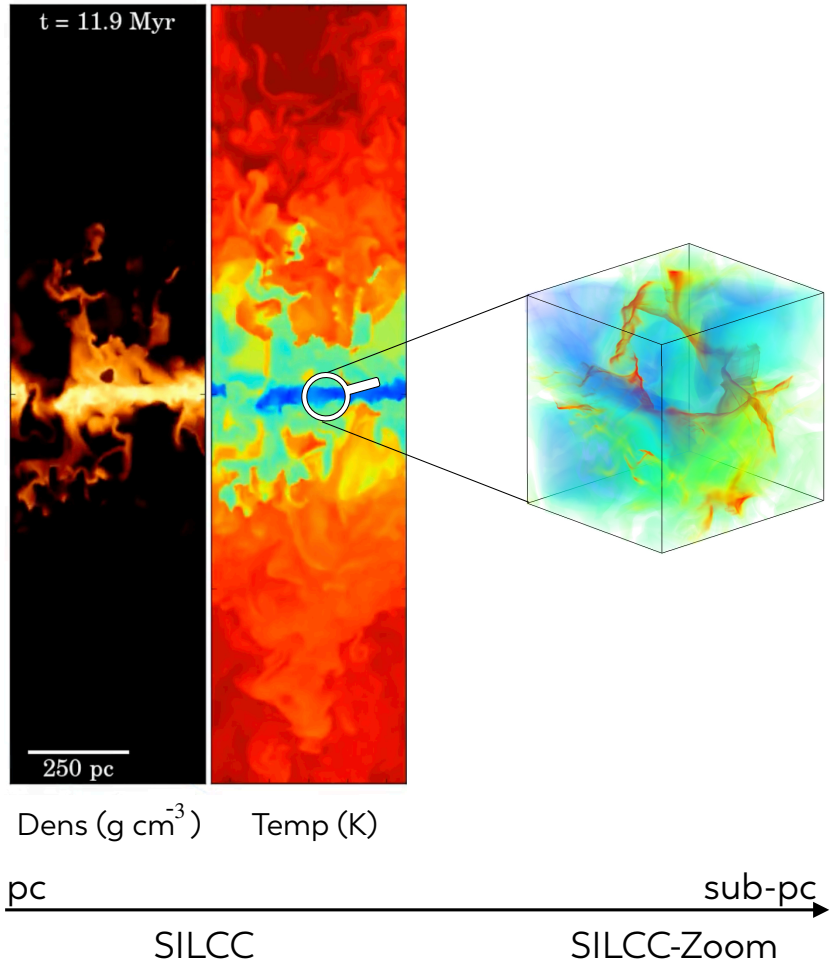

Figure 11: Example of a SILCC box (density and temperature slices on the left) and a SILCC-Zoom region (3-D volume rendering on the right). The magnifying glass shows the approximate scale of the SILCC-Zoom region in regards to the SILCC volume (500 pc $\times$ 500 pc $\times$ $\pm$ 4 kpc) to SILCC-Zoom (around 100 pc side box). Figures are taken from Girichidis et al. (2016) and Seifried et al. (2020).

3.4.2 Changes to the chemistry: radiative cooling

To calculate the radiative cooling rate of the gas in the range of 10^4 K to 10^8 K, we use pretabulated cooling tables. The Chemistry module uses the tables to interpolate the cooling rate on local gas properties (e.g. temperature, metallicity). With this approach the cooling rate is dynamically adjusted as the gas properties change over time.

In this thesis, we updated the cooling rates for metals (all elements apart from H and He) and Helium. For the new tables we utilise the MAPPINGS V code (Binette et al., 1985; Sutherland & Dopita, 1993; Dopita & Sutherland, 2000; Dopita et al., 2013; Sutherland & Dopita, 2017). MAPPINGS V is a 1-D plasma code modelling shocks and photoionisation. One of the code's modes calculates the cooling rate of the optically thin plasma (CIE approximation) depending on the temperature. For these calculations, we can define the exact metallicity of the first 30 elements in the

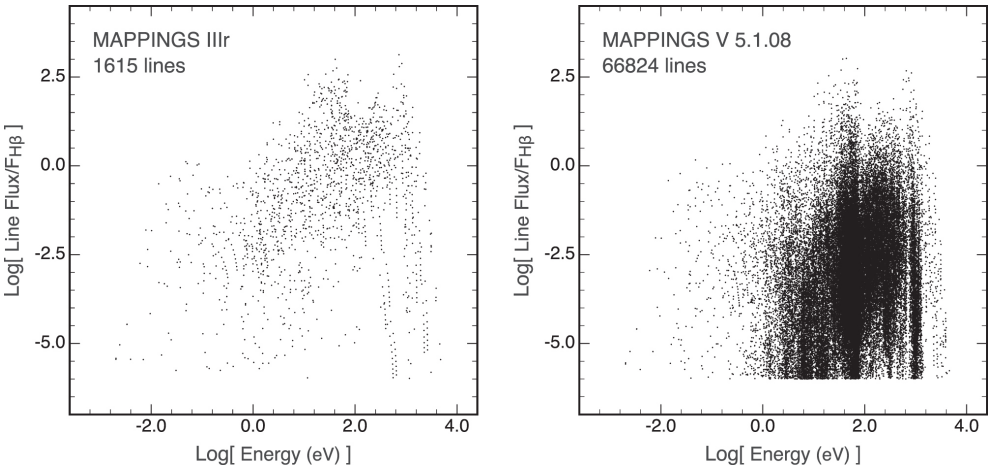

Figure 12: Emission line strengths as a function of energy computed by MAPPINGS III based on old atomic database (left) and by MAPPINGS V based on the newer CHIANTI 8 atomic database (right). The MAPPINGS V code can produce much more detailed X-ray spectra and generate more reliable diagnostics. The figure is taken from Sutherland & Dopita (2017).

plasma (from H to Zn). The decision to replace the old precomputed tables with the new ones was made due to the significant updates to the atomic database on which many plasma codes are based, CHIANTI (first release in Dere et al. 1997, then Young et al. 1998; Landi et al. 1999; Dere et al. 2001 and version 8 from Del Zanna et al. 2015). CHIANTI is a database of atomic parameters and transition rates needed to calculate the line and continuum emission in the CIE plasma. Figure 12 shows how much the database of MAPPINGS V has increased, especially in the X-ray regime (high-temperature plasma), compared to the older version of the MAPPINGS code.

We replaced the following precomputed tables in the Chemistry module: for He and for metals (elements between Li and Zn, CIE, does not include H and He contributions; Gnat & Ferland (2012)). We use the abundances of Sembach et al. (2000) as they are used the same metallicities typically used for our FLASH simulations typically used in the SILCC simulations. The abundances represent solar metallicity in the WIM. A comparison between the old and new cooling curve is shown in Figure 13. The main difference in the cooling rates originates from the fact that they are based on different versions of the atomic database CHIANTI. The difference in treatment of the CIE gas between the CLOUDY version, used for old precomputed tables, and MAPPINGS is minor. Moreover, the newest release of CLOUDY code (Gunasekera et al., 2023) is based on the most up-to-date atomic database. However, this is not the cooling curve used in the simulations before.

In addition to the updated tables, we can now record the amount of cooling energy in each energy band (user-defined, from 0 to 12 keV) in each time step. For that, we would need to include $i + 1$ new field variables: i for energy bins and one for the total cooling energy. This will help us include self-consistent radiative cooling in the full radiative transfer scheme as the cooling can be passed to the radiative transfer module.

The cooling energy of a band i, $E^i_{\rm rc}$, is the difference between the initial, $E_{\rm int,init}$, and the final internal energy of the gas, $E_{\rm int,fin}$, each multiplied by a temperature

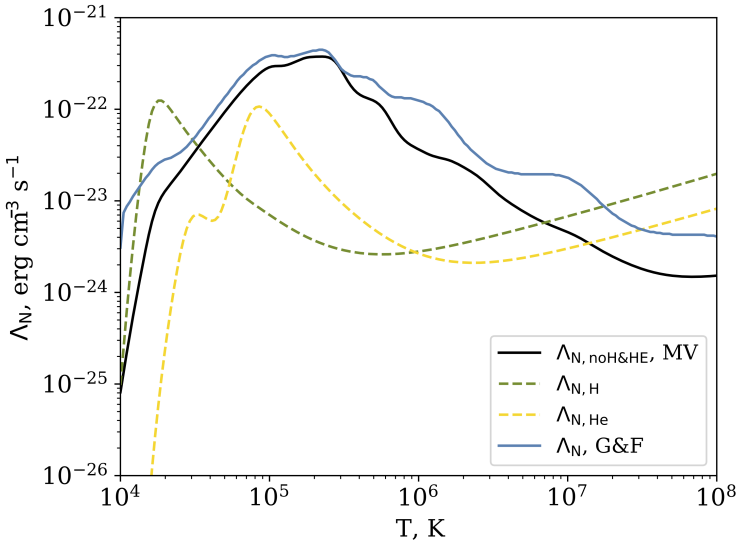

Figure 13: Cooling curve for the old tables (blue, Gnat & Ferland 2012) and for the new tables (black, MAPPINGS V) using solar metallicity (WIM) from (Sembach et al., 2000). Hydrogen and helium contribution from MAPPINGS V are shown in green and yellow respectively.

dependent band fraction f^i. Therefore, to calculate the radiative cooling in a specific energy band, we determine the field variable following:

$$E^i_{\rm rc} = f^i_{\rm init} E_{\rm int,init} - f^i_{\rm fin} E_{\rm int,fin}. \tag{3.22}$$

The new variable generally follows the same evolution as the total energy in CHEMISTRY module. The energy calculation is done for each user-defined energy bin and thus requires as many field variables as energy bins. In that case, we first need to define the energy fraction corresponding to a specific band. We generate a look-up table with MAPPINGS V for the CIE plasma with pre-defined bands. This table contains for each temperature the total cooling rate as well as cooling rate for each of the bands. The fractions f^i are derived from the ratio between the band to the total cooling rate. To determine the cooling rate for any gas temperature we use a cubic interpolation scheme.

3.4.3 1D CHEMISTRY TEST

We test the new radiative cooling table and energy splitting with the Chemistry standalone test. A standalone 1D test is a simplified, controlled simulation to validate and benchmark the chemical network. With this test, we can verify the radiative cooling behaviour under specific conditions without the complexity of a full astrophysical simulation.

As a benchmark test, we initialise the cell with a high thermal energy and et the gas cool in different density environments. We chose three cooling energy bands: 0 – 13.6 eV (optical/FUV), 13.6 – 100 eV (ionising/EUV), and 100+ eV (X-ray). In this test the metallicity and initial chemical abundances are kept constant as this would directly affect the cooling timescale (see Formula 2.3), only the gas density

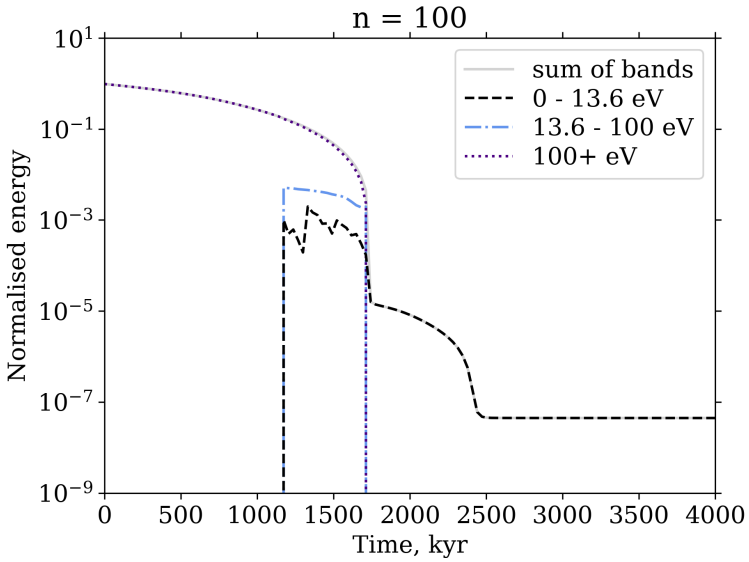

Figure 14: Evolution of the normalised internal energy of the gas cell versus time (for $n = 100$ cm^{-3}). The internal energy is divided into three energy bands: FUV (black dashed line), EUV eV (blue dash-dotted line), and X-ray (purple dotted line). The sum of all bands is represented by a gray solid line. Initially, most of the energy is concentrated in the highest energy band (X-ray), which decays up to the equilibrium state. Once the equilibrium state has been reached only the lowest (FUV) energy band is available (see Section 2.1.3).

is varied. The main goal of this benchmark test is to check if sum of the internal energies in the energy bands add up to the same total internal energy in the old implementation without band splitting. Additionally, we can investigate how the cooling energy will be split across the energy bands.

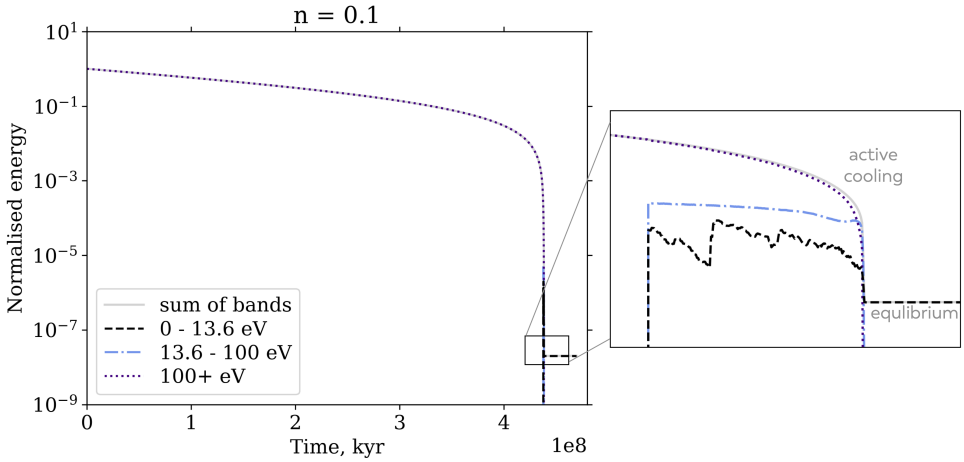

Figure 15: Same as Figure 15 with an ambient density of $n = 0.1$ cm^{-3}). The inset zooms in to the region where the transition from high to low energy bands takes place.

In Figures 14 and 15 we show the time evolution of the energy in each band and the total energy for a density environment of 100 and 0.1 cm^{-3}, respectively. The energies are normalised with the injected energy. The initial cooling phase is dominated by the X-ray band (100+ eV) as the initial gas temperature is high with $T > 10^7$ K. Once the gas has cooled to a temperature of a few 10^6 K we reach a rapid transition period where cooling in the FUV and EUV bands become relevant. Hereby, the EUV (13.6 - 100 eV) band is dominant at temperatures of 10^5 to 10^6 K. Below 10^5 K all cooling takes place in the FUV band. When heating and cooling rates are balanced we also reach an equilibrium state of the gas and the internal energy is constant.

We do not plot the old internal energy in Figure 14 and 15 as the difference between the old and the sum of bands of the internal energy was small. The mean difference between old and new energy is 3.8×10^{-26} with a standard deviation of 4.0×10^{-24}. The total energy remains conserved with the new approach, and the energy bands show the expected behaviour.

Depending on the gas density cooling takes longer for lower densities as can be seen when comparing Figure 14 and 15. This is an expected behaviour as the cooling time scales inverse proportional to the density ($t_{\rm cool} \propto \rho^{-1}$). In this case, the mean difference between old and new energy is 6.8×10^{-30} with a standard deviation of 2.2×10^{-27}. For these tests, we tried to vary other parameters (such as G_0, cosmic ionisation rate, N_H column density), but it does not influence the general behaviour of the gas apart from the expected effects.

We have also checked how much difference the new radiative cooling tables show compared to the old ones. The result is shown in Figure 16. Here, we start from a high-temperature cell (1.7×10^8 K) and let it cool at different densities. The changes are insignificant for the total energy. However, having the most up-to-date available data is always good in simulations, and the effect of the slight difference can be magnified in large-scale simulations.

3.4.4 3D Sedov explosion

To simulate a SN we use the 3D Sedov explosion problem (Sedov, 1959). The Sedov test is a standard numerical benchmark used to test hydrodynamic solvers in simulations. It is based on the analytical solution for a point explosion in a uniform medium, as derived by L.I. Sedov in 1959, often referred to as the Sedov-Taylor blast wave. In this test, 10^{51} erg is instantaneously released at a single point (typically across several cells to approximate the point source) within a uniform medium. This energy creates a strong spherical shock wave that propagates outward from the explosion site. The Sedov solution describes the self-similar evolution of the shock wave's radius and pressure profile as functions of time, ambient density, and the released energy. These equations assume ideal gas conditions and perfect symmetry.

First, to investigate how internal energy is redistributed among different cooling energy bands, we conducted a uniform density Sedov test simulation with band splitting of the cooling energy and without treating any radiation on the fly. The computational domain is a box with a volume of $(80\ {\rm pc})^3$ with isolated boundary conditions. The maximum resolution corresponds to a refinement level of 6, achieving a spatial resolution of 0.625 pc, which is sufficient to capture sharp gradients in pressure and density, particularly at the blast wave. To ensure the Sedov radius

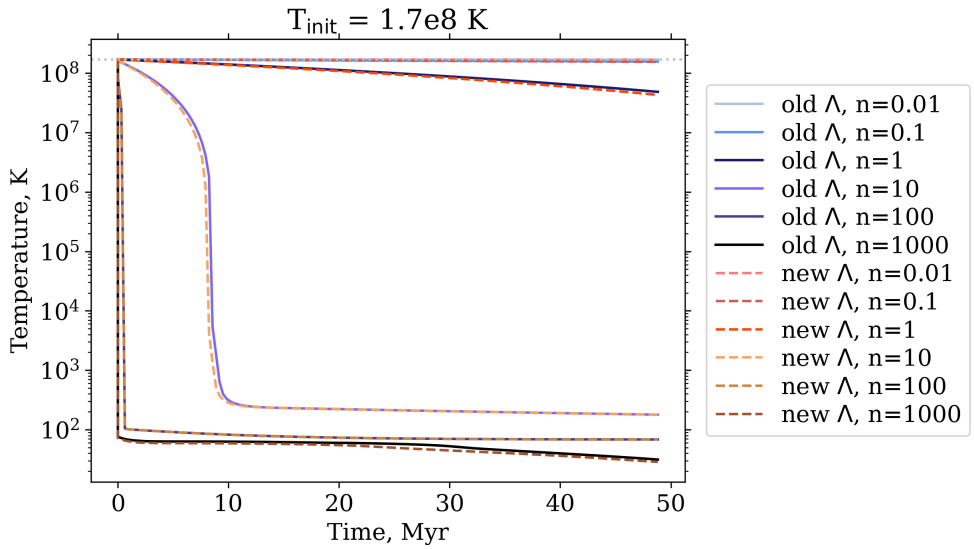

Figure 16: Time evolution of the gas with an initial temperature of 1.7×10^8 k over time, comparing results for different densities (n = 0.01, 0.1, 1, 10, 100, 1000 cm^{-3}) using two cooling functions: "old Λ" (solid lines) and "new Λ" (dashed lines). For high densities (n $\geq$ 10) the temperature decreases rapidly before reaching a kind of equilibrium. At lower densities (n $\leq$ 1) this process is significant slower. The final temperature strongly depends on the density. Both the "old Λ" and "new Λ" trace the same curve and only differ slightly. These small differences may be important if summed over a whole 3D simulation.

is well-resolved, the injection radius is set to 4.2 cells, following the methodology outlined in Gatto et al. (2015).

The initial conditions for the ambient medium are varied, with number densities ranging from $n = 0.1\,cm^{-3}$ to $n = 100\,cm^{-3}$, and temperatures from 10500 K to 60 K, allowing us to examine both diffuse ISM and dense medium regimes starting from approximate equilibrium conditions. This test is designed to track the redistribution of cooled energy across three distinct energy bands: optical/FUV (0 – 13.6 eV), EUV (13.6 – 100 eV), and X-ray (100+ eV). By analysing the temporal evolution of these bands in a uniform medium, we identify the dominant energy band at different stages of the SNR's evolution and clarify how the cooling energy is portioned under different environmental conditions.

The result of the simulation with $n = 100\,cm^{-3}$ and T = 54 K is shown in Figures 17, 18.

As the SN bubble rapidly encounters the dense medium, a sharp rise in the cooling emission is seen at around 3.5 kyr in the lower panel in Figure 17. Initially, a significant portion of the cooling energy is emitted in the X-ray band (violet dotted line). However, around the transition time (around 3.5 kyr), the emission becomes dominated by the EUV band (blue dash-dotted line). In the later stages, as the SNR evolves, the cooling energy shifts predominantly to the FUV band (grey dashed line), consistent with observational expectations. This trend is also evident in the top panel, which shows the cumulative energy across the bands. If we look at the morphology evolution in Figure 18, the optical/FUV band at early times (0.3 kyr) is concentrated near the centre, indicative of strong cooling in the post-shock gas. As time progresses (4.1 — 6.5 kyr), the emission becomes more spatially extended,

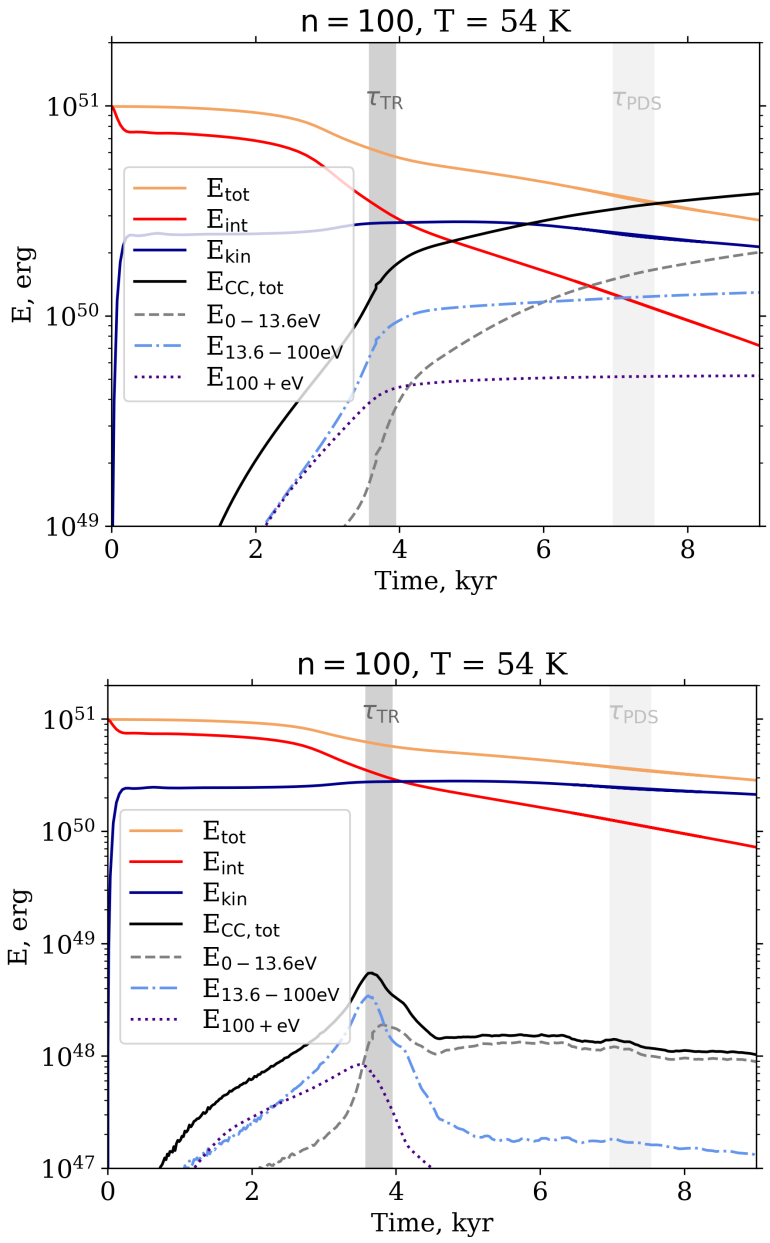

Figure 17: Top panel: evolution of the cumulative cooling bands: 0 – 13.6 eV, FUV/optical (grey dashed line), 13.6 – 100 eV, EUV (blue dash-dotted line), and 100+ eV, X-ray (purple dotted line), total cooling energy (black line) and non-cumulative evolution of the total energy (orange), internal energy (red), kinetic energy (blue) The vertical shaded regions mark key evolutionary stages: the transition time (τ_{TR}) where the SNR transitions from the Sedov-Taylor phase to the radiative phase, and τ_{PDS}, marking the pressure-driven snowplough phase, see the discussion about the evolutionary times in Haid et al. (2016). The highest amount of energy is cooled via FUV/optical band, then EUV and small amount via X-ray band. Bottom panel: evolution of the total energy (orange), internal energy (red), kinetic energy (blue), and cooling bands. E_{int} shows a steady decline as energy is radiatively lost over time. Initially, X-ray emission rises, but as the gas cools efficiently in the dense medium, it rapidly decreases. EUV emission exhibits a smoother peak, as the entire SNR bubble contributes before emission becomes concentrated in the shell after τ_{TR}. The morphological details can be seen in Figure 18.

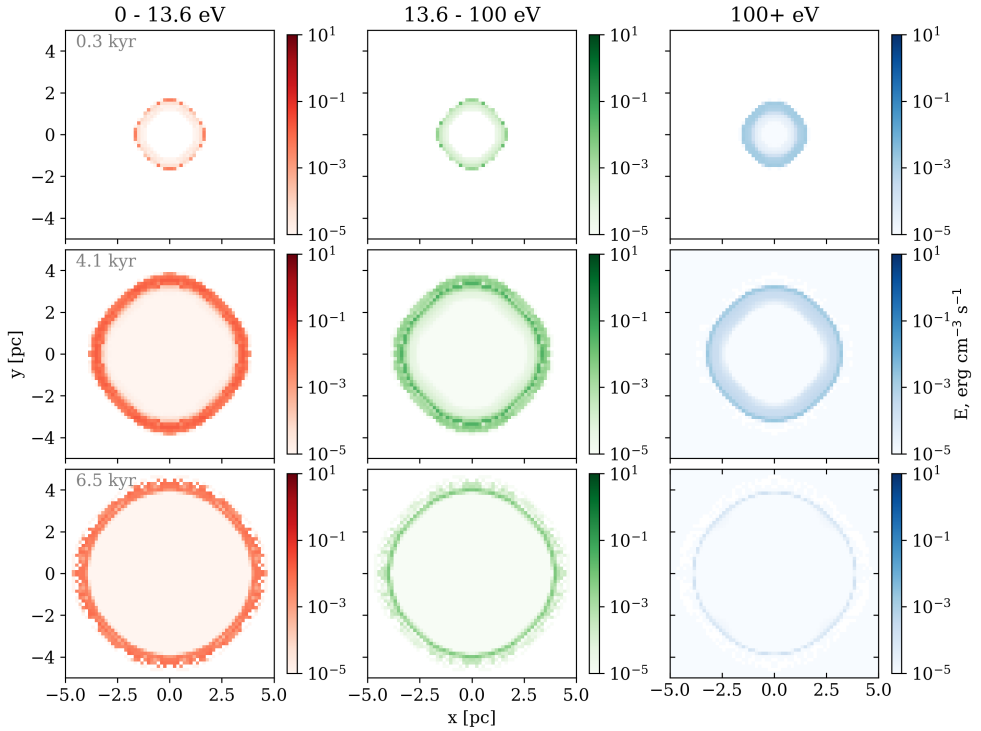

Figure 18: Slices of the cooling emission across three bands: optical/FUV (0 – 13.6 eV), EUV (13.6 – 100 eV), and X-ray (100+ eV) from a SNR expanding in a dense, uniform medium ($n = 100\,\mathrm{cm}^{-3}$). Each row corresponds to a different stage in the SNR evolution: 0.3, 4.1, and 6.5 kyr. At early times (0.3 kyr), X-ray emission dominates the hot central region, while optical and UV emissions are more confined. By 4.1 kyr, the UV forms a distinct shell, while optical emission expands more prominent. At later times (6.5 kyr), the optical band dominates the cooling shell.

forming a shell-like structure reflecting the cooling region's expansion. Also, the emission begins centrally concentrated for the EUV band but forms a sharper shell later. This behaviour is typical of gas cooling at intermediate temperatures, where the emission lines dominate in the UV range. For the X-ray emission: it is limited to the very hot, central region of the SNR. At early times (0.3 kyr), it dominates the inner region where temperatures exceed 10^6 K. However, as the remnant evolves (4.1 — 6.5 kyr), the X-ray emitting region diminishes significantly, indicating rapid cooling of the hottest gas. Overall, at early times (0.3 kyr), the SNR primarily emits in the X-ray and EUV bands from the hot shocked gas. The optical emission is comparatively weaker and more localised. Later, the EUV emission forms a clear shell structure as the shock wave sweeps up and compresses the surrounding dense medium. The X-ray emission diminishes, confined to the central region, while the optical emission dominates the outer shell. For old SNR (6.5 kyr), the optical emission becomes the dominant cooling channel, as most shocked gas has cooled to temperatures favouring this energy band. The UV shell persists, but X-ray emission is minimal.

The result for the test with $n = 0.1\,\mathrm{cm}^{-3}$ and T = 10562 K is shown in Figures 19, 20. The EUV band (blue dash-dotted line) peaks shortly after the transition time (approximately 160 kyr) and gradually declines thereafter as the remnant ex-

pands and cools (PDS time occurs at around 192 kyr; see Section 2.1.6 for details). The FUV band (grey dashed line) increases throughout the evolution of the SNR, although it dominates only around PDS time. The X-ray band (purple dotted line) exhibits a weaker signal due to inefficient cooling in the low-density environment. It may rise briefly at the very beginning of the SNR evolution, when the gas reaches temperatures of around 10^7 K; however, due to the low density, it never becomes bright enough to contribute significantly to the total cooling energy, as expected.

Secondly, we performed a Sedov test using split energy bands in the Chemistry module, employing only the X-ray band ($> 100\,\mathrm{eV}$) as the radiation source, which was treated on-the-fly with the radiative transfer module XrayTheSpot. We again investigate two environments, as in the test described above.

The result of the simulations with $n = 100\,\mathrm{cm}^{-3}$ and T = 54 K are shown in Figure 21. The image shows the X-ray emission morphology of a SNR at two stages of its evolution, 0.6 kyr (top panel) and 15.5 kyr (bottom panel), for different energy bands ranging from 0.1 keV to 8+ keV. The SNR exhibits a centrally bright emission morphology at early times, with higher-energy bands (e.g., 2–8 keV and 8+ keV) showing a compact, intense core, while lower-energy bands (0.1 – 2 keV) display a more extended structure. Over time, as the SNR expands and cools, the emission weakens significantly, particularly in the higher-energy bands, reflecting the decline in X-ray luminosity as the remnant transitions into later evolutionary stages. This behaviour highlights the strong dependence of X-ray emission on both the energy band and the SNR's age. It also shows a similar morphology to real SNRs. If we analyse the energy evolution plot in Figure 22, the first big difference is the slower decrease in total energy comparing to Figure 17. When we treat the X-ray cooling emission as a source of energy, we introduce the additional heating mechanisms such as photoionisation and Compton scattering (see the XrayTheSpot description in Section 3.3.3). Photoionisation deposits energy into the gas by ionising atoms, while Compton scattering transfers energy from high-energy photons to electrons, counteracting cooling. Additionally, X-rays maintain a higher ionisation state of the gas, reducing cooling efficiency since some radiative cooling mechanisms depend on lower ionisation states (though this is not explicitly traced in the code). In dense environments, such as $n = 100\,\mathrm{cm}^{-3}$, these effects are amplified due to more frequent interactions. This leads to a slower decline in internal (and total) energy than in simulations without X-ray traced feedback. This interplay between energy deposition and cooling creates a noticeable difference in energy evolution. The lowest energy band (optical/EUV) gains more energy when X-ray processes are included because of secondary ionisation and heating caused by high-energy X-rays. When X-rays ionise atoms or molecules, they produce energetic free electrons that can cause additional ionisations or excitations within the medium, redistributing energy to lower-energy photons. This leads to increased photoionisation rates and a transfer of energy from the higher energy bands (e.g., > 13.6 eV) into the 0 – 13.6 eV range.

The lower density test (see Figure 23) exhibit much weaker X-ray emission, as shown in previous tests (see Section 3.4.3). To observe such emission, the SNR would need to encounter a nearby dense structure, such as a molecular cloud; where it would create an X-ray bright filament.

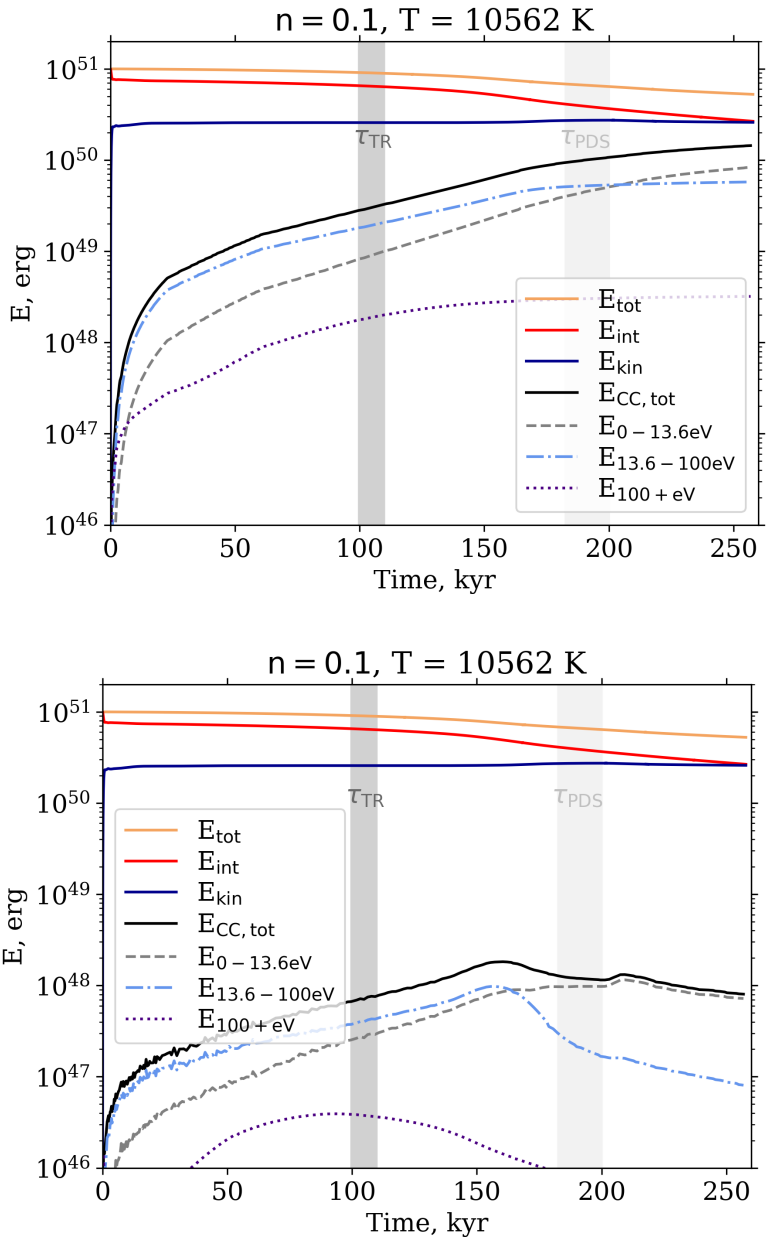

Figure 19: Top panel: Same as Figure 17, but for an environment with a density of $n = 0.1\,\mathrm{cm}^{-3}$ and an initial temperature of $T = 10562\,\mathrm{K}$. Bottom panel: Evolution of total internal energy (red), kinetic energy (blue), total energy (orange), and the cooling bands: 0–13.6 eV (black dashed line), 13.6–100 eV (blue dash-dotted line), and $>$ 100 eV (purple dotted line) for the Sedov test with $n = 0.1\,\mathrm{cm}^{-3}$, $T = 10562\,\mathrm{K}$.

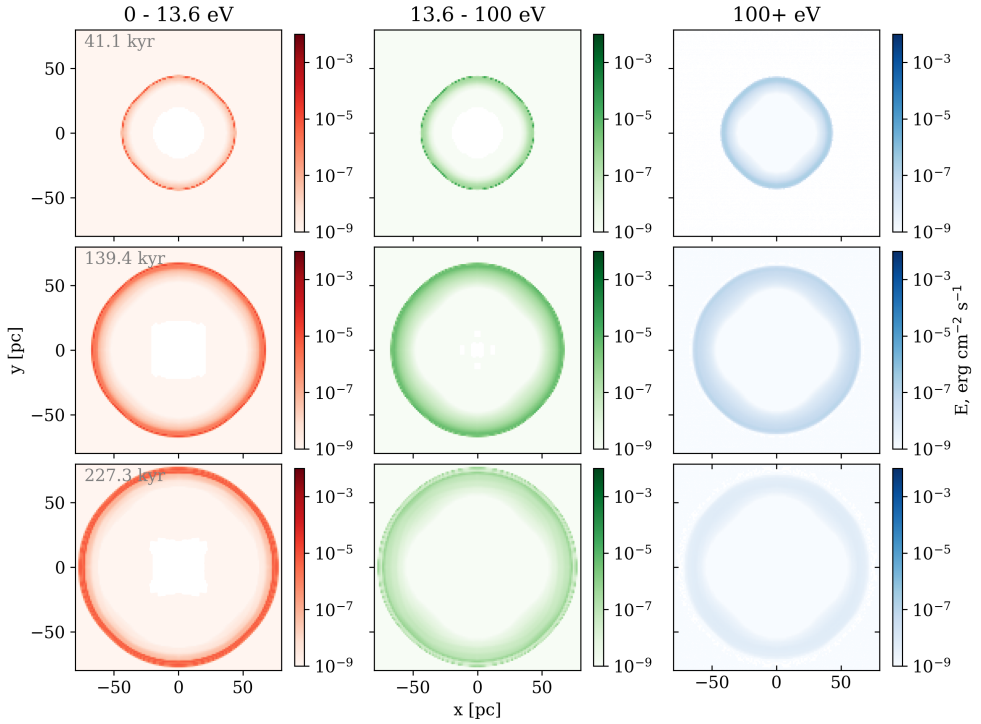

Figure 20: Same as Figure 18, but for but for an environment with a density of $n = 0.1\,\mathrm{cm}^{-3}$ and initial temperature $T = 10562\,\mathrm{K}$.

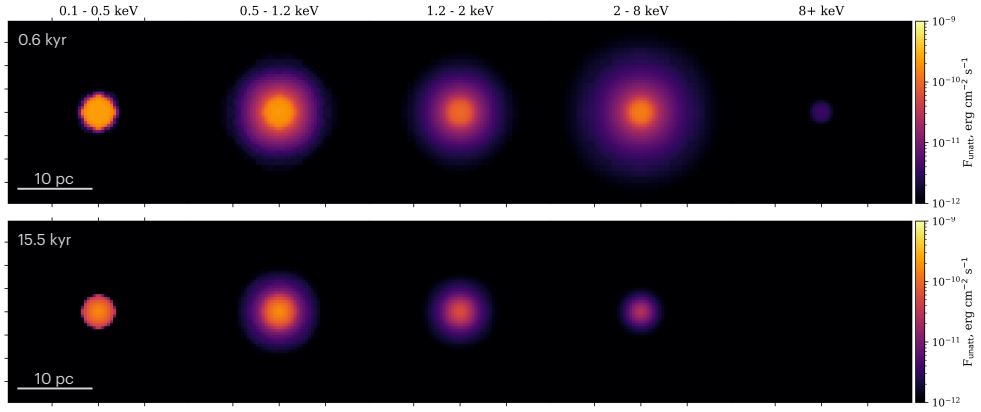

Figure 21: Evolution of the X-ray emission from a SNR at 0.6 kyr (top row) and 15.5 kyr (bottom row) for different energy bands (0.1 – 0.5, 0.5 – 1.2, 1.2 – 2, 2 – 8 keV, and 8+ keV) with initial conditions of $n = 100\,\mathrm{cm}^{-3}$ and T = 10562 K. As the remnant evolves and cools, the intensity of the X-ray emission decreases, especially in the harder bands, while the softer X-ray emission becomes more diffuse.

3.4.5

3D Massive star evolution

Having tested our implementation, we now aim to simulate an observed SNR — RCW 103. RCW 103 is a young Galactic SNR, approximately 2,000 years old, which

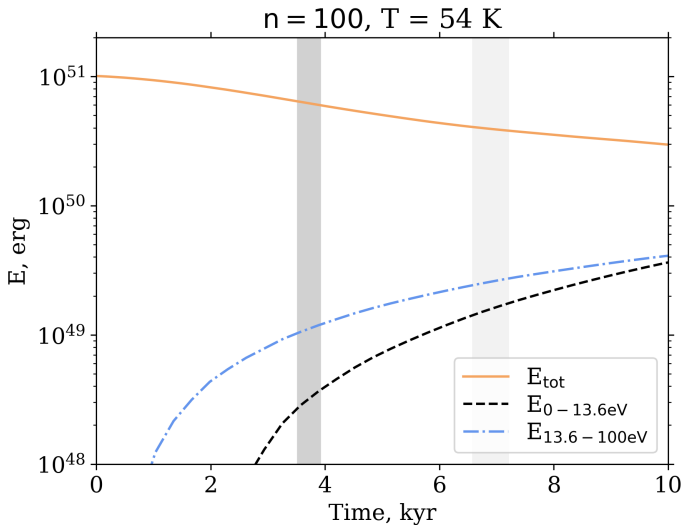

Figure 22: Same as the top panel in Figure 17, but with the X-ray emission traced on-the-fly. We can see a slower decrease in the total energy due to additional sources of heating (cooling X-ray cells) in the simulations.

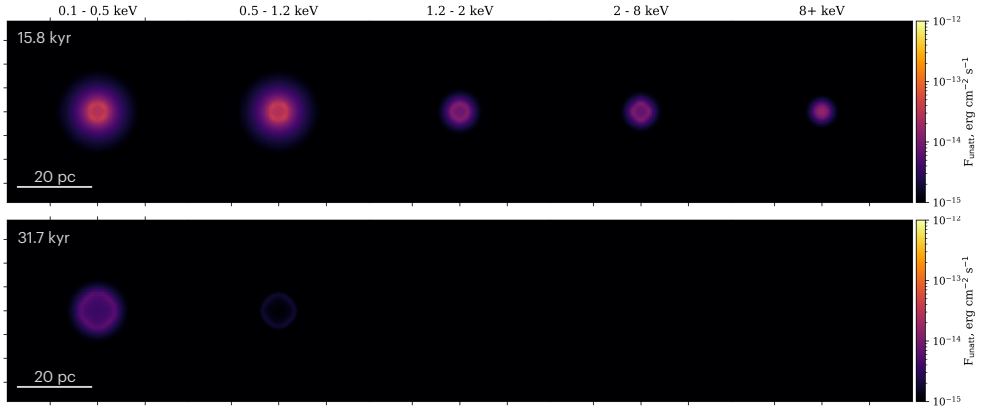

Figure 23: Same as in Figure 21, but for initial conditions $n = 0.1\,\mathrm{cm}^{-3}$ and T = 54 K. Overall, the X-ray emission is much weaker compared to the dense environment test

has begun interacting with the surrounding circumstellar medium. It has been observed across multiple wavelengths, including X-ray, optical, infrared, and radio bands. Despite the non-uniform density distribution at the explosion site, its X-ray morphology appears nearly circular.

To investigate this further, we aim to test the X-ray emission predicted by our simulations under different scenarios: a uniform medium with a magnetic field, or an interaction with a nearby molecular cloud (simplified representation of it). We are initiating several types of simulations. At the initialisation stage, a sink particle is placed at the centre of the computational domain to represent a massive star. The star evolves from the zero-age main sequence (ZAMS) to the SN phase, following the stellar evolution tracks of Ekström et al. (2012), with the implementation described in Gatto et al. (2017). During the main-sequence phase, ionising radiation

and stellar wind feedback are applied, forming a bubble with a radius of approximately 7.2 – 10 pc. Throughout this phase, the simulation timesteps are limited to 1 kyr. Once the star reaches the SN stage, it undergoes an explosion, triggering shock interactions with the surrounding circumstellar medium. At this point, the maximum timestep is restricted to 200 years in order to more accurately capture the evolution of X-ray emission during the various stages of the SNR's expansion. The initial conditions and results of these setups are presented in Chapter 7.

4

THE RESEARCH

Now that the necessary theoretical background has been introduced, the simulation and setups have been outlined, and benchmark tests have been completed, we proceed to the research part of this thesis. In this section, we will describe our scientific papers that address the research questions outlined in the introduction, building upon the established foundation.

In Paper I (Makarenko et al., 2023), titled ”How do supernova remnants cool? - I Morphology, optical emission lines, and shocks," we investigate SNR cooling processes, focusing on their morphology, optical emission lines, and shock dynamics. Using the high-resolution magnetohydrodynamic FLASH simulations SILCC-Zoom, we analyse the interaction of a SNR with a molecular cloud, incorporating detailed radiative cooling through the post-processing module, CESS (Cooling Emission from Simulated Supernova). CESS calculates synthetic optical emission maps (e.g., Hα, Hβ, [N II], [O III], [S II]) and reveals how optical lines and shock properties evolve during the SNR expansion. Our study highlights the distribution of cooling energy across different energy bands: EUV (13.6 – 100 eV) dominates for most of the SNR evolution, X-rays (100+ eV) are significant only briefly at the beginning, and optical/FUV (0 – 13.6 eV) emission becomes prominent for old SNR at the later stage of the evolution. These findings underscore the importance of accounting for detailed cooling processes, the complex structure of the surrounding medium, and projection effects. With CESS, we reproduced realistic optical emission maps, tracing the formation of emission features in 3D and the positions of optical lines relative to shock waves. We also revisited observational diagnostic techniques (e.g., BPT diagrams, optical line ratios), uncovering discrepancies in electron density estimates, temperature, explosion energy, and shock velocities. Our results emphasise the need to consider realistic ISM density distributions and metallicity estimates for accurate optical line diagnostics. These insights are expected to improve current and future observational data interpretations, setting a new standard for physics in SNR simulations. For this paper, I primarily contributed by developing the strategy for the optical diagnostic tool, writing and testing the associated code, analysing the results and writing the paper’s text.

Paper II (Smirnova et al., 2024), titled "How do supernova remnants cool? - II. Machine learning analysis of supernova remnant simulations", focuses on a statistical analysis of optical line emission from simulated SNRs interacting with a molecular cloud formed in the multi-phase interstellar medium, as modelled in the SILCC-Zoom simulations. The study is based on Paper I, with an extended dataset of 22 simulations with and without magnetic fields. In these simulations, the SN was positioned either 25 pc or 50 pc from the molecular cloud’s centre of mass. We first generated synthetic optical emission maps using the CESS code from Paper I. Then, we analysed the dataset using principal component analysis for dimensionality reduction and the k-means clustering algorithm to identify groups (clusters). The results indicate that the presence or absence of magnetic fields does not significantly impact the optical line emission. However, the ambient density distribution

at the SN site strongly influences the remnant's evolution and morphology. The study concludes that in our simulations, it is statistically possible to distinguish between SNe located at distances of 25 pc and 50 pc from the molecular cloud due to the difference in the mean ambient medium density at the site of the SN explosion. But there is no universal density trend with radius in the molecular cloud, so it is impossible to link optical emission with distance from the molecular cloud centre without prior knowledge. Therefore, the mean ambient density at the SN site is a relevant quantity when determining subsequent optical emission. My undergraduate student, Polina Smirnova, conducted this research as her bachelor's thesis project. Over the past two years, we have worked hard to publish this study. I primarily mentored Polina in her everyday science work, contributed significantly to the research and publication throughout the process.

In Paper III, we model the X-ray emission from RCW 103 using hydrodynamical simulations performed with the FLASH code. For the first time, these simulations incorporate a self-consistent, on-the-fly radiative cooling treatment for the X-ray energy band (100+ eV). The simulations begin with a uniform-density medium, with a massive progenitor star (13 or 18 $M_{\odot}$) placed at the centre of the simulation box. The star generates an HII region through its stellar wind and ionising radiation, creating a feedback that shapes the surrounding circumstellar medium. Following the star's Type II SN explosion, we track the post-explosion evolution, focusing on the effects of radiative cooling in X-ray bands. These bands were chosen to mimic the sensitivity ranges of the Chandra X-ray observatory: 0.3 – 0.85 keV, 0.85 – 1.70 keV, 1.7 – 3.0 keV, and above 3.0 keV. Each computational cell acts as a radiation source, with both emission and absorption calculated dynamically. This approach allowed us to produce synthetic X-ray maps of the SNR, capturing the evolution of the diffuse, circular X-ray emission and its interaction with the surrounding circumstellar medium. These results offer valuable insights into the processes shaping RCW 103's morphology and provide a better understanding of how the SNR's structure reflects the interaction between the explosion dynamics and the pre-existing environment. I have been a key contributor by developing the code for tracing radiative cooling from SNRs, generating mock observations of the SNR, and writing the text of the paper draft.

Overall, these papers serve as a bridge between the theoretical framework and the simulations' practical application. They also highlight the relevance of our work within the broader astrophysical research context.

5

HOW DO SUPERNOVA REMNANTS COOL? – I. MORPHOLOGY, OPTICAL EMISSION LINES, AND SHOCKS (PAPER I)

Monthly Notices of the ROYAL ASTRONOMICAL SOCIETY

MNRAS **523,** 1421–1440 (2023) https://doi.org/10.1093/mnras/stad1472
Advance Access publication 2023 May 17

How do supernova remnants cool? – I. Morphology, optical emission lines, and shocks

Ekaterina I. Makarenko [1]★ Stefanie Walch,[1] Seamus D. Clarke [2] Daniel Seifried [1] Thorsten Naab,[3] Pierre C. Nürnberger [1] and Tim-Eric Rathjen [1]

[1]*I. Physikalisches Institut, Universität zu Köln, Zülpicher Str. 77, D-50937 Köln, Germany*
[2]*Institute of Astronomy and Astrophysics, Academia Sinica, No. 1, Section 4, Roosevelt Rd., Taipei 10617, Taiwan*
[3]*Max Planck Institute for Astrophysics, Karl-Schwarzschild-Str. 1, D-85748 Garching, Germany*

Accepted 2023 May 8. in original form 2023 April 3

ABSTRACT

Supernovae (SNe) inject $\sim 10^{51}$ erg in the interstellar medium, thereby shocking and heating the gas. A substantial fraction of this energy is later lost via radiative cooling. We present a post-processing module for the FLASH code to calculate the cooling radiation from shock-heated gas using collisional excitation data from MAPPINGS V. When applying this tool to a simulated SN remnant (SNR), we find that most energy is emitted in the EUV. However, optical emission lines ([O III], [N II], [S II], H α, H β) are usually best observable. Our shock detection scheme shows that [S II] and [N II] emissions arise from the thin shell surrounding the SNR, while [O III], H α, and H β originate from the volume-filling hot gas inside the SNR bubble. We find that the optical emission lines are affected by the SNR's complex structure and its projection on to the plane of the sky because the escaping line luminosity can be reduced by 10–80 per cent due to absorption along the line of sight. Additionally, the subtraction of contaminating background radiation is required for the correct classification of an SNR on the oxygen or sulphur BPT diagrams. The electron temperature and density obtained from our synthetic observations match well with the simulation but are very sensitive to the assumed metallicity.

Key words: MHD – shock waves – methods: numerical – ISM: clouds – ISM: evolution – ISM: supernova remnants.

1 INTRODUCTION

Massive stars ($> 8 M_\odot$) have a short lifetime (only a few million years) and can end their lives as supernovae (SNe) surrounded by the molecular environment in which they formed. As such, about 10–20 per cent of all SN remnants (SNRs) are estimated to interact with dense molecular clouds (MCs; Hewitt & Yusef-Zadeh 2009). Although the interaction of SNRs and the turbulent interstellar medium (ISM) is difficult to treat both analytically and numerically (Haid et al. 2016), a solid analytical description of the evolution of SNRs in homogeneous media has long been established (Sedov 1959; Chevalier 1977; Ostriker & McKee 1988). The density of the gas hit by the expanding SN shock dramatically affects the properties of the shock itself, such as the velocity and temperature of the shock (e.g. McKee & Ostriker 1977; Slane et al. 2015; Chandra 2018). The SNR shock also affects the molecular gas, heating and ionizing it, and driving turbulence. Recently, several authors have studied the evolution of SNRs interacting with the turbulent, multiphase ISM in three-dimensional (3D) simulations (e.g. De Avillez & Breitschwerdt 2005; Gatto et al. 2015; Iffrig & Hennebelle 2015; Walch et al. 2015; Walch & Naab 2015; Martizzi et al. 2016; Seifried et al. 2018; Zhang & Chevalier 2019; Steinwandel et al. 2020). Current simulations of the multiphase ISM show that only 10–20 per cent of all SNRs explode in a high-density environment due to SN clustering (Gatto et al. 2017; Hu et al. 2017; Rathjen et al. 2021; Hislop et al. 2022). This is in agreement with observational estimates by e.g. Hewitt & Yusef-Zadeh (2009).

Observationally, SNRs can be studied across different energy bands due to their cooling radiation that covers the entire wavelength range (Chandra 2018). Most SNRs are observed at radio wavelengths due to their non-thermal synchrotron emission (e.g. Blandford & Cowie 1982). In an early evolutionary stage [Sedov–Taylor (ST) stage, typically $1-2 \times 10^4$ yr after the SN event], SNRs may be observed in the X-ray as the hot, shocked plasma cools (Sasaki et al. 2004, 2013; Slane et al. 2015). In the later transition (TR) phase and in the pressure-driven snowplough (PDS) phase, when the dense, shocked gas cools, one may observe SNRs in the UV and Optical (Dopita, Binette & Tuohy 1984). However, these observations are rarer because of extinction at optical wavelengths and because significant optical emission only occurs when high-density gas is shocked, i.e. when an SNR encounters a dense MC. In Green's catalogue (Green 2019) only about 20 per cent of the SNRs have optical counterparts.

When observable, optical emission-line diagnostics allow us to determine the evolutionary stage of the SNR and to analyse the physical parameters that define its environment. Optical emission tends to originate from the cooling and recombination zone directly downstream of the shock front itself, which is why it can produce a variety of diagnostics for both the material encountered and the physical processes involved (Dopita et al. 1984; Blair & Kirshner 1985). The morphology of the line emission is typically filamentary

★ E-mail: kativmak@gmail.com

or clumpy, possibly revealing the distribution of the dense gas (as predicted by, e.g. McKee & Cowie 1975 and observed by, e.g. Mavromatakis et al. 2001; Boumis et al. 2009; Sánchez-Cruces et al. 2018). The radiation signatures of shock waves can be highly complex, so synthetic observations should take into account the importance of the specific geometric projection (Hester 1987).

Using well-observable optical emission line ratios, active galactic nuclei (AGNs), SNRs, and H II regions can be classified by their main excitation mechanism. For example, when observing [N II] (λ6583), [O III] (λ5007), H α, and H β lines, one can build emission line-ratio diagnostic tool, the so-called BPT diagram (Baldwin, Phillips & Terlevich 1981; Kauffmann et al. 2003; Kewley et al. 2019b). On the BPT diagram, one can distinguish between the shock-dominated line ratios typically found in AGN-host galaxies (typically located in the upper right part of the BPT diagram, where both [O III] (λ5007)/H β and [N II] (λ6583)/H α are elevated; Stasińska et al. 2006; Ho 2008; Pagotto et al. 2021), star-forming galaxies (typically found in the lower left part, where both [O III] (λ5007)/H β as well as [N II] (λ6583)/H α are low; Sánchez et al. 2015), and the mixture of different ionization mechanisms in between these two regimes where SNRs are typically found. The exact position of the dividing line between the star formation (or H II region)-dominated regime and the shock-dominated regime is still debated (Kewley et al. 2001; Kauffmann et al. 2003; Herpich et al. 2016; Kewley, Nicholls & Sutherland 2019a) but the trends in the ionization conditions across the BPT diagram are well known.

In fact, there have already been attempts to reproduce observations of SNRs from simulations (Potter et al. 2014; Toledo-Roy et al. 2014; Bolte, Sasaki & Breitschwerdt 2015; Orlando et al. 2019; Derlopa et al. 2020). These are focused on either the remnant kinematics or the morphology. Our analysis is inspired by the observations and analysis of SNRs in our Galaxy in different optical filters (lines) (see e.g. Fesen, Blair & Kirshner 1985; Mavromatakis 2003; Mavromatakis et al. 2004; Boumis et al. 2005). In this paper, we focus on optical line emission maps that trace the evolution of an SNR interacting with a dense MC. We continue the work and post-process a high-resolution 3D simulation from Seifried et al. (2018) with the MAPPINGS V code (Sutherland & Dopita 2017). MAPPINGS V allows one to calculate the cooling radiation, assuming collisional ionization equilibrium (CIE). In this way, we obtain the cooling energy emitted in various optical lines: [O III], [N II], [S II], H α, and H β. With this information, it is possible to classify and study the parameters of the object, for example using the 'classic' version of the BPT diagram ([N II] (λ6583)/H α versus [O III] (λ5007)/H β) as well as the Veilleux–Osterbrock (VO) diagram ([S II](λ6531)/H α versus [O III](λ5007)/H β; Veilleux & Osterbrock 1987) to build a complete set of optical line diagnostics. Preliminary work was already done in Makarenko et al. (2020).

The paper is structured as follows. Section 2 describes the numerical model, the post-processing with MAPPINGS V, and how we calculate the synthetic emission maps. In Section 3, we discuss the line emission in the context of the remnant's evolution. Next, in Section 4, we present the results, focusing on the procedure of background subtraction, the optical emission of the SNR: attenuation and radiative transfer of optical emission lines, the BPT diagrams, and we determine the parameters of the SN shocks. In Section 5, we present our conclusions.

2 NUMERICAL MODEL

We use one high-resolution, magnetohydrodynamical (MHD) simulation of Seifried et al. (2018) (MC1 MHD) carried out with the adaptive mesh refinement (AMR), finite-volume code FLASH 4.3 (see Fryxell et al. 2000; Dubey et al. 2008). This simulation is part of the SILCC project (Walch et al. 2015; Girichidis et al. 2016; Gatto et al. 2017; Peters et al. 2017; Girichidis et al. 2018; Rathjen et al. 2021, 2023) and the SILCC-Zoom project (Seifried et al. 2017). In Section 2.1, we briefly describe the included physics and assumptions, while we refer to the previous papers for more detailed information.

2.1 Simulations

The SILCC-Zoom simulation initially follows the formation of an MC from the multiphase ISM under solar neighbourhood conditions. The full size of the simulation box is 500 pc × 500 pc × ±5 kpc. With a vertical stratification in the z-direction and an initial gas surface density of $\Sigma_{\rm gas} = 10\ {\rm M}_\odot\ {\rm pc}^{-2}$, this volume presents a small section of the galactic disc.

We follow the estimate of Draine (1978) for the strength of the interstellar radiation field (ISRF), i.e. $G_0 = 1.7$ times the Habing flux. The radiative transfer of the diffuse ISRF is self-consistently modelled using the TREERAY/OPTICALDEPTH module (see Wünsch et al. 2018, for a detailed description of the method).

A non-equilibrium chemistry network based on NL97 Nelson & Langer (1997) is included. It follows 7 species (H, H^+, H_2, C^+, CO, O, and free electrons) and is used to compute the gas heating and cooling processes (for further details, see Glover & Mac Low 2007; Glover et al. 2010; Walch et al. 2015). Because molecular hydrogen forms on dust, we have a simple dust model: the dust-to-gas mass ratio is fixed (a ratio of 1:100 is used), but the dust temperature is calculated separately from the gas temperature, assuming the dust to be in thermal equilibrium. We consider several heating processes, such as heating by the photoelectric effect associated with the absorption of the ISRF photons (for more details, see Walch et al. 2015). However, in the simulation presented here, the predominant source of heating is the strong shock associated with the SNR and the corresponding thermalization of the rarefied gas within the remnant bubble. UV and optical lines originate from the warm and hot ionized gas within the heated bubble and near the bubble rim. For the cooling of the high-temperature gas ($T \gtrsim 2 \times 10^4$ K), we use tabulated cooling functions from Gnat & Ferland (2012) for solar metallicity [warm ionized medium (WIM) model; see below] assuming CIE. The cooling of the cooler gas takes into account the local elemental abundances traced by the chemical network. Our simulation originally assumed that all cooling radiation simply escapes to infinity (a typical assumption for 3D (magneto-)hydrodynamic simulations), which is in principle only valid if the surrounding medium is optically thin at the relevant wavelengths. We will show later on (see Section 4.2) that optical depth effects actually do play a role for the considered SNR. This will be further discussed in future work.

We use metallicities resembling the Milky Way disc near the solar neighbourhood, i.e. we use the WIM model of Sembach et al. (2000). We summarize the most important elements for our analysis in Table 1. The WIM abundance corresponds to the solar abundance by Howk, Savage & Fabian (1999) modified by dust as observed in warm diffuse clouds. The abundances of nitrogen and oxygen adapted for the WIM are from Meyer, Cardelli & Sofia (1997) and Meyer, Jura & Cardelli (1998). The magnetic field value is set to $B = 3\ \mu$G.

The simulation starts off by driving the multiphase ISM with SNe for more than 10 Myr before following the formation of a MC in detail. The zoom-in procedure uses the AMR capabilities of the FLASH code: within a subregion of $\sim(100\,{\rm pc})^3$ we allow the code to adaptively refine down to a minimum cell size of 0.12 pc, while the

Table 1. Metallicities for the main elements (column 1) whose ions are typically observable in the SNRs. The abundances are given as logarithmic values on a scale where A(X) = log (X/H) + 12.00 and increase from left to right. The Dopita2005 (column 2), default 'solar abundance' (column 4), '2 solar ' (column 5) in MAPPINGS V are taken from Asplund et al. (2009). The solar abundance 'WIM' (Sembach et al. 2000) (column 3) is what we use in our simulations.

Element	Dopita2005 A(X)	WIM A(X)	Solar A(X)	2xSolar A(X)
N	7.58	7.88	8.05	8.35
O	8.44	8.50	8.93	9.23
S	6.99	7.07	7.21	7.51

rest of the 500 pc-scale computational domain is kept unchanged. After the forming MC is fully refined ($t_0 = 11.9$ Myr) and a bit more evolved, we explode a single SN at time $t_{SN} = t_0 + 1.53$ Myr and at a distance of $d = 25$ pc from the centre of mass of the cloud along the x-direction. The SN explosion is modelled by injecting a total amount of $E_{SN} = 10^{51}$ erg in the form of thermal energy within a spherical injection region of 4.5 grid cells, which corresponds to 11.7 pc in our case. At this resolution and injection radius, the ST phase is well resolved, and therefore a thermal energy injection scheme is suitable (e.g. see Gatto et al. 2015; Kim & Ostriker 2015). For more details on the simulation, see 'MC1-MHD + 25pc x' in Seifried et al. (2017, 2018). We note that for the analysis and emission line diagnostics presented in the following, we use a slightly smaller volume (65 pc × 76 pc × 68 pc around the explosion centre). We further note that we study a whole set of different simulations in a follow-up paper (Smirnova et al. in preparation).

We follow how the SNR expands and also interacts with the nearby dense MC over time $t_{evol} = t - t_{SN}$. Specifically, the evolution of the remnant in this paper is followed until $t_{evol,fin} = 0.3$ Myr. This is motivated by the following time-scale estimates. The SNR transition time (TR) marks the end of the adiabatic ST phase. Following the calculation of Haid et al. (2016), we obtain an SNR transition time of $t_{TR} \approx 0.042$ Myr for an assumed uniform environmental number density of $n = 1$ cm^{-3} of the SN explosion site. The time at which the remnant would then transit to the PDS phase is $t_{PDS} \approx 0.08$ Myr. With these estimates, we may compare the optical emission obtained from synthetic and real observations. It can also be seen that the time span of 0.3 Myr past explosion should be sufficient to trace the main part of the SNR evolution. We will further discuss these time-scale estimates in Section 3.2.

2.2 MAPPINGS V post-processing and cooling function

While, during the course of the 3D simulation, the numerical scheme only works with a total cooling rate, we are interested to see what fraction of the energy lost by radiative cooling is emitted in the X-ray ($E_X \geq 100$ eV), ionizing UV (EUV; 13.6 eV $\leq E_{EUV} < 100$ eV), or the non-ionizing UV (FUV) and Optical ($E_{FUV} < 13.6$ eV). In particular, we also calculate the emission in the most bright optical emission lines such as [O III], [N II], and [S II], which can be used for object diagnostics.

For this purpose, we use the MAPPINGS V code [for the current version of the code, see Sutherland et al. (2018), also Dopita (1976); Binette, Dopita & Tuohy (1985); Sutherland & Dopita (1993, 2017)] in a post-processing step.[1] This code assumes CIE, meaning that the ionization fractions of each element depend only on the gas temperature, with no dependence on the gas density. This is applicable for SNRs, where the most significant contribution to the (collisionally excited line) emission is produced by shocks and not by photoionization (Levenson et al. 1995; Negus et al. 2021). We can use the CIE approximation since we are mainly interested in the optical emission of the SNR, i.e. in a fairly evolved SNR, which has departed from the ST phase. At the early stages of evolution (when hard X-ray radiation predominates), this approximation should probably not be used, since not all plasma is evenly ionized. After about 3×10^4 yr (for typical densities of 1 cm^{-3}), the ionization state of the plasma no longer plays a role and the gas reaches equilibrium as claimed in Reynolds (2017). In addition, no significant differences have been found when treating an evolved SNR in equilibrium or in non-equilibrium (Sarkar, Gnat & Sternberg 2021).

[1] https://github.com/kativmak/CESS

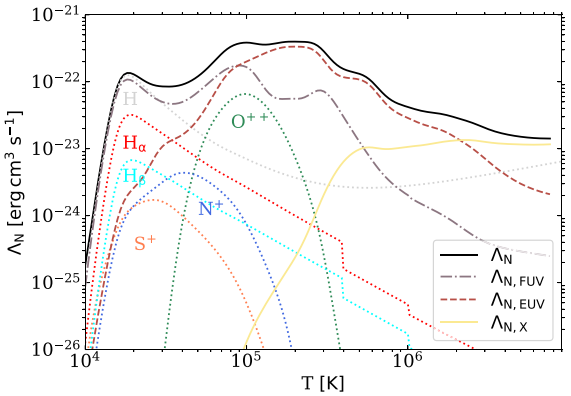

Figure 1. Normalized cooling function, i.e. emissivities Λ_N as a function of the gas temperature calculated using MAPPINGS V for solar metallicity (WIM model; for details on the metal abundances see Sembach et al. (2000) and Table 1). In addition to the total emissivity (black line), we also show the normalized cooling curves in three different energy bands: the far-ultraviolet (FUV) and optical ($E_{FUV} < 13.6$ eV), the ionizing EUV (13.6 eV $\leq E_{EUV} <$ 100 eV), and the X-ray ($E_X \geq 100$ eV). Further, we overplot the contributions of the ions used in the emission line diagnostics.

Using MAPPINGS V and assuming the WIM metallicity model, we produce a detailed cooling curve as a function of the gas temperature by considering emission from hydrogen, helium, and metal atoms and ions, as well as non-atomic emission such as free–free emission. The resulting total emissivity Λ_N (erg s^{-1} cm^3) is the cooling rate Λ (erg s^{-1} cm^{-3}) divided by $n_e n_H$, where n_e is the electron number density, and n_H is the number density of hydrogen nuclei. We use $n_e \approx n_H = 1$ cm^{-3}. We show Λ_N in Fig. 1 (solid black line).

By modifying the MAPPINGS V code, we further divide the total cooling rate into three energy bands (E_{FUV}, E_{EUV}, E_X) but we could define any other number or limits of energy bands. We overplot these three emissivities $\Lambda_{N,\,FUV}$ (dot–dashed grey line), $\Lambda_{N,\,EUV}$ (dashed brown line), and $\Lambda_{N,\,X}$ (yellow line) in Fig. 1. Additionally, we show the contributions of the optical cooling lines (dotted lines: S^+ in orange; N^+ in blue; O^{++} in green; H β in cyan; H α in red; and the combination of all hydrogen lines in light grey). The hydrogen lines dominate at $T \sim 20\,000$ K, while N^+ and O^{++} are tracing higher temperatures. In particular, O^{++} is tracing the hotter gas inside the remnant bubble, whereas the other lines (N^+, S^+) are more prominent at colder temperatures, which we expect to find closer to the bubble edge.

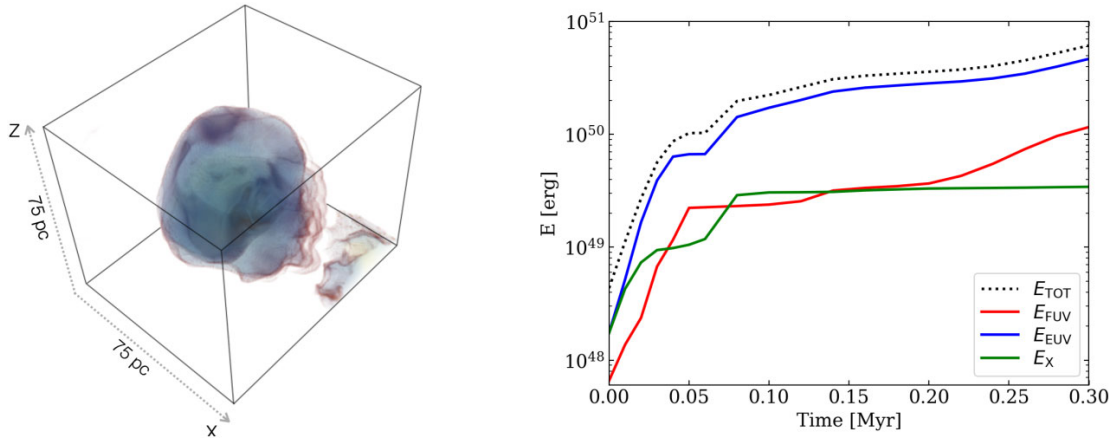

Figure 2. Left-hand panel: Volume rendering of the post-processed SNR at time $t_{evol} = 0.16$ Myr, showing the FUV/Optical ($E_{FUV} < 13.6$ eV, red), EUV (13.6 eV $\leq E_{EUV} < 100$ eV, blue), and X-ray emission ($E_X \geq 100$ eV, green) of the cooling remnant. Each side of the cube is approximately 75 pc. Note that this is only a part of the simulation box. In the lower right corner of the cube, emission from the background is also visible. Right-hand panel: Cumulative cooling energy as a function of the remnant's evolution time. We show the total cooled energy (black) and how it is distributed over the three energy bands. The SN explosion energy is $E_{SN} = 10^{51}$ erg. We find that only a fraction of E_{SN} has been radiated away by $t_{evol,fin}$. Due to the broad density distribution of the surrounding ISM, t_{TR} and t_{PDS} vary substantially over the surface of the expanding remnant, leading to an extended period of cooling (see Section 3.2).

3 POST-PROCESSING OF SNRS

3.1 Time evolution of the cooling energy

In Fig. 2 (left-hand panel), we depict the 3D distribution of the emissivities $\Lambda_{N,FUV}$ (red), $\Lambda_{N,EUV}$ (blue), and $\Lambda_{N,X}$ (green) showing the SNR at $t_{evol} = 0.13$ Myr. We obtain the local Λ_N for each cell by linearly interpolating the pre-computed MAPPINGS V cooling tables for the given gas temperature of the 3D FLASH simulation. Fig. 2 only shows a small part of the simulation domain with a side length of about 75 pc in each direction, centred around the SNR. In the bottom right corner, one can see an emission that is not associated with the young remnant but originates from an older nearby remnant (i.e. background emission). According to an estimate of the typical star formation rate in a galactic environment with an overall gas surface density of $\Sigma_{gas} = 10\,M_\odot\,pc^{-2}$ (Kennicutt 1998), and assuming a standard stellar initial mass function, the typical SN rate in the simulated total volume is ∼15 SN/Myr (Walch et al. 2015). With a typical size of 80−100 pc (De Avillez & Breitschwerdt 2007), old SNRs are likely to contribute to the emission of a selected subregion. We will discuss how to subtract this 'background emission' in Section 4.1 and how the background emission might contaminate the diagnostic of unresolved (not in our Galaxy) SNRs in Section 4.4.

On the right-hand panel of Fig. 2, we show the cumulative cooling energy lost by the young SNR as a function of time. To avoid including the background emission, we explicitly choose a coordinate system within which the explosion centre is located at the origin of the SN bubble and compute the size of the remnant along the principal axes (six directions) for each time-step. To find the edge of the hot bubble, we then search for a sharp drop in the temperature data along each axis. All n_{cells} cells within the sub-cube defined by the extent of the remnant are used to calculate the total, time-dependent, cumulative cooling energy, E_{tot}, as

$$E_{tot}(t_{evol}) = E_{tot}(t_{evol} - \delta t) + \delta t \sum_{i=1}^{n_{cells}} \Lambda_{N,i} n_{H,i}^2 V_i, \quad (1)$$

where t_{evol} is the current time (see Section 2.1), δt is the time difference between the current time and the previous output. We sum over each cell i with volume V_i in the selected sub-cube. Similarly, we compute the cumulative cooling energy in the three different energy bands.

During the first steps of the SNR evolution, most of the cooling energy is emitted in the EUV and X-ray bands. When the supersonic blast just hits the surrounding ISM, it heats the gas to X-ray emitting temperatures beyond a few 10^5 K (see Fig. 1). As the primary shock wave decelerates, the reverse shock becomes non-radiative and the SNR emits thermal X-ray (and strong radio synchrotron emission). The physical processes included are free–free radiation (from forward and reverse shocks), inverse-Compton scattering, and X-ray line emission from the ionized metals (Fe, C, O, Ne, etc.). As can be seen from the right-hand panel in Fig. 2, these first stages do not last long, and the X-ray emission begins to weaken (approximately around 0.01 Myr) as the reverse shock wave has disappeared and the remnant passes into the ST stage. Now the energy is mostly released in the EUV, FUV, and optical bands (note that all further low-energy emission, such as infrared emission, is included in this 'Optical' band), mainly in the low ionization stages of elements like sulphur, nitrogen, and oxygen (see Fig. 2) as well as in hydrogen lines. Since an SNR spends most of its later life radiating in the EUV and optical (before it merges with the surrounding ISM), this emission is a valuable tool for the classification of SNRs and the determination of various parameters such as electron density and temperature of the gas, shock velocity, and energy of the SN explosion. At the time when we stop the simulation ($t_{evol} = 0.3$ Myr), the remnant has lost about 60 per cent of E_{SN}. Within the ST phase, it is expected that slightly more than 70 per cent of E_{SN} are in the form of thermal energy (e.g. Walch & Naab 2015; Haid et al. 2016). Hence, the remnant has mostly, but not fully cooled down by the time we stop the simulation.

3.2 Characteristic times for the SNR evolution

Radiative cooling plays an important role in the evolution of an SNR, especially in an inhomogeneous medium (in our case, next to a MC). This has been shown in the simple one-dimensional models (Chevalier 1977; Cioffi, McKee & Bertschinger 1988) and then in

more complex 3D simulations (Kim & Ostriker 2015; Walch & Naab 2015). Usually, young SNRs are observed during the ST or TR phase and old SNRs during the radiative phase (TR or PDS). These are typically used characteristic times to describe the SNR evolution. It is important to estimate these times to compare synthetic and real observations. In the ST phase (Sedov 1959) the remnant only cools adiabatically, while radiative losses are small and can be neglected. Radiative cooling becomes important in the TR phase. Therefore, the transition to the TR phase is associated with a rise of cooling energy released in the form of optical emission lines due to the temperature dropping below 10^6 K. The PDS phase, in which radiative cooling plays a substantial role, is the longest stage of the SNR evolution before it merges with the ISM.

Due to the complex ISM structure into which the SNR expands in our simulation, it is not possible to calculate unique characteristic times for our remnant. We demonstrate this in Fig. 3, where we first show the volume-weighted density probability distribution function (PDF) of the surrounding gas at the time when the SN explodes (left-hand panel). In Fig. A1, we show the density PDFs for the respective subcubes (see Table 2 in Section 3.1 for how the subcubes were defined) which contain the SNR at three different times, $t_{\rm evol} = 0.01$, 0.13, 0.3 Myr. Although most of the volume near the remnant centre is initially filled with gas with a density of $\rho \sim 10^{-23.5}\,{\rm g\,cm^{-3}}$, the overall range of densities is very broad (spanning more than 7 orders of magnitude in density). Following the calculation from Haid et al. (2016), we plot the corresponding characteristic evolution times for a given environmental density on the right panel of Fig. 3. The end time of our simulation is indicated by the vertical grey-dashed line. We see that the SNR should have evolved well into the PDS stage if it would have exploded in a uniform density medium with $\rho = 10^{-23.5}\,{\rm g\,cm^{-3}}$. However, expanding into different directions from the point of view of the SNR centre, the characteristic times may differ dramatically. This is why we cannot state one $t_{\rm TR}$ and one $t_{\rm PDS}$ for the whole SNR: in a simple picture, different parts of the remnant evolve on different characteristic time-scales.

This explains why the remnant is still cooling at $t_{\rm evol} = 0.3$ Myr. The energy evolution of the SNR can be explained as follows: we first have a sharp rise of EUV optical/FUV emission around 0.05 Myr on the right-hand panel of Fig. 2, because it roughly corresponds to $t_{\rm TR,a}$ for the median SN ambient density $\rho \sim 10^{-23.5}\,{\rm g\,cm^{-3}}$. Then the reverse shock travels into the SNR bubble and we can observe the second sharp rise in energy around 0.1 Myr in the X-ray and EUV, but none of the gas is available yet to emit in the optical band (dense gas has not yet reached $t_{\rm PDS}$ and low-density gas has not yet reached $t_{\rm TR}$). There is a part of low-density ISM gas left (around 10^{-25}–$10^{-26}\,{\rm g\,cm^{-3}}$) which can finally reach $t_{\rm TR}$ and emit in the optical/FUV band significantly later. As a result, we do not see a decrease in the optical/FUV emission after 0.2 Myr of SNR evolution. Only at 0.25 Myr dense gas will be at the PDS stage and part of the low-density gas at the transition phase. No doubt that we need a longer time-scale for all gas to reach a PDS stage. However, 0.3 Myr is still a long enough time-scale to cover all stages of SNR evolution for the most part of the SNR bubble.

3.3 SNR interaction with a MC

This work will consider emission before, during, and after the TR stage for the densest part of the SNR bubble for comparison ($t_{\rm evol} = 0.01$, 0.13, 0.3 Myr). In Fig. 4, from top to bottom, we show the time evolution (from left to right) of the density and temperature in slices through the explosion centre and RGB images of the three different energy bands (X-ray in blue, EUV in green, optical/FUV in red). The SNR bubble is heated to more than 10^6 K, leading to the hydrodynamic expansion of the remnant. Due to the turbulent surrounding medium, the expansion of the remnant is highly asymmetric.

Fig. 4 clearly shows that even though the SN explosion is initially symmetric, the MC distribution dominates in shaping the remnant morphology (Kafatos et al. 1980). The density of the MC gas is several orders of magnitude higher than in the low-density ISM ($n_{\rm H} > 10^3\,{\rm cm^{-3}}$). Therefore, the velocity of the shock wave towards the centre of the cloud is much smaller and, in some places, the shock almost stops not able to propagate further into the MC. Hitting a dense medium also leads to rapid gas ionization. It launches a strong reverse shock that travels into the ejecta. Therefore, the hot interior of the SNR is a source of X-ray emission like we see in observations (see Slane et al. 1999; Long et al. 1991, or the overview by Vink 2012).[2] Moreover, the explosion cannot spread to the centre of the MC (the area of highest density to the left of the explosion centre), but it continues to expand into the more diffuse region towards the upper right corner of the emission maps, forming dense filaments as a result of instabilities. These structures are an essential morphological feature as a criterion for the interaction of an SNR with a cloud, which is also commonly found in real observations (see Fesen et al. 1997; Boumis, Mavromatakis & Paleologou 2002; Boumis et al. 2004; Katsuda et al. 2016; How et al. 2018, and others). In general, we can conclude that the SNR has a very complex structure. In projection, the shocked filaments which are visible in the Optical and EUV overlap with the volume-filling X-ray emission (see also Fig. 2 for the 3D example).

From our 3D simulation data, we plot mass-weighted 2D PDFs in Fig. 5, which show the distribution of the multiphase ISM gas in the temperature–density phase space (top row). From left to right, we show the same times as in Fig. 4, i.e. $t_{\rm evol} = 0.01, 0.13,$ and 0.3 Myr after the explosion took place. Cells which are identified to belong to the SNR sub-cube are shown in colour, while all other cells within the SILCC zoom-in region are shown in grey-scale as these are considered to belong to the background. Due to the highly asymmetric morphology of the remnant, the sub-cube also contains some gas from the shell and the nearby cloud. However, it is quite obvious which gas belongs to the hot interior and the cooling shell and which material is part of the surrounding ISM contained in the sub-cube. At $t_{\rm evol} = 0.01$ Myr, the young remnant can be clearly seen as it incorporates relatively dense gas (the gas near the explosion centre initially has number densities between $n \sim 1 - 10\,{\rm cm^{-3}}$), which is heated to $T \gtrsim 10^{6-7}$ K at $t_{\rm evol} = 0.01$ Myr. The thin shell around the SNR bubble is also distinguishable at this time-step as an almost horizontal branch at $T \gtrsim 10^{4.3}$ K. The hot bubble moves to the left, to lower densities, as the remnant expands, and it almost merges with the hot gas 'branch' at lower densities, which is populated by older background SNRs.

Using MAPPINGS V, we calculate the luminosity of key optical emission lines for each grid cell following equation (1). We show the luminosity-weighted 2D PDFs in rows 2–6 of Fig. 5. The y-axis range is limited to show the warm–hot medium with temperatures between $10^{3.8}\,{\rm K} < T < 10^{5.8}\,{\rm K}$ (as indicated by the dashed horizontal lines in the top panels), as this is the temperature regime where the optical lines are bright (and can physically be exited, see Fig. 1). Again, we distinguish between material within the SN sub-cube (coloured distribution) and background gas (grey-scale). We plot H α (second row), [O III] (λ5007) (third row), H β (fourth row), [S II] (λ6717,

[2]This can be seen in the attached animation, in particular in the X-ray band.

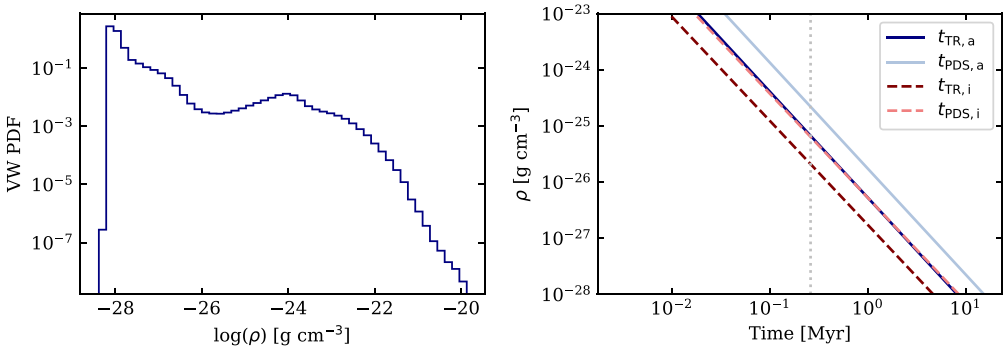

Figure 3. Left-hand panel: Volume-weighted density PDF of the initial whole simulation box ($t_{\rm evol} = 0.0$ Myr). Right-hand panel: Model predictions from Haid et al. (2016) for the $t_{\rm TR}$ and the $t_{\rm PDS}$ in ambient atomic media (solid lines) and in ambient ionized media (dashed lines) with different densities. The vertical grey line illustrates the time until we calculate the SNR evolution, $t_{\rm evol} = 0.3$ Myr.

Table 2. Time evolution (column 1) of the SN box ($a_{x,\,y,\,z}$, columns 2–4) and a shock box (defined from our shock detection routine) along the x, y, and z-axis ($s_{x,\,y,\,z}$, columns 5–7). We use shock boxes to calculate the parameters (temperature, density and luminosity) inside and outside of the SN bubble at different times for Fig. 5. SN box is used in all other cases.

$t_{\rm evol}$ Myr	$a_{x,\,\rm SNbox}$ (pc)	$a_{y,\,\rm SNbox}$ (pc)	$a_{z,\,\rm SNbox}$ (pc)	s_x (pc)	s_y (pc)	s_z (pc)
0.01	64.8	77.5	68.1	16.2	19.5	16.1
0.13	64.8	77.5	68.1	32.4	34.4	40.1
0.3	64.8	77.5	68.1	56	66	55.1

6731) (fifth row), and [N II] (λ6583) (sixth row, one can see only one sulphur line in Fig. 5 because [S II] (λ6717) and [S II] (λ6731) have the same behaviour and properties). For emission lines in Fig. 5, it is impossible to draw a simple luminosity–density dependence.

4 OPTICAL EMISSION LINE DIAGNOSTICS

4.1 Background subtraction: resolved versus unresolved SNRs

The background of our simulation may contain emissions from previous SNRs (e.g. see the lower right corner in the left-hand panel of Fig. 2), which are not the subject of our work but can represent a realistic background as in observations.

In order to carry out the emission line diagnostics, we include the option to reduce the background of the signal, since we can calculate the emission of the warm-hot, diffuse gas right before the SN explosion takes place. The background is defined as the emission calculated for the gas distribution immediately before the SN explosion (at $t_{\rm evol} = 0.0$ Myr). In this way, we compute the background emissivity for each line in 3D. The lines we consider are H α (λ6563), H β (λ4861), [O III] (λ5007), [N II](λ6583), [S II] (λ6717), and [S II] (λ6731). Hence, for every snapshot we analyse, we calculate the line emissivities in 3D and, if background subtraction is switched on, we just subtract the 3D cube of the background from the current 3D cube of cooling emission.

We may now choose a viewing angle, i.e. the position of the outside observer and integrate the 3D cube along the line-of-sight (LOS) to obtain the corresponding flux map. We integrate over the map to obtain the total luminosity ($L_{\rm tot}$, [erg s^{-1}]) of a given line. Assuming the gas to be optically thin, the resulting total luminosity of the background, $L_{\rm bg}$, is given in Table 3 for each of the computed lines. Since the background emission is assumed to be constant in time while the actual line emission from the SNR evolves as a function of time, the background subtraction reduces the overall line flux by different amounts, i.e. the 'attenuation percentage' changes. We list the minimum and maximum values of the attenuation percentage in the third column of Table 3.

In the course of the paper, we follow two different approaches, motivated by real observations: in case the SNR would be located in our Galaxy and could be well resolved (pixel-by-pixel resolved SNR, for example, Fesen et al. 1985; Boumis et al. 2022), we should apply the background subtraction and study the resolved line intensity maps; if the SNR would be located in some nearby galaxy, it would appear as an unresolved SNR and we only consider the integrated line luminosity. In order to mimic the real observations, we generally do not subtract the background in this case, as an unresolved object could not be disentangled from the diffuse emission which is contained in the same beam. However, we discuss resolved maps without background subtraction as well as unresolved maps in case a background subtraction would be possible throughout the next sections. In this way, the simulations can be used to inform real observations on this matter.

An example of the optical emission maps is shown in Fig. 6 and in Fig. B1for the projection along the x-axis from the top ('t') view. A typical observational limit used for real telescopes of 3×10^{-18} erg s^{-1}cm^{-2} arcsec^{-2} [inspired by the local volume mapper (LVM) targeting the Milky Way at 37 arcsec $\sim$ pc scales, 3σ sensitivity; Kollmeier et al. 2017; Emsellem et al. 2022] is not shown here because the lowest intensity is above this limit. Note that we use a single observational limit for all lines.

It is apparent that the different lines trace different environments within the remnant: one originates from the thin layer tracing the recombination zone along the bubble rim and is bright in H β, [N II], and [S II], while the other one originating from volume-filling gas within the bubble is bright in H α and [O III].

4.2 Calculation of line intensity maps

Typically, when observing SNRs in our Galaxy, one does not need to consider the absorption of the cooling radiation by the surrounding gas because of the low ambient gas densities (see Section 1). However, the optical line emission can become opaque if the SN explodes in a relatively dense medium or interacts with a MC. This applies to approximately 10–20 per cent of all SNe in our

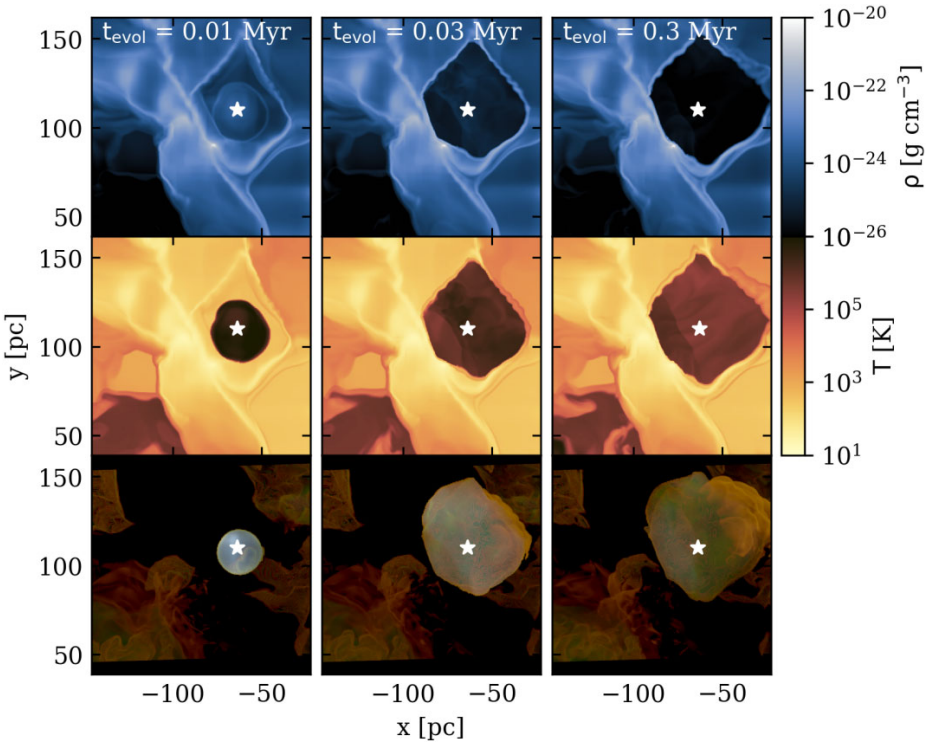

Figure 4. Time evolution (from left to right) of the density (top row) and temperature (middle row) in slices through the explosion centre. The bottom row shows the RGB projection image of the emitted energies in $E_{\rm FUV}$, $E_{\rm EUV}$, and $E_{\rm X}$. The SN position is shown as a white star symbol. The radiation in the upper left corner is not a result of this SN explosion: it is a leftover from other older SNe from the background, see details in Seifried et al. (2018). The dense MC is located to the left of the explosion centre. The distance between the explosion centre and the cloud's centre of mass is 25 pc. The remnant expands in a highly asymmetric fashion as the SN shock dissipates quickly when it encounters the MC.

Galaxy (Hewitt & Yusef-Zadeh 2009). The SNR considered here does interact with a MC. Hence, we check how much the different optical lines are affected by dust absorption along the LOS.

To get an idea of the amount of absorption, we calculate the optical depth for each cell i in the computational domain as:

$$\tau_i = \kappa_{\rm abs} \rho_i V_i^{1/3} f_{\rm d}, \tag{2}$$

where $\kappa_{\rm abs}$ is the dust absorption cross section per mass of dust (cm^2 g^{-1}), $\rho_{\rm i}$ is the density of cell i, V_i is the cell volume, and $f_{\rm d}$ is the dust-to-gas ratio ($f_{\rm d} = 0.01$ is fixed in our simulations). The dust absorption cross-section is taken from Weingartner & Draine (2001): we use the silicate model for Milky Way dust with $R_{\rm V} = 4.0$.

For each projection axis (we consider projections along each principal axis, i.e. along the x-, y-, and z-direction), we may choose to start the LOS at the top ('t'; solid lines) or the bottom ('b'; dashed lines), respectively. Then we calculate the integrated flux:

$$F_{\rm tot} = \int F_i e^{-\tau_{\rm i}} \, {\rm d}s, \tag{3}$$

where $F_{\rm i}$ is the flux of the cell i, $\tau_{\rm i}$ is the optical depth, ds is the area of the cube.

In Fig. 7, we show the attenuation percentage for the 3 LOS together for the 'top' view and for the'bottom view' (see Section 4.1 and Table 3) as during the evolution time for six different emission lines. The violin plot shows the peak in the data using the kernel density plot. The median values of the 'top' and 'bottom' views are shown with white dots. The higher probability to find a value in the data set, the thicker the violin plot is.

The attenuation percentage varies between ∼5 and 85 per cent, depending on the viewing angle. For example, when looking at the remnant projected along the x-axis from the 'top', the dense MC is located between the remnant and the observer. Hence, the attenuation for this LOS is significant, in particular for later times. This is not the case when 'observing' the cube from the bottom, as there is very little dense gas in front of the remnant. Although the H$_\beta$ line has the shortest wavelength and hence the highest $\kappa_{\rm abs}$, its attenuation is mostly weaker than for e.g. [O III]. This indicates that the geometry of the emitting region probably determines the different attenuation percentages of the inspected lines, while the difference in $\kappa_{\rm abs}$ is less important.

In Fig. 8, we plot the time evolution of the total luminosity (i.e. the sum of $F_{\rm tot}$ over all pixels), $L_{\rm tot}$, for the six different lines (H α (λ6563), H β (λ4861), [O III] (λ5007), [N II] (λ6583), [S II] (λ6717), and [S II] (λ6731)). We do not show here the 't' and 'b' views along different axes due to the similar behaviour of $L_{\rm tot}$ values. The solid lines depict the line luminosity that reaches the observer when taking into account the attenuation ('RT'), while the dotted lines show the optically thin case ('no RT'). At a typical distance of ∼5.6 kpc, the LVM detection limit corresponds to a required minimum luminosity of $L_{\rm tot}$ of 3.4×10^{25} erg s^{-1} (K. Kreckel, private communication).

At early times, we have only weak radiation in the optical range (consistent with the right panel of Fig. 2 showing that all the energy goes to the EUV and X-ray bands). This is followed by a sharp

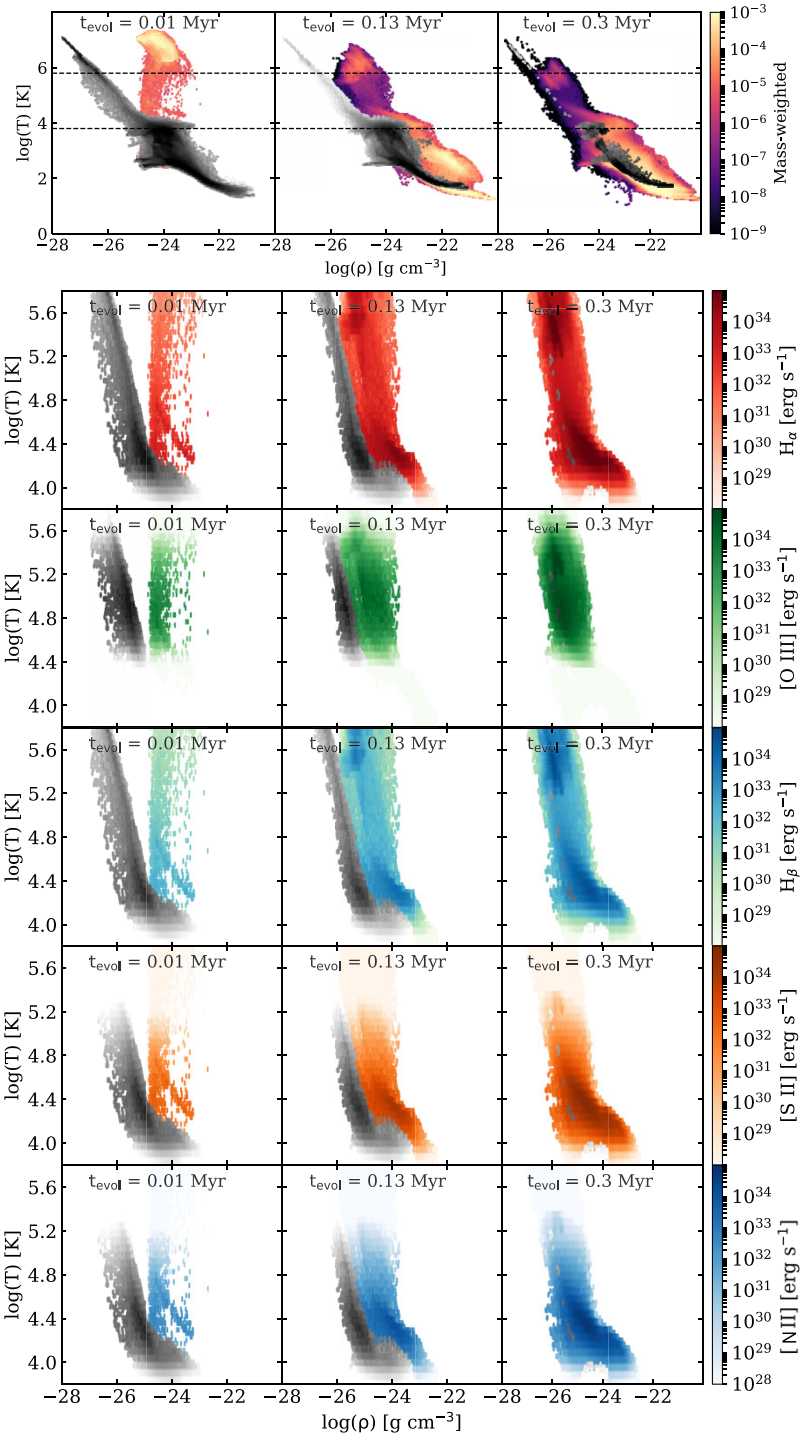

Figure 5. The top row: Mass-weighted 2D PDFs showing the gas distribution in the density-temperature phase space for three different times (from left to right). 'Coloured' is all gas from within, or nearby, the SNR bubble, and 'grey' is what we identify as background gas that is unaffected by the SNR. The dashed horizontal lines mark the temperature range that is selected for the emission-weighted PDFs shown below. 2–5 rows from the top: Gas distributions in the temperature-density phase space colour coded with the calculated optical emission lines (from top to bottom: H α, [O III] (λ5007), H β, [S II] (λ6717, λ6731), and [N II] (λ6583)). Again, the background gas is shown in grey scale. The gas distribution at time $t_{evol} = 0.1$ Myr has a 'V-shape': the right branch is produced by the current SN explosion while the left branch is the background material heated by the previous SNe. As the current SN evolves, the two branches join because the bubble expands and the gas cools.

Table 3. The constant integrated background luminosity for each optical emission line (as indicated in column 1) for the optically thin case (column 2). A percentage showing how much the background subtraction reduces the overall line flux during the time evolution of SNR (column 3; see Section 4.1).

Line	L_{bg} (erg s^{-1})	Min per cent, Max per cent
H α (λ6563)	1.01×10^{38}	8.5–48.0 per cent
H β (λ4861)	2.21×10^{37}	7.3–48.0 per cent
[O III] (λ5007)	7.93×10^{37}	2.5–35.0 per cent
[N II] (λ6583)	4.16×10^{37}	10.5–42.5 per cent
[S II] (λ6717)	2.56×10^{37}	17.5–81.0 per cent
[S II] (λ6731)	1.82×10^{37}	15.5–76.5 per cent

rise in [O III], which is mainly formed at higher temperatures than [S II] and [N II], namely in the volume-filling bubble interior (see Fig. 5). Shortly after, there is a rise in sulphur and nitrogen, when a recombination layer appears at lower temperatures.

4.3 Emission line ratios

Usually, SNe exploding in a dense environment reveal their presence in the form of narrow emission lines in their optical spectra. These collisionally excited lines play an important role in classifying an object as an SNR and determining its physical parameters such as electron temperature, T_e, or electron density, n_e. Once the emission lines and their ratios have been obtained, the following steps can classify an object as an SNR (in the resolved case) according to Mathewson & Clarke (1972), Dopita et al. (1984), Blair & Kirshner (1985), Fesen et al. (1985), Kewley et al. (2001), and Ciardullo et al. (2002):

(i) O III λ5007/H α (sensitive to T_e/n_e),
(ii) O III λ5007/H β (completeness of recombination layer; see Section 4.4),
(iii) N II λ6583/H $\alpha > 0.5$,
(iv) S II λ6731/H $\alpha > 0.4$.

The given line ratio thresholds were first derived based on multiple observations of SNe in our Galaxy, then derived in a purely theoretical optical classification scheme by Kewley et al. (2001) using a combination of stellar population synthesis, photoionization, and shock models, and then improved significantly by observational data from the SDSS survey by Kauffmann et al. (2003).

The time evolution of these optical line ratios is shown in Fig. 9 (with the actual maximum and minimum values summarized in Tables B1 and B2). Due to the uneven evolution of the SNR bubble (as was described in Section 3.2), our object cannot be classified as an SNR for every time step, but the line ratios mainly follow the values that are commonly observed for SNRs. We can see, however, that attenuation of the lines (labelled with 'RT') and background subtraction (labelled with '-bg') has a significant impact on the line ratios for both, the resolved (brown and grey lines) and the unresolved (blue and violet lines) cases.

We start with the [O III]/H α line ratio (row 1 of Fig. 9). The [O III] emission is sensitive to T_e, while H α depends more on n_e. As the primary shock (or reverse shock) travels into the neutral ambient medium (into the bubble centre), T_e increases. Once the SNR starts to cool, the [O III] emission becomes bright in regions with relatively high T_e, i.e. behind the shock and inside the SNR bubble. At the same time, the bubble expands and n_e decreases, such that the H α emission increases more slowly than [O III]. It causes a peak in the [O III]/H α ratio along all LOS at around $t_{evol} = 0.05$ Myr and at $t_{evol} = 0.2$ Myr, correspondingly. In Fig. 3, we show that $t_{evol} = 0.05$ Myr corresponds to the transition time t_{TR} for gas with $\rho = 10^{-23.5}$ g cm^{-3}, which in turn corresponds to the typical density of the MC material.

From the [O III]/H β line ratio (row 2 of Fig. 9), we can get the information about 'complete' and 'incomplete' recombination zones, respectively, shell structure, for the SNR as explained in the theoretical works by Cox & Raymond (1985) and Hartigan, Raymond & Hartmann (1987), and observational works by Raymond et al. (1988) and Boumis et al. (2005). Assuming a limit of around [O III]/H $\beta \lesssim 6$ (as derived in the aforementioned references), we can see that the shocks are completely recombined at the very beginning and at the end of the evolution. Due to the complex density structure of the surrounding ISM, we can get high values of [O III]/H β before $t_{evol} = 0.1$ Myr indicating an 'incomplete' recombination zone. It is not so rare that high [O III]/H β values are obtained in real observations, e.g. CTB 1 (Fesen et al. 1997) or G 17.4–2.3 (Boumis et al. 2002). We show that background subtraction (grey, brown, violet) significantly promotes the appearance of a 'complete' recombination zone. Moreover, comparing the cases of a resolved SN with (grey) and without (brown) attenuation shows that attenuation is particularly important for H β (also compare with Fig. 8) and hence the [O III]/H β ratio. Without attenuation, it has a value smaller than 6 during the whole time.

[N II]/H α (row 3) as well as [S II]/H α (row 4) are line ratios that help to classify an object as an SNR. Typical observed values for [N II]/H α lie in the range of 0.5–1.0 (Boumis et al. 2022). We can classify our object as an SNR for resolved cases (brown and grey) for most of the time where optical emission is presented: from shortly after the explosion to the peak around $t_{evol} = 0.05$ Myr. The behaviour is comparable to the evolution of [O III]/H β (see the description above). For resolved SNRs, attenuation does not play an important role in this case (grey and brown lines have almost the same values). On the other hand, for unresolved SNRs (blue and violet) the criteria to classify an object as an SNR is only fulfilled for one position of the observer (top view, violet-shaded region) after $t_{evol} = 0.05$ Myr. It means that for unresolved SNRs, it is rather difficult to trace the faint nitrogen line emitted when dense gas is shocked. This is consistent with high [N II]/H α line ratios being typically observed in older SNRs.

[S II]/H α (row 4) is a typical tracer of shocked gas. Interestingly, for the cases of a resolved SNR without attenuation (brown) as well as a presumably unresolved SNR with background subtraction (violet), shock emission is identified for almost all times. However, both the unresolved case with attenuation (blue) and the resolved case with attenuation and background subtraction (grey) are mostly below the SNR limit. It shows that attenuation can reduce the sulphur-bright thin shell emission. Hence, it could become impossible to properly identify an SNR in a denser ISM environment. At the same time, an accurate subtraction of the background for unresolved SNRs helps to boost the sulphur emission.

Overall, one can see from Fig. 9 that weak lines (nitrogen and sulphur)'benefit' from background subtraction in the sense that the line ratios are then shifted into the SNR zone. This is not so critical for strong lines (oxygen and hydrogen). However, it is worth noting that the whole analysis strongly depends on how well we can determine the abundance of different elements (i.e. the metallicity) in different parts of the SNR.

For all line ratios, at the end of the evolution of the SNR, the optical emission does not gradually fade yet, as some parts of the SNR are still 'young' and more time is required for the whole remnant to merge with the surrounding ISM.

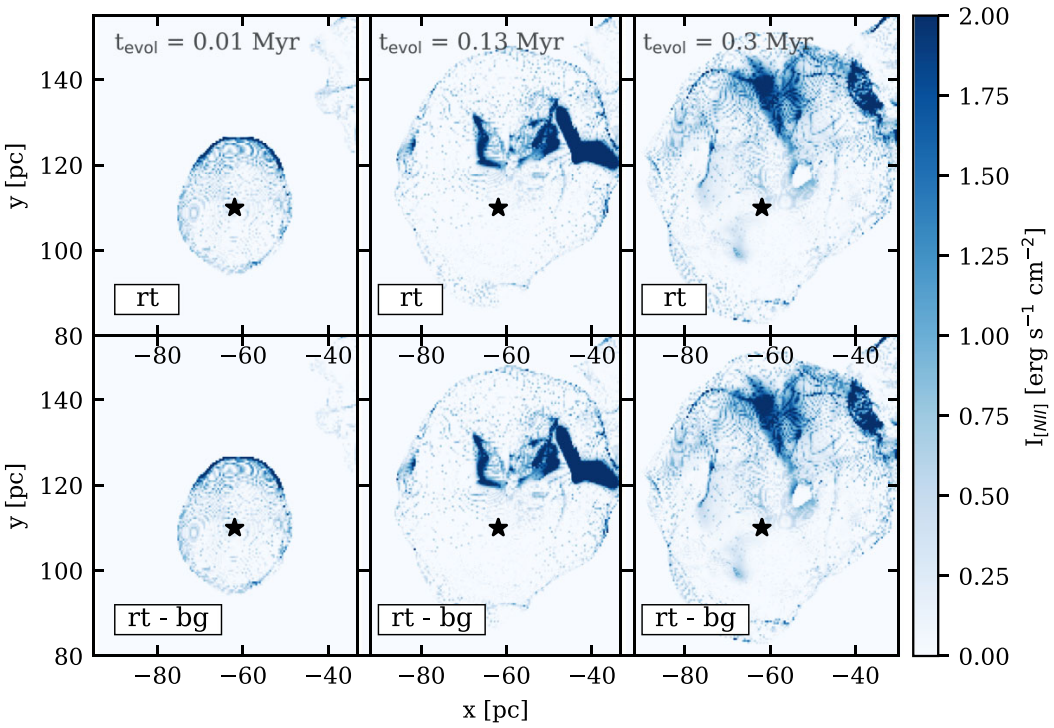

Figure 6. Time evolution (from left to right) of the [N II] λ6583 emission: top row with a simple radiative transfer, bottom row with a simple radiative transfer and background subtraction. Both rows show the *x*-axis projection from the top view. The intensity is normalized to the value 10^{-17}.The intensity of the bubble is the same in both cases, but the background emission is less intense with the background subtraction procedure.

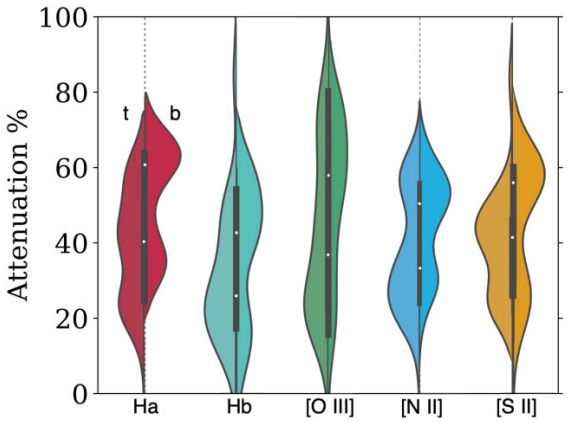

Figure 7. Violin showing the distribution of the percentage of the attenuated flux for 0.3 Myr for each optical line. The white dot is the median for the corresponding value, the tick bar in the centre is the interquartile range. The labels top ('t') and bottom ('b') correspond to different viewing angles of a potential observer looking at the cube from the top or the bottom. 't' and 'b' views are separated for every violin plot by the dashed vertical line. The maximum attenuation value varies for every optical line and differs for the 't' and 'b' views.

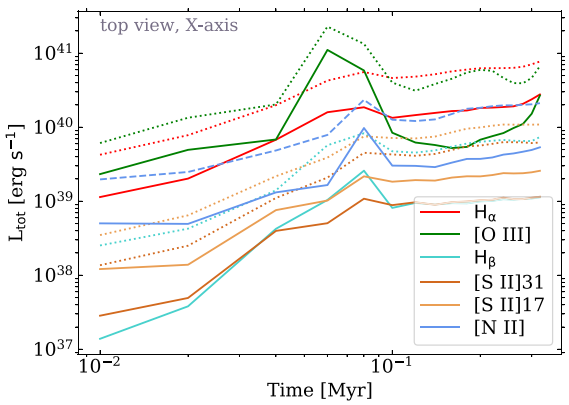

Figure 8. Time evolution of the total luminosity with attenuation (solid lines) and without (dotted lines) for each forbidden optical line. We show only the top view along the X-axis: the top view corresponds to the viewing angle of the potential observer looking at the cube. Other axes show a similar time evolution with the same order of magnitude of L_{tot}.

4.4 BPT diagrams

To investigate the distribution of the shocked gas by the SNR we use the BPT diagram. The BPT diagram is a way to classify the primary excitation source (photoionization or shocks) of an object using observed line ratios. It is often used for unresolved objects such as entire galaxies. The classification mainly depends on the gas metallicity, the EUV field and some other parameters. The BPT diagram compares the ratios of strong optical emission lines: [O III](λ5007)/H β and [N II](λ6583)/H α.

Fig. 10 (top row) shows the BPT diagram computed for our SNR for three different times (from left to right: t_{evol} = 0.01, 0.13,

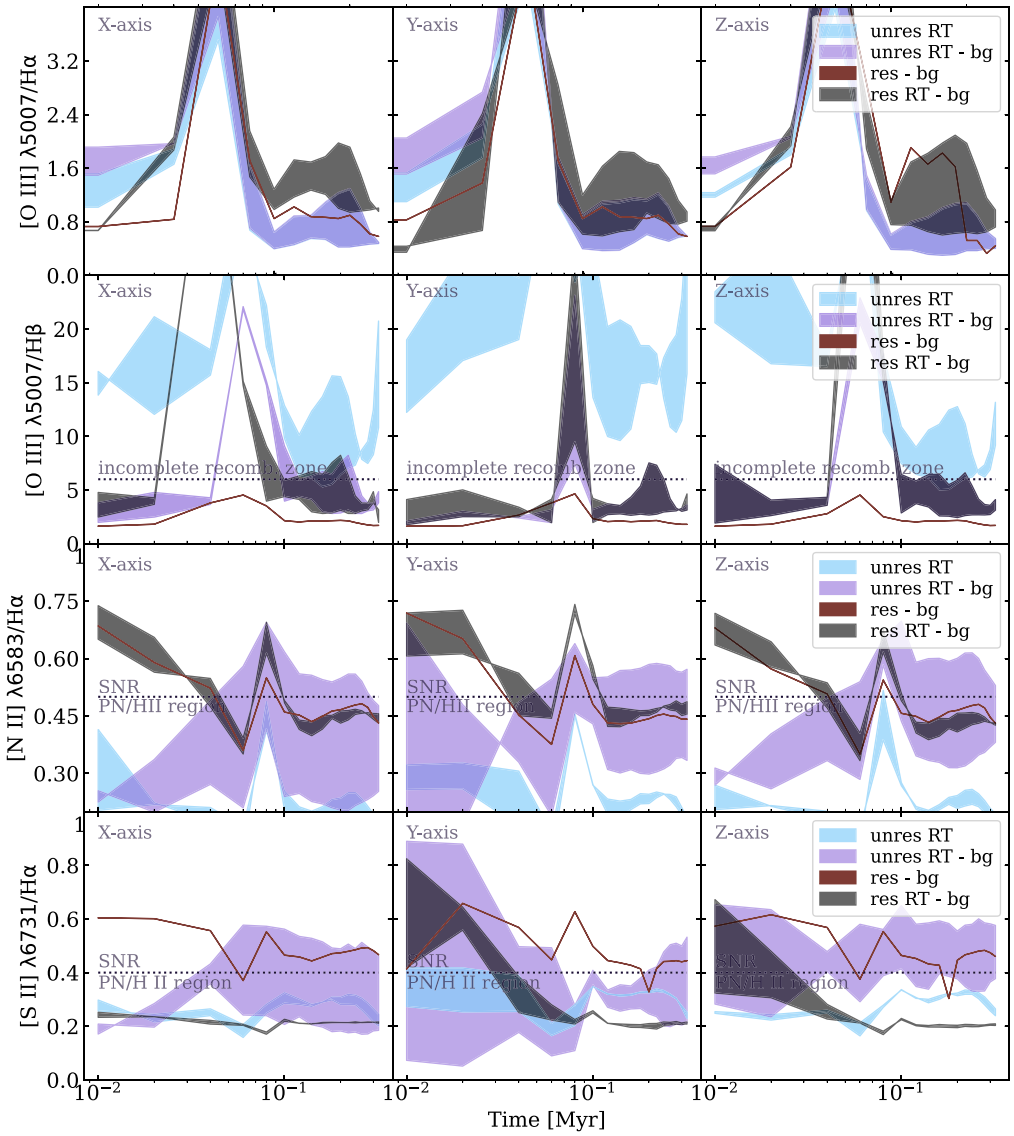

Figure 9. Time evolution of the relevant line ratios for presumably resolved (brown and grey) and unresolved (blue and violet) SNRs for three different projections (left to right). For the [S II] λ6731/H α ratio in unresolved SNRs, we use the sum of the two close sulphur lines ([S II] λ6717 + 6731) because they are in general not resolvable when the SNR is unresolved). For curves labelled with '-bg' the background has been subtracted; all curves labelled with 'RT' consider the line optical depth (see Section 4.2). The shaded regions show partly substantial variations in the line ratios resulting from the two considered observer positions (top and bottom views). These are equal for the presumably optically thin case ('res -bg'). The dotted line shows the theoretical transition between different types of objects (SNR, PN, or H II region). While [O III] is boosted with respect to H α and H β, the sulphur line ratio is decreased by optical depth effects. We find that a unique classification as an SNR is not possible at all times. Background subtraction plays a key role in all line ratios.

0.3 Myr). The colour-coded line ratio distributions are weighted by the [O III]-emissivity and show the result derived for the resolved intensity maps (resolved case with attenuation and background subtraction), considering only pixels that have line intensities above the assumed observational threshold (Section 4.2). For orientation, we also show two curves separating galaxies that are dominated by shocked emission (typically driven by AGN) and those dominated by H II regions (photoionization). The first line is based on purely theoretical work by Kewley et al. (2001) (using e.g. photoionization, shock models, and population synthesis). The second line is derived from the analysis of data from the Sloan Digital Sky Survey (SDSS; York et al. 2000; Stoughton et al. 2002) by Kauffmann et al. (2003).

Note again that, in this work, we only account for collisionally excited emission. We do not include photoionization driven by H II regions because the MC next to the SNR is not yet forming stars. Therefore, we can investigate the line emission contributed by the SNR without any contamination from nearby H II regions. We find that the H II-dominated part of the BPT diagram can be partially populated by emission from the SNR. It is likely that in a fully sampled patch of the galaxy with a multi-phase ISM, star formation

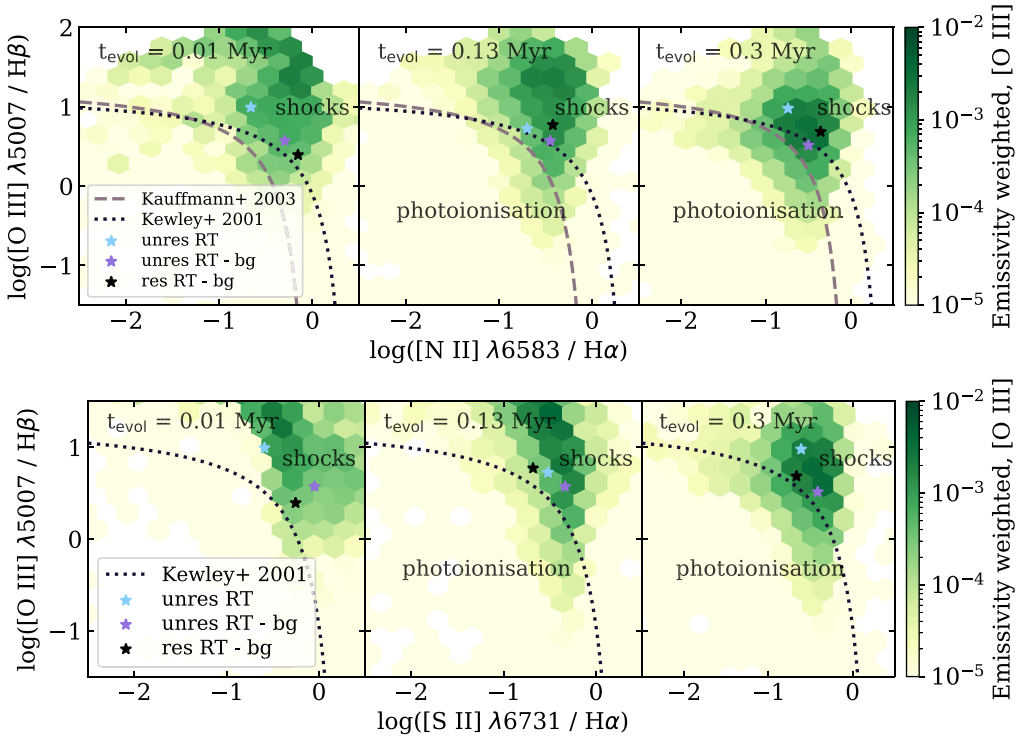

Figure 10. The classical BPT diagram (top row) and the sulphur BPT diagram (bottom row) for three different times (from left to right). The colour bar shows the line ratio distribution for the resolved SNR (with background subtraction and attenuation), weighted by the [O III] emissivity. The mean values for every calculation are star symbols (see the legend for the details). The reference lines classify the line ratios according to the main ionization mechanism, i.e. photoionization (lower left) or shock-ionization (upper right). The dashed line is from Kauffmann et al. (2003) and the dotted line is from Kewley et al. (2001). We find that the full distribution is clearly peaking in the shock-dominated regime, but the means are rather located in a 'mixed region' (between the two regimes), in particular when the background has been subtracted.

and feedback (such as e.g. in Rathjen et al. 2023) the lower left part of the BPT diagram would be dominated by real H II regions (see also Rathjen et al. in preparation).

With time, the SNR line ratio distribution moves from the shock-dominated region to the so-called 'mixed' or 'composite' area: close to the boundary between the nominally H II region-dominated and the shock-dominated emission. On the BPT diagrams that typically have a *V*-shape (due to the two main mechanisms of the excitation source), we are mostly reproducing the right part of the *V*, or the 'shock wing' respectively (Farage et al. 2010; Rich, Kewley & Dopita 2014, green-coloured background in Fig. 10), while we do not have a distinguishable 'H II region' wing (left part of the V), which is expected since we do not include photoionization, star formation, or stellar feedback in this study. This is consistent with previous works (Allen et al. 2008; Kewley et al. 2019a). We expect SNe to contaminate the classification of galaxies as they are populating both shock-dominated and mixed areas. Also, the line ratio distribution of an SNR depends on the SN evolutionary stage, i.e. on the age of the SNR as well as on the ambient gas distribution.

Additionally, we overplot several mean line ratios on the BPT diagrams (star symbols). For the resolved SNR with attenuation and background subtraction (black), the mean is the arithmetic mean of the pixel-based ratio of the corresponding individual emission line maps. We also show the means for the unresolved SNR with (violet) and without (blue) background subtraction and find that removing the background dramatically changes the resulting value: the mean is shifted downward (lower [O III]/H β) and to the right (higher [N II]/H α) so that it gets closer to the dividing line between the shock-dominated and the photoionization dominated regimes. Mostly, the reason for this behaviour is that the emission of [O III] and both hydrogen lines are volume filling (see Section 4.6) and thus, we typically have a lot of it in the background. In case there are further ionizing sources in unresolved maps which are boosting the hydrogen lines, the mean values of the optical line ratios would further move towards the H II region part of the BPT, and hence SNRs could be missed entirely.

We also make use of the [S II] λ6731/H α ratio to plot the sulphur BPT diagram in Fig. 10 (bottom row). In a photoionised region, some UV photons have sufficiently high energy (~23.3 eV) to doubly ionize sulphur (S^{++}). In addition to that, photoionized regions also contain some amount of collisionally excited S^{+}. In SNRs the situation is the opposite: due to the large recombination region behind the shock, the SNR will mainly contain S^{+} rather than S^{++}. This is why the [SII](λ6731)/H α line ratio is a standard diagnostic tool to detect SNRs. The sulphur BPT diagram also contains the Kewley et al. (2001) separation line. During the whole time evolution of the SNR, our mean values are clearly located in the shock-dominated region. This confirms the possibility of correctly classifying an SNR on the sulphur BPT, even for unresolved objects.

Recently, many attempts have been made to improve the BPT diagrams using other optical line ratios (creating a multidimensional optical line ratio space) and modern machine learning techniques to

better classify observed objects or to better constrain their physical conditions (e.g. Vogt et al. 2014; Ho 2019; Stampoulis et al. 2019; Kewley et al. 2019a; Ji & Yan 2020; Zhang et al. 2020; Rhea et al. 2021). However, none of the new models is a universal tool that could be used in both theoretical work and observations. Therefore, despite all these advances in methods, we need more physical models that use BPT diagrams to understand what is driving the excitation of the emitting gas. We will investigate this aspect in future studies using machine learning with a larger data set of SNRs (Smirnova et al. in preparation, based on the full dataset of Seifried et al. 2018).

To visualize the location of pixels with line ratios located in either the shock-dominated (dark green), the mixed (green), or the photoionized (yellow) regimes of the BPT diagram, we plot the 2D projected map (projection along the z-axis) in Fig. 11 for the same time steps as above (from left to right). It is interesting to note that the mixed region follows the outer shock position (which is shown in Section 4.6), which is consistent with theoretical predictions for the position of SNRs in the BPT diagram (Allen et al. 2008; Kewley et al. 2019a). The shock-dominated regions mainly follow the hotter gas in the bubble centre and strongly cooling regions on the bubble surface that emit in the EUV and X-ray. All other parts of the SNR bubble are indistinguishable and appear in the photoionized regime although they are still shock-ionized in our case.

4.5 Physical conditions in the SNR derived from simulations and emission line ratio diagnostics

Optical line ratios are used to determine the physical parameters of observed SNRs. First, one may estimate the electron temperature (T_e) and the electron density (n_e) from the [O III] (λ4363)/[O III] (λ5007) and [S II] (λ6731)/(λ6717) line ratios. The sulphur line ratio is almost independent of T_e Osterbrock & Ferland (2006) and the oxygen line ratio depends only on T_e. That is why we can define T_e and n_e reliably. The sulphur line ratios from our post-processing are presented in Table B1 and fall in the range from 0.2 to 1.0. A typical value for old (evolved) SNRs in the low-density medium is about 1.1–1.5 (Frank, King & Raine 2002). It is worth noting, that our SNR is in a denser medium where the values of [S II] (λ6731)/[S II](λ6717) around 1.0 are common to observe.

We use the PyNeb tool (Luridiana, Morisset & Shaw 2015) – a Python package which computes emission lines using an n −level atom approach. It solves the equilibrium equations for an n-level atom to determine the level populations (from which the emissivities can be calculated).

Using the above-mentioned oxygen and sulphur line ratios, we obtain $n_e \approx 200-1000$ cm^{-3} and $T_e \approx 85\,500-108\,000$ K. The electron density indicates a cooling post-shock recombination layer. The electron temperature corresponds to a hot interior of the SNR bubble (as we mentioned before, see Fig. 5). The time evolution looks like this: we start with a high electron density (about 1100 cm^{-3}) and $T_e \approx 85\,500$ K), which is typical for young SNRs, and end up at a number density $n_e \approx 270$ cm^{-3} and an electron temperature $T_e \approx 10.8 \times 10^4$ K.

To verify the line ratio-based results, we determine our electron number densities $\boldsymbol{n}_e$ from the simulations for each cell using:

$$n_e = \frac{\sum I_{\rm cell} \times \rho_{\rm cell} \times x_{\rm H^+}/m_p}{\sum I_{\rm cell}}, \quad (4)$$

where $x_{\rm H^+}$ is the fractional abundance of ionized hydrogen, $I_{\rm cell}$ is the S^+ intensity in the cell, m_p is the mass of a proton. The result values for n_e are summarized in Table 4. The n_e found in the simulation (from the area where we have sulphur emission in simulations, fourth column) is similar to the one derived using the line ratios and PyNeb (sixth column). Unfortunately, we cannot calculate T_e directly from the simulations. But T_e (from the line ratios, seventh column) and $T_{\rm gas}$ (from the area where we have oxygen emission in simulations, fifth column) have no great differences for the part of the SNR bubble that we compare because we assume thermal equilibrium between the electron and gas temperature. In a conclusion, this method works quite well in describing the mean electron densities (error: 11–40 per cent) and temperatures (error only: 8–20 per cent) despite the variations along the line of sight and between lines of sight. Our best-fitting model seems to always be biased toward overestimating n_e, T_e and this overestimation seems to grow with time (ending with the biggest error of 40 and 20 per cent correspondingly).

Combining our results for the electron density with the fact that the SNR has a diameter of approximately 25–55 pc (the minimum and maximum diameter of the SNR bubble during the $t_{\rm evol}$, see Fig. 4), one may calculate the energy of the explosion using the following equation from (McKee & Cowie 1975):

$$E = 5.5 \times 10^{43} n_e D^3 \text{ erg}, \quad (5)$$

where D is the SNR diameter in parSection This results in $E \approx 8.6 \times 10^{50}-1.8 \times 10^{51}$ erg. These values are comparable to the actual SN explosion energy in our simulation of $E_{\rm SN} = 10^{51}$ erg. Still, the difficulty of measuring a well-defined diameter is a substantial source of inaccuracy in this calculation (after all, our SNR is not spherically symmetric, as can be seen in Fig. 4).

In general, we have quite a good agreement between simulations and optical line ratios numbers. However, T_e and n_e are changing notably during the simulation time (especially in different parts of the bubble that do not evolve simultaneously), so more statistical data are needed to draw a conclusion on the accuracy of the method.

4.6 Detection and analysis of shocks

Shock waves are essential components of young SNRs: for most, the shell structure is defined by the forward shock which moves into the ISM and the reverse shock which moves back towards the centre and into the ejecta.

We use 1D radiative shock models to estimate the shock velocity and their magnetic field strength. In Fig. 12, we compare our mean line ratios (at $t_{\rm evol} = 0.01$ Myr and $t_{\rm evol} = 0.3$ Myr, and we show three different cases in black, blue, and violet) with a grid of models from Alarie & Morisset (2019). Note that the shock models are interpreted on the basis of the same line ratios as in the BPT diagrams (see Fig. 10 and Section 4.4). Additionally, we show the same reference lines (grey dashed and dotted lines) as in Fig. 10. We find that, for the unresolved case (blue stars), the background subtraction (leading to the violet stars) substantially changes the shock parameters which would be determined from the comparison with the shock models.

All our mean line ratios are quite offset from the grid of shock models, so it is essential to mention that the shock diagram is extremely sensitive to the initial abundance of the environment (mainly nitrogen). Of course, one cannot quantitatively define the time-dependent metal enrichment of the ISM from the SN itself from a real observation, so one should be careful when interpreting the results based on the shock diagram. The red dots show additional shock models that we calculate with MAPPINGS V for our specific metal abundances as given in Table 1 and for different gas densities, temperatures, and magnetic field strengths that are better suited to our physical conditions than the given model grids. In particular,

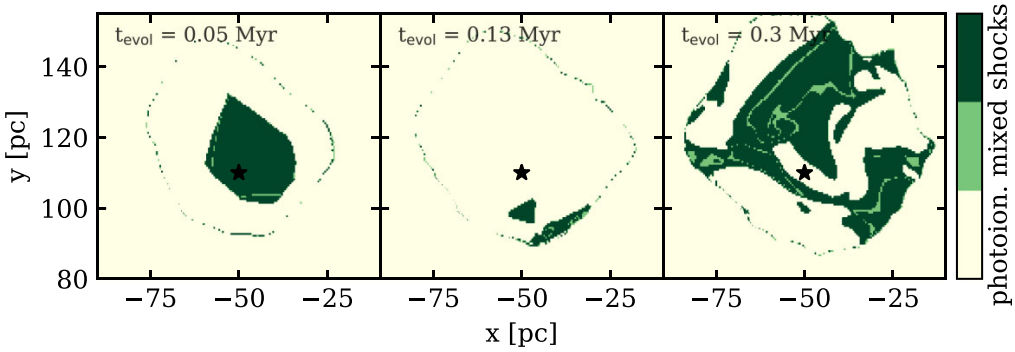

Figure 11. 2D projected maps (along the z-axis) of the SNR at three different times (from left to right) colour coded by the region where the local line ratio would lie within the classical BPT diagram shown in the top row of Fig. 10. The explosion centre is marked with a black star. We can see the outer shock and the inner bubble or the bubble surface, respectively. The line ratio map is very complicated due to the turbulent ISM with which the SNR interacts, which leads to a non-uniform cooling emission.

Table 4. Comparison of electron density (n_e) and electron temperature (T_e) for different t_{evol} (first column). Second and third columns computed for the SN box (corresponds to Table 2, columns 2, 3, 4); fourth column computed for [S II] emission region only in SN box; fifth column computed for [O III] emission region only in SN box and sixth, seventh columns result from the PyNeb.

t_{evol}	SN box				Best-fitting model	
	Total	Total	[S II]	[O III]		
	n_e	T_{gas}	n_e	T_{gas}	n_e	T_e
Myr	(cm^{-3})	(K)	(cm^{-3})	(K)	(cm^{-3})	(K)
0.01	40	949	981	66 621	1100	85 500
0.13	42	2234	390	88 006	500	95 000
0.3	45	12 386	110	99 871	270	108 000

we consider a temperature range from 10^7 to 10^4 K (see Fig. 5) and magnetic field strength from 10^{-4} to 10 μG. Mostly, the gas metallicity (and temperature) is responsible for the different line ratios of the newly computed models.

In MAPPINGS V, it is possible to either use the shock model (left-hand panel) or the shock + precursor model (right panel). Typically, the post-shock regions (of radiative or non-radiative shocks) are sources of ionizing photons. When these regions cool and recombine a continuum flux is produced. It propagates further upstream and forms a photoionization precursor (Cox 1972; Raymond 1991). Because our precursor gas is preionized, the model with the shock + precursor fits better.

Further, we find that the best fit is with models that have shock velocities of 350−500 km s^{-1} and a weak magnetic field (for the right panel) with $Z = 1 - 2\ Z_\odot$ (where $Z_\odot$ is solar metallicity). This is a reasonable estimate of the actual shock velocity (200−400 km s^{-1}) at time $t_{evol} = 0.05$ Myr or for a mean shock velocity (see also Fig. 13 for more details). The shock velocity decreases over time in the simulation from 2400 to 25 km s^{-1}. The weak magnetic field strength is also consistent with our simulations, as we initially set $B = 3$ μG in the simulation (see Section 2.1).

We implemented a shock-detection routine (Lehmann, Federrath & Wardle 2016, based on) that can identify and extract shock regions in the SNR, as shown in Fig. 13. As theoretically predicted, the emission of optical lines does not exactly track the positions of the shock front. The optical emission is generated mainly in the cooling post-shock region, which is visible in Fig. 13. However, we can trace the approximate shock position using [S II] (in orange, as sulphur is collisionally exited). It can even capture the position of the reverse shock. Nitrogen ([N II]) is not so sensitive to the shock position: the emission can be spatially separated from the shock position due to the lower excitation temperature. [O III] can trace the main shape of the SNR bubble but does not correlate with the shock position anyhow. It is clearly seen which areas of the supernova bubble are occupied by different optical lines: [O III] fills the bubble and appears where the gas has already cooled down enough, while the [S II] and [N II] radiation is a thin layer after/before the shock wave. Thus, even if we do not detect the position of the shock wave perfectly using [S II] as a tracer, we can still use it as a good approximation. In addition, from an estimate of the thickness of the [S II] layer, it can be concluded that a simulation resolution of less than one parsec is required to resolve the radiation of cooling SNR shock waves in the optical band. The evolution of the main and reverse shock waves as a 3D projection and on a 2D slice from our simulations are shown in Appendix C.

5 CONCLUSIONS

We develop a post-processing module for the FLASH code, which uses the updated collision data from MAPPINGS V to produce realistic emission maps of simulated SNRs.

We show that a significant amount of cooling energy is released through EUV, FUV, and Optical radiation. Because of the complex and turbulent structure of the surrounding ISM, the characteristic evolution times (from the duration of the ST phase to the transition and PDS phases) of the SNR can differ greatly for different parts of the SNR bubble. The SNR bubble itself is highly asymmetric, leading to significant projection effects.

We produce optical emission line maps (H α, H β, [O III] (λ5007), [S II] (λ6717, 6731), and [N II] (λ6583) that show the same features as in real observations of SNRs interacting with the surrounding ISM. We investigate the following optical line ratios: [O III] (λ5007)/H α, [S II] (λ6717)/(λ6731), [S II] (λ6731)/H α, [N II] (λ6583)/H α, [O III] (λ5007)/H β that we also find to be mostly consistent with observations. We investigate where our SNR appears in the classical and the sulphur BPT diagrams and show that it moves with time from the shock-dominated region to the mixed region (between the regimes of shock-dominated and classical HII regions, which are actually not included here). This behaviour is mainly caused by shock dissipation

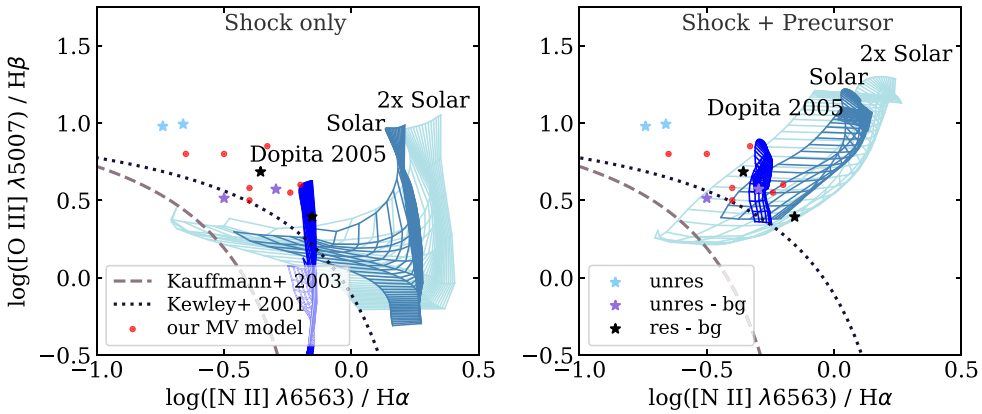

Figure 12. Shock diagnostic diagram based on the same optical line ratios as BPT diagram. Different abundances (showed in blue colours) cover shock velocities ranging from 200 to 1000 km s^{-1} (an increase from top to the bottom for each grid, one line – one velocity), pre-shock density of $n_0 = 1$ cm^{-3}, magnetic parameter between 10^{-4} and 10 μG cm$^{3/2}$ (increase for each abundance set from left to right). Note that the plot displays the line ratios from the shocked gas only. The star symbol and the arrow with the corresponding colour show the mean at $t_{\rm evol} = 0.01$ Myr and $t_{\rm evol} = 0.3$ Myr. The colours are the same as in Fig. 10. Red stars are shock models calculated with MAPPINGS V with our abundances (see Table 1) with different initial parameters, similar to simulations. The shock + precursor model works better for our optical line ratios; however, different abundances (compared to the default ones, shown in the figure) are required to fit the obtained data.

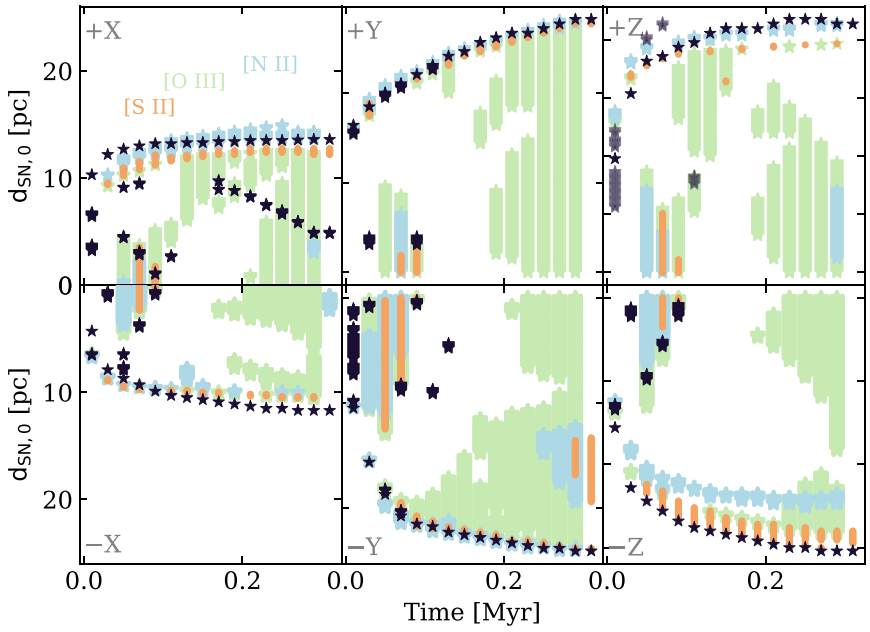

Figure 13. Time evolution of the radiation position relative to the centre of the SN explosion along each axis. [S II] emission (orange), [O III] emission (light green), [N II] emission (light blue), and shock position (black stars). Not all shock wave positions were calculated using the shock finder. The missing points were calculated based on the temperature jump. The shock velocity also can be calculated from these data easily. We start from 800 to 1000 km s^{-1} during the first time steps (0.01 Myr) and then the velocity decreases dramatically to 200–400 km s^{-1} (around 0.05 Myr). At the end of the time evolution (0.3 Myr), the shock velocity is almost constant around 12–50 km s^{-1}. Note that the scatter in velocity is big because it depends on the environmental density. In some directions, shock expands freely ($+Y$ or $-Y$) and in another, it hits the MC and almost stops ($+X$ or $-X$).

in the turbulent ISM. For unresolved SNRs removing the background completely changes the position on the BPT diagram: if there are further ionizing sources in unresolved maps (boosting the hydrogen lines), the SNR position on the BPT diagram would move towards the photoionization part, and hence SNR could be missed entirely.

Furthermore, using sulphur lines, we calculate an electron density $n_{\rm e} \approx$ 200–1000 cm^{-3} and an electron temperature $T_{\rm e} \approx$ 85 500−10.8 × 10^4 K from the oxygen emission. These values are consistent with typical SNR observations and our simulation data. Yet, they indicate the presence of different parts of the SNR: a cooling

post-shock recombination layer is traced by the sulphur emission, and the hot bubble is traced by the oxygen emission. Using the calculated electron density, we estimate the initial supernova energy and find values of $E \approx 8.6 \times 10^{50}-1.8 \times 10^{51}$ erg, which agrees fairly well with the injected explosion energy of $E_{\rm SN} = 10^{51}$ erg. The variation in E arises since the size of the SNR bubble cannot be determined exactly due to the asymmetry of the surrounding turbulent ISM and depends on the evolutionary stage.

In addition, we use shock models to estimate the shock velocity and find values between 350 and 500 km s^{-1}, which are in agreement with the mean velocity calculated from the synthetic observations. For the first time, we can very well reproduce the position of the optical emission and shock waves. We can clearly see the absence of spherical symmetry in both forward and backward shock waves. It is shown that different ions are formed in other regions under different initial conditions. Overall, in order to properly interpret the results, we can show that it is vital to consider the projection effect, a realistic density distribution of the surrounding ISM, and the most accurate metallicity estimate available. All of these factors significantly affect the accuracy of optical line diagnostics.

Finally, accounting for cooling radiation self-consistently in simulations is extremely important throughout the entire evolution of the SNR. It can significantly change the entire dynamics of the remnant's evolution.

ACKNOWLEDGEMENTS

The authors thank the anonymous referee for the fast reviewing process. We also would like to thank Kathryn Kreckel and her group for useful discussions and information about optical observational limits. EIM, SW, and SDC acknowledge funding by the European Research Council through ERC Starting Grant No. 679852 'RADFEEDBACK'. SW, DS, T-ER acknowledge support by the German Science Foundation (DFG) via SFB 956, projects C5 and C6. T-ER and DS acknowledge funding from the programme 'Profilbildung 2020,' an initiative of the Ministry of Culture and Science of the State of Northrhine Westphalia. The sole responsibility for the content of this publication lies with the authors. The software used in this work was partly developed by the DOE NNSA-ASC OASCR Flash Centre at the University of Chicago (Fryxell et al. 2000; Dubey et al. 2008). The following PYTHON packages were used: NUMPY (Harris et al. 2020), SCIPY (Virtanen et al. 2020), MATPLOTLIB (Hunter 2007), YT (Turk et al. 2011). We also used PARAVIEW for the 3D visualization (Ahrens, Geveci & Law 2005).

DATA AVAILABILITY

The data underlying this article will be shared on reasonable request to the corresponding author. The CESS module is available on GitHub.

REFERENCES

Ahrens J., Geveci B., Law C., 2005, Visualization Handbook. Butterworth-Heinemann, Burlington, p. 717
Alarie A., Morisset C., 2019, RMxAA, 55, 377
Allen M. G., Groves B. A., Dopita M. A., Sutherland R. S., Kewley L. J., 2008, ApJS, 178, 20
Asplund M., Grevesse N., Sauval A. J., Scott P., 2009, ARA&A, 47, 481
De Avillez M. A., Breitschwerdt D., 2005, A&A, 436, 585
De Avillez M. A., Breitschwerdt D., 2007, ApJ, 665, L35
Baldwin J. A., Phillips M. M., Terlevich R., 1981, PASP, 93, 5
Binette L., Dopita M. A., Tuohy I. R., 1985, ApJ, 297, 476
Blair W. P., Kirshner R. P., 1985, ApJ, 289, 582
Blandford R. D., Cowie L. L., 1982, ApJ, 260, 625
Bolte J., Sasaki M., Breitschwerdt D., 2015, A&A, 582, A47
Boumis P., Mavromatakis F., Paleologou E. V., 2002, A&A, 385, 1042
Boumis P., Meaburn J., López J. A., Mavromatakis F., Redman M. P., Harman D. J., Goudis C. D., 2004, A&A, 424, 583
Boumis P., Mavromatakis F., Xilouris E. M., Alikakos J., Redman M. P., Goudis C. D., 2005, A&A, 443, 175
Boumis P., Xilouris E. M., Alikakos J., Christopoulou P. E., Mavromatakis F., Katsiyannis A. C., Goudis C. D., 2009, A&A, 499, 789
Boumis P. et al., 2022, MNRAS, 512, 1658
Chandra P., 2018, Space Sci. Rev., 214, 27
Chevalier R. A., 1977, ARA&A, 15, 175
Ciardullo R., Feldmeier J. J., Jacoby G. H., Kuzio de Naray R., Laychak M. B., Durrell P. R., 2002, ApJ, 577, 31
Cioffi D. F., McKee C. F., Bertschinger E., 1988, ApJ, 334, 252
Cox D. P., 1972, ApJ, 178, 159
Cox D. P., Raymond J. C., 1985, ApJ, 298, 651
Derlopa S., Boumis P., Chiotellis A., Steffen W., Akras S., 2020, MNRAS, 499, 5410
Dopita M. A., 1976, ApJ, 209, 395
Dopita M. A., Binette L., Tuohy I. R., 1984, ApJ, 282, 142
Draine B. T., 1978, ApJS, 36, 595
Dubey A. et al., 2008, in Pogorelov N. V., Audit E., Zank G. P., eds, ASP Conf. Ser. vol. 385, Numerical Modelling of Space Plasma Flows. Astron. Soc. Pac., San Francisco, p. 145
Emsellem E. et al., 2022, A&A, 659, A191
Farage C. L., McGregor P. J., Dopita M. A., Bicknell G. V., 2010, ApJ, 724, 267
Fesen R. A., Blair W. P., Kirshner R. P., 1985, ApJ, 292, 29
Fesen R. A., Winkler F., Rathore Y., Downes R. A., Wallace D., Tweedy R. W., 1997, AJ, 113, 767
Frank J., King A., Raine D. J., 2002, Accretion Power in Astrophysics: Third Edition. Cambridge Univ. Press, Cambridge
Fryxell B. et al., 2000, ApJS, 131, 273
Gatto A. et al., 2015, MNRAS, 449, 1057
Gatto A. et al., 2017, MNRAS, 466, 1903
Girichidis P. et al., 2016, MNRAS, 456, 3432
Girichidis P., Seifried D., Naab T., Peters T., Walch S., Wünsch R., Glover S. C. O., Klessen R. S., 2018, MNRAS, 480, 3511
Glover S. C. O., Mac Low M.-M., 2007, ApJS, 169, 239
Glover S. C. O., Federrath C., Mac Low M. M., Klessen R. S., 2010, MNRAS, 404, 2
Gnat O., Ferland G. J., 2012, ApJS, 199, 20
Green D. A., 2019, J. Astrophys. Astron., 40, 36
Haid S., Walch S., Naab T., Seifried D., Mackey J., Gatto A., 2016, MNRAS, 460, 2962
Harris C. R. et al., 2020, Nature, 585, 357
Hartigan P., Raymond J., Hartmann L., 1987, ApJ, 316, 323
Herpich F., Mateus A., Stasińska G., Cid Fernandes R., Vale Asari N., 2016, MNRAS, 462, 1826
Hester J. J., 1987, ApJ, 314, 187
Hewitt J. W., Yusef-Zadeh F., 2009, ApJ, 694, L16
Hislop J. M., Naab T., Steinwandel U. P., Lahén N., Irodotou D., Johansson P. H., Walch S., 2022, MNRAS, 509, 5938
Ho L. C., 2008, ARA&A, 46, 475
Ho I. T., 2019, MNRAS, 485, 3569
How T. G., Fesen R. A., Neustadt J. M. M., Black C. S., Outters N., 2018, MNRAS, 478, 1987
Howk J. C., Savage B. D., Fabian D., 1999, ApJ, 525, 253
Hu C.-Y., Naab T., Glover S. C. O., Walch S., Clark P. C., 2017, MNRAS, 471, 2151
Hunter J. D., 2007, Comput. Sci. Eng., 9, 90
Iffrig O., Hennebelle P., 2015, A&A, 576, A95
Ji X., Yan R., 2020, MNRAS, 499, 5749
Kafatos M., Sofia S., Gull T., Bruhweiler F., 1980, ApJ, 242, 294

Katsuda S., Tanaka M., Morokuma T., Fesen R., Milisavljevic D., 2016, ApJ, 826, 108
Kauffmann G. et al., 2003, MNRAS, 346, 1055
Kennicutt Robert C. J., 1998, ARA&A, 36, 189
Kewley L. J., Dopita M. A., Sutherland R. S., Heisler C. A., Trevena J., 2001, ApJ, 556, 121
Kewley L. J., Nicholls D. C., Sutherland R. S., 2019a, ARA&A, 57, 511
Kewley L. J., Nicholls D. C., Sutherland R., Rigby J. R., Acharya A., Dopita M. A., Bayliss M. B., 2019b, ApJ, 880, 16
Kim C.-G., Ostriker E. C., 2015, ApJ, 802, 99
Kollmeier J. A. et al., 2017, preprint (arXiv:1711.03234)
Lehmann A., Federrath C., Wardle M., 2016, MNRAS, 463, 1026
Levenson N. A., Kirshner R. P., Blair W. P., Winkler P. F., 1995, AJ, 110, 739
Long K. S., Blair W. P., White R. L., Matsui Y., 1991, ApJ, 373, 567
Luridiana V., Morisset C., Shaw R. A., 2015, A&A, 573, A42
Makarenko E. I., Walch S., Clarke S. D., Seifried D., 2020, in Journal of Physics Conference Series, vol. 1640. IOP Publishing, p. 012009
Martizzi D., Fielding D., Faucher-Giguère C.-A., Quataert E., 2016, MNRAS, 459, 2311
Mathewson D. S., Clarke J. N., 1972, ApJ, 178, L105
Mavromatakis F., 2003, A&A, 408, 237
Mavromatakis F., Papamastorakis J., Ventura J., Becker W., Paleologou E. V., Schaudel D., 2001, A&A, 370, 265
Mavromatakis F., Aschenbach B., Boumis P., Papamastorakis J., 2004, A&A, 415, 1051
McKee C. F., Cowie L. L., 1975, ApJ, 195, 715
McKee C. F., Ostriker J. P., 1977, ApJ, 218, 148
Meyer D. M., Cardelli J. A., Sofia U. J., 1997, ApJ, 490, L103
Meyer D. M., Jura M., Cardelli J. A., 1998, ApJ, 493, 222
Negus J., Comerford J. M., Müller Sánchez F., Barrera-Ballesteros J. K., Drory N., Rembold S. B., Riffel R. A., 2021, ApJ, 920, 62
Nelson R. P., Langer W. D., 1997, ApJ, 482, 796
Orlando S. et al., 2019, A&A, 622, A73
Osterbrock D. E., Ferland G. J., 2006, Astrophysics of Gaseous Nebulae and Active Galactic Nuclei. University Science Books
Ostriker J. P., McKee C. F., 1988, Rev. Mod. Phys., 60, 1
Pagotto I., Krajnović D., den Brok M., Emsellem E., Brinchmann J., Weilbacher P. M., Kollatschny W., Steinmetz M., 2021, A&A, 649, 63
Peters T. et al., 2017, MNRAS, 466, 3293
Potter T. M., Staveley-Smith L., Reville B., Ng C. Y., Bicknell G. V., Sutherland R. S., Wagner A. Y., 2014, ApJ, 794, 174
Rathjen T.-E. et al., 2021, MNRAS, 504, 1039
Rathjen T.-E., Naab T., Walch S., Seifried D., Girichidis P., Wünsch R., 2023, MNRAS, 522, 1843
Raymond J. C., 1991, PASP, 103, 781
Raymond J. C., Hester J. J., Cox D., Blair W. P., Fesen R. A., Gull T. R., 1988, ApJ, 324, 869
Reynolds S. P., 2017, in Alsabti A. W., Murdin P., eds, Handbook of Supernovae. Springer International Publishing, p. 1981
Rhea C., Rousseau-Nepton L., Prunet S., Prasow-Emond M., Hlavacek-Larrondo J., Vale Asari N., Grasha K., Perreault-Levasseur L., 2021, ApJ, 910, 129
Rich J. A., Kewley L. J., Dopita M. A., 2014, ApJ, 781, L12
Sánchez-Cruces M., Rosado M., Fuentes-Carrera I., Ambrocio-Cruz P., 2018, MNRAS, 473, 1705
Sánchez S. F. et al., 2015, A&A, 574, A47
Sarkar K. C., Gnat O., Sternberg A., 2021, MNRAS, 504, 583
Sasaki M., Plucinsky P. P., Gaetz T. J., Smith R. K., Edgar R. J., Slane P. O., 2004, ApJ, 617, 322
Sasaki M., Plucinsky P. P., Gaetz T. J., Bocchino F., 2013, A&A, 552, A45
Sedov L. I., 1959, Similarity and Dimensional Methods in Mechanics. Academic Press
Seifried D. et al., 2017, MNRAS, 472, 4797
Seifried D., Walch S., Haid S., Girichidis P., Naab T., 2018, ApJ, 855, 81
Sembach K. R., Howk J. C., Ryans R. S. I., Keenan F. P., 2000, ApJ, 528, 310
Slane P., Gaensler B. M., Dame T. M., Hughes J. P., Plucinsky P. P., Green A., 1999, ApJ, 525, 357
Slane P., Bykov A., Ellison D. C., Dubner G., Castro D., 2015, Space Sci. Rev., 188, 187
Stampoulis V., van Dyk D. A., Kashyap V. L., Zezas A., 2019, MNRAS, 485, 1085
Stasińska G., Cid Fernandes R., Mateus A., Sodré L., Asari N. V., 2006, MNRAS, 371, 972
Steinwandel U. P., Moster B. P., Naab T., Hu C.-Y., Walch S., 2020, MNRAS, 495, 1035
Stoughton C. et al., 2002, AJ, 123, 485
Sutherland R. S., Dopita M. A., 1993, ApJS, 88, 253
Sutherland R. S., Dopita M. A., 2017, ApJS, 229, 34
Sutherland R., Dopita M., Binette L., Groves B., 2018, Astrophysics Source Code Library, record ascl:1807.005
Toledo-Roy J. C., Velázquez P. F., Esquivel A., Giacani E., 2014, MNRAS, 437, 898
Turk M. J., Smith B. D., Oishi J. S., Skory S., Skillman S. W., Abel T., Norman M. L., 2011, ApJS, 192, 9
Veilleux S., Osterbrock D. E., 1987, ApJS, 63, 295
Vink J., 2012, A&AR, 20, 49
Virtanen P. et al., 2020, Nat. Methods, 17, 261
Vogt F. P. A., Dopita M. A., Kewley L. J., Sutherland R. S., Scharwächter J., Basurah H. M., Ali A., Amer M. A., 2014, ApJ, 793, 127
Walch S., Naab T., 2015, MNRAS, 451, 2757
Walch S. et al., 2015, MNRAS, 454, 238
Weingartner J. C., Draine B. T., 2001, ApJ, 548, 296
Wünsch R., Walch S., Dinnbier F., Whitworth A., 2018, MNRAS, 475, 3393
York D. G. et al., 2000, AJ, 120, 1579
Zhang D., Chevalier R. A., 2019, MNRAS, 482, 1602
Zhang X., Feng Y., Chen H., Yuan Q., 2020, ApJ, 905, 97

SUPPORTING INFORMATION

Supplementary data are available at *MNRAS* online.

suppl_data

Please note: Oxford University Press is not responsible for the content or functionality of any supporting materials supplied by the authors. Any queries (other than missing material) should be directed to the corresponding author for the article.

APPENDIX A: VOLUME WEIGHTED PDF FOR THE SNR BOX

From a volume-weighted PDF time evolution of SNR box only (the left-hand panel of Fig. 2) on Fig. A1 we can see how the distribution of density is changing while the SNR interacts with the MC. At the very beginning, we have most of the gas in a dense phase with the peak around 10^{-23} g cm^{-3}, but after 0.13 Myr there is already a second peak at 10^{-25} g cm^{-3}, due to the dispersion of the MC with shock, which moves to 10^{-26} g cm^{-3} at time 0.3 Myr. That is why, it is far from a realistic view to use any unique physical time-scales for the whole SNR simulation box, which typically uses the approach of the uniform density ISM.

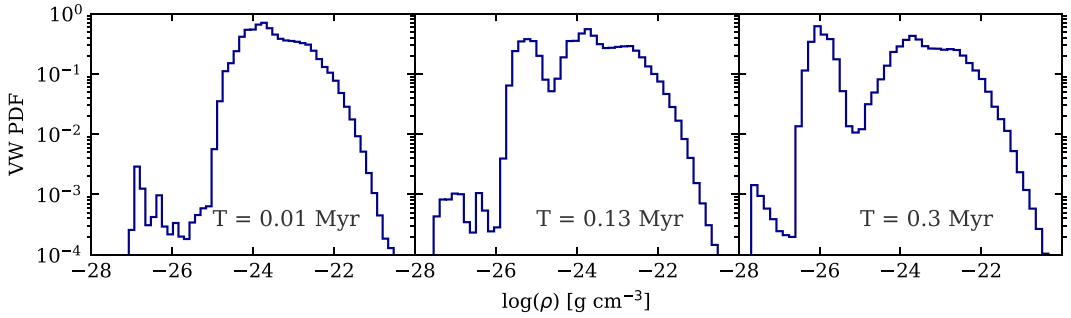

Figure A1. Time evolution (from left to right) of the volume-weighted PDF of the SNR box.

Table B1. Minimum and maximum value of line ratios derived from synthetic observations in the optical band for resolved SNRs. These values are calculated taking into account two possible positions of the observer (top or bottom view of the cube). We also marked in the first column, along which axis the projection was made.

Obtained value	[O III] (λ5007)/H β	[O III] (λ5007)/H α	[N II] (λ6583)/H α	[S II] (λ6731)/H α	[S II] (λ6717)/(λ6731)
-bg x-axis	[0.6, 2.5]	[0.8, 6.1]	[0.4, 0.7]	[0.5, 0.6]	[0.6, 1.0]
RT-bg x-axis	[1.9, 22.1]	[0.8, 7.5]	[0.4, 0.7]	[0.2, 0.3]	[0.4, 0.9]
-bg y-axis	[0.6, 2.8]	[0.7, 7.0]	[0.4, 0.7]	[0.3, 0.6]	[0.5, 0.7]
RT-bg y-axis	[1.8, 23.1]	[0.6, 8.3]	[0.4, 0.7]	[0.2, 0.8]	[0.2, 0.7]
-bg z-axis	[0.6, 2.5]	[0.6, 6.1]	[0.4, 0.7]	[0.3, 0.6]	[0.6, 1.0]
RT-bg z-axis	[1.9, 22.9]	[0.6, 6.7]	[0.4, 0.7]	[0.2, 0.7]	[0.5, 1.0]

Table B2. Minimum and maximum value of line ratios derived from synthetic observations in the optical band for unresolved SNRs. Note that we do not have here a close sulphur line ratio, because these lines are not resolved for these types of objects. See other details in Table B1.

Obtained value	[O III] (λ5007)/H β	[O III] (λ5007)/H α	[N II] (λ6583)/H α	[S II] (λ6731)/H α
RT x-axis	[2.0, 22.1]	[0.4, 6.7]	[0.1, 0.5]	[0.2, 0.3]
RT-bg x-axis	[5.3, 98.8]	[0.4, 5.8]	[0.2, 0.7]	[0.2, 0.6]
RT y-axis	[1.8, 23.1]	[0.4, 6.8]	[0.2, 0.5]	[0.2, 0.4]
RT-bg y-axis	[9.3, 75.5]	[0.4, 5.8]	[0.1, 0.7]	[0.2, 0.9]
RT z-axis	[1.9, 22.9]	[0.4, 7.1]	[0.1, 0.5]	[0.2, 0.3]
RT-bg z-axis	[4.8, 82.5]	[0.4, 6.9]	[0.3, 0.7]	[0.2, 0.6]

APPENDIX B: LINES EMISSION MAPS AND LINE RATIOS

This section provides examples of 2D emission maps in different optical emission lines after the post-processing procedure for three consecutive time points. One can see the difference between the volume-filling radiation and the radiation at the edge. In addition, emission projection effects are visible: increased radiation from the supernova bubble regions in the middle panel of all pictures and an overlay of instabilities from different planes in the upper right side of the bubble. Note that here background emissions have not been subtracted for demonstration purposes. Previous SNRs are visible in almost every image in the upper right corner.

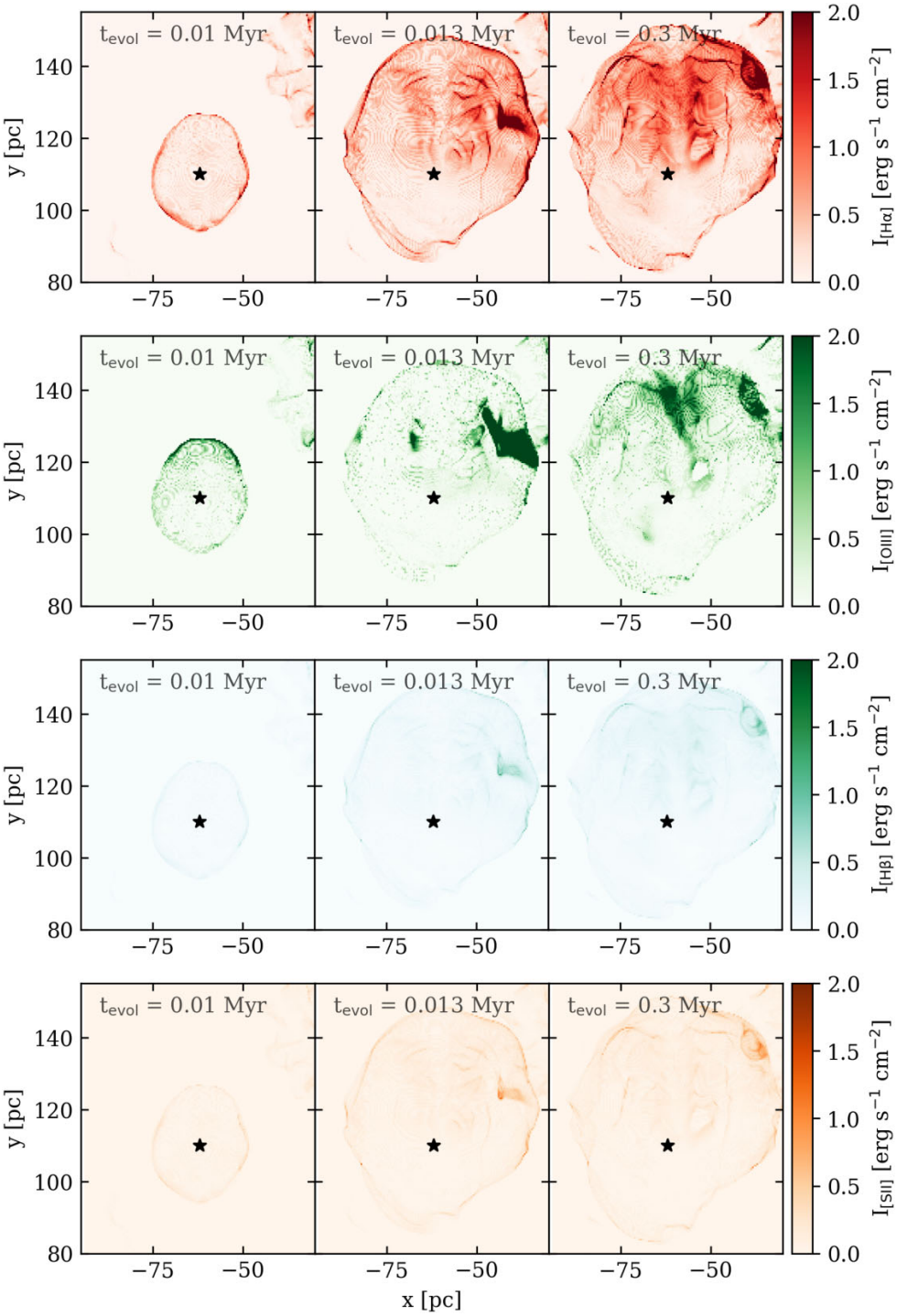

Figure B1. Time evolution (from left to right) of the [H α] λ6563, [O III] (λ5007), [H β] λ4861, [S II] λ6731 emission (from top to bottom). Intensity is normalised to the value 10^{-17}.

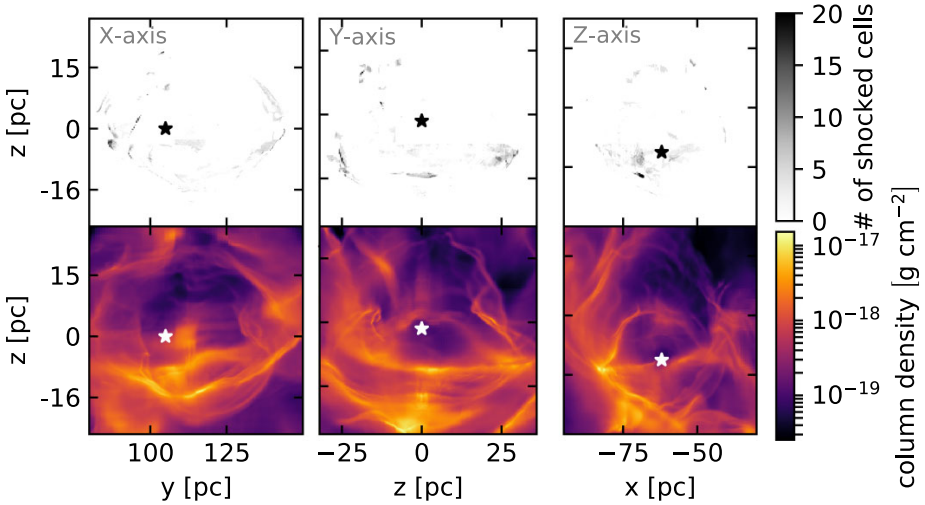

Figure C1. Top row: Projection of the shock cells along three the *z*, *y*, and *x* for time 0.13 Myr. Bottom row: Column density, same parameters as for the top plot. The star symbol shows the position of the SN explosion.

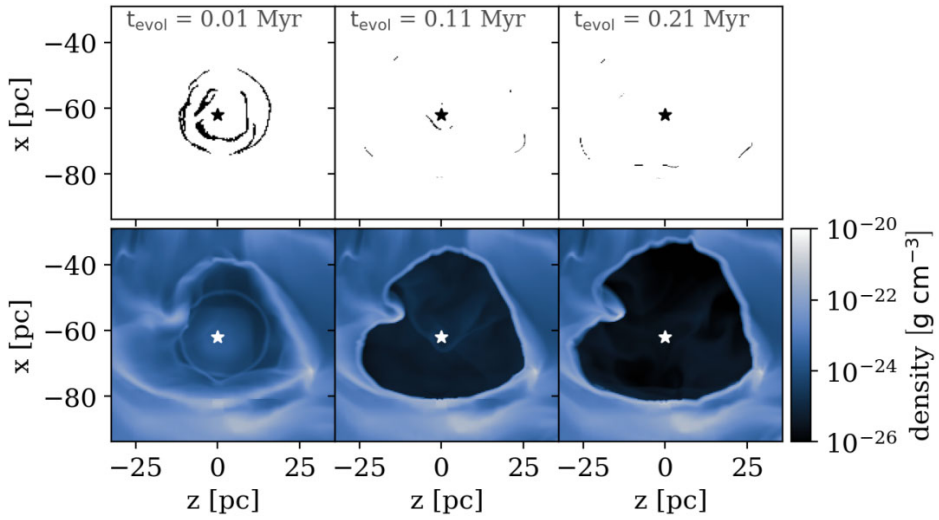

Figure C2. Top row: Time evolution from left to right of the position of shocked cells (forward and reverse shock) on the slice. Bottom row: Slice density.

APPENDIX C: SHOCK CELLS AND DENSITY PROJECTION

This section is intended to show the position of the shock waves in the 2D and 3D cases. Fig. C1 shows the projections of the supernova bubble along three different axes for the cells where the shock was detected (top row) and the density projection (bottom row). Due to the increase in colour from white to black, you can see the overlap of some areas of the bubble (due to the asymmetry) and the strengthening of the shock waves. However, it is difficult to see this in the density projection figure. Fig. C2 shows the section of the supernova bubble in cells with detected shock waves and their time evolution (from left to right). Here, you can see the initial shock wave from the centre and the reverse shock wave, which has a very complex shape due to the non-uniform density structure of the surrounding media.

This paper has been typeset from a TEX/LATEX file prepared by the author.

6

HOW DO SUPERNOVA REMNANTS COOL? – II. UNSUPERVISED MACHINE LEARNING STUDY (PAPER II)

A&A, 693, A38 (2025)
https://doi.org/10.1051/0004-6361/202451108

Astronomy & Astrophysics

How do supernova remnants cool?

II. Machine learning analysis of supernova remnant simulations

P. Smirnova[1,⋆], E. I. Makarenko[1,⋆], S. D. Clarke[2], E. Glukhov[3], S. Walch[1,4], I. Vaezzadeh[1], and D. Seifried[1]

[1] I. Physikalisches Institut, Universität zu Köln, Zülpicher Str. 77, 50937 Köln, Germany
[2] Institute of Astronomy and Astrophysics, Academia Sinica, No. 1, Sec. 4, Roosevelt Rd., Taipei 10617, Taiwan
[3] Stony Brook University, 100 Nicolls Rd, Stony Brook, NY 11794, USA
[4] Center for Data & Simulation science, Universität zu Köln, Albertus-Magnus-Platz, 50923 Köln, Germany

Received 13 June 2024 / Accepted 16 November 2024

ABSTRACT

Context. About 15%-60% of all supernova remnants are estimated to interact with dense molecular clouds. In these high-density environments, radiative losses are significant. The cooling radiation can be observed in forbidden lines at optical wavelengths.
Aims. We aim to determine whether supernovae at different positions within a molecular cloud (with or without magnetic fields) can be distinguished based on their optical emission (e.g. Hα (λ 6563), Hβ (λ 4861), [O III] (λ 5007), [S II] (λ 6717, 6731), and [N II] (λ 6583)) using machine learning (e.g. principle component analysis and k-means clustering).
Methods. We have conducted a statistical analysis of the optical line emission of simulated supernovae interacting with molecular clouds that formed from the multi-phase interstellar medium modelled in the SILCC-Zoom simulations with and without magnetic fields. This work is based on the post-processing of simulations that have been carried out with the 3D (magneto)hydrodynamic code FLASH. Our dataset consists of 22 simulations. The supernovae were placed at a distance of either 25 pc or 50 pc from the molecular cloud's centre of mass. First, we calculated optical synthetic emission maps (taking into account dust attenuation within the simulation sub-cube) with a post-processing code based on MAPPINGS V cooling tables. Second, we analysed the dataset of synthetic observations using principle component analysis to identify clusters with the k-means algorithm. In addition, we made use of BPT diagrams as a diagnostic of shock-dominated regions.
Results. We find that the presence or absence of magnetic fields has no statistically significant effect on the optical line emission. However, the ambient density distribution at the site of the supernova changes the entire evolution and morphology of the supernova remnant. Due to the different ambient densities in the 25 pc and 50 pc simulations, we are able to distinguish them in a statistically significant manner. Although, optical line attenuation within the supernova remnant can mimic this result depending on the attenuation model that is used. That is why, multi-dimensional analysis of optical emission line ratios in this work does not give extra information about the environmental conditions (ambient density and ambient magnetic field) of supernova remnant.

Key words. magnetic fields – magnetohydrodynamics (MHD) – methods: statistical – ISM: supernova remnants

1. Introduction

Typically, massive stars of 8–40 $M_\odot$ explode as a type II supernova (SN) at the end of their lifetime. Around 15–60% of these SNe are estimated to interact with a nearby molecular cloud (MC) (Hewitt & Yusef-Zadeh 2009; Zhou et al. 2023). Interaction with the dense environment of a MC shapes the evolution of the SN remnant (SNR). First, the SN explodes, producing a medium mostly filled with hot gas (McKee & Ostriker 1997; Kavanagh et al. 2013; Alsabti & Murdin 2017). The ejecta undergoes free expansion, in which the shocks produced by the explosion significantly affect the gas, which becomes hot, ionised, and turbulent. In the next step, it evolves to the Sedov-Taylor (adiabatic blast wave) stage and the ejecta energy is transferred to the ambient gas, but the net energy is conserved (Sedov 1959; Truelove & McKee 1999; Haid et al. 2016). At this stage (typically around 10^4 years after the explosion, but the exact number depends on the ambient density distribution), the young SNR can be observed in the X-ray and even γ-ray regimes (Borkowski et al. 2001; Aharonian et al. 2004; Vink 2012; Sasaki et al. 2012; Slane et al. 2014). The third stage starts when radiative losses become significant, at which point a shell-like structure appears. Due to the cooling, the remnant starts to emit at UV and optical wavelengths, while further expanding into (snow-ploughing through) the ambient medium (Fesen 1985; Mavromatakis et al. 2002; Boumis et al. 2008; Fesen et al. 2024). About 20% of the SNRs in our Galaxy have such optical counterparts (Green 2019). In the final stage, the remnant dissolves in the interstellar medium (ISM) (Ostriker & McKee 1988).

The evolution of a SN in a homogeneous medium has already been well studied (McKee & Ostriker 1997; Cioffi 1988; Haid et al. 2016; Jiménez et al. 2019), but in reality, SNe are immersed in a complex ISM – a highly inhomogeneous environment with a wide range of densities and temperatures. Therefore, simulations of MCs are essential to our comprehension of the structure of the ISM, and as a result to modelling realistic SNRs. Recently, great progress has been made in simulations of the complex multi-phase ISM and the interaction of SNe with the turbulent ISM (e.g. de Avillez & Breitschwerdt 2005; Gatto et al. 2015; Walch et al. 2015; Walch & Naab 2015; Zhang & Chevalier 2019; Haid et al. 2019; Ganguly et al. 2023) or

⋆ Corresponding authors; smirnova@ph1.uni-koeln.de, makarenko@ph1.uni-koeln.de

with MCs in particular (Iffrig & Hennebelle 2015; Seifried et al. 2017; Seifried et al. 2018). These simulations help to answer many physical questions; for example the effect of SNe on the star formation rate (Padoan & Nordlund 2011; Gatto et al. 2015), and the energy and momentum contribution of SNe to the ISM (Walch & Naab 2015).

Makarenko et al. (2023) studied optical emission (Hα (λ 6563), Hβ (λ 4861), [O III] (λ 5007), [S II] (λ 6717, 6731), [N II] (λ 6583)) from SNRs, employing the post-processing module CESS (Cooling Emission in the optical band from Supernovae in (M)HD Simulations)[1] used for the FLASH code. We employed the updated collision data output from MAPPINGS V (Sutherland & Dopita 2017). Makarenko et al. (2023) show that it is crucial to consider both the attenuation effect due to the dust within the SNR bubble using a simple radiative transfer, and a realistic density distribution from the surrounding ISM, as this significantly affects the line emission, and hence the diagnostics based on different lines. Correspondingly, the more complex simulations we have, the more difficult it is to disentangle and study the impact of each parameter (e.g., temperature, density, magnetic field) on the simulation outcome using non-statistical methods.

With the rapid development of supercomputers (and simulations), and an increasing number of telescopes (and accumulated observations), large datasets are now common in astrophysics (e.g. Perryman et al. 1997; Abdurro'uf et al. 2022; Smart et al. 2021). Because of this, the search for relations between physical parameters can be hampered by the large amount of data, and indeed correlations can be found between more than two parameters. In this case, tools such as unsupervised machine learning can be extremely useful: one such tool that is suitable for searching for correlations between a large number of parameters is principal component analysis (PCA). Principal component analysis transforms a large set of variables to a smaller one that still contains most of the information from the larger set, losing a little accuracy for simplicity. Einasto et al. (2011) presented a method that uses PCA to investigate the strength of correlations between the properties of superclusters of galaxies (data from SDSS DR7) and search for the presence of distance-dependent selection effects in the supercluster catalogue. Principal component analysis can also be applied for dimension reduction or to visualise data (Bressan et al. 2021). Several other algorithms can also be applied, such as t-distributed stochastic neighbour embedding (t-SNE), as is used by Anders et al. (2018), to better distinguish chemical sub-populations in the solar vicinity, rather than looking at 2D abundance maps. Once the dimensions are reduced, it is important to robustly find clusters with unsupervised methods.

The k-means algorithm (MacQueen 1967; Hartigan & Wong 1979) searches for proximity in multi-dimensional space (in our case in the reduced dimensional space). For example, the algorithm was used in Rubin & Gal-Yam (2016) to divide light curves into classes with a fixed number of clusters. The Sloan Digital Sky Survey (SDSS) used the k-means algorithm to identify clusters of different stellar spectral classes as well as rare objects and outliers (Sánchez Almeida & Allende Prieto 2013).

Further, there have been many attempts recently to improve the classification of SNe in BPT (Baldwin, Phillips, & Terlevich) diagrams (Baldwin et al. 1981; Kauffmann et al. 2003; Kewley et al. 2019), since the classification of different astrophysical objects is not always unambiguous or does not reflect all physical features. The BPT diagrams allow for the main excitation source of an object (shocks or photo-ionisation) to be determined using optical line ratios. The idea of using multi-dimensional data classification for emission-line galaxies with the support vector machine algorithms has been tried both for observations (Stampoulis et al. 2019) and for theoretical models (Kopsacheili et al. 2020). There have been several attempts to improve the BPT diagrams using other optical line ratios (creating a multi-dimensional optical line ratio space), and modern machine learning techniques to better classify observed objects or to better constrain their physical conditions (e.g. Vogt et al. 2014; Ho 2019; Zhang et al. 2020; Ji & Yan 2020; Rhea et al. 2021). However, none of the new models constitute a universal tool that could be used in both theoretical work and observations. Here we test whether BPT diagrams are a sensitive diagnostic tool to uncover the environmental conditions of young SNRs.

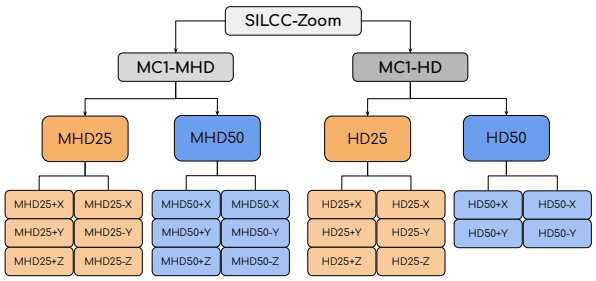

Fig. 1. Hierarchical structure of the dataset from the SILCC-Zoom project. We have in total 22 simulations: 'MC1-MHD' (with a magnetic field) and 'MC1-HD' (without a magnetic field). Each of the 'MD25', 'MHD50', 'HD25', 'HD50' datasets contains all possible positions of SN event (±X, ±Y, ±Z). Further details can be found in Seifried et al. (2018).

In this paper, we have performed a statistical study using unsupervised machine learning by post-processing (magneto-) hydrodynamic (MHD) simulations, comparing different initial conditions such as magnetic field strength and distances from the SN explosion to the centre of mass of the nearby MC that the remnant interacts with. We used multi-dimensional data consisting of multiple optical line ratios. The emission lines were calculated by post-processing the 3D simulations with the MAPPINGS V code. Our analysis reveals whether line ratios are sensitive to variations in the pre-shock density distribution and the presence of the magnetic field at the site of the SNR.

The paper is structured as follows. In Section 2, we describe the simulation setups, as well as the post-processing routine used to calculate optical emission lines. Section 3 describes the statistical methods (normalisation, pre-processing, and clustering) applied to our data and BPT diagrams. We present our results in Section 4 and discuss the importance of the ambient ISM properties and the attenuation effect for the optical emission of SNR. The conclusions are given in Section 5.

2. Dataset

We use SILCC-Zoom simulations of SNe interacting with MCs from Seifried et al. (2018) using the FLASH code (Fryxell et al. 2000) as an initial dataset. The dataset description can be found in Fig. 1 (for more details, see Walch et al. (2015); Girichidis et al. (2016); Seifried et al. (2017); Seifried et al. (2018)). In Section 2.1, we briefly summarise the simulation setup. In Section 2.2, we describe the post-processing tool from Makarenko et al. (2020, 2023) which was used to produce optical emission cubes and maps.

[1] https://github.com/kativmak/CESS

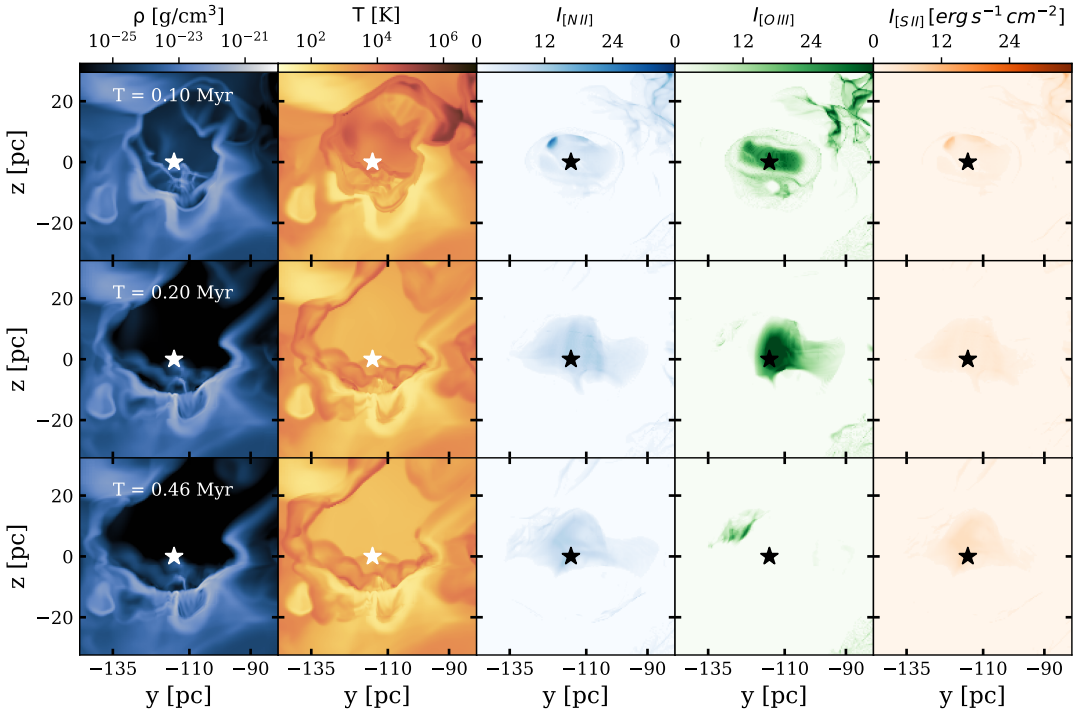

Fig. 2. Time evolution (from top to bottom) of (from left to right): density slice, temperature slice, [N II] (λ6583 Å) intensity projection, [O III] (λ5007 Å) intensity projection, and [S II] (λ6731 Å) intensity projections for the 'MHD50+X' simulation. The star symbol in each panel represents the position of the SN explosion. The SN explosion disrupts part of the dense MC, as can be seen from the density slice (first column). This MC and SN interaction gives rise to the optical emission from the SNR. From the temperature evolution of the SNR bubble (second column), we can see the hot gas (10^{6-7} K) cooling down over 0.46 Myr, and forming the complex structures at the edge of the SNR and MC that are subsequently visible in the optical emission. Among three optical lines (third to fifth columns), the [O III] is the strongest as it is a 'volume-filling emission'. [N II] and [S II] originate from a thin cooling layer right behind the shock front.

2.1. Simulations

In the SILCC project (Walch et al. 2015; Girichidis et al. 2016), we modelled the evolution of a section of a galactic disc (500 pc × 500 pc × ± 5 kpc), with an initial gas surface density of $\Sigma_{\rm gas}$ = 10 $M_\odot$ pc^{-2} with initial conditions similar to the ones present in the solar neighbourhood. The simulations took into account SN feedback, magnetic fields (in MHD runs, $B_{0,x} \sim 4\,\mu$G is the initial field strength in the disc mid-plane) and self-gravity with a non-equilibrium treatment of the H_2 and CO chemistry of the gas. The SNe rate is in agreement with the Kennicutt–Schmidt relation for our surface density (Robert & Kennicutt 1998) (15 Myr^{-1}). The SNe explosions heat and stir the gas and a complex multi-phase ISM appears. A zoom-in strategy was used to resolve the formation of MCs to scales of ~0.12 pc in the SILCC-Zoom simulations (Seifried et al. 2017; Seifried et al. 2018). We selected two basic simulations: one hydrodynamical (HD) without magnetic fields and one MHD with magnetic fields: MC1-HD and MC1-MHD. The general properties of the MCs that we shall study further are given in Table 1.

After the formation of MCs (we denote this time as t_0), and some further evolution, a new SN was exploded at time $t_{\rm SN} = t_0$ + 1.53 Myr. In Seifried et al. (2018), a new simulation was run for each SN exploding at different distances (25 pc or 50 pc simulations are used here), and at positions with respect to the centre of mass of the cloud along the x, y and z directions in a zoom-in region (see Fig. 1). Each SN explosion was modelled by adding

Table 1. Main parameters of MCs.

Simulation	Total mass ($M_\odot$)	Volume (pc^3)	H_2 fraction ($M_\odot$)
MC1-HD	7.3×10^4	$88 \times 78 \times 71$	2.1×10^4
MC1-MHD	7.8×10^4	$88 \times 78 \times 71$	1.3×10^4

Notes. Name of the simulation dataset (first column), total mass (first column), considered sub-volume volume (second column), and molecular hydrogen fraction within the selected sub-volume (third column).

10^{51} erg of thermal energy into the radius, $R_{\rm inj}$, around the explosion centre. We made sure to resolve the Sedov-Taylor radius with at least 4 simulation cells, corresponding to 0.48 pc (Gatto et al. 2015). We followed each SNR evolution for 0.46 Myr. It is interesting to consider different SN positions because of the variation in density distribution at the site of the SN explosion ($10^{-27.5}$–$10^{-21.5}$ g cm^{-3} at 25 pc, and 10^{-28}–10^{-21} g cm^{-3} at 50 pc). As a result, the optical emission, which arises from interactions with a dense medium, will also look different. The aim of this paper is to explore how this difference is manifested.

Examples of the time evolution of temperature and density are shown in Fig. 2, from top to bottom in columns 1 and 2, respectively. As is seen in the upper right corner of the temperature evolution, the SN blows out the gas from the cavity towards

Table 2. Median percentage of attenuation for each line with the error in each dataset.

Dataset	Median % of the line attenuation				
	[S II]	[N II]	[O III]	Hα	Hβ
MHD25	18 ± 10	25 ± 9	39 ± 10	32 ± 10	19 ± 11
HD25	34 ± 5	39 ± 5	40 ± 7	40 ± 5	34 ± 5
MHD50	34 ± 14	38 ± 12	43 ± 12	39 ± 10	35 ± 14
HD50	37 ± 9	36 ± 10	34 ± 14	33 ± 10	28 ± 13

Notes. Mean percentage of attenuation (Cols. 2–6), the name of the dataset (Col. 1). The attenuation of each optical line is taken into account, as is described in Section 2.2.

the region of lower density. During this process, the gas cools down and starts to emit in the optical ([N II], [O III], and [S II] lines; third, fourth, and fifth columns of Fig. 2 correspondingly). At the end of the evolution (t = 0.46 Myr), the optical emission fades away, as the majority of the SNR bubble is cooled below typical optical emission temperatures (less than a few 10^4 K). Because the different parts of the bubble evolve on different timescales (due to the complex shock-cloud interaction), we can still see optical emission at t = 0.46 Myr in the central region and in the upper right part of the SNR bubble.

2.2. Optical emission post-processing

To prepare our simulations and reduce the computational cost of post-processing, we cut out sub-cubes using the biggest SNR bubble radius as a border (which can be measured at t = 0.46 Myr). Each sub-cube is 64.8 pc on a side. In this case, we took into account the emission mainly from the SNR and avoided significant contamination from the background (previous SN events) in our analysis.

We followed the method of Makarenko et al. (2023), which introduces the post-processing module CESS for the FLASH code, which uses the collision data from MAPPINGS V (Sutherland & Dopita 2017; Sutherland et al. 2018) to reproduce optical emission maps of simulated SNRs.

In summary, the post-processing procedure is as follows. First, from the .hdf5 simulation output, we cut out a sub-cube of the region containing the SNR (64.8 pc on a side), and re-gridded the AMR grid to a uniform grid (every cell is 0.12 pc^3). Then, we calculated the emitted luminosity for every cell in the 3D computational domain using the temperature-cooling rate dependency, known from MAPPINGS V. After that, we integrated along a given line of sight, taking into account the attenuation (projecting the 3D cube to a 2D map):

$$F_{\rm tot} = \int F_i e^{-\tau_{\rm i}}\, ds \tag{1}$$

where $F_{\rm i}$ is the flux of the cell i, $\tau_{\rm i}$ is the optical depth, and ds is the area of the cube. The optical depth, $\tau_{\rm i}$, was calculated in the following manner:

$$\tau_i = \kappa_{\rm abs}\rho_i V_i^{1/3} f_{\rm d}, \tag{2}$$

where $\kappa_{\rm abs}$ is the dust absorption cross section per mass of dust (cm^{2}g^{-1}), $\rho_{\rm i}$ is the density of cell i, V_i is the cell volume, and $f_{\rm d}$ is the dust-to-gas ratio ($f_{\rm d}$ = 0.01 is fixed in our simulations). The dust absorption cross-section was taken from Weingartner & Draine (2001) (Milky Way dust with R_V = 4.0). The attenuation percentage for each line in our dataset can be found in Table 2.

The attenuation effect can be high for the optical emission lines due to gas and dust attenuation. Here we took into account only attenuation within the SNR simulation domain. This attenuation effect leads to fewer SNRs detected in the optical regime in our Galaxy compared to radio and X-ray (Green 2019). Thus, we reproduced optical emission line maps (Hα (λ 6563 Å), Hβ (λ 4861 Å), [O III] (λ 5007 Å), [S II] (λ 6717 Å, 6731 Å), and [N II] (λ 6583 Å) that show the same features as in real observations of SNRs interacting with the dense medium. We investigated the following optical line ratios: [O III] (λ 5007)/Hα, [S II] (λ 6731)/Hα, [N II] (λ 6583)/Hα, and [O III] (λ 5007)/Hβ. These line ratios are typically used in BPT diagrams as shown in Section 3.4. As a result, we have a 4D dataset. We calculated line ratios at each timestep (0.02 Myr) during the SNR evolution time (0.46 Myr) along the x axis from one side of the cube in 22 simulations (see Fig. 1).

3. Statistical analysis

3.1. Data normalisation

In order to make a comparison between data points, the dataset must be normalised according to the chosen transformation function. We would like the normalised variables to be in units relative to the standard deviation of the sample. To get the normalised variables, we performed the following normalisation for each data point:

$$z = \frac{d - \mu}{\sigma},$$

where d is initial (raw) data, μ is the mean of the sample, and σ is the standard deviation. This is standard practice for PCA to remove the effects of different means and scales between the features. As an input for this procedure, we took optical line ratios in a linear space.

3.2. Dimension reduction: Principal component analysis

We have four optical line ratios (see Section 2.2) and their time evolution over 0.46 Myr. This yields a 4D dataset. We first reduced our dataset to 2D, to aid in data interpretation, while retaining as much information as possible (for 3D, see Appendix C, Fig. C.1; the third dimension contributes less than 10% significance, and therefore using 2D does not lead to lower accuracy). Principal components (PCs) are directions in feature space along which the original data exhibits the greatest variance. By retaining the two PCs with the largest variances, we minimise the loss of information during dimensionality reduction. The larger the variance of the PC axis, the larger the dispersion of the data along it (the more information it carries), and therefore the less information is lost. This enables us to visualise the data in two dimensions.

The loading represents the weight (or contribution) of a specific original variable to the PC. The loadings for each line ratio are shown in Table 3 for each PC of the dataset. Despite PC1 and PC2 being represented by a mixture of features, we focussed on the ones with the highest variance. It is easy to see that for PC1 the line ratio [S II]/Hα is the most significant. S^+ is a known tracer of SNRs, as it is a collisionally excited ion that can form in a large recombination zone behind the SNR shock. For PC2, it is [O III]/Hα and [O III]/Hβ that are the most significant. O^{++} is forming within a significant region of the SNR bubble, as it has a higher excitation temperature than S^+ or N^+. Due to this, the observed area f the SNR bubble, where we can observe O^{++},

Table 3. Loading for principal axes in feature space.

Dataset	PC	Coefficients of the line ratio			
		[S II]/Hα	[N II]/Hα	[O III]/Hα	[O III]/Hβ
$MC1_{att}$	PC1	–0.62	0.26	0.36	0.39
	PC2	0.12	–0.52	0.70	0.70

Notes. Loadings for PC1 or PC2 (Col. 2)represent the directions of maximum variance in the dataset for each line ratio (Cols. 3–6). The variance captured by PC1 and PC2 is spread across multiple features, indicating that those features contribute together to the variance in a similar manner.

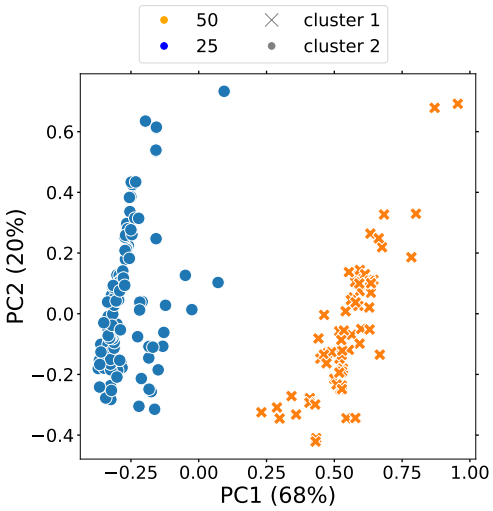

Fig. 3. 'MHD25', 'MHD50', 'HD25', 'HD50' datasets (e.g. '$MC1_{att}$') after using the PCA algorithm. 'MHD25'+'HD25' is shown in orange, and 'MHD50'+'HD50' is in blue. The predicted clusters are marked with circles and crosses. The higher the percentage for each PC, the higher the relative variance in the dataset that is observed in the direction of the corresponding eigenvector (for the absolute values, see Table 3). We used $n_{clust} = 2$ in the k-means algorithm. The data is clearly separated into two distinct clusters.

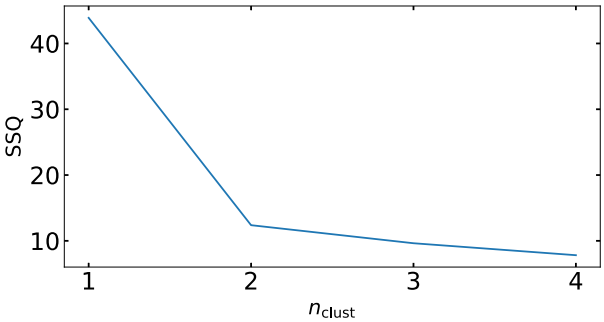

Fig. 4. Elbow plot for all dataset ('$MC1_{att}$'). On the x-axis the number of clusters is presented, while on the y axis the total within the sum of squared distances (SSQ) is plotted. We see a kink in the line at $n_{clust} = 2$, which indicates that the optimal number of clusters to be used by the k-means algorithm is 2.

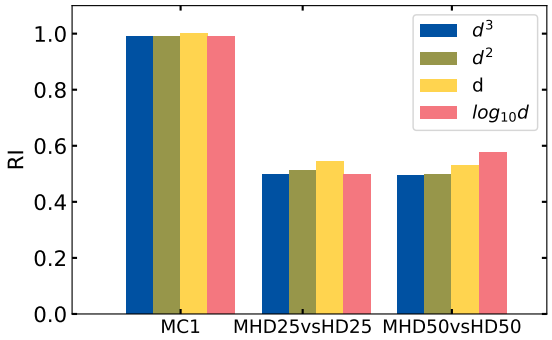

Fig. 5. Rand index value on the y-axis for different datasets on the x-axis: all data try to define two clusters ('MC1', first column), 'MHD25' vs. 'HD25' (second column), and 'MHD50' vs. 'HD50' (third column). The colours show the different data transformations: polynomial with blue and green, standard with yellow, and logarithm with red (see the legend for details). The higher the Rand index, the more effective the clustering. The best results were obtained with standard and polynomial data for the first column (all data, distance difference).

differs in various simulations, and can be used as a parameter to distinguish them. The result of the PCA algorithm is shown in Fig. 3 and Appendix A, Fig. A.1. We note that the data in the figures is already clustered (circles and crosses). We describe the clustering process in Section 3.3.

Apart from the PCA, we also tried to reduce the dimensionality of the dataset using the t-SNE algorithm (see Appendix B, Fig. B.1). This is a non-linear algorithm, in contrast to PCA. We found no qualitative difference between its results and those from PCA, so in the following analysis, we have only used the PCA algorithm.

3.3. Clustering: k-means and Rand index

After reducing the dimensionality of the dataset, we grouped the points in 2D space into clusters using the k-means algorithm. This algorithm seeks to minimise the sum of the squared Euclidean distances between each point and the centroid of the cluster to which it has been assigned. For the k-means algorithm, we need to provide the number of expected clusters as an input parameter. The elbow method (Thorndike 1953) is a technique to determine the number of clusters (n_{clust}) to use in the k-means clustering algorithm. First, the elbow method calculates the sum of the squares of the distances between all points and then calculates the mean. When we choose $n_{clust} = 1$, the sum of the squared distances within the cluster is the largest. As the value of n_{clust} increases, the sum of squared distances (SSQ) within the cluster decreases. Finally, to determine the best choice of n_{clust}, we plot n_{clust} versus the SSQ, as is shown in Fig. 4. At the point $n_{clust} = 2$, the SSQ decreases dramatically, or forms an 'elbow'. This point is considered the optimal value of the number of clusters. In Fig. 3 the colours represent the real dataset, and the symbols represent the identified clusters after performing the k-means algorithm (and vice versa in Fig. A.1).

To verify the clusters we identify with the k-means algorithm, we can use the Rand index. The Rand index indicates the similarity between the given (original) clusters and the predicted clusters. It is defined as RI = $\frac{a}{b}$, where a is the number of agreeing pairs (original clusters vs predicted clusters), and b is the total number of pairs. The closer the Rand index is to 1.0, the better the clustering. Fig. 5 shows the Rand index for different samples. For example, there were 198 data points in the '$MC1_{att}$' dataset, and for 'MHD25'+'HD25', 98 data points

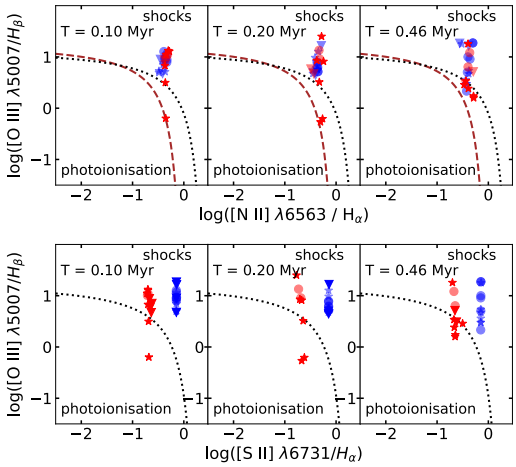

Fig. 6. Time evolution (from left to right) of the classical BPT diagram (upper row) and sulphur BPT diagram (lower row) for 'MHD25', 'HD25' (blue) and 'MHD50', 'HD50' (red). Star symbols show MHD simulations and circle symbols show HD simulations. The dotted reference line is Kewley et al. (2001), and the dashed line is from Kauffmann et al. (2003) for the upper row. The dotted reference line for the lower row is from Kewley et al. (2001). For both figures, reference lines separate the photoionisation region (star-forming, lower left corner) and the shock-dominated region (upper right corner). The SNRs in the upper figure are typically located in the "mixed region" (between the reference lines) or in the region of shocks as collisions are the main excitation mechanism for strong optical lines. For the lower figure, SNRs are typically located in the shocks region. The sulphur BPT diagram can classify SNRs according to the different ambient densities ('MHD25'+'HD25' vs. 'MHD50'+'HD50'), as was shown with k-means.

were correctly linked to the clusters (initial and predicted point coincided), which leads us to RI = 98/198 ∼ 0.5. Various transformations of the initial data (polynomial – d^2 or d^3, unscaled – d, and logarithmic – $\log_{10} d$) were also considered before proceeding with the PCA so as not to bias the result. Despite this, the best Rand index is obtained for the unscaled data, for the dataset '$MC1_{att}$'. In this case, we can almost perfectly identify the 'MHD25'+'HD25' and 'MHD50'+'HD50' groups again after the statistical analysis if we compare the resulting clusters from the k-means algorithm with the initial dataset. We note that we do not use the information about labels for the initial dataset in our analysis. The Rand index for 'MHD50+HD50' and 'MHD25+HD25' is ∼0.5, which means that we cannot distinguish different clusters for simulations with and without a magnetic field.

3.4. BPT diagram

The BPT diagram is a diagram based on strong optical line ratios (typically, [O III]/Hβ and [N II]/Hα). It helps to classify the dominant mechanism of ionisation in the observed object (e.g. an individual object like a SNR or in the whole galaxy). Two reference lines (Kewley et al. 2001; Kauffmann et al. 2003) (defined by theoretical modelling and SDSS catalogue analysis York et al. 2000) separate objects that are ionised by hot stars (star-forming emission or H II regions, lower left part) or by hard radiation of shocks (upper right part). Mostly, SNRs are located between the theoretical lines (in the so-called 'mixed region') or in the shock-dominated region. The BPT diagram for our dataset ('$MC1_{att}$') is shown in the upper row in Fig. 6. Colours indicate different datasets: 'MHD25', 'HD25' – blue; 'MHD50', 'HD50' – red. The shape of the markers shows the presence or absence of a magnetic field: HD is represented by circles, and MHD be stars. The mean values for different simulations of SNRs start at t = 0.1 Myr at the border of the "mixed region", or at the lower limit of the shocks region, then at t = 0.2 Myr and move up from the classification line as the gas cools down and shocks start to be observable in the optical band. Finally, at t = 0.4 Myr, shocks are mostly dissipated, optical line ratios have become weaker, and SNRs move back to the mixed region. This is a typical SNR evolution on the BPT diagram. We can conclude that this BPT diagram does not reveal different evolutionary paths for our dataset.

As was concluded in the PCA analysis above, the [S II](λ 6731)/Hα line ratio is the most important to detect SNRs and trace the various initial conditions (e.g. density distribution) at the SNR site. Therefore, we also plot a sulphur BPT diagram in the bottom row of Fig. 6. The colours and symbols are the same as in the classical BPT diagram and the separation line is taken from Kewley et al. (2001). During the evolution of the SNR, our mean value is clearly in the shock-dominated region, apart from a few points in the photoionisation region. The sulphur BPT diagram is sensitive enough to distinguish between the different ambient density distributions at the site of the SNRs. That is why at any moment of the evolution, our line ratios are divided into two groups: 'MHD25'+'HD25' and 'MHD50'+'HD50'. The [S II](λ 6731)/Hα line ratio is also very similar for these two groups of simulations and almost does not change. Due to the known dependence of the [S II] doublet on the electron ambient density (Smith et al. 1993; Draine 2011), the similarity of the line ratios could be a consequence of the ambient media distribution at the SNR site. This is discussed further in Section 4.

4. Results

4.1. Different distances of supernovae to the molecular cloud

To test the influence of the initial density distribution on the optical emission of a SNR, two positions of the SN relative to the centre of the MC were considered. The first is located at 25 pc, and the second one at 50 pc. The PCA and t-SNE algorithms both show the statistical difference between these two cases, as we can see from the following k-means clustering and the Rand index in Fig. 5. The reason for this is the presence or absence of a denser medium near the site of the SN explosion. For strong optical emission in forbidden lines, a fairly dense environment that will be compressed by the shock wave is required, which will then radiate at low energies of the optical range in the late stages of the evolution of the SNR. This could cause the rise of optical emission in 25 pc simulations at a different time as each evolutionary stage of the SN strongly depends on the surrounding medium.

To explain why we see a statistical difference between the 25 pc and 50 pc simulations, we performed an analysis of the surrounding (ambient) ISM, as is detailed below. First, we defined the shock front (forward and reverse, but only forward shock detection was used) of the SNR using a shock finding routine based on Lehmann et al. (2016). This allows us to determine the shock cells based on the conditions of velocity divergence and the density gradient. Second, we cast six rays starting from the SN explosion position to locate the position of the primary shock with respect to the explosion centre. It was then possible to mask the SNR bubble, and calculate the median density and interquartile range only of the ambient (unshocked) medium. Taking into

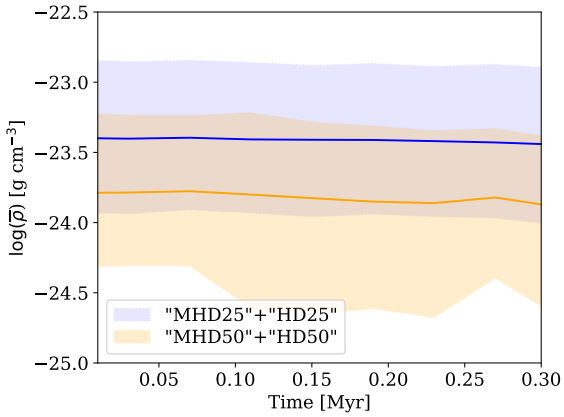

Fig. 7. Evolution of the mean density of the ambient medium for the 'MHD25'+'HD25' (blue) and 'MHD50'+'HD50' (orange) datasets (the mean of means for both datasets). We note that the mean was originally calculated in linear space over each set and presented in log space in the figure. The shaded region shows the interquartile range (25th and 75th percentiles of the data). The 'MHD25'+'HD25' dataset has higher values overall (by around 0.4 orders of magnitude) than the 'MHD50'+'HD50' dataset.

account the time evolution of the media surrounding our SNR (0.4 Myr), we can check how different the distribution of the medium is at 25 pc compared to 50 pc. The result of this procedure for the whole dataset is shown in Fig. 7. The mean ambient density for 'MHD25'+'HD25' (blue) is, on average, higher than for 'MHD50'+'HD50' (orange), as can be inferred from the evolution of the mean and interquartile range around 0.4 orders of magnitude. Although this difference does not appear to be significant, a difference is seen for optical radiation. Optical emission is brighter in older SNRs (where the shock wave velocities are usually less than 200 km s^{-1}). This brightness is determined by the density of the ambient medium encountered by the shock front.

If our SNe were placed at different positions in the MC they would encounter different ambient densities that would not necessarily depend on their radial distance from the MC centre. We would be able to differentiate them only in the case of different mean densities: for example, as in the cases of 25 pc and 50 pc in our simulations.

4.2. Magnetohydrodynamic versus hydrodynamic runs

The presence of a magnetic field at the explosion site does not directly affect the optical emission from the SNR. However, the magnetic field influences the morphological evolution of the SNR (as well as the shock waves). Moreover, due to compression, the magnetic field strength at the rim of the SNR bubble grows from 4 to 100 μG. Singly ionised particles (S^+, N^+) are usually formed in approximately the same temperature zone behind the shock wave. If there are any thermal instabilities combined with a magnetic field or other shock wave parameters favouring regions where hydrogen is ionised (even when N^+ and S^+ are able to recombine) the optical line ratios may change. Therefore, the difference in the optical line ratio depends on the initial conditions and magnetic field presence. This can be noted from the grid of shock models calculated using MAPPINGS V (Allen et al. 2008).

We have investigated if the magnetic field (initial condition B-field of 4 μG) influences the optical line ratios. For

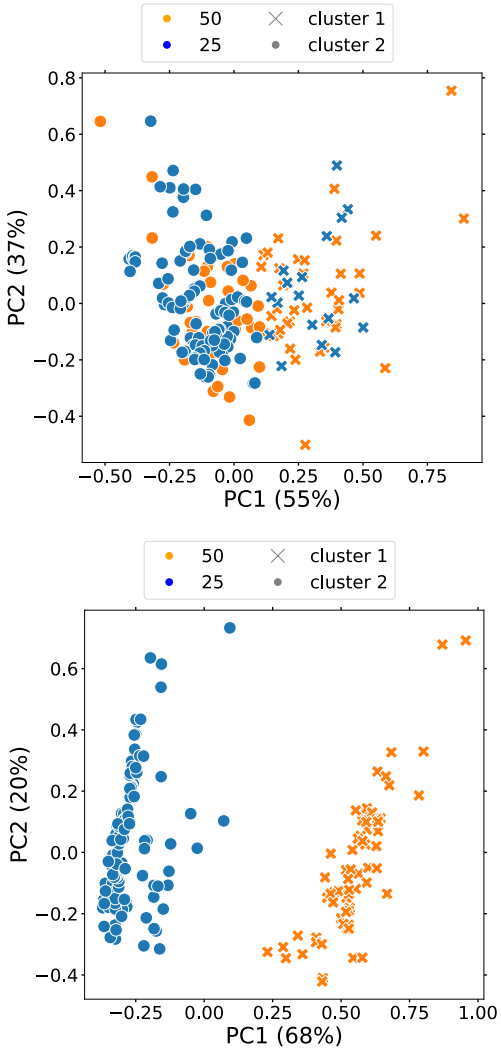

Fig. 8. Clustering of all data ('MC1') with k-means after PCA algorithm for line ratios without attenuation ('$MC1_{unatt}$', top panel) and with attenuation ('$MC1_{att}$', bottom panel). Colours represent real datasets; symbols represent predicted datasets. The best result shows the line ratios with attenuation (bottom panel). There, we can separate the different distances from the SN explosion to the centre of mass of the MC.

all simulations, we have two simulation runs – one with the magnetic field (MHD) and one without it (HD). Studying the optical lines we could not confirm any statistically significant deviation depending on the magnetic field. Thus, we show that the optical line ratios do not depend on the magnetic field during the SNR stage to a large extent, or the strength of the magnetic field should be significantly higher. The magnetic field is also expected to be much more important for high-energy bands (e.g. UV, X-ray, γ-ray).

4.3. Attenuation effect

Makarenko et al. (2023) demonstrate that attenuation within the SNR cube should be taken into account, as it changes the classification of an object as an SNR based on the optical line ratios. In this work, we see a similar pattern. In Figs. 8 and 9, attenuation

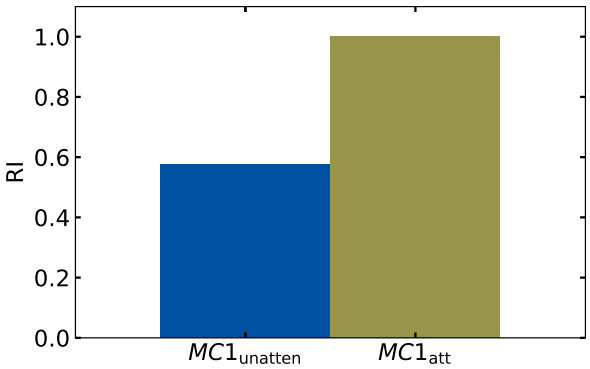

Fig. 9. Rand index value (y-axis) for unattenuated ('$MC1_{unaten}$') and attenuated ('$MC1_{att}$') line ratios from Fig. 8. The line ratio with attenuation (green) shows the best Rand index.

plays a crucial role in the search for the effect of a magnetic field or the distribution of matter at the site of an SNR on optical emission. To check that the [S II](λ6731)/Hα line ratio is a reliable tracer of the local properties at the SNR site, we need to be sure that attenuation is not mimicking some form of noise for the unattenuated optical lines brightnesses. We tested this by applying random noise to the unattenuated brightness values, at a level corresponding to the range of attenuation between its maximum and minimum values (approximately 80% and 20%, respectively; see Paper I, Makarenko et al. (2023), Figure 7), to examine the edge case. Therefore, we did not use the average values provided in Table 2. We repeated this analysis 1000 times. As a result, we can obtain point separations, for example, on a sulphur BPT diagram in Appendix D, Fig. D.1 using noise. This means that the [S II](λ6731)/Hα line ratio is not a universal determinant of the presence of shock waves from an SNR in the environment, and can be confused for other effects. Therefore, we advise caution when using this type of BPT diagram to come to conclusions about correlations between the line ratios and initial conditions at the site of the SNR.

5. Conclusions

In this paper, we have analysed optical emission from the SILCC-Zoom simulation dataset of SNRs interacting with MCs with and without magnetic fields. We have post-processed a dataset of 22 simulations using the CESS package.

To perform a statistical study, we further used the PCA algorithm to pre-process the data, and clustered it using the k-means algorithm. The Rand index allows us to compare how well the initial labels of the dataset fit with the clusters obtained without any prior information on the data. The Rand index has a value of 1 for the predicted different positions of the SNe with respect to MCs (dataset '$MC1_{att}$'), which means that our initial classification matches the clustered data. This means that in our simulations we can distinguish different distances to the centre of the MC (25 pc and 50 pc) due to the difference in the mean ambient medium density at the site of the SN explosion. As there is no universal trend of density with radius in MCs, it is not possible to link optical emission with distance from the MC centre. Therefore, the mean ambient density at the site of the SN is a relevant quantity in determining subsequent optical emission. The Rand index shows no statistically significant differences between the simulations with or without a magnetic field, so we cannot distinguish them. Analysing the nitrogen BPT diagram of the optical emission, all our SNRs are mainly located in the mixed region, and the variation between various simulations is minimal. For the sulphur BPT diagram, we see the same division of the dataset as in our clustering analysis, depending on the ambient density distribution at the SN explosion site. Due to that, we performed an independent analysis of unattenuated optical line luminosity adding random noise. We show that we can mimic the results of the sulphur BPT diagram with attenuation using unattenuated optical lines and some random noise. Multi-dimensional analysis of optical emission line ratios does not give extra information about the environmental conditions of the SNR. Therefore, we propose to not blindly trust the optical line diagnostic as a probe for the environment near the SNR and as a classification tool for the SNRs.

Nevertheless, we can conclude that realistic modelling of the ISM is an essential component of SNR modelling. The density distribution at the explosion site will affect not only the attenuation of optical emission, but also the rate of evolution of the SNR. This leads to different amounts of optical emission throughout the simulations, as was shown for a single SNR in Paper I (Makarenko et al. 2023). Finally, the use of statistical analysis of a large dataset is necessary at present. This allows for a less biased assessment of the importance of different parameters (density distributions and magnetic field) on the optical emission of SNRs.

Acknowledgements. We thank the anonymous referee for constructive comments which helped us to improve the manuscript. E.I.M. S.W. and D.S. acknowledge the support of the Deutsche Forschungsgemeinschaft (DFG) via the Collaborative Research Center SFB 1601 'Habitats of massive stars across cosmic time' (subprojects B1, B4 and B5). The following PYTHON packages were used: NUMPY (Harris et al. 2020), SCIPY (Virtanen et al. 2020), MATPLOTLIB (Hunter 2007), YT (Turk et al. 2011), SCIKIT-LEARN (Pedregosa et al. 2011), PANDAS (McKinney et al. 2010).

References

Abdurro'uf, Accetta, K., Aerts, C., et al. 2022, ApJS, 259, 35
Aharonian, F. A., Akhperjanian, A. G., Aye, K. M., et al. 2004, Nature, 432, 75
Allen, M. G., Groves, B. A., Dopita, M. A., Sutherland, R. S., & Kewley, L. J. 2008, ApJS, 178, 20
Alsabti, A. W., Murdin, P. 2017, Handbook of Supernovae (Springer)
Anders, F., Chiappini, C., Santiago, B. X., et al. 2018, A&A, 619, A125
Baldwin, J. A., Phillips, M. M., & Terlevich, R. 1981, PASP, 93, 5
Borkowski, K. J., Lyerly, W. J., & Reynolds, S. P. 2001, ApJ, 548, 820
Boumis, P., Alikakos, J., Christopoulou, P. E., et al. 2008, A&A, 481, 705
Bressan, G., Barnaba, C., Peresan, A., & Rossi, G. 2021, Phys. Earth Planet. Interiors, 320, 106787
Cioffi D. F., M. C. F. B. E. 1988, ApJ, 334, 252
de Avillez, M. A., & Breitschwerdt, D. 2005, A&A, 436, 585
Draine, B. T. 2011, Physics of the Interstellar and Intergalactic Medium (Princeton Series in Astrophysics)
Einasto, M., Liivamägi, L. J., Saar, E., et al. 2011, A&A, 535, A36
Fesen R. A., Blair W. P., . K. R. P. 1985, ApJ, 292, 29
Fesen, R. A., Drechsler, M., Strottner, X., et al. 2024, arXiv e-prints [arXiv:2403.00317]
Fryxell, B., Olson, K., Ricker, P., et al. 2000, ApJS, 131, 273
Ganguly, S., Walch, S., Seifried, D., Clarke, S. D., & Weis, M. 2023, MNRAS, 525, 721
Gatto, A., Walch, S., Low, M. M. M., et al. 2015, MNRAS, 449, 1057
Girichidis, P., Walch, S., Naab, T., et al. 2016, MNRAS, 456, 3432
Green, D. A. 2019, J. Astrophys. Astron., 40, 36
Haid, S., Walch, S., Naab, T., et al. 2016, MNRAS, 460, 2962
Haid, S., Walch, S., Seifried, D., et al. 2019, MNRAS, 482, 4062
Harris, C. R., Millman, K. J., van der Walt, S. J., et al. 2020, Nature, 585, 357
Hartigan, J. A., & Wong, M. A. 1979, JSTOR: Appl. Statist., 28, 100
Hewitt, J. W., & Yusef-Zadeh, F. 2009, ApJ, 694, L16
Ho, I. T. 2019, MNRAS, 485, 3569
Hunter, J. D. 2007, Comput. Sci. Eng., 9, 90
Iffrig, O., & Hennebelle, P. 2015, A&A, 576, A95

Ji, X., & Yan, R. 2020, MNRAS, 499, 5749
Jiménez, S., Tenorio-Tagle, G., & Silich, S. 2019, MNRAS, 488, 978
Kauffmann, G., Heckman, T. M., Tremonti, C., et al. 2003, MNRAS, 346, 1055
Kavanagh, P. J., Sasaki, M., Points, S. D., et al. 2013, A&A, 549, A99
Kewley, L. J., Dopita, M. A., Sutherland, R. S., Heisler, C. A., & Trevena, J. 2001, ApJ, 556, 121
Kewley, L. J., Nicholls, D. C., Sutherland, R., et al. 2019, ApJ, 880, 16
Kopsacheili, M., Zezas, A., & Leonidaki, I. 2020, MNRAS, 491, 889
Lehmann, A., Federrath, C., & Wardle, M. 2016, MNRAS, 463, 1026
MacQueen, J. B. 1967, in Proceedings of the fifth Berkeley Symposium on Mathematical Statistics and Probability, 1, eds. L. M. L. Cam, & J. Neyman (University of California Press), 281
Makarenko, E. I., Walch, S., Clarke, S. D., & Seifried, D. 2020, in J. Phys. Conf. Ser., 1640, 012009
Makarenko, E. I., Walch, S., Clarke, S. D., et al. 2023, MNRAS, 523, 1421
Mavromatakis, F., Boumis, P., Papamastorakis, J., & Ventura, J. 2002, A&A, 388, 355
McKee, C. F., & Ostriker, J. P. 1997, ApJ, 218, 148
McKinney, W., et al. 2010, in Proceedings of the 9th Python in Science Conference, 445, Austin, TX, 51
Ostriker, J. P., & McKee, C. F. 1988, Rev. Mod. Phys., 60, 1
Padoan, P., & Nordlund, Å. 2011, ApJ, 730, 40
Pedregosa, F., Varoquaux, G., Gramfort, A., et al. 2011, J. Mach. Learn. Res., 12, 2825
Perryman, M. A. C., Lindegren, L., Kovalevsky, J., et al. 1997, A&A, 323, L49
Rhea, C., Rousseau-Nepton, L., Prunet, S., et al. 2021, ApJ, 923, 169
Robert, C., & Kennicutt, J. 1998, ApJ, 498, 541
Rubin, A., & Gal-Yam, A. 2016, ApJ, 828, 111
Sánchez Almeida, J., & Allende Prieto, C. 2013, ApJ, 763, 50
Sasaki, M., Pietsch, W., Haberl, F., et al. 2012, A&A, 544, A144
Sedov, L. I. 1959, Similarity and Dimensional Methods in Mechanics (Academic Press)
Seifried, D., Walch, S., Girichidis, P., et al. 2017, MNRAS, 472, 4797
Seifried, D., Walch, S., Haid, S., Girichidis, P., & Naab, T. 2018, ApJ, 855, 81
Slane, P., Bykov, A., Ellison, D. C., Dubner, G., & Castro, D. 2014, Space Sci. Rev., 188, 187
Smart, R. L., Sarro, L. M., Rybizki, J., et al. 2021, A&A, 649, A6
Smith, R. C., Kirshner, R. P., Blair, W. P., Long, K. S., & Winkler, P. F. 1993, ApJ, 407, 564
Stampoulis, V., van Dyk, D. A., Kashyap, V. L., & Zezas, A. 2019, MNRAS, 485, 1085
Sutherland, R. S., & Dopita, M. A. 2017, ApJS, 229, 34
Sutherland, R., Dopita, M., Binette, L., & Groves, B. 2018, MAPPINGS V: Astrophysical plasma modeling code, Astrophysics Source Code Library [record ascl:1807.005]
Thorndike, R. 1953, Psychometrika, 18, 267
Truelove, J. K., & McKee, C. F. 1999, ApJS, 120, 299
Turk, M. J., Smith, B. D., Oishi, J. S., et al. 2011, ApJS, 192, 9
Vink, J. 2012, A&A Rev., 20, 49
Virtanen, P., Gommers, R., Oliphant, T. E., et al. 2020, Nature Methods, 17, 261
Vogt, F. P. A., Dopita, M. A., Kewley, L. J., et al. 2014, ApJ, 793, 127
Walch, S., & Naab, T. 2015, MNRAS, 451, 2757
Walch, S., Girichidis, P., Naab, T., et al. 2015, MNRAS, 454, 246
Weingartner, J. C., & Draine, B. T. 2001, ApJ, 548, 296
York, D. G., Adelman, J., Anderson, John E., J., et al. 2000, AJ, 120, 1579
Zhang, D., & Chevalier, R. A. 2019, MNRAS, 482, 1602
Zhang, X., Feng, Y., Chen, H., & Yuan, Q. 2020, ApJ, 905, 97
Zhou, X., Su, Y., Yang, J., et al. 2023, ApJS, 268, 61

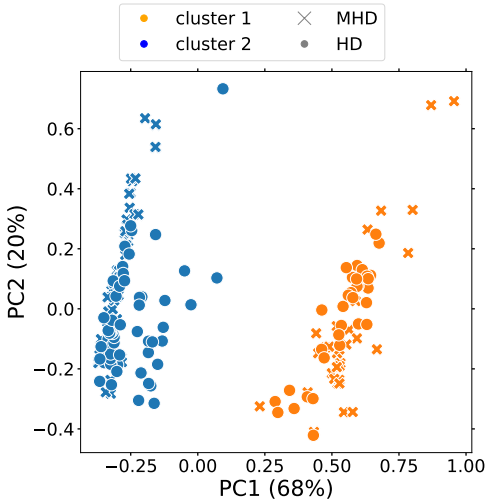

Fig. A.1: 'MHD25', 'MHD50', 'HD25', 'HD50' datasets (e.g. 'MC1$_{att}$') after using the PCA algorithm. 'MHD' simulations are marked with crosses, and 'HD' simulations with circles. The predicted clusters are marked with blue and orange. The higher the percentage for each PC the higher the relative variance in the dataset that is observed in the direction of the corresponding eigenvector (for the absolute values see Table 3). We use n_{clust} = 2 in the k-means algorithm. The data is clearly separated into two distinct clusters by distance: 25 pc and 50 pc (see Fig. 3), while MHD and HD labels are mixed.

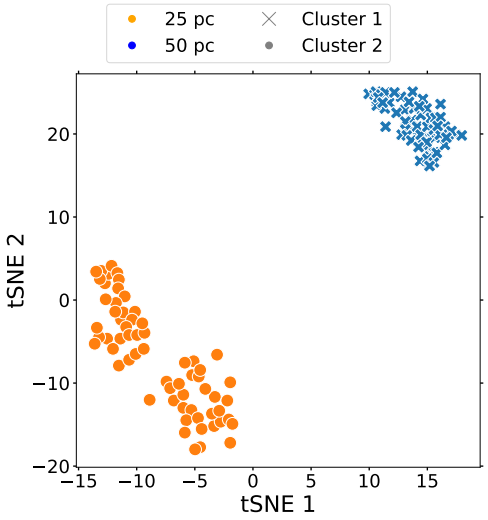

Fig. B.1: 'MHD25', 'MHD50', 'HD25', 'HD50' datasets (or 'MC1$_{att}$') after using the t-SNE algorithm. We use n_{clust} = 2 in the k-means algorithm. Even though three clusters can be visually distinguished, this separation is not related to the presence or absence of a magnetic field. It is also not related to other physical parameters that we might associate with each cluster. That is why, the data is separated into two distinct clusters as for the PCA algorithm for this dataset.

Appendix A: PCA analysis for MHD vs HD

In Fig. A.1 we present the results of the PCA algorithm for the whole dataset ('MC1$_{att}$') divided by k-means in two clusters (n$_{clust}$ = 2). We add labels to identify simulations with (MHD) and without magnetic field (HD). We note that the labels are not used in the PCA or k-means, we use them only to check the classification of the dataset. The data is clearly separated into two distinct clusters, but not by magnetic field presence (the colours do not match the shapes, as described in the figure caption). Therefore we can conclude that we can not distinguish between simulations with and without magnetic field. For the Rand index (see Fig. 5) it reaches a value of 0.5 which also means that the labels do not match the resulting clusters (for non-normalised Rand index).

Appendix B: t-SNE statistical analysis

Non-linear algorithms such as t-SNE for the dimension reduction of the dataset perform better than the linear ones (as PCA), especially for the preservation of local structures (e.g. clusters) of data. However, for our dataset, there was no difference between these algorithms. An example of t-SNE and k-means algorithm for the 'MC1$_{att}$' dataset is shown in Fig. B.1. We can define the same clusters as with the PCA algorithm in Fig. 3. Therefore, we use in this work PCA as it is computationally less expensive.

Appendix C: 3D representation of the statistical analysis (PCA)

In this work, we used a 2-D representation of the data after the PCA analysis (i.e. we took only the two most important components). Here we show the 3D distribution of the data (three PCs) in Fig. C.1. The third dimension contributes little to cluster classifications (only 10–13%). In addition, the third dimension is not helpful for better-separating points in space, therefore a 2D representation is optimal for the k-means clustering.

Appendix D: Sulphur BPT diagram with noise

To assess whether [S II](λ 6731)/Hα is reliable to identify different ambient density distributions at the SNR site, we plot the sulphur BPT diagram for the unattenuated optical emission lines with added random noise. Typically, [S II](λ 6731)/Hα is widely used to classify an object as an SNR as it is relatively strong and easy to observe. However, we found that attenuation plays an important role in this line ratio and can be confused with random noise as in the upper panel of Fig. D.1.

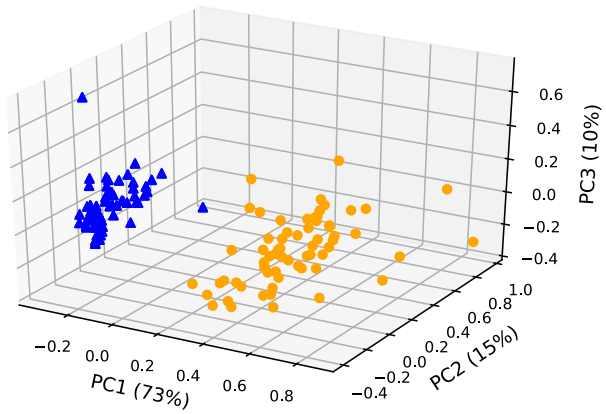

Fig. C.1: 3D representation of the data 'MHD25'+'HD25' (blue) and 'MHD50'+'HD50' (orange) after the PCA step. The predicted clusters are marked with circles and triangles. The contribution of each PC is as follows: 73% for PC1, 15% for PC2, and 10% for PC3. As in Fig. 3, we can still clearly see two clusters. However, visually, PC3 does not allow more efficient separation of clusters. Thus, in this work, 2D visualisation was mainly used (only the two PCs).

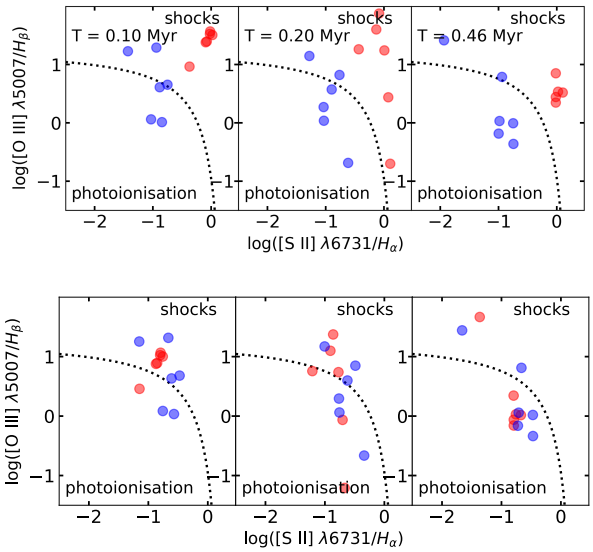

Fig. D.1: Sulphur BPT diagram for unattenuated line emission with added random noise. Colours are the same as in Fig. 6. On the lower panel, noise is higher than the real attenuation percentage (around 80% ± 10%, see Table 2). On the upper panel, noise is lower than the calculated attenuation (around 20% ± 10%). The upper panel's circles can be well separated during the whole time evolution (from left to right).

7

MODELLING THERMAL X-RAY EMISSION FROM RCW 103 (PAPER III)

Astronomy & Astrophysics manuscript no. output
January 20, 2026

Modelling thermal X-ray emission from RCW 103

E. I. Makarenko[1], B. Gaches[2], M. I. N. Kobayashi[1], J. Mackey[3], S. Walch[1]

[1] I. Physikalisches Institut, Universität zu Köln, Zülpicher Str. 77, D-50937 Köln, Germany
e-mail: makarenko@ph1.uni-koeln.de
[2] Faculty of Physics, University of Duisburg-Essen, Lotharstr. 1, Duisburg 47057, Germany
[3] Dublin Institute for Advanced Studies, Astronomy & Astrophysics Section, DIAS Dunsink Observatory, Dublin, D15 XR2R, Ireland

Received October 2025

ABSTRACT

Context. RCW 103 is a young, approximately 2000 years old, galactic supernova remnant (SNR), that has started interacting with the surrounding circumstellar medium. Observations have revealed that despite the non-uniform density distribution at the explosion site, the SNR exhibits an almost circular X-ray morphology.
Aims. In this work, we aim to model the X-ray emission from RCW 103 using 3D hydrodynamical simulations and explain the circular morphology.
Methods. Our model is the first implementation of radiative cooling emission from a SNR treated self-consistently on-the-fly in the ISM using the FLASH code. We calculate the emission and absorption using a backward ray tracing scheme where each cell within the SNR is treated as a source of radiation. We start with a uniform interstellar medium and form an HII region around a massive star (13 or 18 solar masses) with wind and ionising radiation feedback. At the end of the massive star's life, we explode a supernova (type II) and follow the radiative cooling emission in several X-ray energy bands (0.3 – 0.85 keV, 0.85 – 1.70 keV, 1.7 – 3.0 keV, and 3+ keV).
Results. We create synthetic maps of the simulated SNR RCW 103 that closely resemble the observed circular diffuse X-ray emission. The simulated emissions, particularly in the soft X-ray band (below 1.7 keV), arise from the swept-up mass in the wind bubble and its interaction with the SNR forward shock.

Key words. ISM: supernova remnants – Hydrodynamics – Radiation mechanisms: thermal – X-rays: individuals

1. Introduction

Massive stars (M > 8 $M_\odot$) exert substantial feedback during their lifetime through powerful stellar winds and ionising radiation (Weaver et al. 1977; Heger et al. 2003). This feedback shapes the surrounding circumstellar medium (CSM), resulting in complex density structures around the massive star, including cavities, shells, and clumps. Following the massive star core collapse and subsequent supernova (SN) explosion, the expanding shock wave interacts with the non-uniform CSM, generating shock fronts that compress and heat the surrounding material (Chevalier 1982; Blondin et al. 1998). The importance of radiative cooling at this stage cannot be underestimated. It plays a main role in regulating the temperature and dynamics of the post-shock material, influencing the evolution of the supernova remnant (SNR) (McKee & Ostriker 1977; Slane et al. 2016). SNRs produce emission across the whole electromagnetic spectrum, ranging from gamma rays to radio waves (Kavanagh et al. 2013; Brose et al. 2022), as the SNR evolves and propagates through the interstellar medium (ISM).

Diffuse X-ray emission in the ISM arises from a combination of high-energy processes. SN explosions and stellar winds from massive stars heat the surrounding gas to temperatures of 10^6 to 10^8 K, producing thermal X-ray emission as the gas cools (McKee & Ostriker 1977; Koyama et al. 1995). Additionally, fast electrons generated by these energetic events can induce a cascade of secondary ionisations, further contributing to the X-ray flux (Dalgarno & McCray 1972). Photoionisation, particularly in regions surrounding hot stars or compact objects, also plays a significant role, as high-energy photons ionise atoms and produce secondary X-ray emission (Kallman & McCray 1982; Grimes et al. 2005; Mineo et al. 2012b). Interactions between X-ray binaries and the ISM enhance the diffuse emission through scattering and reprocessing by interstellar dust and gas, resulting in a complex and spatially extended X-ray background (White et al. 1988; Mineo et al. 2012a; Lutovinov et al. 2013). These mechanisms shape the observed X-ray characteristics of the ISM. Approximately 300 supernova remnants (SNRs) have been detected in our galaxy, with around 40 per cent observed in the X-ray band (Green 2024). X-ray observations are crucial for identifying SNRs, as they are generally optically thin when there are no dense interstellar clouds or regions with higher column densities nearby. X-ray emission reveals the hot plasma state produced by the shock heating and provides insights into the dynamics of the remnants (Raymond & Smith 1977). This makes the X-ray band one of the primary methods for detecting and studying nearby SNRs, with high-resolution observations from telescopes like Chandra (for example, Hwang et al. (2004); Reynolds et al. (2007)), XMM-Newton (for example, Sasaki et al. (2004); Troja et al. (2006); Badenes et al. (2008)) and XRISM (XRISM Collaboration et al. 2024).

RCW 103 is a young (around 2000 years, Nugent et al. (1984); Carter et al. (1997)) Galactic SNR that has begun interacting with the surrounding CSM and a nearby molecular cloud (MC). The estimated distance to the SNR is around 3.1 kpc from the systemic velocity of the HI line (Reynoso et al. 2004). RCW

103 is approximately eight arcminutes in diameter. The angular size corresponds to a physical size of roughly 7.2 pcs across. RCW 103 is most probably a core-collapse SNR as it has a compact object 1E 161348–5055 with a hard X-ray point source emission inside (Tuohy & Garmire 1980). The progenitor mass of the SNR is still debated (either 18 $M_\odot$ from Frank et al. 2015, less than 18 $M_\odot$ from Zhou et al. 2019, 12-13 $M_\odot$ from Braun et al. 2019 or 10-12 $M_\odot$ from Narita et al. 2023). RCW 103 has been observed in gamma (Xing et al. 2014), X-ray (with Chandra, Frank et al. 2015; XMM-Newton, Narita et al. 2023), optical (various lines, Ruiz 1983; Hα, Russeil et al. 2005), IR (Oliva et al. 1990; Chawner et al. 2020), and radio (Caswell et al. 1980) bands. Despite the SNR having a non-uniform density distribution at the site of the explosion (Paron et al. 2006), the X-ray morphology is almost circular.

In this paper, we model the X-ray emission from RCW 103 using 3D radiative hydrodynamical simulations. Using the magnetohydrodynamic code FLASH, our model is one of the first implementations of radiative cooling emission in the X-ray band from a SNR treated self-consistently on the fly. We calculate the emission and absorption on the fly using a backward ray tracing scheme TreeRay/XrayTheSpot, and each cell within the SNR is treated as a radiation source. We start with a uniform ISM and form an HII region around a massive star (13 or 18 $M_\odot$) with ionising radiation feedback and wind. At the end of the massive star's life, we explode the SN (type II) and follow the radiative cooling emission in several X-ray energy bands (similar to Chandra: 0.1 – 0.3 keV, 0.3 – 0.85 keV, 0.85 – 1.70 keV, 1.7 – 3.0 keV, and 3+ keV). We observe how the shock evolves, starting to interact with the CSM material. We created synthetic maps of the simulated SNR to reveal the origin and evolution of the circular diffuse X-ray emission. The description of the numerical method and initial condition of simulations are given in Section 2, the results are presented in Section 3, and we discuss possible caveats of the model with the feasibility of improvement in Section 4. The conclusions are presented in Section 5.

2. Numerical methods

We use the adaptive mesh refinement, hydrodynamic code FLASH (Fryxell et al. 2000) for our RCW 103 simulations. The modification of the Chemistry module allows us to calculate the cooling energy in different energy bands (user-defined) from extended sources (in our case, SNRs). We calculate the emission and absorption on the fly using backward ray tracing with TreeRay/XrayTheSpot module (Wünsch et al. 2021; Gaches et al. 2023) using every cell as a radiation source. It is coupled to the Chemistry non-equilibrium network (Nelson & Langer 1999), where we updated parts of the radiative cooling for metals and helium. We explain the details in Section 2.4 and Appendix A.

2.1. Initial conditions

As we know from various observations (see Table 1), RCW 103 has a physical size of approximately 7.2 pc at a distance of 3.1 pc. The ISM surrounding RCW 103 exhibits a complex structure characterised by interactions between the remnant's shock front and a MC. Paron et al. (2006) detected HCO^+ and ^{12}CO emissions near the southern boundary of RCW 103, indicating dense molecular material interacting with the remnant. Notably, a depletion of HCO^+ was observed behind the shock front, suggesting chemical changes due to shock interactions. Additionally, no atomic hydrogen (HI) emission was detected where the molecular gas was observed. Westerlund (1969) identified OB stars in the vicinity of RCW 103, implying that the region's stellar population may have influenced the local ISM density and composition before the SN event. While specific density measurements are not defined in these studies, the presence of molecular emissions and massive stars suggests regions of elevated density within the surrounding medium.

Due to that, the simulations in this paper were performed with a uniform density medium with a higher than average ambient density (100 cm^{-3}). As soon as we know the morphology of the remnant in this simple case, we can also add turbulence, a clump of molecular gas or a density gradient of the ambient medium. This approach allows us to disentangle the environmental effects influencing the synthetic X-ray morphology.

2.2. Radiatve transfer, ionising radiation and stellar wind

The TreeRay radiative transfer scheme from Wünsch et al. (2018) calculates radiation transport using a hierarchical octal tree structure to group cells and efficiently store/determine radiation fluxes. The scheme combines the tree-based algorithm with a backward integration method, where rays trace the radiation sources through the computational domain. It accounts for the absorption and emission properties of the medium by summing contributions along the rays. TreeRay consists of a general part and submodules to treat different physical processes needed to solve the radiation transport equation.

For accounting of attenuation we use the submodule TreeRay/OpticalDepth (Wünsch et al. 2018) where contributions from different directions is summed to obtain the corresponding optical depths instead of solving the radiation transport equation. This module is nessesary to include when using the Chemsitry module, described in Section 2.3.

We use the TreeRay/OnTheSpot submodule (Wünsch et al. 2021) for treating the interaction of ionising radiation from massive stars with the ISM. It uses an on-the-spot approximation from Osterbrock (1988), e.g. recombinations are exactly balanced by photoionisation or immediate local absorption of ionising photons, simplifying the treatment of diffuse radiation. It employs a tree-based structure to calculate radiation fluxes, allowing for computational efficiency. The ionising radiation is treated using a ray-tracing algorithm, employing HEALPix spheres (Górski et al. 2005) to discretise the angular distribution of rays. This approach ensures uniform coverage of the radiation field. Each ray is integrated step-by-step through the medium, computing the ionisation balance and energy deposition. For more technical details and benchmark tests, see Wünsch et al. (2021).

To simulate the stellar wind, we inject mass and energy in a sphere around the sink particle (representing a massive star). With a mass loss rate and a terminal wind velocity (see Figure 1) from the tabulated stellar tracks (Ekström et al. 2012), we can calculate the total mass injected by the wind to the ISM normalised by the volume of injection. Then, we rescale the velocity field according to the change in mass to conserve the momentum and the internal energy to conserve the total energy. In this work, we use a momentum injection scheme for the wind. The mass of the star (sink particle) is updated at each time step, subtracting the mass loss rate. At the last time, step, right before the SN explosion, the sink particle is removed from the simulation domain, and the rest of the mass will be injected within the injection radius of the SN. For more details and formulas, see Gatto et al. (2017).

Table 1. Overview of the observed parameters of the RCW 103 SNR.

Age	2000 yr (Carter et al. 1997)
Distance	3.1 kpc (Reynoso et al. 2004)
Progenitor	10 – 18 $M_\odot$ Frank et al. (2015); Braun et al. (2019); Zhou et al. (2019); Narita et al. (2023)
Size	8' (or around 7.2 – 10 pc across)
Detected in:	radio, IR, optical, X-ray (Chandra, XMM-Newton), gamma

Table 2. Summary of the simulation runs (column 1) for different masses of progenitor stars (column 2), including ionising radiation and stellar wind feedback. The table lists the ionising photon production rate (column 5), ambient density of the medium (column 6) , and the evolution time until core-collapse SN event and beyond (column 7)

Simulation run	Progenitor star $M_\odot$	Ionising radiation	Stellar wind	Q [photons/s]	n [cm^{-3}]	Evolution time Myr
13IonWind	13	✓	✓	2.2×10^{48}	100	18.9
18IonWind	18	✓	✓	2.8×10^{47}	100	11.9

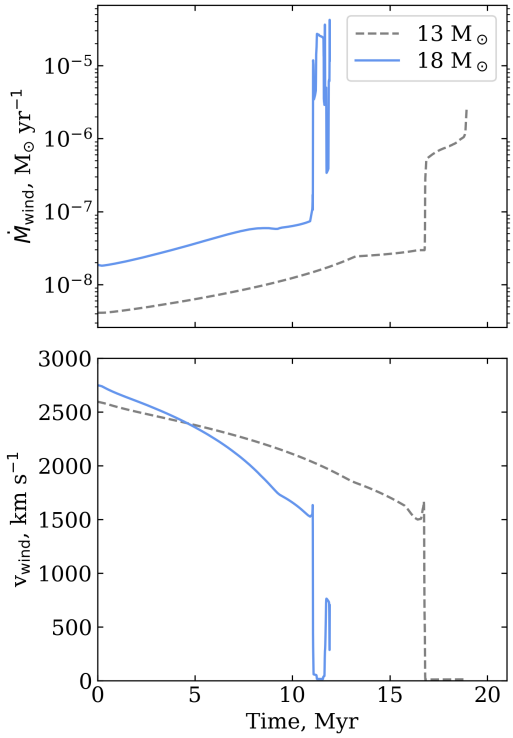

Fig. 1. Mass-loss rates for the stellar winds (top panel) and stellar wind terminal velocities (bottom panel) for 13 $M_\odot$ and 18 $M_\odot$ stars. The stellar feedback lasts longer for the less massive star (roughly 20 Myr, grey line) comparing to 12 Myr (blue line), but the mass loss rate is higher for a 18 $M_\odot$ star (blue line).

2.3. Chemistry

In this work we use a chemical network that consists of 17 species, of which 9 are solved numerically, the so-called the NL99 network (Glover & Clark 2012). The rest of the species are calculated through conservation equations. It consists of a model for hydrogen chemistry (Glover & Mac Low 2007a,b) and a model for CO chemistry (Nelson & Langer 1999) with updated reaction rates from Gong et al. (2017). For more details about the network or how the X-ray radiation is coupled to the chemistry, see Mackey et al. (2019) and Gaches et al. (2023).

2.4. Radiative cooling

To compute the radiative cooling rate of gas in the temperature range of 10^4 K to 10^8 K, we utilise pre-tabulated cooling tables. The Chemistry module uses these tables to interpolate the cooling rate based on local gas properties, including temperature and metallicity. This approach ensures that the cooling rate dynamically adjusts as the gas properties evolve over time.

In this study, we replaced the precomputed tables in the Chemistry module for helium (He) and for metals (elements between Li and Zn, in collisional ionisation equilibrium (CIE), excluding contributions from hydrogen and helium; see Gnat & Ferland (2012)). We adopted elemental abundances from Sembach et al. (2000), as these are consistent with the metallicities typically used in our FLASH simulations, particularly in the SILCC project (Walch et al. 2015; Girichidis et al. 2016; Gatto et al. 2017; Peters et al. 2017; Girichidis et al. 2018; Rathjen et al. 2021). These abundances correspond to solar metallicity in the warm ionised medium (WIM). A comparison between the old and new cooling curves is presented in Fig. A.1. The primary difference in the cooling rates arises from using different versions of the atomic database CHIANTI. Although the difference in the treatment of CIE gas between the CLOUDY version (utilised in the old precomputed tables) and MAPPINGS is minor, the latest release of the CLOUDY code (Gunasekera et al. 2023) incorporates the most up-to-date atomic data. However, it is important to note that this updated cooling curve was not employed in the earlier simulations.

In addition to the updated tables, we can now record the amount of cooling energy in each energy band (user-defined, from 0 to 12 keV) in each time step. For that, we would need to include $i + 1$ new field variables: i for energy bins and one for the total cooling energy. This will help us include self-consistent radiative cooling in the full radiative transfer scheme as the cooling can be passed to the radiative transfer module.

The cooling energy of a band i, E^i_{rc}, is the difference between the initial, $E_{int,init}$, and the final internal energy of the gas, $E_{int,fin}$, each multiplied by a temperature dependent band fraction f^i. Therefore, to calculate the radiative cooling in a specific energy band, we determine the field variable following:

$$E^i_{rc} = f^i_{init} E_{int,init} - f^i_{fin} E_{int,fin}. \quad (1)$$

The new variable generally follows the same evolution as the total energy in Chemistry module. The energy calculation is done for each user-defined energy bin and thus requires as many field variables as energy bins (for X-ray energy bands, see Fig. 2). In that case, we first need to define the energy fraction corresponding to a specific band. We generate a look-up table with MAPPINGS V for the CIE plasma with pre-defined bands. This table contains for each temperature the total cooling rate as well as the cooling rate for each of the bands. The fractions f^i are derived from the ratio between the band to the total cooling rate. To determine the cooling rate for any gas temperature we use a cubic interpolation scheme.

2.5. X-ray emission

The XRayTheSpot module, developed by Gaches et al. (2023) for the FLASH code, introduces a technical framework to model X-ray radiation in the ISM with energies ranging from 0.1 to 10 keV. Its primary advantage is incorporating temperature-dependent cross-sections for photoionisation and Compton scattering. It significantly improves accuracy over earlier models that relied on fixed cross-sections for cold, neutral gas at solar metallicity. This approach accounts for collisional ionisation equilibrium, with ionisation fractions calculated using the ChiantiPy atomic database. The method ensures precise treatment of metals' contribution to photoionisation and the temperature dependence of Compton scattering, which becomes critical at high energies. For example, at temperatures exceeding 10^5 K, reduced cross-sections enhance the gas's optical transparency to X-rays, enabling better heating and radiation escape modelling.

XRayTheSpot is a part of the radiative backwards ray-tracing module TreeRay (Wünsch et al. 2018, 2021). It employs the Barnes-Hut multipole acceptance criterion for accurately mapping gas cells to evaluation points along the rays, allowing it to resolve localised and diffuse X-ray sources effectively. This detailed treatment enhances the accuracy of synthetic X-ray maps and provides insights into feedback mechanisms driven by X-ray radiation in dense star-forming regions and evolved SNRs.

In this paper, we would use the TreeRay/XRayTheSpot in combination with Chemistry to calculate the radiative cooling self-consistently from each cell of the simulated SNR in a specific X-ray energy band.

2.6. Simulation setup

To simulate RCW 103, we begin with a uniform density box, where the box has a side of 15 pc with sub-pc resolution (typically around 0.1 - 0.65 pc). We introduce a sink particle at the centre of the box, representing a massive star that evolves from the zero-age main sequence (ZAMS) to the supernova phase (according to the stellar tracks from Ekström et al. 2012, detailed description of implementation in the code see in Gatto et al. 2017). During the main-sequence phase, we apply ionising radiation and stellar wind feedback, which forms a bubble with a radius of approximately 10 pc, consistent with the expected SNR size interacting with the CSM and we use an upper limit for the timestep of around 1 kyr. As the star reaches the SN stage, it explodes, initiating shock interactions with the surrounding CSM. At this point, we decrease the simulation timestep to 200 years to capture the evolution of X-ray emissions at various stages of the SNR expansion.

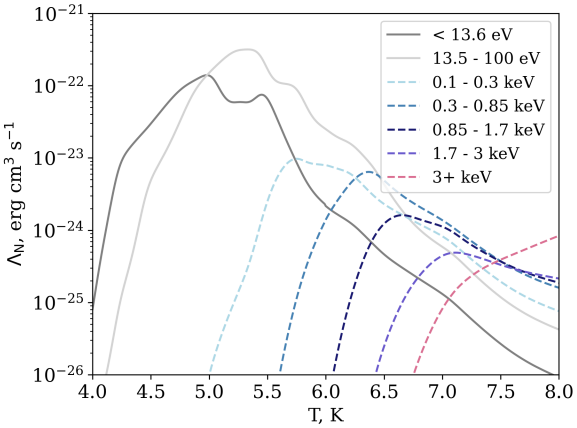

Fig. 2. Split cooling curve for metals (all elements, apart from H and He are included) generated with CIE model with MAPPINGS V into energy bands: 0 – 13.6 eV, 13.6 – 100 eV and five X-ray energy bands (mock Chandra bands for RCW 103).

3. Results

3.1. 3D Sedov test

We use the 3D Sedov explosion problem (Sedov 1959), a standard numerical benchmark for testing hydrodynamic solvers to simulate the SN. This model is based on the analytical solution for an explosion in a uniform medium, where 10^{51} erg of energy is released, generating a spherical shock wave that evolves self-similarly. Our simulation domain is $(80\ \mathrm{pc})^3$ with isolated boundaries and a maximum resolution of 0.65 pc, sufficient to resolve the blast wave. The injection radius is set to 4.2 cells, following Gatto et al. (2015). Initial ambient conditions vary from $n = 0.1\,\mathrm{cm}^{-3}$ to $n = 100\,\mathrm{cm}^{-3}$ and temperatures of 10500 K to 54 K, covering both diffuse ISM and dense medium regimes.

First, to study energy redistribution across cooling bands, we split the cooling into optical (0 – 13.6 eV), UV (13.6 – 100 eV), and X-ray (100+ eV) components. The results are shown in Figures B.1, B.2. In our simulations we find distinct cooling patterns: with high density ($n = 100\ \mathrm{cm}^{-3}$, $T = 54$ K), cooling is dominated by the optical band, with emission peaking in the shocked shell at late times ($t > 5$ kyr). UV emission forms a sharp shell, while X-ray emission is confined to the hot, central region, diminishing over time as the remnant cools. Conversely, in low-density environments ($n = 0.1\,\mathrm{cm}^{-3}$), $T = 10500$ K), X-ray emission is weak, reflecting inefficient cooling. Optical and UV emissions are more sustained, with the UV band peaking later as higher-energy photons are produced during the remnant's evolution.

Second, we include X-ray cooling in radiative transfer simulations using XRayTheSpot. It introduces additional heating mechanisms, such as photoionisation and Compton scattering, which slow the loss of internal energy. The results are shown in Figure B.3. These effects are more prominent in dense media, where frequent interactions enhance energy deposition and reduce cooling efficiency. X-ray processes also promote ionisation, redistributing energy from high-energy bands to lower-energy photons via secondary ionisations. This results in higher energy deposition in the optical/FUV band (0 – 13.6 eV), which affects the cooling dynamics and changes the energy evolution. These findings fit well with observed SNR morphologies.

3.2. Morphology of the synthetic X-ray observations of RCW 103

In Fig. 3 we show the X-ray emission of the simulated SNR at two times, 1352 yr (top row) and 2000 yr (bottom row), for our different energy bands. The simulated morphology shares similarities with the observed X-ray structure of RCW 103, particularly the brighter, flatter southeastern shell. Both exhibit asymmetry, likely resulting from interactions between the supernova shock and a non-uniform CSM. However, differences in finer structural details and brightness distributions may arise from limitations in modelling certain physical processes, or discrepancies in the initial CSM conditions, such as density gradients and magnetic fields. Additionally, the high-energy X-ray emission (above 3 keV) interacts minimally with the ISM, largely escaping the simulation box without significant interaction due to low cross-section (Gaches et al. 2023). In contrast, the soft X-ray emission (below 1 keV) is strongly affected by the surrounding density structures of the CSM. These softer X-rays display brighter regions where the plasma has cooled slightly, resulting in a more complex and dynamic emission pattern that traces the detailed morphology of the CSM.

Varying the initial mass of the progenitor star (e.g., 13 or 18 $M_{\odot}$) mainly affects the total time of the simulations and has only a minor impact on the size of the wind bubble. Consequently, distinguishing the progenitor mass of RCW 103 based solely on the wind bubble's morphology is not feasible without tracing the elemental enrichment from the supernova explosion.

We are currently running a higher-resolution run with a smaller simulation box and lower density to resolve the wind from the massive star and fit it exactly to the observed radius of RCW 103.

If we compare the observed X-ray fluxes for RCW 103: 1.8 $\times$ 10^{-10} ergs cm^{-2} s^{-1} (0.6 keV to 2.0 keV) for ROSAT and our synthetic observations are not that far off: for 2000 yr we get unattenuated total flux of 3.6 $\times$ 10^{-9} ergs cm^{-2} s^{-1} in the band of 0.1 - 3 keV. We can achieve around the same fluxes by adding some attenuation at one of the rims of the SNR (similar to observations) and trying to include instrument effects.

4. Discussion

4.1. Evolution of the massive star

To capture the correct X-ray morphology of the SNR, we need to have accurate pre-SN feedback. The stellar evolution models used in this paper, presented by (Ekström et al. 2012), include key processes such as rotation and mass loss to simulate the development of stars across a broad mass range. However, some aspects of stellar evolution, particularly regarding stellar winds, are either simplified or omitted. One significant omission is the role of magnetic fields, which are not accounted for in the models. Magnetic fields can substantially impact stellar winds, channelling them and influencing angular momentum loss. This can alter mass-loss rates and affect the further evolution of massive stars. The representation of late-stage mass-loss processes (during the red supergiant or luminous blue variable phases) is also limited. These stages often involve episodic and enhanced mass loss, which can significantly alter a star's subsequent evolution. Addressing these aspects in future models would improve the understanding of the role of stellar winds in stellar evolution and lead to more accurate predictions.

4.2. Magnetic field

Including magnetic fields in the SNR, simulations can significantly change the remnant's morphology, often leading to pronounced asymmetries. MHD simulations have demonstrated that ambient magnetic fields can distort the expansion of SNRs, resulting in non-spherical shapes. For instance, studies have shown that gradients in ambient magnetic field strength can produce asymmetric bilateral SNRs, with differing brightness levels in the radio limbs depending on the observer's line of sight (Orlando et al. 2007). Additionally, simulations indicate that the presence of a uniform magnetic field can lead to the development of tubular or rectangular structures in SNRs, as the magnetic pressure influences the shock wave propagation (Meyer et al. 2022). Therefore, accurately modelling magnetic fields is essential for interpreting the thermal X-ray characteristics of SNRs. The magnetic fields can be included in future SNR simulations.

4.3. Thermal conduction

Thermal conduction is an essential physical process for modelling the SNRs' X-ray emission. It affects the temperature distribution, density structure, and evolution of the hot, shocked gas in the remnant. Thermal conduction smooths sharp temperature gradients by transferring heat from the hot interior to cooler regions (Guo et al. 2024). The X-ray emission depends strongly on the temperature of the gas. Smoothing the temperature gradients changes the proportion of gas emitting in different X-ray energy bands. It also helps maintain a more stable temperature by redistributing the heat, delaying or suppressing rapid cooling in localised regions (Slavin et al. 2017).

However, thermal conduction can be suppressed a lot in regions with tangled magnetic fields, which reduce the effective heat transport perpendicular to field lines which will occur near the shock front/shell of the SNR (see the example in 2.5D simulations in Orlando et al. (2008)). In this case, the magnetic field should also be included to consider thermal conduction correctly. This simulation can be planned, but anisotropic thermal conduction will require further code development.

4.4. Cosmic rays

Incorporating accurate cosmic ray (CR) injection at the shock front of a SNR can significantly influence its X-ray morphology. Efficient CR acceleration alters the shock dynamics, resulting in higher compression ratios and lower post-shock temperatures. However, the primary impact is on non-thermal X-ray emission rather than thermal X-rays. For example, the absence of observational evidence for shell formation strongly suggests that non-thermal pressures from CRs play a crucial dynamical role in the late-stage evolution of SNRs (Diesing & Gupta 2024). Thermal X-ray emission may be reduced as a significant fraction of the shock energy is diverted into accelerating CRs rather than heating the plasma (Helder et al. 2009). Thought, this typically includes only about 10% of the injected SN energy (Habegger & Zweibel 2024). Regions typically exhibiting bright thermal X-ray emission might thus appear dimmer in observations. For instance, studies of SNR RX J1713.7-3946 (Berezhko & Völk 2010) have shown that efficient CR acceleration can explain the observed deficiency in thermal X-rays, with the remnant's emission dominated by non-thermal synchrotron radiation from high-energy electrons.

While modelling CR injection is essential for understanding the overall dynamics, shock physics and non-thermal X-ray

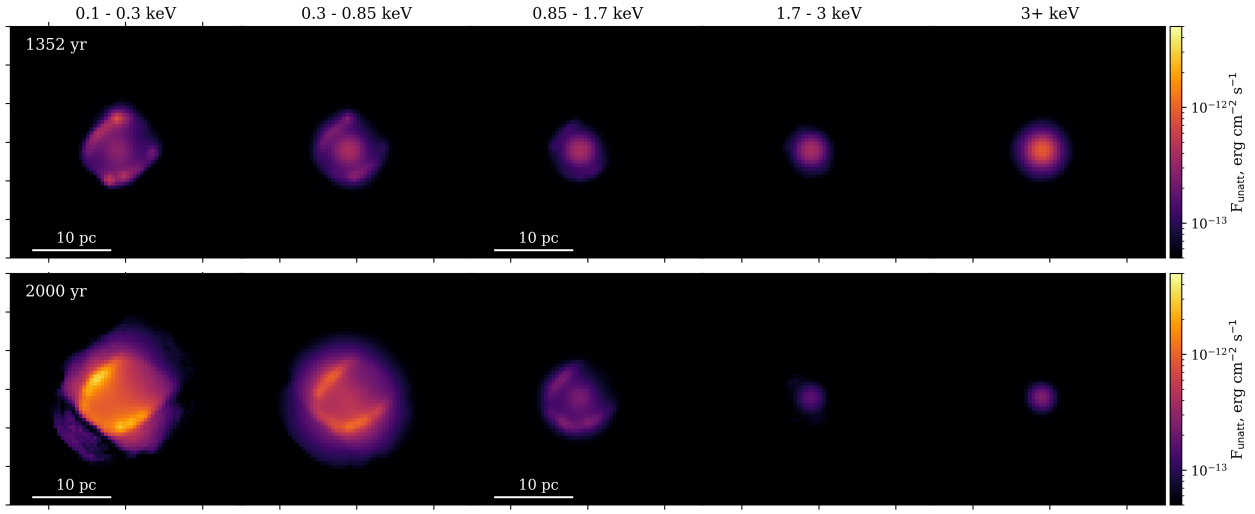

Fig. 3. Slices of the X-ray emission from a simulated 18 $M_\odot$ SNR at 1352 yr (top row) and 2000 yr (bottom row) post-explosion for different energy bands (0.1 – 0.3, 0.3 – 0.85, 0.85 – 1.7, 1.7 – 3 keV, and 3+ keV). The asymmetric shape arises due to stellar wind feedback and ionising radiation, which sculpted the CSM prior to the SN explosion. Brighter regions in the energy range 0.1 – 1.7 keV correspond to areas of swept-up dense material shaped by the stellar wind.

emission, it is less critical for interpreting the thermal X-ray morphology of SNRs.

5. Conclusions

In this paper, we used the first implementation of radiative cooling in the X-ray energy bands (from 0.1 keV to 10 keV), calculated on-the-fly within FLASH simulations of RCW 103. We explored the formation of the circular X-ray morphology of RCW 103 based on three-dimensional hydrodynamic simulations. Our findings show that considering the pre-SN feedback, particularly stellar wind, is crucial. The shell from the stellar wind becomes brighter in the soft X-ray band (0.1–1.7 keV). At the same time, the bubble's interior remains luminous only briefly in the higher energy band (1.7+ keV) at the beginning of the SNR's evolution.

Despite the complex environment near the OB association, we propose that the primary features of the X-ray morphology result from the interaction between the forward shock and the wind bubble. The SNR structure exhibits asymmetry, likely due to a nearby molecular cloud or turbulence, typical for massive star-forming regions. In such cases, the stellar wind bubble may be distorted, leading only to bright emission along certain edges. This effect was observed in low-resolution simulations, where the wind was poorly resolved, preventing the appearance of symmetric X-ray emission. Chandra images reveal that RCW 103 has two hemispheres with differing radii in the northwest and southeast directions. Overall, our simulations can reproduce key features of the RCW 103 SNR X-ray morphology well. However, higher-resolution simulations and a more detailed treatment of the surrounding ISM (including turbulence and nearby molecular gas) are necessary. These aspects will be explored in future work.

Acknowledgements. E.I.M. and S.W. acknowledge the support of the Deutsche Forschungsgemeinschaft (DFG) via the Collaborative Research Center SFB 1601 'Habitats of massive stars across cosmic time' (subproject B5). The following Python packages were used: NumPy (Harris et al. 2020), Matplotlib (Hunter 2007), YT (Turk et al. 2011).

References

Badenes, C., Hughes, J. P., Cassam-Chenaï, G., & Bravo, E. 2008, ApJ, 680, 1149
Berezhko, E. G. & Völk, H. J. 2010, A&A, 511, A34
Binette, L., Dopita, M. A., & Tuohy, I. R. 1985, ApJ, 297, 476
Blondin, J. M., Wright, E. B., Borkowski, K. J., & Reynolds, S. P. 1998, ApJ, 500, 342
Braun, C., Safi-Harb, S., & Fryer, C. L. 2019, MNRAS, 489, 4444
Brose, R., Sushch, I., & Mackey, J. 2022, MNRAS, 516, 492
Carter, L. M., Dickel, J. R., & Bomans, D. J. 1997, PASP, 109, 990
Caswell, J. L., Haynes, R. F., Milne, D. K., & Wellington, K. J. 1980, MNRAS, 190, 881
Chawner, H., Gomez, H. L., Matsuura, M., et al. 2020, MNRAS, 493, 2706
Chevalier, R. A. 1982, ApJ, 259, 302
Dalgarno, A. & McCray, R. A. 1972, ARA&A, 10, 375
Del Zanna, G., Dere, K. P., Young, P. R., Landi, E., & Mason, H. E. 2015, A&A, 582, A56
Dere, K. P., Landi, E., Mason, H. E., Monsignori Fossi, B. C., & Young, P. R. 1997, A&AS, 125, 149
Diesing, R. & Gupta, S. 2024, arXiv e-prints, arXiv:2411.18679
Dopita, M. A. & Sutherland, R. S. 2000, ApJ, 539, 742
Dopita, M. A., Sutherland, R. S., Nicholls, D. C., Kewley, L. J., & Vogt, F. P. A. 2013, ApJS, 208, 10
Ekström, S., Georgy, C., Eggenberger, P., et al. 2012, A&A, 537, A146
Frank, K. A., Burrows, D. N., & Park, S. 2015, ApJ, 810, 113
Fryxell, B., Olson, K., Ricker, P., et al. 2000, ApJS, 131, 273
Gaches, B. A. L., Walch, S., Wünsch, R., & Mackey, J. 2023, MNRAS, 522, 4674
Gatto, A., Walch, S., Low, M. M. M., et al. 2015, MNRAS, 449, 1057
Gatto, A., Walch, S., Naab, T., et al. 2017, MNRAS, 466, 1903
Girichidis, P., Seifried, D., Naab, T., et al. 2018, MNRAS, 480, 3511
Girichidis, P., Walch, S., Naab, T., et al. 2016, MNRAS, 456, 3432
Glover, S. C. O. & Clark, P. C. 2012, MNRAS, 421, 9
Glover, S. C. O. & Mac Low, M.-M. 2007a, ApJS, 169, 239
Glover, S. C. O. & Mac Low, M.-M. 2007b, ApJ, 659, 1317
Gnat, O. & Ferland, G. J. 2012, ApJS, 199, 20
Gong, M., Ostriker, E. C., & Wolfire, M. G. 2017, ApJ, 843, 38
Górski, K. M., Hivon, E., Banday, A. J., et al. 2005, ApJ, 622, 759
Green, D. A. 2024, arXiv e-prints, arXiv:2411.03367
Grimes, J. P., Heckman, T., Strickland, D., & Ptak, A. 2005, ApJ, 628, 187
Gunasekera, C. M., van Hoof, P. A. M., Chatzikos, M., & Ferland, G. J. 2023, Research Notes of the American Astronomical Society, 7, 246
Guo, M., Kim, C.-G., & Stone, J. M. 2024, arXiv e-prints, arXiv:2411.12809
Habegger, R. & Zweibel, E. G. 2024, arXiv e-prints, arXiv:2412.12249
Haid, S., Walch, S., Naab, T., et al. 2016, MNRAS, 460, 2962
Harris, C. R., Millman, K. J., van der Walt, S. J., et al. 2020, Nature, 585, 357

Heger, A., Fryer, C. L., Woosley, S. E., Langer, N., & Hartmann, D. H. 2003, ApJ, 591, 288
Helder, E. A., Vink, J., Bassa, C. G., et al. 2009, Science, 325, 719
Hunter, J. D. 2007, Computing in Science and Engineering, 9, 90
Hwang, U., Laming, J. M., Badenes, C., et al. 2004, ApJ, 615, L117
Kallman, T. R. & McCray, R. 1982, ApJS, 50, 263
Kavanagh, P. J., Sasaki, M., Points, S. D., et al. 2013, A&A, 549, A99
Koyama, K., Petre, R., Gotthelf, E. V., et al. 1995, Nature, 378, 255
Lutovinov, A. A., Revnivtsev, M. G., Tsygankov, S. S., & Krivonos, R. A. 2013, MNRAS, 431, 327
Mackey, J., Walch, S., Seifried, D., et al. 2019, MNRAS, 486, 1094
McKee, C. F. & Ostriker, J. P. 1977, ApJ, 218, 148
Meyer, D. M. A., Velázquez, P. F., Petruk, O., et al. 2022, MNRAS, 515, 594
Mineo, S., Gilfanov, M., & Sunyaev, R. 2012a, MNRAS, 419, 2095
Mineo, S., Gilfanov, M., & Sunyaev, R. 2012b, MNRAS, 426, 1870
Narita, T., Uchida, H., Yoshida, T., Tanaka, T., & Tsuru, T. G. 2023, ApJ, 950, 137
Nelson, R. P. & Langer, W. D. 1999, ApJ, 524, 923
Nugent, J. J., Pravdo, S. H., Garmire, G. P., et al. 1984, ApJ, 284, 612
Oliva, E., Moorwood, A. F. M., & Danziger, I. J. 1990, A&A, 240, 453
Orlando, S., Bocchino, F., Reale, F., Peres, G., & Pagano, P. 2008, ApJ, 678, 274
Orlando, S., Bocchino, F., Reale, F., Peres, G., & Petruk, O. 2007, A&A, 470, 927
Osterbrock, D. E. 1988, PASP, 100, 412
Paron, S. A., Reynoso, E. M., Purcell, C., Dubner, G. M., & Green, A. 2006, PASA, 23, 69
Peters, T., Naab, T., Walch, S., et al. 2017, MNRAS, 466, 3293
Rathjen, T.-E., Naab, T., Girichidis, P., et al. 2021, MNRAS, 504, 1039
Raymond, J. C. & Smith, B. W. 1977, ApJS, 35, 419
Reynolds, S. P., Borkowski, K. J., Hwang, U., et al. 2007, ApJ, 668, L135
Reynoso, E. M., Green, A. J., Johnston, S., et al. 2004, PASA, 21, 82
Ruiz, M. T. 1983, AJ, 88, 1210
Russeil, D., Adami, C., Amram, P., et al. 2005, A&A, 429, 497
Sasaki, M., Plucinsky, P. P., Gaetz, T. J., et al. 2004, ApJ, 617, 322
Sedov, L. I. 1959, Similarity and Dimensional Methods in Mechanics
Sembach, K. R., Howk, J. C., Ryans, R. S. I., & Keenan, F. P. 2000, ApJ, 528, 310
Slane, P., Bykov, A., Ellison, D. C., Dubner, G., & Castro, D. 2016, in Multi-scale Structure Formation and Dynamics in Cosmic Plasmas, ed. A. Balogh, A. Bykov, J. Eastwood, & J. Kaastra, Vol. 51, 187
Slavin, J. D., Smith, R. K., Foster, A., et al. 2017, ApJ, 846, 77
Sutherland, R. S. & Dopita, M. A. 1993, ApJS, 88, 253
Sutherland, R. S. & Dopita, M. A. 2017, ApJS, 229, 34
Troja, E., Bocchino, F., & Reale, F. 2006, ApJ, 649, 258
Tuohy, I. & Garmire, G. 1980, ApJ, 239, L107
Turk, M. J., Smith, B. D., Oishi, J. S., et al. 2011, The Astrophysical Journal Supplement Series, 192, 9
Walch, S., Girichidis, P., Naab, T., et al. 2015, MNRAS, 454, 238
Weaver, R., McCray, R., Castor, J., Shapiro, P., & Moore, R. 1977, ApJ, 218, 377
Westerlund, B. E. 1969, AJ, 74, 882
White, N. E., Stella, L., & Parmar, A. N. 1988, ApJ, 324, 363
Wünsch, R., Walch, S., Dinnbier, F., et al. 2021, MNRAS, 505, 3730
Wünsch, R., Walch, S., Dinnbier, F., & Whitworth, A. 2018, MNRAS, 475, 3393
Xing, Y., Wang, Z., Zhang, X., & Chen, Y. 2014, ApJ, 781, 64
XRISM Collaboration, Audard, M., Awaki, H., et al. 2024, PASJ[arXiv:2408.14301]
Young, P. R., Landi, E., & Thomas, R. J. 1998, A&A, 329, 291
Zhou, P., Vink, J., Safi-Harb, S., & Miceli, M. 2019, A&A, 629, A51

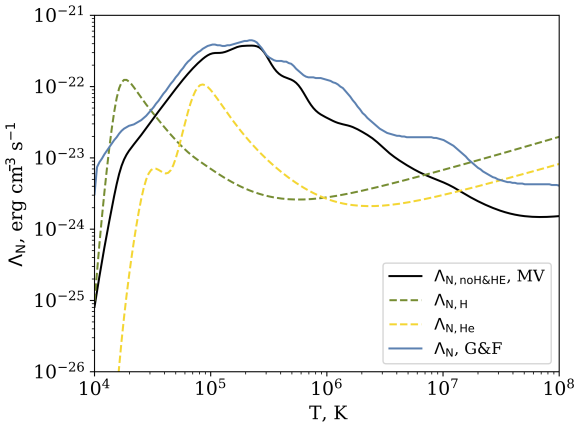

Fig. A.1. Cooling curve for the old tables (blue, Gnat & Ferland 2012) and for the new tables (black, MAPPINGS V), solar metallicity (Sembach et al. 2000). H and He contribution from MAPPINGS V is shown in green and yellow respectively.

Appendix A: Updated cooling curve

We updated the cooling rates for metals (all elements except hydrogen and helium) and helium in our simulations using the MAPPINGS V code (Binette et al. 1985; Sutherland & Dopita 1993; Dopita & Sutherland 2000; Dopita et al. 2013; Sutherland & Dopita 2017). MAPPINGS V is a 1D shock and photoionisation plasma modelling code. This code calculates the cooling rates of optically thin plasma under the CIE approximation while allowing for precise metallicity inputs for the first 30 elements (H to Zn). This update was motivated by significant advancements in the CHIANTI atomic database (Dere et al. 1997; Young et al. 1998; Del Zanna et al. 2015), which underpins both MAPPINGS V and other plasma codes. The completeness of MAPPINGS V database, particularly in the X-ray regime, is apparent compared to earlier versions (Sutherland & Dopita 2017). In the Chemistry module, we replaced the precomputed tables for helium and metals (excluding H and He) from Gnat & Ferland (2012) with new tables matching the solar-like metallicities of Sembach et al. (2000). Figure A.1 highlights how cooling curves differ primarily due to updated atomic data, with minor variations in CIE gas treatment between CLOUDY (used for the older tables) and MAPPINGS V.

Appendix B: 3D Sedov test

To investigate energy redistribution across cooling bands, we split cooling into optical (0 – 13.6 eV), UV (13.6 – 100 eV), and X-ray (100+ eV) components (Figures B.1, B.2). In dense media ($n = 100\,\mathrm{cm}^{-3}$, $T = 54\,\mathrm{K}$), cooling is dominated by the optical band, peaking in the shocked shell at late times ($t > 5\,\mathrm{kyr}$). UV emission forms a distinct shell, while X-ray emission is confined to the hot core and fades as the remnant cools. In contrast, low-density environments ($n = 0.1\,\mathrm{cm}^{-3}$, $T = 10500\,\mathrm{K}$) exhibit weak X-ray emission due to inefficient cooling, with optical and UV emissions persisting longer and the UV band peaking later.

Key evolutionary stages are defined by τ_{TR} (transition from Sedov-Taylor to radiative phase) and τ_{PDS} (pressure-driven snowplough phase), following Haid et al. (2016). The equations are as follows:

$$\tau_{\mathrm{TR}} = 4.15 \times (n_0/1\mathrm{cm}^{-3})^{-0.52} \times 10^4\mathrm{yr}, \tag{B.1}$$

$$\tau_{\mathrm{PDS}} = 7.80 \times (n_0/1\mathrm{cm}^{-3})^{-0.52} \times 10^4\mathrm{yr}, \tag{B.2}$$

where n_0 is the ambient number density. These formulas assume a standard metallicity and cooling curve, typical for neutral ISM conditions.

To include X-ray cooling effects, we performed radiative transfer simulations using XrayTheSpot (Figure B.3). This introduces additional heating mechanisms, such as photoionisation and Compton scattering, which slow the decline of internal energy. These effects are amplified in dense media, enhancing energy deposition and redistributing energy from high-energy bands to lower-energy photons via secondary ionisations. As a result, the 0 – 13.6 eV band gains more energy, altering cooling dynamics and energy evolution, consistent with observed SNR morphologies.

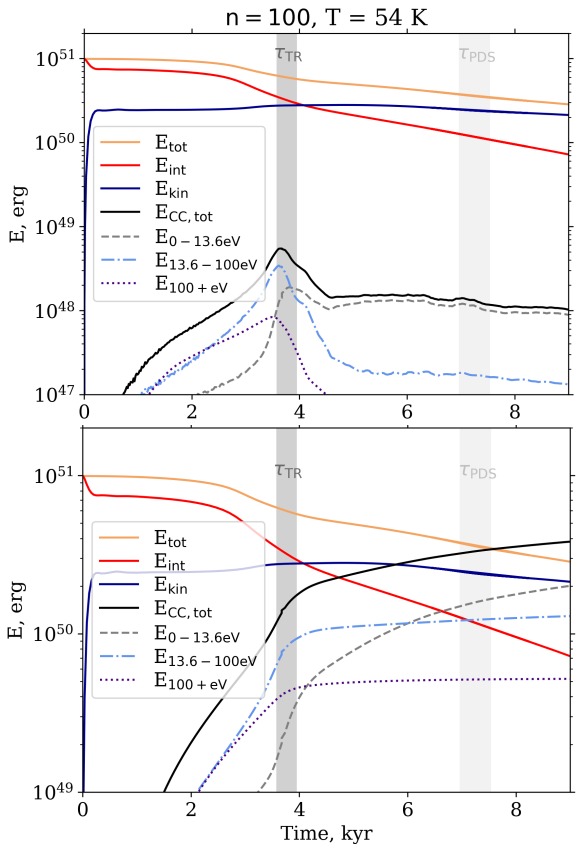

Fig. B.1. Top panel: evolution of the total internal energy (orange) and cooling bands. First, we see the sharp rise in X-ray and as gas cools very efficiently in the dense medium it drops. The EUV emission also has a smoother peak as the whole SNR bubble is emitting and then there is mainly a shell after the τ_{TR}. The details of the morphology can be seen in Figure B.2. Bottom panel: evolution of the cumulative cooling bands: 0 – 13.6 eV, FUV/optical (black dashed line), 13.6 – 100 eV, EUV (blue dash-dotted line), and 100+ eV, X-ray (purple dotted line). The vertical shaded regions mark key evolutionary stages: the transition time (τ_{TR}) where the SNR transitions from the Sedov-Taylor phase to the radiative phase, and τ_{PDS}, marking the pressure-driven snowplough phase. The internal energy E_{int} is showing a steady decline as energy is radiatively lost over time. The highest amount of energy is cooled via the FUV/optical band, then EUV and a small amount via the X-ray band.

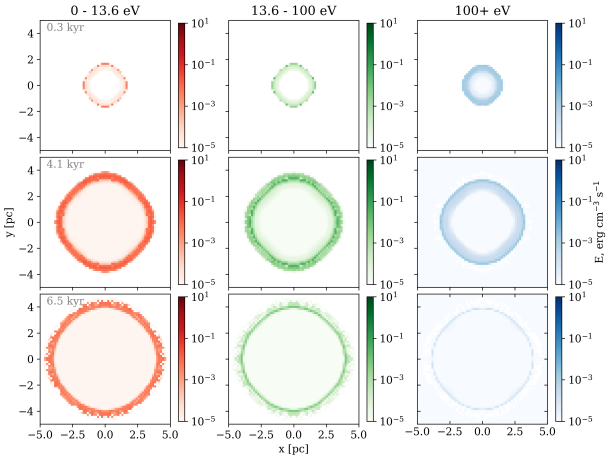

Fig. B.2. Slices of cooling emission from a SNR in a dense medium (n = 100 cm^{-3}) across three bands: optical/FUV (0 – 13.6 eV), ionising/EUV (13.6 – 100 eV), and X-ray (100+ eV). Rows show evolution at 0.3 kyr, 4.1 kyr, and 6.5 kyr. Initially (0.3 kyr), X-rays dominate the hot centre, with confined optical and UV emission. By 4.1 kyr, the UV forms a clear shell, and optical emission becomes more prominent. At 6.5 kyr, the optical band dominates the cooling shell, while X-ray emission fades.

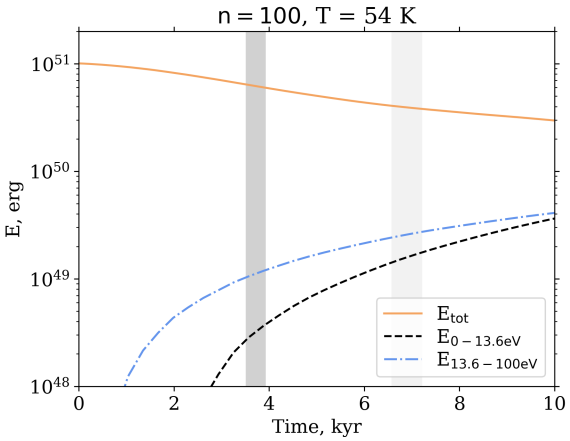

Fig. B.3. Same as the bottom panel in Figure B.1, but with the X-ray emission traced on-the-fly and non-cumulative total energy. We can see a slower decrease in the total energy due to additional sources of heating (cooling X-ray cells) and different energy distribution across FUV and EUV bands.

8

SUMMARY AND CONCLUSION

8.1 Summary

This thesis investigates the significance of radiative cooling from SN shocks in the ISM. We begin by post-processing SILCC-Zoom simulations to examine how the energy released via radiative cooling from SNe shocks interacting with the complex ISM is distributed across different energy bands and developed realistic models of optical emission from SNRs. Next, machine learning techniques are applied to the large volume of simulation data to identify key parameters influencing optical emission. Finally, X-ray energy band cooling is implemented directly into simulations, with the RCW 103 SNR as a test case, paving the way for fully integrated on-the-fly radiative cooling in simulations.

In the first paper (Makarenko et al., 2023), we explore the radiative cooling and observational characteristics of SNRs using high-resolution magnetohydrodynamic (MHD) simulations combined with post-processing radiative transfer modelling. The study is a post-processing of the SILCC-Zoom simulations. These simulations track molecular clouds formation, the ISM's evolution and the complex interaction of SNRs with a multiphase ISM. To analyse the contribution of radiative cooling, we developed a package, CESS, based on the plasma code MAPPINGS V, assuming collisional ionisation equilibrium cooling. As a result, a small part of the cooling radiation goes to the thermal X-ray (100+ eV) at the beginning of the SNR evolution. A significant portion of the cooling is shown to occur via the ionising radiation/UV energy band (13.6 – 100 eV). The remaining energy goes to the optical emission lines at the later stages of SNR evolution. Optical depth effects in this case significantly influence the escape of radiation. The interaction between the SNR and the surrounding ISM produces a complex morphology, with shock waves changing the plasma's local density, temperature, and ionisation states. These processes are critical in shaping the optical emission spectra and provide observational diagnostics, such as BPT diagrams, to interpret SNR properties. Optical emission in SNRs often originates from dense, shocked regions where ionisation and cooling are most efficient. However, the projectional alignment of these regions can lead to misinterpretations of their true spatial relationship with the shock front. It is especially relevant for emission from forbidden lines, such as [O III] and [N II], which are sensitive to density and temperature conditions and can appear offset from the shock structure. Additionally, we investigate the projectional effects and their impact on interpreting SNRs in observational data. The relative position of optical emission to the shock front and the contamination from background or foreground sources can complicate the identification and characterisation of SNRs, particularly in unresolved cases (typically, SNRs that are located outside of our Galaxy). Background contamination and line-of-sight blending can obscure the remnant's actual morphology and emission properties for unresolved SNRs, where the spatial scales are smaller than the observational resolution. We can use synthetic observations

generated from high-resolution simulations to disentangle these effects. Our model helps predict SNRs' observable signatures, accounting for complex ISM properties and projectional effects.

In the second paper (Smirnova et al., 2024), we extend the study of the cooling mechanisms and optical emission properties of SNRs interacting with molecular clouds using a combination of high-resolution SILCC-Zoom simulations, post-processing (CESS module) and machine learning techniques. The full dataset of these simulations (22 simulations) has both MHD and HD runs. Due to that, we can analyse the role of magnetic fields and environmental density in shaping the SNR evolution. SN was exploded at distances of 25 pc and 50 pc from the molecular cloud's centre of mass, allowing for a comparative assessment of how varying local conditions affect SNR dynamics and emission characteristics. Our study finds that optical emission is primarily influenced by the ambient density distribution, which dictates the evolution and morphology of the remnant. Magnetic fields, in contrast, do not significantly alter the optical line emission properties. This can happen either because the magnetic field of the simulated ISM should be stronger or because we do not take into account the magnetic field of the massive star progenitor. In any case, the magnetic fields that arise in such a setup (from the ISM B-field 4 μG to 100 – 130 μG at the shell of the SNR) are not strong enough to be distinguished in optical emission in the statistically significant manner. Overall, synthetic emission maps generated from the simulations reveal that denser environments produce more compact and radiatively efficient remnants, whereas remnants in lower-density regions evolve more diffusely. These differences allow for the statistical distinction between SNRs originating in varied ambient conditions, but attenuation effects caused by gas and dust can complicate this interpretation by mimicking environmental signatures. The analysis of optical line ratios, including [O III], [N II], and [S II], suggests that while these diagnostics provide valuable insights into the cooling processes, they are insufficient to fully characterise the surrounding ISM conditions, such as magnetic field strength or precise density variations. We highlight the need for statistical analyses and complementary diagnostics to improve our understanding of SNR-ISM interactions. The importance of combining detailed simulation datasets with advanced statistical methods will bridge the gap between theoretical predictions and observational data.

In the third paper, we model the X-ray emission from RCW 103 using hydrodynamical simulations implemented with the FLASH code. This includes the self-consistent, on-the-fly radiative cooling treatment from the SNR. The simulations begin with a uniform density box and a massive star (20 $M_{\odot}$) placed in the centre. It forms an HII region with wind and ionising radiation feedback around the star. Following a Type II SN explosion, we tracked radiative cooling in X-ray bands mimicking Chandra (0.3–0.85 keV, 0.85–1.70 keV, 1.7–3.0 keV, and 3+ keV). Using a backward ray-tracing scheme, each cell was treated as a radiation source, with emission and absorption calculated on the fly. In the first scenario – the so-called bow shock emission scenario – the progenitor star receives a slight kick before the SN stage. The simulated emissions, particularly in the soft X-ray band (below 1.7 keV), originate from the swept-up mass within the wind bubble and its interaction with the forward shock of the SNR. Pre-SN feedback plays a significant role in generating this emission, alongside the contribution from the surrounding ISM. Synthetic SNR maps reveal the evolution of circular diffuse X-ray emission. We propose that, in this scenario, the primary features of the X-ray morphology result from the complex interaction between the forward SN shock and the wind bubble.

In addition to these processes, other scenarios suggest that environmental effects may also influence the observed morphology of RCW 103. External factors such as nearby molecular clouds or ambient magnetic fields of ISM could contribute significantly to shaping the remnant's structure. To better understand the dominant cause—or combination of causes—behind the morphology, further observations are required. These could include polarisation maps or data revealing the magnetic field structure within the remnant. Moreover, simulating emissions in other observed bands would help constrain the contributing factors. This study represents a first step towards clarifying the physical processes shaping the RCW 103 X-ray morphology.

8.2 Conclusion

Supernovae significantly influence the ISM's chemical composition, thermal structure, and dynamics by injecting heavy elements, energy, and momentum. SNe heat the surrounding gas, induce turbulence, and power galactic outflows, all impacting star formation and molecular cloud formation while generating cosmic rays that further modify ISM conditions. Radiative cooling, a crucial energetic process during the SNR phase, is central to the mechanisms governing these interactions, and this work aims to address the key questions outlined in Chapter 1.

In this thesis, to address these challenges, first, a post-processing module CESS based on MAPPINGS V code is developed. We first evaluate how important radiative cooling is in the post-processing step for an SNR interacting with a MC and check which energy band most of the energy goes into. The distribution looks like this: the major part (around 80%) goes to ionising radiation/UV (13.6 – 100 eV), then to the optical band/FUV (0 – 13.6 eV) at the later stages of SNR evolution (around 15%) and the rest to the X-ray (100 eV+) at the very beginning of the SNR evolution. The CESS modules enables precise calculations of optical line emission from shock-heated gas (up to 10^8 K). This module generates detailed synthetic optical emission maps of SNRs interacting with MCs, allowing for direct comparisons with observational data. This approach demonstrated that environmental factors, such as ISM density and magnetic field strength, significantly affect the SNR morphology and optical emission. We examine how environmental variations and projection effects influence the observability of SNRs in the optical regime. Background contamination, projection effects, and the location of optical emission relative to the shock front all play key roles in distinguishing resolved and unresolved SNRs.

Further, we explore the influence of initial conditions, such as magnetic fields and ISM density distributions, on SNRs' optical line emission and evolutionary characteristics. To do it in a statistically significant manner, we use a dataset of 22 simulations. We found that magnetic fields have minimal impact on optical emission, and ambient density at the site of the explosion determines the remnant's morphology and radiative properties.

To include the radiative transfer treatment of radiative cooling, we performed simulations with FLASH of a SNR exhibiting thermal X-ray emission from shocks. We modelled the X-ray emission from RCW 103 using three-dimensional hydrodynamical simulations, achieving the first self-consistent, on-the-fly treatment of radiative cooling. We tracked X-ray emission across multiple bands by simulating the evolution and feedback of a massive star, followed by a Type II supernova explosion. The interaction of the shock wave with circumstellar material, pre-existing

ISM structures, or magnetic fields can reproduce the observational features of RCW 103's X-ray morphology.

These advancements mark a significant step forward in bridging the gap between simulations and observations. Including neglected physics, such as radiative cooling, provides critical insights into the physics of SNRs in the ISM.

8.3 Outlook

While current simulations provide valuable insights into the evolution of SNRs and their impact on the ISM, several aspects can be improved to increase their realism and predictive power. Some improvements can be addressed in the short term, while others require longer-term advancements in computational techniques and resources. In the following sections, we outline key areas for potential development and discuss strategies to incorporate them into future simulations.

One of the key improvements for future simulations is incorporating on-the-fly ionising radiation from SNRs in the energy range of 13.6 – 100 eV. As demonstrated in Paper I, the majority of radiative cooling energy is emitted in this band, making it a critical component for accurately modelling the feedback processes of SNRs. Accounting for this ionising radiation is more challenging than X-ray emission due to the lack of readily available cross-sections in current modules like OnTheSpot. Determining the efficiency of photon interaction in this energy range requires careful consideration and new developments in the code. This is an ongoing research study with significant implications for star-forming regions, where the dense environment would amplify the effects of ionising radiation. Changes in density, temperature, and ionisation state of the plasma would strongly influence the dynamics and energy deposition of SNRs into the ISM, potentially altering the evolution of the surrounding medium and the formation of new stars.

Another point that can be improved is the metallicity scaling of the cooling curve. Varying the metallicity in simulations significantly impacts the cooling curve, influencing the evolution of SNRs. Metals, as the most efficient coolants at specific temperatures (e.g., oxygen and iron at 10^5 – 10^6 K), play a crucial role in determining the rate at which energy is radiated away. Higher metallicity enhances cooling efficiency, leading to faster energy dissipation and smaller, denser remnants. Conversely, lower metallicity reduces cooling, resulting in longer-lived, hotter SNRs. This dependency on metallicity is vital for accurately modelling the ISM, as the chemical composition directly affects feedback processes and the thermal state of the surrounding medium. We also made available other commonly used metallicities (LMC, SMC) that are not proportionally scaled compared to the solar metallicities. Different metallicities are compared in Figure 24, where each cooling peak's most efficient coolant is marked.

A significant point is that currently, our simulations do not account for metal enrichment, as real SNRs significantly alter the chemical composition of the gas through ejecta. Including metal enrichment would drastically change the remnant's evolution and is crucial for realistic comparisons between simulations and observations (for example, see 3D simulations of SN 1987A, Orlando et al. 2020). This is particularly important for generating mock images for high-resolution X-ray spectroscopy or optical forbidden-line diagnostics. As a first step, yields from massive star evolution codes could be employed to model key coolants such as Fe or progenitor tracers like C, N, and O, with the amounts tailored to massive star evolution

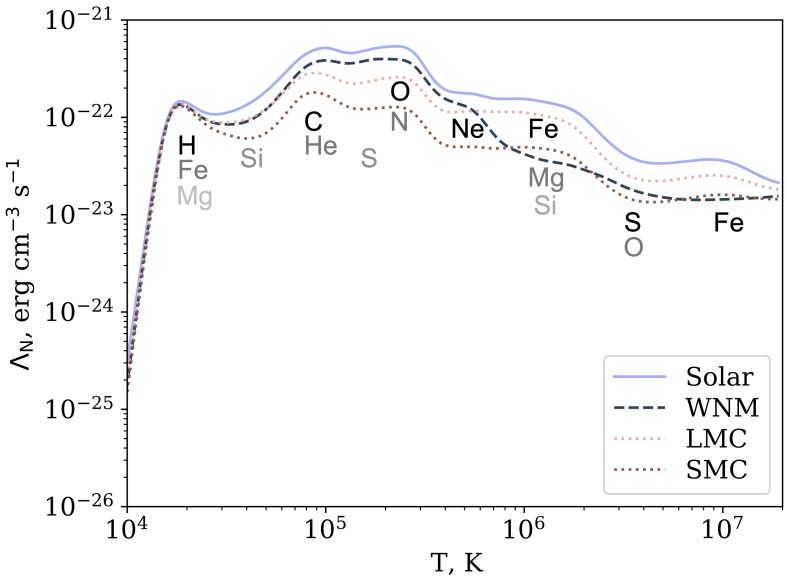

Figure 24: The radiative cooling curve for four different metallicities. WIM from Sembach et al. (2000) differs significantly from the standard ones (solar, LMC, SMC) and cannot be achieved by scaling the solar metallicity cooling curve. This discrepancy emphasises the importance of generating cooling curves using plasma codes such as MAPPINGS V, which account for detailed contributions from the first 30 elements of the periodic table. At best, observed metallicities for a specific object should be used to generate the cooling curve for simulations.

scenarios. Dynamically tracking all elements and ions would provide the most accurate representation, but such an approach is currently computationally not feasible. For example, adding three passive scalars in the simulations, such as Mg XI (to trace material from the stellar interior and gain insights into the nucleosynthesis process), Si XIV (one of the strongest lines in SNRs, that provides information about the explosion and shock heating), and Fe XXV (provides information about the inner layers of the progenitor star and the thermal structure of the plasma) would allow us to test how computationally expensive such additions are. These lines require a relatively short simulation time, as SNRs remain bright in X-rays for a limited period. Yet, they would still provide valuable insights, enabling direct comparisons between our simulations and XRISM (X-Ray Imaging and Spectroscopy Mission) observations.

To improve the physical accuracy of SNRs in our simulations, it is essential to extend the Chemistry module to account for non-equilibrium ionisation (NEI) conditions, rather than relying solely on the assumption of collisional ionisation equilibrium (CIE). During the early stages of SNR evolution, the plasma is often far from equilibrium due to rapid changes in temperature and density, resulting in ionisation and recombination timescales that significantly affect the ionisation states of elements (Vink, 2020). Implementing NEI would require tracking all ionisation states of various elements, which is a substantial computational challenge for the current version of our code. However, other astrophysical codes have successfully addressed this issue (e.g. Teşileanu et al. 2008; Mathew et al. 2024), offering potential strategies that could be adapted or incorporated into our framework. It will

require substation changes in the CHEMISTRY model (if not a completely new module). But employing NEI would provide a more realistic representation of plasma conditions, particularly in young SNRs, and enhance the realism of both the physical model and synthetic observations.

Another physical process that can be included in simulations is thermal conduction. Thermal conduction is the process by which heat is transferred from hotter to cooler regions within a gas due to collisions between particles. In the context of SNRs, incorporating thermal conduction into simulations would primarily affect the internal distribution of hot gas rather than the overall dynamics or large-scale interaction with the surrounding ISM. By smoothing temperature gradients within the remnant, thermal conduction would redistribute energy from the shock-heated interior to cooler regions, altering the density and temperature structure of the hot gas (Guo et al., 2024). This redistribution can significantly influence synthetic X-ray images by changing the brightness and morphology of the emission (Slavin et al., 2017), as well as modifying the cooling efficiency by shifting the conditions under which radiative processes occur. The characteristic timescale for thermal conduction depends on the temperature and density of the gas. It is typically short (on the order of 10^4 – 10^5 years) in an SNR's hot, diffuse interior. The characteristic length scale depends on the balance between conductive heat transport and radiative cooling (Cowie & McKee, 1977). Adding thermal conduction to SNR simulations would, therefore, provide a more realistic representation of the hot gas distribution and improve the reliability of synthetic X-ray observations.

As a last point, we can mention that currently, approximately 10% of the explosion energy is injected as cosmic rays, but this approach needs to be adjusted. With the development of a new shock-detection module and an improved cosmic ray prescription (Watanabe et al., in preparation), it will be possible to explore the impact of cosmic rays in different environmental conditions and to quantify the effective energy budget allocated to cosmic rays more accurately. Incorporating cosmic rays into simulations would also alter plasma conditions at the shock front, as cosmic rays influence these regions' pressure, temperature, ionisation states and non-thermal emission (for example, see simulations of SNRs with cosmic rays and magnetic fields by Diesing & Gupta 2024). For large-scale galaxy models, it is essential to develop effective models based on detailed SNR simulations that account for cosmic ray production (see the review by Ruszkowski & Pfrommer 2023) and SNR emission. These models must integrate the effects of varying surrounding properties, such as density and metallicity, to predict how SNR feedback shapes the ISM across diverse environments. By incorporating these elements into mock observations of entire galaxies, we can simulate observables such as X-ray and radio emission or optical forbidden lines, bridging small-scale SNR dynamics and large-scale galactic evolution. This multi-scale approach enables a better understanding of how cosmic ray feedback and SNR-driven turbulence influence star formation and ISM structure in galaxy-wide contexts.

ABBREVIATIONS

AMR	Adaptive mesh refinement
CESS	Cooling Emission from Simulated Supernova
CNM	Cold neutral medium
CSM	Circumstellar medium
EUV	Extreme ultraviolet (radiation)
FUV	Far-ultraviolet
HD	Hydrodynamics
ISM	Interstellar medium
MC	Molecular cloud
MHD	Magnetohydrodynamics
PDS	Pressure driven snow-plough (phase)
SN	Supernova
SNR	Supernova remnant
ST	Sedov-Taylor (phase)
TR	Transition (phase)
UV	Ultraviolet
WIM	Warm Ionised Medium
XRISM	X-Ray Imaging and Spectroscopy Mission
ZAMS	Zero Age Main Sequence

BIBLIOGRAPHY

Agertz, O. & Kravtsov, A. V., On the Interplay between Star Formation and Feedback in Galaxy Formation Simulations. 2015, ApJ, 804, 18

Allen, M. G., Groves, B. A., Dopita, M. A., Sutherland, R. S., & Kewley, L. J., The MAPPINGS III Library of Fast Radiative Shock Models. 2008, ApJS, 178, 20

Alsabti, A. W. & Murdin, P. 2017a, Handbook of Supernovae

Alsabti, A. W. & Murdin, P. 2017b, Handbook of Supernovae

Anderson, L. D., Camilo, F., Faerber, T., et al., Supernova Remnant Candidates Discovered by the SARAO MeerKAT Galactic Plane Survey. 2024, arXiv e-prints, arXiv:2409.16607

Baade, W. & Zwicky, F., On Super-novae. 1934, Proceedings of the National Academy of Science, 20, 254

Baczynski, C., Glover, S. C. O., & Klessen, R. S., Fervent: chemistry-coupled, ionizing and non-ionizing radiative feedback in hydrodynamical simulations. 2015, MNRAS, 454, 380

Bahcall, J. N. 1989, Neutrino Astrophysics

Bakes, E. L. O. & Tielens, A. G. G. M., The Photoelectric Heating Mechanism for Very Small Graphitic Grains and Polycyclic Aromatic Hydrocarbons. 1994, ApJ, 427, 822

Bedogni, R. & Woodward, P. R., Shock wave interactions with interstellar clouds. 1990, A&A, 231, 481

Berger, M. J. & Colella, P., Local Adaptive Mesh Refinement for Shock Hydrodynamics. 1989, Journal of Computational Physics, 82, 64

Berger, M. J. & Oliger, J., Adaptive Mesh Refinement for Hyperbolic Partial Differential Equations. 1984, Journal of Computational Physics, 53, 484

Bergin, E. A., Hartmann, L. W., Raymond, J. C., & Ballesteros-Paredes, J., Molecular Cloud Formation behind Shock Waves. 2004, ApJ, 612, 921

Bethe, H. A., Energy Production in Stars. 1939, Physical Review, 55, 434

Bethe, H. A., Supernova mechanisms. 1990, Reviews of Modern Physics, 62, 801

Bietenholz, M. F., Hester, J. J., Frail, D. A., & Bartel, N., The Crab Nebula's Wisps in Radio and Optical. 2004, ApJ, 615, 794

Binette, L., Dopita, M. A., & Tuohy, I. R., Radiative shock-wave theory. II. High-velocity shocks and thermal instabilities. 1985, ApJ, 297, 476

Blair, W. P. & Kirshner, R. P., Improved optical spectrophotometry of supernova remnants in M 33. 1985, ApJ, 289, 582

Blair, W. P., Sankrit, R., & Raymond, J. C., Hubble Space Telescope Imaging of the Primary Shock Front in the Cygnus Loop Supernova Remnant. 2005, AJ, 129, 2268

Bohlin, R. C., Savage, B. D., & Drake, J. F., A survey of interstellar H I from Lalpha absorption measurements. II. 1978, ApJ, 224, 132

Bouchut, F., Klingenberg, C., & Waagan, K., A multiwave approximate Riemann solver for ideal MHD based on relaxation. I: Theoretical framework. 2007, Numerische Mathematik, 108, 7

Bouchut, F., Klingenberg, C., & Waagan, K., A multiwave approximate Riemann solver for ideal MHD based on relaxation II: Numerical implementation with 3 and 5 waves. 2010, Numerische Mathematik, 115, 647

Branch, D. & Wheeler, J. C. 2017, Supernova Explosions

Brown, P. N., Byrne, G. D., & Hindmarsh, A. C., VODE: A Variable-Coefficient ODE Solver. 1989, SIAM Journal on Scientific and Statistical Computing, 10, 1038

Burrows, A., Hayes, J., & Fryxell, B. A., On the Nature of Core-Collapse Supernova Explosions. 1995, ApJ, 450, 830

Burton, M. G., Hollenbach, D. J., & Tielens, A. G. G. M., Line Emission from Clumpy Photodissociation Regions. 1990, ApJ, 365, 620

Chevalier, R. A., The interaction of supernovae with the interstellar medium. 1977, ARA&A, 15, 175

Chevalier, R. A., Supernova Remnants in Molecular Clouds. 1999, ApJ, 511, 798

Chevance, M., Krumholz, M. R., McLeod, A. F., et al. 2023, in Astronomical Society of the Pacific Conference Series, Vol. 534, Protostars and Planets VII, ed. S. Inutsuka, Y. Aikawa, T. Muto, K. Tomida, & M. Tamura, 1

Cioffi, D. F., McKee, C. F., & Bertschinger, E., Dynamics of Radiative Supernova Remnants. 1988, ApJ, 334, 252

Clark, P. C., Glover, S. C. O., Klessen, R. S., & Bonnell, I. A., How long does it take to form a molecular cloud? 2012, MNRAS, 424, 2599

Colella, P. & Woodward, P. R., The Piecewise Parabolic Method (PPM) for gas-dynamical simulations. 1984, Journal of Computational Physics, 54, 174

Compton, A. H., A Quantum Theory of the Scattering of X-rays by Light Elements. 1923, Physical Review, 21, 483

Condon, J. J. & Ransom, S. M. 2016, Essential Radio Astronomy

Cowie, L. L. & McKee, C. F., The evaporation of spherical clouds in a hot gas. I. Classical and saturated mass loss rates. 1977, ApJ, 211, 135

Dale, J. E., The modelling of feedback in star formation simulations. 2015, New A Rev., 68, 1

Dalgarno, A., Yan, M., & Liu, W., Electron Energy Deposition in a Gas Mixture of Atomic and Molecular Hydrogen and Helium. 1999, ApJS, 125, 237

de Avillez, M. A. & Breitschwerdt, D., Volume filling factors of the ISM phases in star forming galaxies. I. The role of the disk-halo interaction. 2004, A&A, 425, 899

Del Zanna, G., Dere, K. P., Young, P. R., Landi, E., & Mason, H. E., CHIANTI - An atomic database for emission lines. Version 8. 2015, A&A, 582, A56

Dere, K. P., Landi, E., Mason, H. E., Monsignori Fossi, B. C., & Young, P. R., CHIANTI - an atomic database for emission lines. 1997, A&AS, 125, 149

Dere, K. P., Landi, E., Young, P. R., & Del Zanna, G., CHIANTI-An Atomic Database for Emission Lines. IV. Extension to X-Ray Wavelengths. 2001, ApJS, 134, 331

Diesing, R. & Gupta, S., Nonthermal Signatures of Radiative Supernova Remnants II: The Impact of Cosmic Rays and Magnetic Fields. 2024, arXiv e-prints, arXiv:2411.18679

Dobbs, C. L., Bonnell, I. A., & Pringle, J. E., The formation of molecular clouds in spiral galaxies. 2006, MNRAS, 371, 1663

Dobbs, C. L., Krumholz, M. R., Ballesteros-Paredes, J., et al. 2014, in Protostars and Planets VI, ed. H. Beuther, R. S. Klessen, C. P. Dullemond, & T. Henning, 3–26

Dopita, M. A., Binette, L., Dodorico, S., & Benvenuti, P., Radiative shock-wave theory. I. Chemical abundance diagnostics and galactic abundance gradients. 1984, ApJ, 276, 653

Dopita, M. A. & Sutherland, R. S., The Importance of Photoelectric Heating by Dust in Planetary Nebulae. 2000, ApJ, 539, 742

Dopita, M. A., Sutherland, R. S., Nicholls, D. C., Kewley, L. J., & Vogt, F. P. A., New Strong-line Abundance Diagnostics for H II Regions: Effects of κ-distributed Electron Energies and New Atomic Data. 2013, ApJS, 208, 10

Doroshkevich, A. G. & Novikov, I. D., Mean Density of Radiation in the Metagalaxy and Certain Problems in Relativistic Cosmology. 1964, Soviet Physics Doklady, 9, 111

Draine, B. T. 2011, Physics of the Interstellar and Intergalactic Medium

Dubey, A., Daley, C., Zuhone, J., et al., Imposing a Lagrangian particle framework on an Eulerian hydrodynamics infrastructure in FLASH. 2012, ApJ Supplement, 201, 27

Dubey, A., Reid, L. B., Weide, K., et al., Extensible Component Based Architecture for FLASH, A Massively Parallel, Multiphysics Simulation Code. 2009, arXiv e-prints, arXiv:0903.4875

Dubner, G. & Giacani, E., Radio emission from supernova remnants. 2015, A&A Rev., 23, 3

Ekström, S., Georgy, C., Eggenberger, P., et al., Grids of stellar models with rotation. I. Models from 0.8 to 120 $M_{\odot}$ at solar metallicity (Z = 0.014). 2012, A&A, 537, A146

Federrath, C., Roman-Duval, J., Klessen, R. S., Schmidt, W., & Mac Low, M. M., Comparing the statistics of interstellar turbulence in simulations and observations. Solenoidal versus compressive turbulence forcing. 2010, A&A, 512, A81

Ferrand, G., Decourchelle, A., Ballet, J., Teyssier, R., & Fraschetti, F., 3D simulations of supernova remnants evolution including non-linear particle acceleration. 2010, A&A, 509, L10

Fesen, R. A., Blair, W. P., & Kirshner, R. P., Optical emission-line properties of evolved galactic supernova remnants. 1985, ApJ, 292, 29

Fesen, R. A. & Kirshner, R. P., Spectrophotometry of the supernova remnant IC 443. 1980, ApJ, 242, 1023

Fichtner, Y. A., Mackey, J., Grassitelli, L., Romano-Díaz, E., & Porciani, C., Connecting stellar and galactic scales: Energetic feedback from stellar wind bubbles to supernova remnants. 2024, A&A, 690, A72

Frank, A., Ray, T. P., Cabrit, S., et al. 2014, in Protostars and Planets VI, ed. H. Beuther, R. S. Klessen, C. P. Dullemond, & T. Henning, 451

Fryxell, B., Olson, K., Ricker, P., et al., FLASH: An Adaptive Mesh Hydrodynamics Code for Modeling Astrophysical Thermonuclear Flashes. 2000, ApJS, 131, 273

Gaches, B. A. L., Bisbas, T. G., & Bialy, S., The impact of cosmic-ray attenuation on the carbon cycle emission in molecular clouds. 2022, A&A, 658, A151

Gaches, B. A. L., Walch, S., Wünsch, R., & Mackey, J., Tree-based solvers for adaptive mesh refinement code FLASH - IV. An X-ray radiation scheme to couple discrete and diffuse X-ray emission sources to the thermochemistry of the interstellar medium. 2023, MNRAS, 522, 4674

Ganguly, S., Walch, S., Clarke, S. D., & Seifried, D., SILCC-Zoom: the dynamic balance in molecular cloud substructures. 2024, MNRAS, 528, 3630

Ganguly, S., Walch, S., Seifried, D., Clarke, S. D., & Weis, M., Unravelling the structure of magnetized molecular clouds with SILCC-Zoom: sheets, filaments, and fragmentation. 2023, MNRAS, 525, 721

Gatto, A., Walch, S., Low, M. M. M., et al., Modelling the supernova-driven ISM in different environments. 2015, MNRAS, 449, 1057

Gatto, A., Walch, S., Naab, T., et al., The SILCC project - III. Regulation of star formation and outflows by stellar winds and supernovae. 2017, MNRAS, 466, 1903

Girichidis, P., Seifried, D., Naab, T., et al., The SILCC project - V. The impact of magnetic fields on the chemistry and the formation of molecular clouds. 2018, MNRAS, 480, 3511

Girichidis, P., Walch, S., Naab, T., et al., The SILCC (SImulating the LifeCycle of molecular Clouds) project - II. Dynamical evolution of the supernova-driven ISM and the launching of outflows. 2016, MNRAS, 456, 3432

Glover, S. C. O. & Clark, P. C., Is molecular gas necessary for star formation? 2012, MNRAS, 421, 9

Glover, S. C. O., Federrath, C., Mac Low, M. M., & Klessen, R. S., Modelling CO formation in the turbulent interstellar medium. 2010, MNRAS, 404, 2

Glover, S. C. O. & Mac Low, M.-M., Simulating the Formation of Molecular Clouds. I. Slow Formation by Gravitational Collapse from Static Initial Conditions. 2007a, ApJS, 169, 239

Glover, S. C. O. & Mac Low, M.-M., Simulating the Formation of Molecular Clouds. II. Rapid Formation from Turbulent Initial Conditions. 2007b, ApJ, 659, 1317

Gnat, O. & Ferland, G. J., Ion-by-ion Cooling Efficiencies. 2012, ApJS, 199, 20

Godunov, S. K., A difference method for numerical calculation of discontinuous solutions of the equations of hydrodynamics. 1959, Mat. Sb. (N.S.), 47(89), 271

Goldsmith, P. F., Molecular Depletion and Thermal Balance in Dark Cloud Cores. 2001, ApJ, 557, 736

Goldsmith, P. F. & Langer, W. D., Molecular cooling and thermal balance of dense interstellar clouds. 1978, ApJ, 222, 881

Gong, M., Ostriker, E. C., & Wolfire, M. G., A Simple and Accurate Network for Hydrogen and Carbon Chemistry in the Interstellar Medium. 2017, ApJ, 843, 38

González-Servín, M. & González-Avilés, J. J., Numerical MHD simulations of solar flares and their associated small-scale structures. 2024, Monthly Notices of the Royal Astronomical Society, 528, 5098

Górski, K. M., Hivon, E., Banday, A. J., et al., HEALPix: A Framework for High-Resolution Discretization and Fast Analysis of Data Distributed on the Sphere. 2005, ApJ, 622, 759

Green, D. A., A revised catalogue of 294 Galactic supernova remnants. 2019, Journal of Astrophysics and Astronomy, 40, 36

Green, D. A., An updated catalogue of 310 Galactic supernova remnants and their statistical properties. 2024, arXiv e-prints, arXiv:2411.03367

Grenier, I. A., Black, J. H., & Strong, A. W., The Nine Lives of Cosmic Rays in Galaxies. 2015, ARA&A, 53, 199

Gritschneder, M., Naab, T., Walch, S., Burkert, A., & Heitsch, F., Driving Turbulence and Triggering Star Formation by Ionizing Radiation. 2009, ApJ, 694, L26

Gunasekera, C. M., van Hoof, P. A. M., Chatzikos, M., & Ferland, G. J., The 23.01 Release of Cloudy. 2023, Research Notes of the American Astronomical Society, 7, 246

Guo, M., Kim, C.-G., & Stone, J. M., Evolution of Supernova Remnants in a Cloudy Multiphase Interstellar Medium. 2024, arXiv e-prints, arXiv:2411.12809

Habing, H. J., The interstellar radiation density between 912 A and 2400 A. 1968, Bull. Astron. Inst. Netherlands, 19, 421

Hacar, A., Clark, S. E., Heitsch, F., et al. 2023, in Astronomical Society of the Pacific Conference Series, Vol. 534, Protostars and Planets VII, ed. S. Inutsuka, Y. Aikawa, T. Muto, K. Tomida, & M. Tamura, 153

Haid, S., Walch, S., Naab, T., et al., Supernova blast waves in wind-blown bubbles, turbulent, and power-law ambient media. 2016, MNRAS, 460, 2962

Haid, S., Walch, S., Seifried, D., et al., The relative impact of photoionizing radiation and stellar winds on different environments. 2018, MNRAS, 478, 4799

Hanasz, M., Strong, A. W., & Girichidis, P., Simulations of cosmic ray propagation. 2021, Living Reviews in Computational Astrophysics, 7, 2

Heger, A., Fryer, C. L., Woosley, S. E., Langer, N., & Hartmann, D. H., How Massive Single Stars End Their Life. 2003, ApJ, 591, 288

Helfand, D. J., Gotthelf, E. V., & Halpern, J. P., Vela Pulsar and Its Synchrotron Nebula. 2001, ApJ, 556, 380

Hennebelle, P. & Inutsuka, S.-i., The role of magnetic field in molecular cloud formation and evolution. 2019, Frontiers in Astronomy and Space Sciences, 6, 5

Hester, J. J., Raymond, J. C., & Blair, W. P., The Balmer-dominated Northeast Limb of the Cygnus Loop Supernova Remnant. 1994, ApJ, 420, 721

Hewitt, J. W., Rho, J., Andersen, M., & Reach, W. T., Spitzer Observations of Molecular Hydrogen in Interacting Supernova Remnants. 2009, ApJ, 694, 1266

Hillebrandt, W. & Niemeyer, J. C., Type IA Supernova Explosion Models. 2000, ARA&A, 38, 191

Hollenbach, D. & McKee, C. F., Molecule formation and infrared emission in fast interstellar shocks. I. Physical processes. 1979, ApJS, 41, 555

Hollenbach, D. J. & Tielens, A. G. G. M., Photodissociation regions in the interstellar medium of galaxies. 1999, Reviews of Modern Physics, 71, 173

Hopkins, P. F., A new class of accurate, mesh-free hydrodynamic simulation methods. 2015, MNRAS, 450, 53

Hoyle, F. & Fowler, W. A., Nucleosynthesis in Supernovae. 1960, ApJ, 132, 565

Iffrig, O. & Hennebelle, P., Mutual influence of supernovae and molecular clouds. 2015, A&A, 576, A95

Jackson, J. D. 1998, Classical Electrodynamics, 3rd Edition

Kennicutt, Robert C., J., The Global Schmidt Law in Star-forming Galaxies. 1998, ApJ, 498, 541

Kim, C.-G. & Ostriker, E. C., Three-phase Interstellar Medium in Galaxies Resolving Evolution with Star Formation and Supernova Feedback (TIGRESS): Algorithms, Fiducial Model, and Convergence. 2017, ApJ, 846, 133

Kim, C.-G., Ostriker, E. C., & Raileanu, R., Superbubbles in the Multiphase ISM and the Loading of Galactic Winds. 2017, ApJ, 834, 25

Klein, R. I., McKee, C. F., & Colella, P., On the Hydrodynamic Interaction of Shock Waves with Interstellar Clouds. I. Nonradiative Shocks in Small Clouds. 1994, ApJ, 420, 213

Klessen, R. S. & Glover, S. C. O., Physical Processes in the Interstellar Medium. 2016, Saas-Fee Advanced Course, 43, 85

Kolmogorov, A. N., Dissipation of Energy in Locally Isotropic Turbulence. 1941, Akademiia Nauk SSSR Doklady, 32, 16

Kowal, G., Lazarian, A., Vishniac, E. T., & Otmianowska-Mazur, K., Numerical Tests of Fast Reconnection in Weakly Stochastic Magnetic Fields. 2009, ApJ, 700, 63

Kritsuk, A. G., Lee, C. T., & Norman, M. L., A supersonic turbulence origin of Larson's laws. 2013, MNRAS, 436, 3247

Landau, L. D., To the Stars theory. 1932, Phys. Zs. Sowjet, 1, 285

Landau, L. D. & Lifshitz, E. M. 1959, Fluid mechanics

Landau, L. D. & Lifshitz, E. M. 1960, Electrodynamics of continuous media

Landi, E., Landini, M., Dere, K. P., Young, P. R., & Mason, H. E., CHIANTI - an atomic database for emission lines. III. Continuum radiation and extension of the ion database. 1999, A&AS, 135, 339

Larson, R. B., Turbulence and star formation in molecular clouds. 1981, MNRAS, 194, 809

Lazarian, A., Eyink, G. L., Jafari, A., et al., 3D turbulent reconnection: Theory, tests, and astrophysical implications. 2020, Physics of Plasmas, 27, 012305

Lepp, S. & Shull, J. M., The kinetic theory of H2 dissociation. 1983, ApJ, 270, 578

Li, W., Leaman, J., Chornock, R., et al., Nearby supernova rates from the Lick Observatory Supernova Search - II. The observed luminosity functions and fractions of supernovae in a complete sample. 2011, MNRAS, 412, 1441

Lohner, R., An adaptive finite element scheme for transient problems in CFD. 1987, Computer Methods in Applied Mechanics and Engineering, 61, 323

Mac Low, M.-M. & McCray, R., Superbubbles in Disk Galaxies. 1988, ApJ, 324, 776

Mackey, J., Walch, S., Seifried, D., et al., Non-equilibrium chemistry and destruction of CO by X-ray flares. 2019, MNRAS, 486, 1094

MacNeice, P., Olson, K. M., Mobarry, C., de Fainchtein, R., & Packer, C., PARAMESH: A parallel adaptive mesh refinement community toolkit. 2000, Computer Physics Communications, 126, 330

Makarenko, E. I., Walch, S., Clarke, S. D., et al., How do supernova remnants cool? - I. Morphology, optical emission lines, and shocks. 2023, MNRAS, 523, 1421

Maloney, P. R., Hollenbach, D. J., & Tielens, A. G. G. M., X-Ray–irradiated Molecular Gas. I. Physical Processes and General Results. 1996, ApJ, 466, 561

Masson, J., Chabrier, G., Hennebelle, P., Vaytet, N., & Commerçon, B., Ambipolar diffusion in low-mass star formation. I. General comparison with the ideal magnetohydrodynamic case. 2016, A&A, 587, A32

Mathew, A., Mackey, J., Celeste, M., Haworth, T. J., & Mellema, G., A multi-ion non-equilibrium solver for ionised astrophysical plasmas with arbitrary elemental abundances. 2024, arXiv e-prints, arXiv:2409.18904

Mathis, J. S., Mezger, P. G., & Panagia, N., Interstellar radiation field and dust temperatures in the diffuse interstellar medium and in giant molecular clouds. 1983, A&A, 128, 212

Micelotta, E. R., Matsuura, M., & Sarangi, A., Dust in Supernovae and Supernova Remnants II: Processing and Survival. 2018, Space Sci. Rev., 214, 53

Micic, M., Glover, S. C. O., Federrath, C., & Klessen, R. S., Modelling H_2 formation in the turbulent interstellar medium: solenoidal versus compressive turbulent forcing. 2012, MNRAS, 421, 2531

Mihalas, D. 1978, Stellar atmospheres

Naab, T. & Ostriker, J. P., Theoretical Challenges in Galaxy Formation. 2017, ARA&A, 55, 59

Nelson, R. P. & Langer, W. D., The Dynamics of Low-Mass Molecular Clouds in External Radiation Fields. 1997, ApJ, 482, 796

Nelson, R. P. & Langer, W. D., On the Stability and Evolution of Isolated BOK Globules. 1999, ApJ, 524, 923

Nomoto, K., Maeda, K., Tanaka, M., & Suzuki, T., Gamma-Ray Bursts and magnetar-forming Supernovae. 2011, Ap&SS, 336, 129

Nomoto, K., Thielemann, F. K., & Yokoi, K., Accreting white dwarf models for type I supernovae. III. Carbon deflagration supernovae. 1984, ApJ, 286, 644

Orlando, S., Ono, M., Nagataki, S., et al., Hydrodynamic simulations unravel the progenitor-supernova-remnant connection in SN 1987A. 2020, A&A, 636, A22

Osterbrock, D. E. & Ferland, G. J. 2006, Astrophysics of gaseous nebulae and active galactic nuclei

Ostriker, J. P. & McKee, C. F., Astrophysical blastwaves. 1988, Reviews of Modern Physics, 60, 1

Padoan, P. & Nordlund, Å., The Star Formation Rate of Supersonic Magnetohydrodynamic Turbulence. 2011, ApJ, 730, 40

Padoan, P., Pan, L., Haugbølle, T., & Nordlund, Å., Supernova Driving. I. The Origin of Molecular Cloud Turbulence. 2016, ApJ, 822, 11

Padovani, M., Galli, D., & Glassgold, A. E., Cosmic-ray ionization of molecular clouds. 2009, A&A, 501, 619

Pattle, K., Fissel, L., Tahani, M., Liu, T., & Ntormousi, E. 2023, in Astronomical Society of the Pacific Conference Series, Vol. 534, Protostars and Planets VII, ed. S. Inutsuka, Y. Aikawa, T. Muto, K. Tomida, & M. Tamura, 193

Peters, T., Naab, T., Walch, S., et al., The SILCC project - IV. Impact of dissociating and ionizing radiation on the interstellar medium and Hα emission as a tracer of the star formation rate. 2017, MNRAS, 466, 3293

Pihlström, Y. M., Sjouwerman, L. O., Frail, D. A., et al., Detection of Class I Methanol (CH_3OH) Maser Candidates in Supernova Remnants. 2014, AJ, 147, 73

Puls, J., Vink, J. S., & Najarro, F., Mass loss from hot massive stars. 2008, A&A Rev., 16, 209

Rathjen, T.-E., Naab, T., Girichidis, P., et al., SILCC VI - Multiphase ISM structure, stellar clustering, and outflows with supernovae, stellar winds, ionizing radiation, and cosmic rays. 2021, MNRAS, 504, 1039

Rathjen, T.-E., Naab, T., Walch, S., et al., SILCC - VII. Gas kinematics and multiphase outflows of the simulated ISM at high gas surface densities. 2023, MNRAS, 522, 1843

Rathjen, T.-E., Walch, S., Naab, T., et al., SILCC – VIII: The impact of far-ultraviolet radiation on star formation and the interstellar medium. 2024, arXiv e-prints, arXiv:2410.00124

Raymond, J. C., Shock waves in the interstellar medium. 1979, ApJS, 39, 1

Reed, J. E., Hester, J. J., Fabian, A. C., & Winkler, P. F., The Three-dimensional Structure of the Cassiopeia A Supernova Remnant. I. The Spherical Shell. 1995, ApJ, 440, 706

Reynolds, S. P., Supernova remnants at high energy. 2008, ARA&A, 46, 89

Rho, J. & Petre, R., Mixed-Morphology Supernova Remnants. 1998, ApJ, 503, L167

Roman-Duval, J., Federrath, C., Brunt, C., et al., The Turbulence Spectrum of Molecular Clouds in the Galactic Ring Survey: A Density-dependent Principal Component Analysis Calibration. 2011, ApJ, 740, 120

Roman-Duval, J., Jackson, J. M., Heyer, M., Rathborne, J., & Simon, R., Physical Properties and Galactic Distribution of Molecular Clouds Identified in the Galactic Ring Survey. 2010, ApJ, 723, 492

Rozwadowska, K., Vissani, F., & Cappellaro, E., On the rate of core collapse supernovae in the milky way. 2021, New A, 83, 101498

Ruszkowski, M. & Pfrommer, C., Cosmic ray feedback in galaxies and galaxy clusters. 2023, A&A Rev., 31, 4

Rybicki, G. B. & Lightman, A. P. 1979, Radiative processes in astrophysics

Sedov, L. I. 1959, Similarity and Dimensional Methods in Mechanics

Seifried, D., Haid, S., Walch, S., Borchert, E. M. A., & Bisbas, T. G., SILCC-Zoom: H_2 and CO-dark gas in molecular clouds - the impact of feedback and magnetic fields. 2020, MNRAS, 492, 1465

Seifried, D., Walch, S., Girichidis, P., et al., SILCC-Zoom: the dynamic and chemical evolution of molecular clouds. 2017, MNRAS, 472, 4797

Seifried, D., Walch, S., Haid, S., Girichidis, P., & Naab, T., Is Molecular Cloud Turbulence Driven by External Supernova Explosions? 2018, ApJ, 855, 81

Sembach, K. R., Howk, J. C., Ryans, R. S. I., & Keenan, F. P., Modeling the Warm Ionized Interstellar Medium and Its Impact on Elemental Abundance Studies. 2000, ApJ, 528, 310

Slane, P., Bykov, A., Ellison, D. C., Dubner, G., & Castro, D., Supernova Remnants Interacting with Molecular Clouds: X-Ray and Gamma-Ray Signatures. 2015, Space Sci. Rev., 188, 187

Slavin, J. D., Smith, R. K., Foster, A., et al., Numerical Simulations of Supernova Remnant Evolution in a Cloudy Interstellar Medium. 2017, ApJ, 846, 77

Smirnova, P., Makarenko, E. I., Clarke, S. D., et al., How do supernova remnants cool? II. Machine learning analysis of supernova remnant simulations. 2024, arXiv e-prints, arXiv:2411.12839

Snodin, A. P., Brandenburg, A., Mee, A. J., & Shukurov, A., Simulating field-aligned diffusion of a cosmic ray gas. 2006, MNRAS, 373, 643

Solomon, P. M., Rivolo, A. R., Barrett, J., & Yahil, A., Mass, Luminosity, and Line Width Relations of Galactic Molecular Clouds. 1987, ApJ, 319, 730

Spitzer, L. 1978, Physical processes in the interstellar medium

Strömgren, B., The Physical State of Interstellar Hydrogen. 1939, ApJ, 89, 526

Sutherland, R. S. & Dopita, M. A., Cooling Functions for Low-Density Astrophysical Plasmas. 1993, ApJS, 88, 253

Sutherland, R. S. & Dopita, M. A., Effects of Preionization in Radiative Shocks. I. Self-consistent Models. 2017, ApJS, 229, 34

Taylor, G., The Formation of a Blast Wave by a Very Intense Explosion. I. Theoretical Discussion. 1950, Proceedings of the Royal Society of London Series A, 201, 159

Teşileanu, O., Mignone, A., & Massaglia, S., Simulating radiative astrophysical flows with the PLUTO code: a non-equilibrium, multi-species cooling function. 2008, A&A, 488, 429

Tielens, A. G. G. M. 2005, The Physics and Chemistry of the Interstellar Medium

van Dishoeck, E. F. & Black, J. H., Comprehensive Models of Diffuse Interstellar Clouds: Physical Conditions and Molecular Abundances. 1986, ApJS, 62, 109

Vink, J. 2020, Physics and Evolution of Supernova Remnants

Walch, S., Girichidis, P., Naab, T., et al., The SILCC (SImulating the LifeCycle of molecular Clouds) project - I. Chemical evolution of the supernova-driven ISM. 2015, MNRAS, 454, 238

Walch, S. & Naab, T., The energy and momentum input of supernova explosions in structured and ionized molecular clouds. 2015, MNRAS, 451, 2757

Weisskopf, M. C., Hester, J. J., Tennant, A. F., et al., Discovery of Spatial and Spectral Structure in the X-Ray Emission from the Crab Nebula. 2000, ApJ, 536, L81

Wolfire, M. G., Hollenbach, D., McKee, C. F., Tielens, A. G. G. M., & Bakes, E. L. O., The Neutral Atomic Phases of the Interstellar Medium. 1995, ApJ, 443, 152

Woltjer, L., Supernova Remnants. 1972, ARA&A, 10, 129

Woosley, S. E. & Weaver, T. A., The physics of supernova explosions. 1986, ARA&A, 24, 205

Wünsch, R., Radiation transport methods in star formation simulations. 2024, Frontiers in Astronomy and Space Sciences, 11, 1346812

Wünsch, R., Walch, S., Dinnbier, F., et al., Tree-based solvers for adaptive mesh refinement code FLASH - II: radiation transport module TreeRay. 2021, MNRAS, 505, 3730

Wünsch, R., Walch, S., Dinnbier, F., & Whitworth, A., Tree-based solvers for adaptive mesh refinement code FLASH - I: gravity and optical depths. 2018, MNRAS, 475, 3393

Wurster, J., Price, D. J., & Bate, M. R., Can non-ideal magnetohydrodynamics solve the magnetic braking catastrophe? 2016, MNRAS, 457, 1037

Young, P. R., Landi, E., & Thomas, R. J., CHIANTI: an atomic database for emission lines. II. Comparison with the SERTS-89 active region spectrum. 1998, A&A, 329, 291

Zeldovich, Y. B. & Raizer, Y. P. 1966, Elements of gasdynamics and the classical theory of shock waves

Zhou, X., Su, Y., Yang, J., et al., A Systematic Study of Associations between Supernova Remnants and Molecular Clouds. 2023, ApJS, 268, 61

DATA AVAILABILITY

The data underlying this thesis will be shared on reasonable request to the supervisor.